Nuclear Quantum Dynamics: exploration and comparison of trajectory-based methods

Thomas Plé

PhD Thesis

Speciality: Physics

Doctoral School 397
Physics and Chemistry of Materials

Nuclear Quantum Dynamics: exploration and comparison of trajectory-based methods

Defended by

Thomas Plé

on December 15, 2020

Reviewers	Stuart Althorpe	University of Cambridge
	Michele Ceriotti	COSMO - EPFL
Examinators	Delphine Cabaret	IMPMC - Sorbonne Université
	Federica Agostini	Université Paris-Saclay
Advisors	Fabio Finocchi	INSP - CNRS
	Simon Huppert	INSP - Sorbonne Université
	Sara Bonella	CECAM - EPFL

Contents

iv

1 Introduction

Numerical simulations in chemistry and physics are today not only used to obtain the solution of non trivial models that are not analytically solvable, but mostly to interpret the outcome of experiments and to design new molecules or materials with desired properties. The two latter tasks often demand an unprecedented accuracy, which is in conflict with the development of methods that generally include many approximation steps. In this thesis work, we develop and explore numerical methods to address a particularly challenging aspect of the simulation of molecular and condensed matter systems: the inclusion of nuclear quantum effects in the calculation of time-dependent correlation functions, which are directly related to spectroscopy. In spite of recent developments and interesting progress, this problem is still largely open and has both theoretical and practical interest.

To exemplify the relevance of nuclear quantum effects, we focus on Hydrogen, the lightest and most abundant element in the Universe, which is a basic constituent of inorganic matter and living organisms. Its nucleus, even though it is much heavier than the electron, has a De Broglie wavelength at room temperature of the order of the Angström, comparable in many situations with interatomic distances. Thus, for this key element, quantum properties, such as tunnelling or zero-point energy, are often not negligible. Nuclear quantum effects (NQEs) are therefore relevant not only to describe processes of experimental significance occurring at low temperature [1, 2] or high pressure [3, 4, 5], but also surprisingly close to ambient conditions, as in the case of reactions involving proton transfer [6, 7] or displaying significant isotopic effects [8, 9, 10, 11, 12, 13]. The growing interest in quantum computing, and, in general, in engineering of materials approaching scales where classical mechanics fails, further motivates work in this area. It is therefore of great interest to understand and model the quantum behavior of nuclei both from the statistical and dynamical points of view. In this thesis, we explore theories and develop numerical methods that treat both aspects, with a special focus on quantum dynamics. The field of quantum dynamics being very large, we will limit our scope to nuclear systems at thermal equilibrium, with the electronic degrees of freedom treated in the Born-Oppenheimer approximation (*i.e.* assuming an adiabatic separation between the electronic and nuclear time scales).

Currently, most simulations involving large atomic systems, for example in biochemistry, use empirical potential energy surfaces to account for the electronic degrees of freedom (in the Born-Oppenheimer approximation) and treat the nuclei as classical particles. These empirical potential energy surfaces are often designed to reproduce some experimental properties using classical dynamics for the nuclei. The quantum nature of the nuclei is thus hidden in the construction of the empirical potential. This behavior greatly hinders the reliability and generalizability of such potentials which break down when nuclear quantum effects are strong. Moreover this approach is not fully satisfying conceptually as it does not improve our understanding of the quantum processes at the atomic scale.
On the other hand, first-principles methods to compute the Born-Oppenheimer potential energy (such as the density functional theory) have so far been restricted to relatively small systems and short time scales. However, in the recent years, very fast progress has been made in the advanced methods aiming at reliably interpolating the results of first-principles calculations, for example using polarizable force fields [14, 15, 16, 17] or machine-learning techniques [18, 19, 20, 21, 22, 23, 24]. These methods provide accurate potential energy surfaces at a much lower computational cost and can be used to study larger systems over longer time scales. These accurate potentials, however, which do not include NQEs implicitly, can give disappointing results when coupled to classical dynamics of the nuclei [24, 25]. NQEs should therefore be accounted for explicitly to obtain fully quantum simulations of both electrons and nuclei which could in principle explain and predict experimental results in various conditions of temperature and pressure, and in complex chemical environments.

For distinguishable particles, the evaluation of **time-independent** statistical properties has been essentially solved within the framework of path integrals (PI) by mapping the quantum thermal density into a Boltzmann-like function for an isomorphic classical system [26, 27, 28, 29], often referred to as a "ring-polymer". In this isomorphism, each quantum particle is represented via a set of replicas, or beads, governed by a purely coordinate-dependent potential. The representation is exact in the limit of an infinite number of replicas and its numerical convergence can be systematically tested as a function of this number. Classical techniques can then be applied to sample the density with a cost that increases linearly with the number of replicas compared to the classical case.
Although path integrals do provide the reference method, their numerical cost can become problematic if not prohibitive for systems requiring large number of replicas for convergence, especially when first-principles interactions are needed. This motivated the development of alternative approaches, in particular the family of the

Quantum Thermal Bath (QTB) and quantum thermostat schemes, that reproduce statistical quantum properties such as zero point energy via a Langevin equation with colored noise [30, 31]. Although not rigorously derivable, these equations can be integrated at a cost comparable to that of classical calculations and they have proved useful for several interesting many-dimensional systems [4, 5, 32, 33, 34, 35].

On the other hand, the modelling of nuclear quantum dynamics, *i.e.* the computation of **time-dependent** properties of the nuclei, remains a very important theoretical challenge. These dynamical properties, captured by time correlation functions (see section 2.2.2), are relevant as they can be probed through different experimental techniques such as infrared/Raman spectroscopy or measurement of rate constants. Since direct resolution of the time-dependent Schrödinger equation is impossible for large systems due to its exponential scaling with the number of degrees of freedom, approximate schemes must be designed. Some methods attempt to mitigate the exponential scaling with smart choices of basis to represent the wavefunction. Examples of these methods are the Multi-Configuration Time-Dependent Hartree (MCTDH, see ref. [36]) and the Discrete Variable Representation (DVR, see ref. [37]). These methods can yield highly accurate results but are computationally very intensive and, for completely realistic interactions, are usually limited to systems containing at most a dozen degrees of freedom.
The real-time path integral formulation of quantum dynamics also enables, in principle, to compute time-dependent properties exactly. It is however computationally problematic as it relies on averaging over an infinite number of paths weighted by a phase factor. This phase factor prevents using standard statistical methods (such as importance sampling) and oscillates widely so that a brute force average is very difficult. This incarnation of the so-called sign problem in quantum dynamics makes the use of path integrals as problematic as the exponential scaling of the Schrödinger equation. Thus real-time PIs are often impossible to manage for large systems (although accurate approximate schemes have been devised for systems in which only a small subset of degrees of freedom must be treated accurately[38, 39]). More computationally affordable approaches therefore have to be explored in order to study larger systems.
In this thesis, we will focus on trajectory-based methods as they provide computationally efficient approximations for treating mildly quantum particles. Indeed, in most conditions of temperature and pressure, even the Hydrogen nucleus does not display highly quantum behaviors such as deep tunneling or quantum coherence. The most relevant quantum effect for this thesis is thus zero-point energy, that can be well reproduced by trajectory-based methods. Furthermore, in systems containing

large numbers of degrees of freedom, the decoherence due to the interaction with a complex environment often reduce the time scales in which quantum effects are relevant, enabling a reasonable description with methods using some form of classical propagation to derive short-time approximations of the quantum propagator. A family of such methods exploits the dynamics of the PI ring polymer in order to approximate nuclear quantum dynamics. The most common representatives of this family are Centroid Molecular Dynamics [40, 41, 42, 43, 44] (CMD) and Ring-Polymer Molecular Dynamics [45] (RPMD).

Closer descendants of time-dependent path integrals are found in the family of semi-classical methods. These are derived from stationary phase approximations of the quantum time propagator or of pairs of propagators appearing in the expression of time correlation functions (TCFs). One of the simplest and widely used methods in this family is the Linearized Semi-Classical Initial Value Representation (LSC-IVR, sometimes also referred to as classical Wigner) which couples quantum statistics and classical dynamics to approximate quantum time correlation functions at thermal equilibrium [46]. This method relies on the Wigner thermal distribution which allows to rewrite quantum statistical mechanics in a (generalized) phase space, with strong analogies to classical mechanics. The Wigner distribution is thus a bridge between the quantum and classical formalisms (more details in sections 2.2.2 and 3.1). However, its computation presents some notable practical difficulties and, since the analytic form of this distribution is generally unknown, one must rely on numerical methods to estimate it. This calculation is highly non-trivial (for reasons that will become clear in section 2.2) and the design of approximations for the Wigner distribution is an important topic of research (see for example refs. [47, 48, 49, 50, 51, 52]). In section 3.1 we present some of the most common approximations to the Wigner density and in chapter 4, we introduce a new approximation which constitutes the core of this thesis.

Recently, many other trajectory-based schemes have been proposed to compute dynamical properties (see for example [53, 54, 55, 56]). Most notably for this thesis, the QTB trajectories also allow to compute approximate quantum TCFs [4]. The QTB presents some limitations such as zero-point energy leakage (ZPEL, see refs. [57] and section 3.3 of this work) but recent improvements have been made to monitor and correct the ZPEL in QTB simulations [58]. These developments open up its use for more systems with more reliable results and, in this work, a particular focus will be given to the comparison of the QTB to more standard methods.

Within this flourishing diversity of methods, it is important to be able to distinguish and compare the different approximations. Currently, two limiting cases constitute the "bare minimum" for an approximate quantum dynamics method: it must be

exact in the classical (high-temperature) limit and for the harmonic potential. All of the approaches presented in this work fulfill this criterion and those that do not are typically considered less interesting by the community. Comparison of methods beyond these limiting cases is however quite difficult and we usually lack quantitative and rigorous arguments. Therefore, one of the main goal of this thesis is to systematically compare a set of common methods (along with the newly developed ones) on a collection of simple models in order to better understand in which cases and how they differ. As we shall see, this comparison enables to compare the performance of different approaches with respect to spectral features that are typically associated with some kind of coherence: overtones, combination bands, and Fermi resonances. This is interesting – and has motivated recent numerical research [59] – because the inability to reproduce this kind of features is often attributed to the (generalized) classical dynamics adopted. Here we shall provide analytical results and numerical evidence suggesting that the situation is more complex and that classical dynamics cannot "always be blamed".

The thesis is organized as follows. In chapter 2, we lay down the theoretical framework of quantum statistical mechanics and set the notations. In this chapter, we focus on the definition of time-dependent properties and in particular of time correlation functions. In chapter 3, we present the trajectory-based methods for approximate quantum dynamics that are the most relevant for this work and provide the necessary details for their implementation. The chapters 4, 5 and 6 contain the original contribution of this work, organized as follows. In chapter 4, we introduce a new approximation to the Wigner distribution based on the Edgeworth expansion. We also describe an original generalized Langevin dynamics, the Wigner-Langevin Dynamics (WiLD), that conserves this approximation and we show, on some model systems, that it can be used as an *ad hoc* approximation to quantum dynamics. The new sampling scheme for the Wigner distribution, combined with classical dynamics, also provides an interesting variation on the theme of linearized initial value representation. We analyze the advantages offered by the more accurate sampling of the initial conditions that we propose, compared to alternatives. In chapter 5, we compare the results of different approximate methods on simple models for some relevant anharmonic effects in vibrational spectra (overtones, combination bands and Fermi resonances). We derive analytical expressions, within the perturbation theory, that allow to quantitatively compare the accuracy of the different methods and shed some light on the origin of their differences. Finally, in chapter 6, we extend our analysis to more realistic and complex systems (namely liquid and solid-phase water) in order to assess the performance of the newly

introduced methods and to test the generalizability of the observations of chapter 5.

2 Theoretical Framework

In this chapter, we lay down the theoretical framework for statistical mechanics at thermal equilibrium and define the objects of interest for this work. We will particularly focus on defining time correlation functions in the quantum framework (some relevant trajectory-based methods used to compute them are reviewed in chapter 3).

This chapter is meant to set the notations and will be used as reference in the following of the thesis. Most of its content is detailed in ref. [60] and other standard statistical mechanics textbooks.

In this chapter and in chapter 3, we will present the formalism for a unidimensional system modeled by the (time-independent) potential $V(q)$. The generalization to multiple degrees of freedom to treat atomic systems within the Born-Oppenheimer approximation is straightforward (unless stated otherwise).

2.1 Classical statistical mechanics at thermal equilibrium

We consider in this section a classical system and denote (q, p) the phase space vector with q the position and p the momentum. In the canonical ensemble, the thermal equilibrium of this classical system is characterized by the Boltzmann probability density on the phase space:

$$\rho_{\mathrm{cl}}(q,p) = \frac{e^{-\beta(p^2/2m+V(q))}}{\int \mathrm{d}q\mathrm{d}p\; e^{-\beta(p^2/2m+V(q))}} \tag{2.1}$$

with $\beta = 1/k_B T$ the inverse thermal energy and m the mass of the system. In the following, we will only consider the case of a time-independent potential $V(q)$, yielding a time-independent probability density.

Statistical properties of the system are computed by averaging an observable (a function of the phase space vector for a classical system) over the Boltzmann density. Statistical physical properties fall into two categories: time-independent (static)

properties and time-dependent (dynamical) properties. The average kinetic energy (which is related to the temperature by the equipartition principle) is an example of a static property. On the other hand, infrared and Raman vibrational spectra (for example) are dynamical properties of the system. The average value of the observable $A(q,p)$ is a static property given by:

$$\langle A \rangle_{\text{cl}} = \int \mathrm{d}q\mathrm{d}p \; \rho_{\text{cl}}(q,p) A(q,p) \tag{2.2}$$

$\langle A \rangle_{\text{cl}}$ can be estimated by averaging over a large number of configurations, drawn randomly according to the Boltzmann distribution. This random draw can be performed using Monte Carlo methods (for example with the Metropolis algorithm) or thermostatted molecular dynamics (for example with Langevin dynamics).

Dynamical properties are more involved than static properties since they depend on time (and more precisely on time differences since the distribution is time-independent). Most relevant dynamical quantities can be related to time correlation function (TCFs). The TCF of observables $A(q,p)$ and $B(q,p)$ with a time difference t that we will denote $c_{AB}(t)$ is given by:

$$\begin{aligned} c_{AB}(t) &= \int \mathrm{d}q\mathrm{d}p \; \rho_{\text{cl}}(q,p) A(q,p) e^{i\mathcal{L}_{cl}t} B(q,p) \\ &= \langle A(q,p) B(q_t,p_t) \rangle_{\text{cl}} \end{aligned} \tag{2.3}$$

The time evolution operator $e^{i\mathcal{L}_{cl}t}$ acts on $B(q,p)$ by replacing (q,p) by the phase space point (q_t,p_t) obtained after a Newtonian evolution over a time t starting from position q and momentum p. The classical Liouville operator $i\mathcal{L}_{cl}$ is given by:

$$i\mathcal{L}_{\text{cl}} = \frac{p}{m}\frac{\partial}{\partial q} - \frac{\partial V(q)}{\partial q}\frac{\partial}{\partial p} \tag{2.4}$$

and provides the equations of motion of the classical system.

The direct application of equation (2.3) to estimate TCFs implies sampling initial configurations (q,p) from the Boltzmann distribution (using the Monte Carlo approach for example), computing the first observable $A(q,p)$, propagating the phase space vector using the classical equations of motion to obtain (q_t,p_t), multiplying the second observable to obtain $A(q,p)B(q_t,p_t)$ and finally averaging the results over all samples for each time t. Another method exploits the property of ergodicity, i.e. the fact that a single MD trajectory explores all microstates with the correct probability distribution. For an ergodic dynamics, the Wiener-Khinchin theorem [61] states that TCFs can be extracted from the Fourier transform of a single trajectory, which is numerically more efficient than the direct method. Ergodicity can be assumed in

the case of large systems (in the thermodynamic limit), even for conservative (NVE) dynamics, or it can be actively enforced using a mild thermostat (for example a Langevin thermostat with a small coupling to the thermal bath). While the thermostat will modify the Newtonian dynamics (and thus the time correlation functions), it is sometimes possible to either minimize the coupling to the thermostat or to recover the correct TCF via post-processing (see for example ref. [62]).

2.2 Quantum statistical mechanics at thermal equilibrium

The thermal equilibrium state of a quantum system is characterized by the thermal density operator $\hat{\rho}$ defined as:

$$\hat{\rho} = \frac{e^{-\beta\hat{H}}}{\mathrm{Tr}\left[e^{-\beta\hat{H}}\right]} = \frac{e^{-\beta\hat{H}}}{\mathcal{Z}} \tag{2.5}$$

with $\hat{H}$ the Hamiltonian operator of the system, $\mathrm{Tr}[\,\cdot\,]$ the trace function and $\mathcal{Z} = \mathrm{Tr}\left[e^{-\beta\hat{H}}\right]$ the partition function. Note that, as for the classical case, we only consider here time-independent Hamiltonians. In the following, we will use unidimensional notations. The generalization to multiple degrees of freedom is straightforward in the case of distinguishable particles (often referred to as boltzmannons in contrast with fermions and bosons). The density operator can then be used to express both static and dynamical properties.

2.2.1 Static properties

The thermal average of a physical observable described by the operator $\hat{A}$ is given by:

$$\left\langle \hat{A} \right\rangle = \mathrm{Tr}\left[\hat{\rho}\hat{A}\right] \tag{2.6}$$

In practice, to compute a physical property, one has to choose a representation basis. For example, if one can solve the Schrödinger equation for the system, the density operator can be rewritten as a statistical mixture of wavefunctions. We will also present two alternative representations, namely the path integrals form of the density operator and its phase-space expression using Wigner's formalism.

Statistical mixture of wavefunctions

Let us denote $|\Psi_i\rangle$ the eigenstates (wavefunctions) of the Hamiltonian operator with eigenvalues E_i (energies). One can rewrite the density operator as:

$$\hat{\rho} = \frac{\sum_i e^{-\beta E_i} |\Psi_i\rangle \langle \Psi_i|}{\sum_i e^{-\beta E_i}} \tag{2.7}$$

and compute any thermal average as:

$$\left\langle \hat{A} \right\rangle = \frac{\sum_i e^{-\beta E_i} \langle \Psi_i | \hat{A} | \Psi_i \rangle}{\sum_i e^{-\beta E_i}} \tag{2.8}$$

This expression is straightforward to apply when one can solve the Schrödinger equation. For large systems however, analytical or numerical solution of the Schrödinger equation is usually out of reach. In such cases, it is more efficient to use Feynman's path integrals representation of the density operator.

Path integrals expression

In the framework of path integrals, one usually focuses on observables that depend on position only (that we will denote $A(\hat{q})$) and expands the trace in (2.6) in position representation, yielding:

$$\langle A(\hat{q}) \rangle = \frac{1}{\mathcal{Z}} \int \mathrm{d}q \, \langle q | e^{-\beta \hat{H}} | q \rangle \, A(q) \tag{2.9}$$

where $A(q)$ is now simply a function of q. The difficulty is then to compute the diagonal elements of the density operator $\langle q | e^{-\beta \hat{H}} | q \rangle$. To do so, we separate the Hamiltonian in a kinetic term K and potential term V: $\hat{H} = K(\hat{p}) + V(\hat{q})$. Since $\hat{q}$ and $\hat{p}$ do not commute, the Hamiltonian operator is not diagonal in position representation and thus one cannot directly express $e^{-\beta \hat{H}} |q\rangle$. Separately however, $e^{-\beta K(\hat{p})}$ and $e^{-\beta V(\hat{q})}$ can be expressed in position representation. It is then tempting to split the exponential but since $\hat{q}$ and $\hat{p}$ do not commute,

$$e^{-\beta \hat{H}} \neq e^{-\beta K(\hat{p})} e^{-\beta V(\hat{q})} \tag{2.10}$$

One can show that at high temperature *i.e.* for a small inverse temperature $\epsilon \to 0$, one obtains:

$$e^{-\epsilon \hat{H}} = e^{-\frac{\epsilon}{2} V(\hat{q})} e^{-\epsilon K(\hat{p})} e^{-\frac{\epsilon}{2} V(\hat{q})} + \mathcal{O}\left(\epsilon^3\right) \tag{2.11}$$

By noting that $e^{-\beta\hat{H}} = \left(e^{-\frac{\beta}{\nu}\hat{H}}\right)^{\nu}$ for any integer ν, we obtain the symmetric Trotter break up of the density operator:

$$e^{-\beta\hat{H}} = \left(e^{-\frac{\beta}{2\nu}V(\hat{q})}e^{-\frac{\beta}{\nu}K(\hat{p})}e^{-\frac{\beta}{2\nu}V(\hat{q})}\right)^{\nu} + \mathcal{O}\left(\frac{\beta^3}{\nu^2}\right) \tag{2.12}$$

and the exact density operator is recovered in the limit $\nu \to \infty$. Note that the error is of second order in $1/\nu$ in eq. (2.12) because we accumulate ν times the error of (2.11).

By inserting resolutions of the identity in position representation $\hat{\mathrm{I}} = \int \mathrm{d}x \ |x\rangle \langle x|$ between each of the ν slices, we obtain the path integral expression of the diagonal elements of the density operator:

$$\frac{1}{\mathcal{Z}} \langle q|e^{-\beta\hat{H}}|q\rangle = \lim_{\nu\to\infty} \int \mathrm{d}q_1 \ldots \mathrm{d}q_{\nu-1} \ \rho_{\text{PI}}(q_1, \ldots, q_{\nu-1}, q) \tag{2.13}$$

with ρ_{PI} the path integral distribution given by [60]:

$$\rho_{\text{PI}}(q_1, \ldots, q_\nu) = \frac{\exp\left\{-\frac{\beta}{\nu}\sum_{i=1}^{\nu}\left(\frac{1}{2}m\omega_\nu^2(q_i - q_{i-1})^2 + V(q_i)\right)\right\}}{\int \mathrm{d}q_1 \ldots \mathrm{d}q_\nu \ \exp\left\{-\frac{\beta}{\nu}\sum_{i=1}^{\nu}\left(\frac{1}{2}m\omega_\nu^2(q_i - q_{i-1})^2 + V(q_i)\right)\right\}} \tag{2.14}$$

with $\omega_\nu = \nu/\beta\hbar$ and the cyclic condition $q_0 = q_\nu$. The density matrix is thus formally rewritten as the classical distribution of an extended system $(q_1, \ldots, q_\nu)$ of dimension ν. This extended system is composed of ν (classical) replica of the system (the so-called "beads") at positions q_i $(i = 1, \ldots, \nu)$ which are independently subject to the physical potential $V(q_i)$ and are connected to their nearest neighbors q_{i+1} and q_{i-1} via a harmonic potential of frequency ω_ν. This extended system is often called a "ring-polymer" (see figure 2.1) in analogy with the models of polymer physics. This rewriting is known as the quantum-classical isomorphism devised by Feynman. It is also often referred to as "imaginary-time" path integrals by analogy with the similar process used to rewrite the quantum time propagator $e^{-i\hat{H}t/\hbar}$, the operator $e^{-\beta\hat{H}}$ is then referred to as the imaginary-time propagator.

Using (2.14) and its cyclic invariance, one can compute static properties as:

$$\langle A(\hat{q})\rangle = \lim_{\nu\to\infty} \int \mathrm{d}q_1 \ldots \mathrm{d}q_\nu \ \rho_{\text{PI}}(q_1, \ldots, q_\nu)\left(\frac{1}{\nu}\sum_{i=1}^{\nu} A(q_i)\right) \tag{2.15}$$

In this form, $\langle A(\hat{q})\rangle$ is obtained as a classical average for an equivalent system in an extended space, subject to an effective potential expressed in (2.14) and one can use one of the various simulation techniques devised for classical systems in order to sample the distribution ρ_{PI} such as Monte Carlo (PIMC) or thermostatted

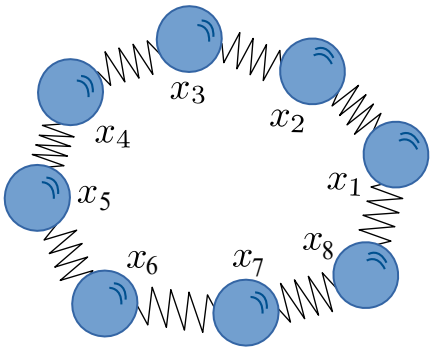

Fig. 2.1.: Schematic representation of the ring polymer path integral for $\nu = 8$. Each bead $x_1, \ldots, x_\nu$ (represented by the blue circles) is subject to the physical potential and connected to its nearest neighbors via a harmonic potential (represented by the springs).

molecular dynamics (PIMD). At high temperature, the error made when splitting the imaginary-time propagator is small and thus equation (2.13) converges with few beads. We can also see that the stiffness of the harmonic springs connecting the beads is proportional to ν/β so that in the high-temperature limit, the ring polymer is very stiff and collapses to one point so that the classical expressions of paragraph 2.1 are recovered. On the other hand, at low temperature, the ring polymer is very floppy and delocalized so that equation (2.13) requires many beads to converge. The details of the convergence depends on the specific shape of the potential and on the observables one needs to compute so that it must be systematically checked for each system.

The Wigner thermal distribution

Up to this point, we mainly focused on static properties depending on position only. It is more involved to compute momentum-dependent observables or mixed position-momentum observables. Indeed, because of the Heisenberg uncertainty principle, a quantum system cannot be localized in phase-space and thus a joint position-momentum probability density, such as the Boltzmann density, cannot be defined. Still, mixed position-momentum representations of the density operator can be built which share important aspects with the Boltzmann density. One such representation is the Wigner thermal distribution [63] defined as:

$$\rho_{\mathrm{w}}(q,p) = \frac{1}{2\pi\hbar}\int \mathrm{d}\Delta\; e^{\frac{ip\Delta}{\hbar}} \left\langle q - \frac{\Delta}{2}\right| \hat{\rho} \left| q + \frac{\Delta}{2}\right\rangle \tag{2.16}$$

This representation maps the density operator to a phase space distribution (which tends to the Boltzmann density at high temperature)[1]. This distribution has some important properties: first, its position and momentum marginal distributions are the position and momentum probability densities respectively:

$$\int \mathrm{d}p\ \rho_{\mathrm{w}}(q,p) = \langle q|\hat{\rho}|q\rangle \tag{2.17}$$

$$\int \mathrm{d}q\ \rho_{\mathrm{w}}(q,p) = \langle p|\hat{\rho}|p\rangle \tag{2.18}$$

and consequently, the Wigner distribution is normalized ($\int \mathrm{d}q\mathrm{d}p\ \rho_{\mathrm{w}}(q,p) = 1$). Second, the Wigner distribution allows to write the average of any observable $\hat{A}$ in the form of a phase-space average:

$$\left\langle \hat{A} \right\rangle = \int \mathrm{d}q\mathrm{d}p\ \rho_{\mathrm{w}}(q,p) A_w(q,p) \tag{2.19}$$

where $A_w(q,p)$ is the Wigner transform of the operator $\hat{A}$ defined as:

$$A_w(q,p) = \int \mathrm{d}\Delta\ e^{\frac{ip\Delta}{\hbar}} \left\langle q - \frac{\Delta}{2}\right| \hat{A} \left| q + \frac{\Delta}{2}\right\rangle \tag{2.20}$$

If the operator $\hat{A}$ is a function of position only (resp. momentum only) $A(\hat{q})$ (resp. $A(\hat{p})$), then the Wigner transform is simply equal to the function $A(q)$ (resp. $A(p)$), so that (2.19) is very similar to the classical expression (2.2) with the only difference that the Boltzmann density is replaced by the Wigner density. However, the apparent simplicity of equation (2.19) is only superficial as the evaluation of the Wigner distribution is a challenge in itself. Indeed, even if the non-diagonal elements of the density operator $\left\langle q - \frac{\Delta}{2}\right| \hat{\rho} \left| q + \frac{\Delta}{2}\right\rangle$ can be expressed as an open path integral, the phase factor $e^{\frac{ip\Delta}{\hbar}}$ poses tremendous numerical difficulties. Indeed, for a high-dimensional system, this phase factor can wildly oscillate and becomes impossible to sample accurately. This major difficulty is often called the "oscillating sign problem". Moreover, the phase factor also implies that the Wigner distribution is usually not positive everywhere (it is real by construction) and thus cannot be considered a true probability density (it is often called a quasi-probability density). Consequently, it is not directly possible to use the standard tools designed to sample probability distributions.

Despite these difficulties, the Wigner density is relevant to compute static and, more importantly, dynamical properties (as we will see in the next section) and thus

[1] Note that the concept of Wigner distribution is more general and can be used for any density operator to obtain a mixed representation in two conjugate variables. For example, it is used in signal analysis to build a time-frequency map of a complex signal $s(t)$ as $s_{\mathrm{w}}(t,\omega) = \int \mathrm{d}\tau e^{i\omega\tau} s(t-\tau/2)s^*(t+\tau/2)$

the development of numerically favorable approximations is an important topic of research. In chapter 3, we will describe some of the most common approximations to the Wigner density and in chapter 4, we propose and assess a new approximation based on the so-called Edgeworth expansion.

2.2.2 Time correlation functions

Time correlation functions (TCFs) are dynamical properties of a system that can be probed through different experimental techniques such as infrared/Raman spectroscopy or measurement of rate constants.

For a classical system, TCFs are real functions of time defined by equation (2.3) that respect the so-called *detailed balance* $c_{AB}(t) = c_{BA}(-t)$ (see ref. [64]).

In contrast, different quantum TCFs can be defined, that display slightly different behaviors but are all related to each other by simple transformations, and all tend to the classical TCF at high temperature. In this section, we review the most common definitions of quantum TCFs, as used for the different methods that we describe in the next chapter.

Standard form

The standard form of quantum time correlation function is defined as:

$$C_{AB}(t) = \mathrm{Tr}\left[\hat{\rho}\hat{A}\hat{B}_t\right] \tag{2.21}$$

where $\hat{A}$ and $\hat{B}$ are two observables and we denote the time propagated operator $\hat{B}_t = e^{i\hat{H}t/\hbar}\hat{B}e^{-i\hat{H}t/\hbar}$ with $e^{-i\hat{H}t/\hbar}$ and $e^{i\hat{H}t/\hbar}$ the forward and backward time propagators. If the Schrödinger equation can be solved for the system of interest, one can rewrite the TCF in terms of wavefunctions as:

$$C_{AB}(t) = \frac{1}{\mathcal{Z}}\sum_{i,j} e^{-\beta E_i}\,\langle\Psi_i|\hat{A}|\Psi_j\rangle\,\langle\Psi_j|\hat{B}|\Psi_i\rangle\,e^{it(E_j-E_i)/\hbar} \tag{2.22}$$

The TCF is thus a sum of complex exponential terms, oscillating at frequencies that correspond to the energy differences between the eigenstates. When the solution to the Schrödinger equation is not available, it is useful to express C_{AB} in terms of the Wigner distribution as it is the basis of the linearized approaches presented in the

next chapter. To that end, we expand the trace in position representation and insert a resolution of the identity to obtain:

$$C_{AB}(t) = \int \mathrm{d}x\mathrm{d}y \, \langle x|\hat{\rho}\hat{A}|y\rangle \, \langle y|\hat{B}_t|x\rangle \tag{2.23}$$

We then introduce the change of variable $x = q - \Delta/2$, $y = q + \Delta/2$ to obtain:

$$C_{AB}(t) = \int \mathrm{d}q\mathrm{d}\Delta \left\langle q - \frac{\Delta}{2}\middle|\hat{\rho}\hat{A}\middle|q + \frac{\Delta}{2}\right\rangle \left\langle q + \frac{\Delta}{2}\middle|\hat{B}_t\middle|q - \frac{\Delta}{2}\right\rangle \tag{2.24}$$

where q is the middle point between x and y and $\Delta = y - x$. By noting that the Dirac delta function can be expressed as $\delta(\Delta + \Delta') = \frac{1}{2\pi\hbar}\int \mathrm{d}p \; e^{ip(\Delta+\Delta')/\hbar}$ we can rewrite:

$$\begin{aligned} C_{AB}(t) &= \frac{1}{2\pi\hbar}\int \mathrm{d}q\mathrm{d}p \left(\int \mathrm{d}\Delta \; e^{ip\Delta/\hbar}\left\langle q - \frac{\Delta}{2}\middle|\hat{\rho}\hat{A}\middle|q + \frac{\Delta}{2}\right\rangle\right) \\ &\qquad \times \left(\int \mathrm{d}\Delta' \; e^{ip\Delta'/\hbar}\left\langle q - \frac{\Delta'}{2}\middle|\hat{B}_t\middle|q + \frac{\Delta'}{2}\right\rangle\right) \\ &= \frac{1}{2\pi\hbar}\int \mathrm{d}q\mathrm{d}p \; [\hat{\rho}\hat{A}]_w(q,p)[\hat{B}_t]_w(q,p) \end{aligned} \tag{2.25}$$

where $[\,\cdot\,]_w$ represents the Wigner transform defined in equation (2.20). It is easy to show that $[\hat{B}_t]_w(q,p)$ is always real (for any Hermitian operator $\hat{B}$) but $[\hat{\rho}\hat{A}]_w(q,p)$ is not generally real since the product $\hat{\rho}\hat{A}$ is not necessarily Hermitian. As a result, $C_{AB}(t)$ is a complex quantity and is therefore usually difficult to approximate using classical-like methods. The equivalent of the detailed balance for the standard TCF reads:

$$C_{AB}(t) = C_{BA}(-t)^* \tag{2.26}$$

The real part of the standard TCF, on the other hand, displays a more 'classical-like' behavior. We then take the real part of (2.25) and multiply and divide by $[e^{-\beta\hat{H}}]_w(q,p)$ to obtain:

$$\bar{c}_{AB}(t) = \mathrm{Re}[C_{AB}(t)] = \int \mathrm{d}q\mathrm{d}p \; \rho_{\mathrm{w}}(q,p) \; f_A(q,p) \; [\hat{B}_t]_w(q,p) \tag{2.27}$$

with:

$$f_A(q,p) = \frac{\mathrm{Re}\left[[e^{-\beta\hat{H}}\hat{A}]_w(q,p)\right]}{[e^{-\beta\hat{H}}]_w(q,p)} \tag{2.28}$$

and we used the fact that $\rho_{\mathrm{w}}(q,p) = [e^{-\beta\hat{H}}]_w(q,p)/2\pi\hbar\mathcal{Z}$. The real part of the standard TCF follows the detailed balance $\bar{c}_{AB}(t) = \bar{c}_{BA}(-t)$. One can then rewrite

$[\hat{B}_t]_w(q,p)$ in terms of a quantum Liouvillian using the Wigner-Moyal series (see refs. [65, 66]) which yields:

$$\bar{c}_{AB}(t) = \int \mathrm{d}q\mathrm{d}p\ \rho_{\mathrm{w}}(q,p)\ f_A(q,p)\ e^{i\mathcal{L}_Q t} B_w(q,p) \tag{2.29}$$

with:

$$i\mathcal{L}_Q = \frac{p}{m}\frac{\partial}{\partial q} - \sum_{n=1,\mathrm{odd}}^{\infty} \frac{1}{n!}\left(\frac{i\hbar}{2}\right)^{n-1} \frac{\partial^n V}{\partial q^n}\frac{\partial^n}{\partial p^n} \tag{2.30}$$

This form is similar to the expression of the classical TCF and it suggests a straightforward procedure to compute the quantum TCF: sample phase space points according to the Wigner thermal distribution, evaluate the modified observable f_A at these points and multiply by the second observable at a later time t obtained using a quantum time propagation. Each of these steps however is much more challenging than their classical counterpart. Indeed, quantum time propagation is notoriously difficult for large systems and, as already stated, the computation of the Wigner distribution is demanding in itself. The third difficulty, which is milder, lies in the evaluation of $f_A(q,p)$.

Using the definition of the Moyal $\star$ product [67, 68, 69], we can rewrite:

$$\begin{aligned}
[e^{-\beta\hat{H}}\hat{A}]_w(q,p) &= [e^{-\beta\hat{H}}]_w(q,p) \star A_w(q,p) \\
&= [e^{-\beta\hat{H}}]_w(q,p) e^{\frac{i\hbar}{2}\left(\frac{\overleftarrow{\partial}}{\partial q}\frac{\overrightarrow{\partial}}{\partial p} - \frac{\overleftarrow{\partial}}{\partial p}\frac{\overrightarrow{\partial}}{\partial q}\right)} A_w(q,p) \\
&= \sum_{n=0}^{\infty} \frac{1}{n!}\left(\frac{i\hbar}{2}\right)^n [e^{-\beta\hat{H}}]_w(q,p) \left(\frac{\overleftarrow{\partial}}{\partial q}\frac{\overrightarrow{\partial}}{\partial p} - \frac{\overleftarrow{\partial}}{\partial p}\frac{\overrightarrow{\partial}}{\partial q}\right)^n A_w(q,p)
\end{aligned} \tag{2.31}$$

where the arrows indicate the direction in which the derivatives act and the power for derivatives corresponds to the order of derivation. Noting that all odd orders in (2.31) are purely imaginary and therefore vanish in the real part of the TCF, we obtain:

$$f_A(q,p) = \frac{\sum_{n=0}^{\infty} \frac{(-1)^n\hbar^{2n}}{(2n)!\ 2^{2n}} \rho_{\mathrm{w}}(q,p) \left(\frac{\overleftarrow{\partial}}{\partial q}\frac{\overrightarrow{\partial}}{\partial p} - \frac{\overleftarrow{\partial}}{\partial p}\frac{\overrightarrow{\partial}}{\partial q}\right)^{2n} A_w(q,p)}{\rho_{\mathrm{w}}(q,p)} \tag{2.32}$$

While this expression seems difficult to evaluate, it greatly simplifies when considering linear observables of $\hat{p}$ and $\hat{q}$. If we denote $\hat{A} = a\hat{q} + b\hat{p}$, we simply have $A_w(q,p) = aq + bp$ and the only term that does not cancel in the above series is the zero order term, yielding $f_{aq+bp}(q,p) = aq + bp$ which is just the classical observable. For example, the momentum autocorrelation function (ATCF), on which we will

mostly focus in the following since it is related to physically relevant observables such as vibrational spectra and diffusion constants, can be written:

$$\bar{c}_{pp}(t) = \int \mathrm{d}q\mathrm{d}p \; \rho_{\mathrm{w}}(q,p) \; p \; e^{i\mathcal{L}_Q t} p \tag{2.33}$$

which formally resembles the classical momentum ATCF if we replace ρ_{w} by the classical probability distribution ρ_{cl} and the Liouvillian $i\mathcal{L}_Q$ by $i\mathcal{L}_{cl}$. The real part of the standard correlation function is well suited for quasi-classical approximations such as LSC-IVR (Linearized Semi-Classical Initial Value Representation) or the QTB (Quantum Thermal Bath) as we will see in the next chapter.

The real part of the standard correlation function can be related to the full correlation function using the following relation on their Fourier transforms:

$$\mathcal{F}\{C_{AB}\}(\omega) = \frac{2}{1+e^{-\beta\hbar\omega}} \; \mathcal{F}\{\bar{c}_{AB}\}(\omega) \tag{2.34}$$

where $\mathcal{F}\{\,\cdot\,\}$ denotes the Fourier transform. For example:

$$\mathcal{F}\{C_{AB}\}(\omega) = \frac{1}{2\pi}\int_{-\infty}^{\infty} \mathrm{d}t \; e^{-i\omega t} C_{AB}(t) \tag{2.35}$$

Relation (2.34) can be easily derived from the definition of the two TCFs in the basis of the eigenstates of the Hamiltonian operator.

Kubo-transformed correlation function

The Kubo-transformed correlation function is defined as:

$$K_{AB}(t) = \frac{1}{\beta\mathcal{Z}}\int_0^\beta \mathrm{d}\lambda \; \mathrm{Tr}\Big[e^{-(\beta-\lambda)\hat{H}}\hat{A}e^{-\lambda\hat{H}}\hat{B}_t\Big] \tag{2.36}$$

Although this form seems more complicated than the standard correlation function, it is real and respects the detailed balance $K_{AB}(t) = K_{BA}(-t)$. It is also equal to the classical correlation function in the harmonic case. The Kubo-transformed correlation is at the basis of the approximations in which the dynamics of the fictitious ring polymer of the PI picture is used to compute TCFs, namely CMD (Centroid Molecular Dynamics), RPMD (Ring Polymer Molecular Dynamics) and Matsubara dynamics (see next chapter). In these approaches, the integral over λ in (2.36) is discretized and replaced by a sum over the polymer beads and we can picture the observable $\hat{A}$ as being "smeared" along the imaginary-time path.

The Kubo-transformed correlation function can be related to the standard correlation function using the relation:

$$\mathcal{F}\{C_{AB}\}(\omega) = \frac{\beta\hbar\omega}{1-e^{-\beta\hbar\omega}}\mathcal{F}\{K_{AB}\}(\omega) \tag{2.37}$$

and hence to the real part of the standard correlation function using:

$$\mathcal{F}\{\bar{c}_{AB}\}(\omega) = \frac{\beta\hbar\omega/2}{\tanh(\beta\hbar\omega/2)}\mathcal{F}\{K_{AB}\}(\omega) \tag{2.38}$$

Symmetrized correlation function

The symmetrized correlation function is defined as:

$$\begin{aligned} G_{AB}(t) &= \frac{1}{\mathcal{Z}}\operatorname{Tr}\left[e^{-\beta\hat{H}/2}\hat{A}e^{-\beta\hat{H}/2}e^{i\hat{H}t/\hbar}\hat{B}e^{-i\hat{H}t/\hbar}\right] \\ &= \frac{1}{\mathcal{Z}}\operatorname{Tr}\left[\hat{A}e^{i\hat{H}\tau_c^*/\hbar}\hat{B}e^{-i\hat{H}\tau_c/\hbar}\right] \end{aligned} \tag{2.39}$$

with the complex time $\tau_c = t - i\beta\hbar/2$. Contrary to the standard correlation function, the symmetrized correlation function is real and follows the detailed balance $G_{AB}(t) = G_{BA}(-t)$. It has been used in some rather unconventional approaches where the real time t is treated as a parameter (on the same footing as the temperature) in order to reduce the dynamical problem to a sampling problem [70, 71].

The symmetrized correlation function can be related to the standard correlation [60] using the following relation on their Fourier transforms :

$$\mathcal{F}\{C_{AB}\}(\omega) = e^{\beta\hbar\omega/2}\mathcal{F}\{G_{AB}\}(\omega) \tag{2.40}$$

3 State of the Art in trajectory-based methods

As stated in the introduction, we focus in this thesis on trajectory-based methods for quantum dynamics. These methods involve strong approximations but allow to treat relatively large condensed phase systems – that are inaccessible to more refined methods – and can satisfactorily capture zero-point energy (ZPE) effects, which are often the main quantum contributions for these systems in which decoherence is generally very fast. In this chapter, we briefly review the most common approaches for numerical computation of approximate quantum time correlation functions (TCFs) using generalized classical trajectories. This list is not intended to be exhaustive but presents the methods that are the most relevant for the following chapters.

Throughout this chapter, we illustrate the different methods using the following unidimensional Morse potential:

$$V(q) = D\left[e^{-2\alpha q} - 2e^{-\alpha q}\right] \tag{3.1}$$

with $D = 20$ kcal/mol and $\alpha = 2.5$ Å^{-1}. This potential is very useful to model iono-covalent bonds, for example O-H bonds [72] and is often used to test approximate methods for quantum dynamics. The parameters are chosen to provide a strong degree of anharmonicity and in order to highlight the differences between the approximate methods. The observations made for this potential are not necessarily transferable to other systems. However, it is a relevant benchmark and comparing the methods on this potential allows to emphasize important differences in the approximated dynamics. Furthermore, this model introduces the problem of anharmonic resonances which is the main topic of chapter 5.

3.1 Linearized Semi-Classical methods

Equation (2.29) provides an expression of the quantum TCF that closely resembles the classical expression and separates the problem of quantum dynamics at thermal

19

equilibrium in two sub-problems: the sampling of the Wigner thermal density on the one hand and quantum time propagation on the other hand. Linearized methods simplify the latter by truncating the quantum Liouvillian (2.30) at first order in $\hbar$ yielding:

$$i\mathcal{L}_Q = \frac{p}{m}\frac{\partial}{\partial q} - \frac{\partial V(q)}{\partial q}\frac{\partial}{\partial p} + \mathcal{O}\left(\hbar^2\right) = i\mathcal{L}_{cl} + \mathcal{O}\left(\hbar^2\right) \tag{3.2}$$

thus effectively replacing quantum time propagation by classical dynamics. The procedure of the Linearized Semi-Classical Initial Value Representation (LSC-IVR) thus consists in sampling initial conditions from the Wigner density and averaging over a large number of classical (NVE) trajectories propagated from these points. The LSC-IVR approximation to the real part of the standard TCF (2.29) is then:

$$\begin{aligned} c_{AB}^{\text{LSC-IVR}}(t) &= \int \mathrm{d}q\mathrm{d}p\ \rho_{\text{w}}(q,p)\ f_A(q,p)\ e^{i\mathcal{L}_{cl}t} B_w(q,p) \\ &= \int \mathrm{d}q\mathrm{d}p\ \rho_{\text{w}}(q,p)\ f_A(q,p)\ B_w(q_t,p_t) \end{aligned} \tag{3.3}$$

where (q_t, p_t) is the phase space point obtained after a classical propagation of duration t starting from (q,p). If one can compute the Wigner density exactly, one can show that LSC-IVR is exact in the short time limit, the harmonic limit and the classical limit [73].

A qualitative analysis of replacing quantum dynamics by classical dynamics, can be obtained via real-time path integrals. In this framework, quantum dynamics consists in a sum of forward-backward paths that carry a phase factor which depends on the difference between the two paths. The classical evolution forces the forward and backward paths to be infinitely close together, thus cancelling the phase factor. For infinitesimally short paths, this approximation is correct since the forward and backward paths cannot deviate from one another (thus validating the short time limit). At high temperature, all the paths collapse to give classical dynamics (thus validating the classical limit). For a harmonic potential, the forward and backward paths are naturally identical and the harmonic dynamics is classical since the first correction to classical dynamics in the quantum Liouvillian depends on the third order derivative of the potential which is null for a harmonic potential. We refer to refs. [73, 74, 75] for more details.

Forcing the forward and backward paths to be identical, however, affects the physical effects that can be captured using this approach. Indeed, it is often stated that coherence effects are lost. While this is true of purely quantum interference features, this statement may deserve a more careful analysis since some coherence effects are preserved by the classical evolution. We will discuss this point in more details

in Chapter 5. Furthermore, one can show that the classical Liouvillian does not in general conserve the Wigner density:

$$i\mathcal{L}_{cl}\ \rho_{\mathrm{w}}(q,p) \neq 0 \tag{3.4}$$

and thus the LSC-IVR approximation to $\bar{c}_{AB}(t)$ does not satisfy detailed balance. This implies that the dynamics may display unphysical properties like zero-point energy leakage (ZPEL) where energy unphysically flows along the propagation from the high-frequency degrees of freedom to the low-frequency degrees of freedom [76] (we will describe this effect in more details in section 3.3 since the ZPEL also affects the Quantum Thermal Bath method).

The main technical difficulty for the LSC-IVR is to sample points according to the Wigner density. As already stated, the Wigner density is a challenging quantity to compute due to the phase factor in its definition and of its quasi-probability nature (not positive everywhere). Many approaches have been devised to approximate the Wigner density that often rely on (local or global) harmonic approximations. We will review here the most popular of these approximations, namely the Local Harmonic Approximation[47] (LHA) and the related Local Gaussian Approximation [49] (LGA) and the Feynman-Kleinert Linearized Path Integral [51](FK-LPI). We also briefly introduce the Phase Integration Method [52](PIM) that was a starting point for the new approximation that we present in chapter 4. In the following, we will prefix LSC to the name of the sampling method when we refer to the combination of LSC-IVR with initial conditions given by the aforementioned method. For example, LSC-LGA refers to LSC-IVR with initial conditions given by the LGA.

Despite these difficulties, the LSC-IVR has proven to be a useful tool to describe quantum effects on the vibrational spectra of molecules and solids, for very anharmonic energy potentials with negligible tunneling (see ref. [77] for a review of different applications of LSC-IVR to realistic systems). In fact, in complex high-dimensional interacting systems, coherence effects tend to be small and decay fast on relevant time-scale for correlation of observables so that classical dynamics is able to catch most of the relevant effects on the TCF.

3.1.1 The Local Harmonic and Gaussian Approximations

To obtain the Local Harmonic Approximation (LHA), we start by splitting the Wigner density (2.16) into the marginal position distribution $\langle q|\hat{\rho}|q\rangle$ and the conditional momentum distribution:

$$\rho_{\mathrm{w}}(q,p) = \langle q|\hat{\rho}|q\rangle \left(\int \mathrm{d}\Delta \; e^{\frac{ip\Delta}{\hbar}} \frac{\left\langle q-\frac{\Delta}{2}\right| \hat{\rho} \left|q+\frac{\Delta}{2}\right\rangle}{2\pi\hbar \langle q| \hat{\rho} |q\rangle} \right) \tag{3.5}$$

In order to obtain an analytical expression of the ratio $\langle q-\Delta/2| \hat{\rho} |q+\Delta/2\rangle \,/\, \langle q|\hat{\rho}|q\rangle$, one expands the potential at second order around q as:

$$V(q+\epsilon) = V(q) + \frac{\partial V(q)}{\partial q}\epsilon + \frac{1}{2}m\Omega^2(q)\epsilon^2 + \mathcal{O}\left(\epsilon^3\right) \tag{3.6}$$

where the local frequency $\Omega^2(q)$ is given by the mass-weighted hessian:

$$\Omega^2(q) = \frac{1}{m}\frac{\partial^2 V(q)}{\partial q^2} \tag{3.7}$$

Using this approximation, one can rewrite the ratio of the matrix elements of $\hat{\rho}$ as [47, 49]:

$$\frac{\left\langle q-\frac{\Delta}{2}\right| \hat{\rho} \left|q+\frac{\Delta}{2}\right\rangle}{\langle q| \hat{\rho} |q\rangle} = \exp\left\{-\frac{m\Phi(q)}{2\beta\hbar^2}\Delta^2\right\} \tag{3.8}$$

where

$$\Phi(q) = \frac{\beta\hbar\Omega(q)/2}{\tanh(\beta\hbar\Omega(q)/2)} \tag{3.9}$$

is the "quantum correction factor" (QCF) which is the ratio of the average thermal energy of a quantum harmonic oscillator of frequency $\Omega(q)$ to the classical average thermal energy k_BT. One can then compute analytically the integral over Δ and obtain the local harmonic approximation to the Wigner thermal distribution:

$$\rho_{\mathrm{w}}(q,p) \approx \langle q|\hat{\rho}|q\rangle \frac{\exp\left(-\beta\frac{p^2}{2m}\Phi^{-1}(q)\right)}{\sqrt{2\pi m\Phi(q)/\beta}} \tag{3.10}$$

One should note that the harmonic approximation only concerns the conditional momentum distribution and that the full anharmonicity is kept for the evaluation of the position distribution. In practice, sampling the Wigner distribution through LHA consists in sampling the marginal position distribution using standard imaginary-time path integrals and, for each position obtained in this way, one computes the local frequency (3.7), deduces the QCF (3.9) and then samples the Gaussian conditional momentum distribution of equation (3.10). The definition of the QCF in

equation (3.9) holds only when the curvature of the potential is positive. If it is not the case, for example when the potential displays a barrier, $\Omega^2(q)$ is negative and $\Omega(q)$ is imaginary. Using analytic continuation, one can extend the definition of $\Phi(q)$ in the case of imaginary frequencies[49] :

$$\Phi(q) = \frac{\beta\hbar|\Omega(q)|/2}{\tan(\beta\hbar|\Omega(q)|/2)} \quad \text{if } \Omega^2(q) < 0 \tag{3.11}$$

However, in order to have a meaningful momentum distribution, the QCF $\Phi(q)$ must be positive which it is not if $\Omega^2(q) < -\left(\frac{\pi}{\beta\hbar}\right)^2$. Thus for potential energy barriers with a strong curvature, the LHA fails to describe the momentum distribution. To circumvent this problem Liu and Miller [49] proposed the Local Gaussian Approximation which is a simple (*ad hoc*) modification of the QCF:

$$\Phi(q) = \begin{cases} \dfrac{\beta\hbar\Omega(q)/2}{\tanh(\beta\hbar\Omega(q)/2)} & \text{if } \Omega^2(q) > 0 \\ \\ \dfrac{\tanh(\beta\hbar|\Omega(q)|/2)}{\beta\hbar|\Omega(q)|/2} & \text{if } \Omega^2(q) < 0 \end{cases} \tag{3.12}$$

Figure 3.1 shows the QCF in function of the adimensional parameter $\beta\hbar\omega/2$ where $\omega = |\Omega|\text{sign}(\Omega^2)$. We can see that for large negative values of $\beta\hbar\omega/2$, the QCF is negative for the LHA while it slowly tends to zero for the LGA. Thus, the momentum distribution is always well defined for the LGA.

For a multidimensional system of size N, the local frequency is a $N \times N$ matrix obtained from the Hessian of the potential as:

$$\Omega^2_{ij} = \frac{1}{\sqrt{m_i m_j}} \frac{\partial^2 V(q)}{\partial q_i \partial q_j} \tag{3.13}$$

If we denote $(\omega_i^2)_{i=1\ldots N}$ the eigenvalues of $\Omega^2(q)$, we define the QCF matrix $\Phi(q)$ as diagonal in the same basis as $\Omega^2(q)$ with eigenvalues $(\phi_i)_{i=1\ldots N}$ such that:

$$\phi_i = \begin{cases} \dfrac{\beta\hbar\omega_i/2}{\tanh(\beta\hbar\omega_i/2)} & \text{if } \omega_i^2 > 0 \\ \\ \dfrac{\tanh(\beta\hbar|\omega_i|/2)}{\beta\hbar|\omega_i|/2} & \text{if } \omega_i^2 < 0 \end{cases} \tag{3.14}$$

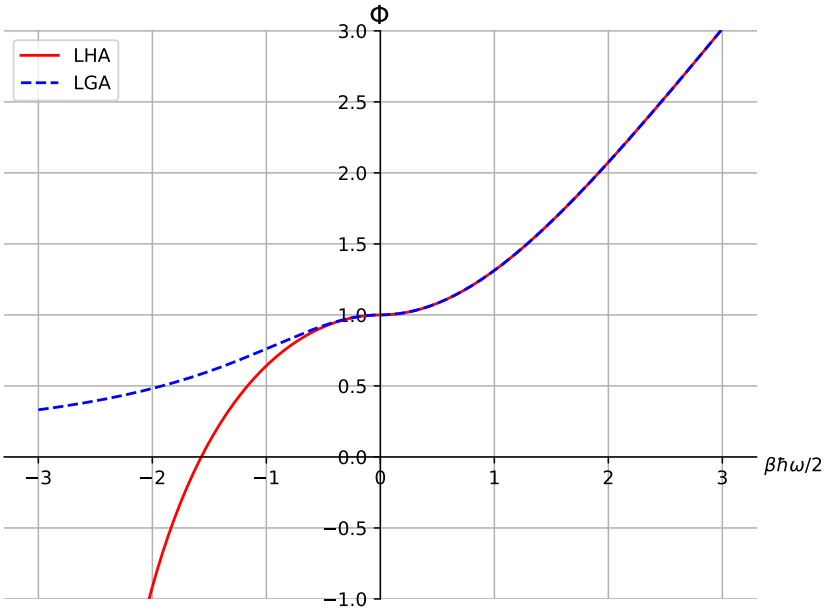

Fig. 3.1.: Quantum correction factor Φ in function of $\beta\hbar\omega/2$ for the LHA and the LGA. The LHA curve becomes negative for $\beta\hbar\omega/2 < -\pi/2$ (The negative x-axis corresponds to imaginary values of the local frequency Ω with $\omega = |\Omega|\text{sign}(\Omega^2)$)

The conditional momentum distribution is then a generalized Gaussian distribution and the LGA approximation to the N-dimensional Wigner distribution is then:

$$\rho_w(q,p) \approx \langle q|\hat{\rho}|q\rangle \frac{\exp\left(-\frac{\beta}{2}p^T M^{-\frac{1}{2}}\Phi^{-1}(q)M^{-\frac{1}{2}}p\right)}{\sqrt{2\pi|M||\Phi(q)|/\beta}} \tag{3.15}$$

with M the diagonal mass matrix. One should note that for high-dimensional systems, the Hessian of the potential, and thus the local frequencies, can be costly quantities to compute. While the Hessian may be available analytically for model potentials, it is usually not easily accessible for first-principles methods and requires much more computational efforts than the evaluation of the forces. Moreover, the inversion of the full $N \times N$ Hessian required to compute the QCF is also computationally intensive so that it may be required to approximate the Hessian matrix (for example by setting to zero the off-diagonal elements corresponding to atoms that are far apart in order to sparsify the matrix). Despite this technical difficulty, the LHA with LSC-IVR has been successfully used to compute vibrational energy relaxation rate constants in low-temperature liquid oxygen [78]. The LGA has also been applied with satisfying results to compute the IR spectra of different models of liquid-phase [79] and solid-phase [59] water.

3.1.2 Feynman-Kleinert Linearized Path Integrals

The FK-LPI method presented in ref. [51] allows to rewrite the Wigner density in a semi-harmonic form by combining the variational harmonic representation of path integrals designed by Feynman and Kleinert [50] with the centroid-constrained quasi density operator formalism of Jang and Voth [42]. We will not present here the derivation but only the final results necessary for implementation.

The idea of the FK-LPI is to separate the path integral representation of the density operator into a marginal centroid density (the distribution of the "center of mass" of the path integral) and a conditional fluctuation distribution. The approximation at the heart of the FK-LPI is to consider that the fluctuations around the centroid are harmonic (Gaussian). The frequency of the harmonic fluctuations is a function of the centroid position and is optimized according to the variational principle of Feynman and Kleinert [50]. The centroid potential is obtained self-consistently by smearing the potential on the harmonic fluctuations.

The FK-LPI approximation to the Wigner thermal distribution is given by:

$$\rho_{\text{w}}(q,p) \approx \int \mathrm{d}x_c \; \rho_{\text{c}}(x_c) \frac{\exp\left(-\beta\left[\frac{1}{2}m\theta^2(x_c)(q-x_c)^2 + \frac{p^2}{2m}\Phi_{\text{FK}}^{-1}(x_c)\right]\right)}{2\pi\beta^{-1}\sqrt{\Phi_{\text{FK}}(x_c)/\theta^2(x_c)}} \tag{3.16}$$

where x_c denotes the position of the centroid of the path integral. The harmonic frequency $\theta(x_c)$ of the fluctuations around the centroid is given by [51, 80] :

$$\theta^2(x_c) = \begin{cases} \Omega_{\text{FK}}^2(x_c) \Big/ \left(\dfrac{\beta\hbar\Omega_{\text{FK}}(x_c)/2}{\tanh(\beta\hbar\Omega_{\text{FK}}(x_c)/2)} - 1\right) & \text{if } \Omega_{\text{FK}}^2(x_c) > 0 \\ \\ \left|\Omega_{\text{FK}}^2(x_c)\right| \Big/ \left(1 - \dfrac{\beta\hbar|\Omega_{\text{FK}}(x_c)|/2}{\tan(\beta\hbar|\Omega_{\text{FK}}(x_c)|/2)}\right) & \text{if } \Omega_{\text{FK}}^2(x_c) < 0 \end{cases} \tag{3.17}$$

and is self-consistently defined with the optimal FK squared frequency:

$$\Omega_{\text{FK}}^2(x_c) = \int \mathrm{d}x \; \frac{1}{m}\frac{\partial^2 V(x)}{\partial x^2} \; \frac{\exp\left(-\frac{\beta}{2}m\theta^2(x_c)(x-x_c)^2\right)}{\sqrt{2\pi/m\beta\theta^2(x_c)}} \tag{3.18}$$

At a given centroid position, the computation of $\Omega_{\text{FK}}^2(x_c)$ and $\theta^2(x_c)$ is obtained through a self-consistent cycle as follows: (i) start with an initial guess of Ω_{FK}^2 to obtain θ^2 (or directly guess θ^2). (ii) compute a new Ω_{FK}^2 using equation (3.18) (usually done via Monte Carlo, *i.e.* by drawing a set of random positions around x_c according to the Gaussian distribution). (iii) deduce a new θ^2 from Ω_{FK}^2 using equation (3.17) and repeat steps (ii)-(iii) until convergence.

The momentum distribution in equation (3.16) is characterized by the FK quantum correction factor (FK-QCF) $\Phi_{\text{FK}}(x_c)$ defined as in the LGA but replacing the local frequency with $\Omega^2_{\text{FK}}(x_c)$ in equation (3.12). The centroid probability density $\rho_c(x_c)$ can be expressed consistently within the FK approximation (from the smeared potential, obtained by averaging the potential V over the Gaussian fluctuations, see ref [51] for detailed expressions). A common approach, however, is to use instead the centroid distribution sampled via standard PIMD.

In practice, one first samples centroid positions according to the centroid probability density ρ_c. For each centroid position x_c, one computes $\Omega^2_{\text{FK}}(x_c)$, $\theta^2(x_c)$ and $\Phi_{\text{FK}}(x_c)$ using the previously mentioned self-consistent cycle and samples the fluctuation phase space (q,p) using the conditional Gaussian distribution of equation (3.16). From the (q,p) points, one may then perform classical dynamics to obtain the FK-LPI approximation to the LSC-IVR correlation functions.

For a N-dimensional system, $\Omega^2_{\text{FK}}(x_c)$, $\theta^2(x_c)$ and $\Phi_{\text{FK}}(x_c)$ are $N \times N$ matrices. The FK frequency matrix is defined as:

$$[\Omega^2_{\text{FK}}(x_c)]_{ij} = \int \mathrm{d}x \; \frac{1}{\sqrt{m_i m_j}} \frac{\partial^2 V(x)}{\partial x_i \partial x_j} \frac{\exp\left(-\frac{\beta}{2}(x-x_c)^T M^{\frac{1}{2}} \theta^2(x_c) M^{\frac{1}{2}} (x-x_c)\right)}{\sqrt{2\pi/|M\beta\theta^2(x_c)|}} \tag{3.19}$$

We can then diagonalize $\Omega^2_{\text{FK}}(x_c)$ and define $\theta^2(x_c)$ and $\Phi_{\text{FK}}(x_c)$ as diagonal in the same basis as $\Omega^2_{\text{FK}}(x_c)$ with eigenvalues defined similarly as in equation (3.14) for $\Phi_{\text{FK}}(x_c)$ and (3.17) for $\theta^2(x_c)$. The conditional fluctuation distribution is then a generalized Gaussian distribution and the FK-LPI approximation to the N-dimensional Wigner distribution is then:

$$\rho_{\text{w}}(q,p) \approx \int \mathrm{d}x_c \; \rho_{\text{c}}(x_c) \frac{e^{-\frac{\beta}{2}\left[(q-x_c)^T M^{\frac{1}{2}} \theta^2(x_c) M^{\frac{1}{2}} (q-x_c) + p^T M^{-\frac{1}{2}} \Phi^{-1}_{\text{FK}}(x_c) M^{-\frac{1}{2}} p\right]}}{2\pi\beta^{-1}\sqrt{|\Phi_{\text{FK}}(x_c)|/|\theta^2(x_c)|}} \tag{3.20}$$

with M the diagonal mass matrix.

The FK-LPI method is applicable to relatively large systems as long as the effective frequency matrix can be efficiently computed. Note that ref. [81] provides a rewriting of equation (3.19) that only involves the first derivative of the potential (which is much cheaper to compute than the Hessian) which opens up the method to larger systems. For example, Poulsen *et al.* used LSC-IVR with FK-LPI initial conditions to study the quantum diffusion in liquid para-hydrogen [82] at very low temperature, and spectral properties of liquid water at room temperature and low-temperature He(4) [81].

3.1.3 Comparison on the Morse potential

We now compare LGA and FK-LPI approximations to the Wigner density of the Morse potential of equation (3.1) and compare the results of the two methods for dynamical quantities (here, the momentum ATCF).

Sampling of the Wigner distribution

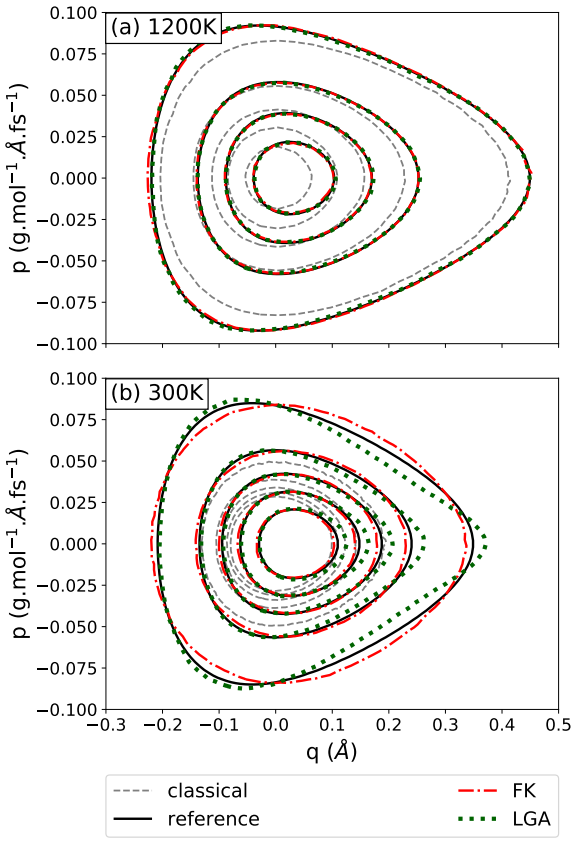

Fig. 3.2.: Wigner thermal distribution for the Morse potential of equation (3.1) (with $D = 20$ kcal/mol and $\alpha = 2.5$ Å^{-1}) approximated using the Local Gaussian Approximation (dotted green) and the Feynman-Kleinert approximation (dash-dotted red) at 1200K (panel a) and 300K (panel b). Contour levels are 1.5, 10, 20, 30, 40 fs.Å^{-2}.(g/mol)$^{-1}$.

Figure 3.2 shows the Wigner density approximated by the two methods and compared to the classical Boltzmann density and the exact Wigner density obtained from solving the Schrödinger equation. The Wigner density is computed at 1200K (panel a) where the Wigner thermal distribution is close to the Boltzmann density, and

300K (panel b) where quantum effects are important and the quantum distribution is much wider than the classical one because of zero-point energy. We can see that both LGA and FK-LPI are very good approximations to the Wigner density at high temperature. At 300K, both methods are able to capture the broadening of the distribution due to zero-point energy. However, the precise shape of the distribution is not very well described. In chapter 4, we will examine this distribution in more details and compare the LGA and FK-LPI to the new Edgeworth approximation that we propose.

Momentum autocorrelation spectrum

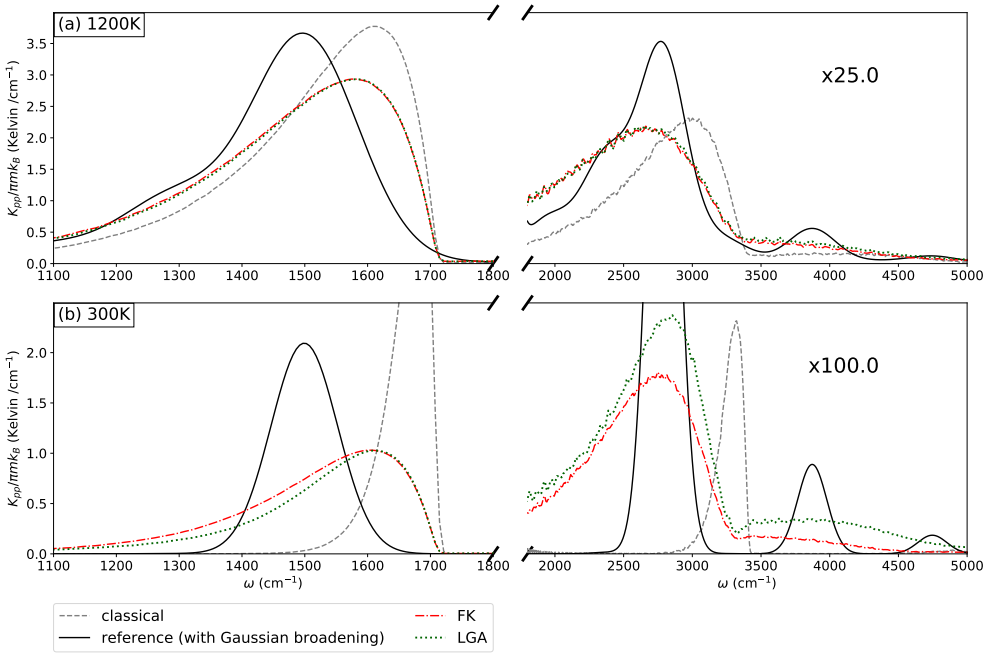

Fig. 3.3.: Kubo-transformed momentum autocorrelation spectrum for LGA+LSC-IVR (dotted green), FK+LSC-IVR (dash-dotted red), exact (solid black) and classical (dashed grey) at 1200K (panel a) and 300K (panel b) for the Morse potential of equation (3.1) (with $D = 20$ kcal/mol and $\alpha = 2.5$ Å^{-1}). The reference spectrum is broadened by convolution with a Gaussian function chosen to approximately match the heights of the other spectra (the spectral weight of the peaks is not modified).

We now turn to dynamical properties. Figure 3.3 shows the Kubo-transformed momentum autocorrelation spectrum for the Morse potential obtained using LSC-LGA (dotted green curve) and LSC-FK (dash-dotted red curve) compared to the classical spectrum and the spectrum obtained by solving the Schrödinger equation.

At 1200K, the main spectral feature (around 1500 cm^{-1}) is markedly asymmetric and exhibits a slight shift between the classical and quantum spectra. The quantum spectrum of a finite dimension system consist in a series of Dirac delta-functions, centered at the difference frequencies between the eigenmodes of the system (see section 2.2.2). Here for visualization purposes, these delta-peaks are artificially replaced with Gaussian functions (each of the same width, chosen so that the height of the features approximately matches the classical one). Therefore the asymmetric shape of the main spectral feature actually arises from a series of peaks with decreasing intensities. In the classical case on the other hand, the broadening of the peak is due to anharmonic effects (the softening of the Morse potential at large q). At this high temperature, both LSC-IVR spectra are very similar and display a broad main peak. The position and overall amplitude of the overtone around 2750 cm^{-1} is rather well captured by the LSC-IVR (zoom on the overtones region on the right side of figure 3.3).

At 300K, the shift between the classical and quantum spectra is larger and the classical peaks are narrower and less asymmetric (indicating less exploration of the anharmonicity of the Morse potential). For both approximate methods, the main peak is very broad and spans over the classical and quantum peaks with a maximum situated in between. The overtone is correctly placed and is much stronger than the classical one. We notice a difference in the overtone amplitude between the approximate spectra that comes from the differences in the approximation of the Wigner density at low temperature. Most notably for chapter 5 (which compares the treatment of overtones and resonances by the different approximated methods for quantum dynamics), the overtones are more intense with LGA initial conditions than FK-LPI and we will show that it is related to the different treatment of position-momentum correlations in the initial distribution (*i.e.* the precise shape of the Wigner distribution).

3.1.4 The Phase Integration Method

Recently, in Ref. [52], a different method was proposed to sample the Wigner thermal distribution: the Phase Integration Method (PIM), that employs an Edgeworth expansion in order to eliminate the phase factor in the definition of the Wigner distribution. Contrary to LGA or FK-LPI, it does not rely on a harmonic approximation and allows under certain conditions to recover negative parts of the Wigner density. These improvements, however, come at an increase of the numerical cost. In chapter 4, we will derive a new and simpler version of the Edgeworth approximation (which still provides similar accuracy compared to the one in ref. [52]). The main equations

of the original PIM formalism and a sketch of their derivation can be found in appendix A.

3.2 Path Integral Methods

Path-Integrals Molecular Dynamics (PIMD) allows to compute exact static properties (as explained in chapter 2) but does not allow in general to compute dynamical properties that involve real-time quantum propagation. Nonetheless, different approaches have been proposed to compute approximate (Kubo-transformed) TCFs from the dynamics of imaginary-time path integrals. The two main methods are the Centroid Molecular Dynamics (CMD, see refs. [40, 41, 42, 43, 44]) and Ring-Polymer Molecular Dynamics (RPMD, see ref. [45]). Althorpe *et al.* recently showed that these two methods can be obtained as approximations to a more fundamental dynamics: the Matsubara dynamics. Even though this method is too computationally demanding to be applied to realistic systems, it is conceptually interesting and we chose to present it first and then show how RPMD and CMD can be deduced from it.

3.2.1 Matsubara dynamics

Matsubara dynamics approximates the Kubo-transformed TCF by considering the dynamics of a smooth ring polymer path integral. Ref. [66] describes the full derivation of Matsubara dynamics and we report here only the main steps. We also only consider the simpler case of observables $\hat{A}$ and $\hat{B}$ which depend only on the position. The integral over λ in the definition of the Kubo-transformed TCF (2.36) can be discretized in ν slices (with the assumption of odd ν) of size β/ν to obtain the exact (in the limit $\nu \to \infty$) ring-polymer expression of the Kubo-transformed TCF:

$$K_{AB}^{[\nu]}(t) = \frac{1}{\mathcal{Z}} \int \mathrm{d}q\, \mathrm{d}p \left[e^{-\beta \hat{H}} \hat{A}\right]_\nu (q,p)\, e^{i\mathcal{L}_\nu t} \left(\frac{1}{\nu} \sum_{i=1}^{\nu} B(q_i)\right) \tag{3.21}$$

with

$$\left[e^{-\beta \hat{H}} \hat{A}\right]_\nu (q,p) = \int \mathrm{d}\Delta \left(\frac{1}{\nu} \sum_{i=1}^{\nu} A(q_i)\right) \prod_{l=1}^{\nu} \left\langle q_{l-1} - \frac{\Delta_{l-1}}{2} \middle| e^{-\frac{\beta}{\nu}\hat{H}} \middle| q_l + \frac{\Delta_l}{2} \right\rangle e^{ip_l \Delta_l/\hbar} \tag{3.22}$$

and the ring-polymer quantum Liouvillian:

$$i\mathcal{L}_\nu = \sum_{l=1}^{\nu} \left[\frac{p_l}{m}\frac{\partial}{\partial q_l} - \sum_{n=1,\text{odd}}^{\infty} \frac{1}{n!}\left(\frac{i\hbar}{2}\right)^{n-1} \frac{\partial^n V(q_l)}{\partial q_l^n}\frac{\partial^n}{\partial p_l^n} \right] \tag{3.23}$$

We used the notation $q = (q_1, \ldots, q_\nu)$ and the cyclic condition $q_0 = q_\nu$ (and similarly for p and Δ). Let us now introduce the normal modes (Q, P) of the free ring polymer. The normal modes are defined as a change of variable which transforms the Hamiltonian of a free ring polymer (see equation (2.14) with $V = 0$) into a sum of independent harmonic oscillators with different normal frequencies. The normal mode transformation from q to Q is given by:

$$Q_n = \frac{1}{\sqrt{\nu}} \sum_{l=1}^{\nu} T_{ln} q_l \qquad \text{for} n = -(\nu-1)/2, \ldots, (\nu-1)/2 \tag{3.24}$$

and its inverse:

$$q_l = \sum_{n=-(\nu-1)/2}^{(\nu-1)/2} T_{ln}\sqrt{\nu} Q_n \tag{3.25}$$

and similarly for the transformation from p to P. The $\nu \times \nu$ unitary transfer matrix T is defined as:

$$T_{ln} = \begin{cases} \sqrt{1/\nu} & \text{if } n = 0 \\ \sqrt{2/\nu}\sin(2\pi ln/\nu) & \text{if } n = 1, \ldots, (\nu-1)/2 \\ \sqrt{2/\nu}\cos(2\pi ln/\nu) & \text{if } n = -1, \ldots, -(\nu-1)/2 \end{cases} \tag{3.26}$$

Each normal mode is associated with the normal frequency:

$$\omega_n = \frac{2\nu}{\beta\hbar}\sin\left(\frac{n\pi}{\nu}\right) \qquad \text{for} n = -(\nu-1)/2, \ldots, (\nu-1)/2 \tag{3.27}$$

One should notice that the transfer matrix defines a discrete Fourier transform. The low-frequency normal modes thus describe large scale motion of the polymer (for example the zero-frequency mode Q_0, that we will refer to as the centroid, describes rigid motion of the whole polymer) and high-frequency modes define local fluctuations inside the ring polymer. Consequently, if the high-frequency normal modes are filtered out, one obtains a smooth ring-polymer. The Matsubara modes are defined as the M first normal modes in the limit $\nu \to \infty$ (and $M \ll \nu$). Their normal frequencies are given by:

$$\tilde{\omega}_n = \lim_{\nu\to\infty} \omega_n = \frac{2n\pi}{\beta\hbar} \quad , n = -(M-1)/2, \ldots, (M-1)/2 \tag{3.28}$$

The ring-polymer quantum Liouvillian (3.23) can be expressed in terms of the normal modes by using (3.25) and separated into a part which depends on the Matsubara modes only $i\mathcal{L}_M$ and a part containing the dynamics of the high-frequency modes and the interactions between Matsubara and non-Matsubara modes $i\mathcal{L}_{\text{error}}(\nu, M)$, in the limit $\nu \to \infty$:

$$\lim_{\nu\to\infty} i\mathcal{L}_\nu = i\mathcal{L}_M + \lim_{\nu\to\infty} i\mathcal{L}_{\text{error}}(\nu, M) \tag{3.29}$$

Matsubara dynamics is obtained by discarding $i\mathcal{L}_{\text{error}}(\nu, M)$ and taking the limit $M \to \infty, M \ll \nu$. When doing so, the Liouvillian of the ring polymer is reduced to:

$$i\mathcal{L}_M = \sum_{n\in\mathcal{M}} \frac{P_n}{m}\frac{\partial}{\partial Q_n} - \frac{\partial U_M(Q)}{\partial Q_n}\frac{\partial}{\partial P_n} \tag{3.30}$$

with $n \in \mathcal{M}$ denoting $n = -(M-1)/2, \ldots, (M-1)/2$ and the Matsubara potential defined as:

$$U_M(Q) = \lim_{\nu\to\infty} \frac{1}{\nu}\sum_{l=1}^{\nu} V\left(\sum_{n\in\mathcal{M}} T_{ln}\sqrt{\nu}Q_n\right) \tag{3.31}$$

From the form of the Matsubara Liouvillian, one can notice that Matsubara dynamics is simply a classical dynamics on the potential U_M. Moreover, when discarding the non-Matsubara modes from the Liouvillian, one can completely integrate them out of equation (3.21) to obtain the Matsubara approximation to the Kubo-transformed TCF:

$$K_{AB}^{\text{Mats}}(t) = \lim_{\substack{M\to\infty \\ M\ll\nu}} \int \mathrm{d}Q\mathrm{d}P\ \rho_{\text{M}}(Q,P) A_M(Q) e^{i\mathcal{L}_M t} B_M(Q) \tag{3.32}$$

where the Matsubara quasi-density is given by:

$$\rho_{\text{M}}(Q,P) = \frac{e^{-\beta\left[\frac{P^2}{2m} + U_M(Q) - i\theta_M(Q,P)\right]}}{\int \mathrm{d}Q\mathrm{d}P\ e^{-\beta\left[\frac{P^2}{2m} + U_M(Q) - i\theta_M(Q,P)\right]}} \tag{3.33}$$

with the phase factor:

$$\theta_M(Q,P) = \sum_{n\in\mathcal{M}} P_n \tilde{\omega}_n Q_{-n} \tag{3.34}$$

The observables are expressed in terms of Matsubara modes similarly as $U_M(Q)$ such that

$$A_M(Q) = \lim_{\nu\to\infty} \frac{1}{\nu}\sum_{l=1}^{\nu} A\left(\sum_{n\in\mathcal{M}} T_{ln}\sqrt{\nu}Q_n\right) \tag{3.35}$$

and similarly for $B_M(Q)$. One should note that, even in the limit $M \to \infty$, the Matsubara correlation function does not converge to the exact Kubo-transformed correlation function since, in general, non-Matsubara modes will mix over time with Matsubara modes (due to the interaction part contained in $i\mathcal{L}_{\text{error}}(\nu, M)$ in equation

(3.29)), perturbing the simple Matsubara dynamics. One can show, however, that it is exact in the short-time limit, the harmonic limit and the classical limit. Matsubara dynamics is thus exact in the same limits as LSC-IVR but it has the advantage of conserving the initial quantum distribution (see ref. [66], section 4.C) so that it is not subject to inaccuracies such as zero-point energy leakage.

The quasi-density $\rho_{\text{M}}(Q,P)$ is the analogue of the Wigner distribution for the Matsubara modes. When the exact quantum dynamics is replaced by Matsubara dynamics, this distribution takes the simple form of a classical Boltzmann density with the potential U_M, multiplied by a phase factor. Since Matsubara dynamics is classical, the main difficulty is thus to sample initial conditions according to ρ_{M}. However, as the number of Matsubara modes increase, the phase tends to oscillate wildly, leading to a severe "sign problem". This sign problem thus prevents Matsubara dynamics from being a practical method for computing quantum time correlation functions of complex systems. It is however a useful conceptual tool for analyzing more practical approximations such as RPMD and CMD (that we will describe in the next sections) and for designing new approximations [55, 56]. Ref. [44] shows in more details how RPMD and CMD are obtained from Matsubara dynamics.

3.2.2 Ring-Polymer Molecular Dynamics

At $t=0$, the Matsubara time-correlation function reads:

$$K_{AB}^{\text{Mats}}(0) = \lim_{\substack{M\to\infty \\ M \ll \nu}} \int \mathrm{d}Q\mathrm{d}P\ \rho_{\text{M}}(Q,P) A_M(Q)\ B_M(Q) \tag{3.36}$$

By performing the change of variable $\Pi_n = P_n - im\tilde{\omega}_n Q_{-n}$ and using analytic continuation to shift Π_n to the real axis (see ref. [44] and its supplementary information), one can transform the phase factor in the Matsubara distribution (3.33) into a harmonic potential term. The resulting distribution is the standard imaginary-time ring polymer probability density (expressed in terms of Matsubara modes) given by:

$$\rho_{\text{RP}}(Q,\Pi) = \frac{e^{-\beta\left[\frac{\Pi^2}{2m}+U_M(Q)+\sum_{n\in\mathcal{M}}\frac{1}{2}m\tilde{\omega}_n^2 Q_n^2\right]}}{\int \mathrm{d}Q\mathrm{d}\Pi\ e^{-\beta\left[\frac{\Pi^2}{2m}+U_M(Q)+\sum_{n\in\mathcal{M}}\frac{1}{2}m\tilde{\omega}_n^2 Q_n^2\right]}} \tag{3.37}$$

This expression has no phase factor and the corresponding density can be sampled by a molecular dynamics (in the extended variable space) without facing a sign problem. However, at $t\neq 0$, one cannot in general perform the analytic continuation trick (except in the harmonic case) because the propagated operator $e^{i\mathcal{L}_M t}B_M(Q)$

depends on P in a nontrivial way. The RPMD approximation consists in forcing the analytic continuation at $t \neq 0$ and in replacing the Matsubara Liouvillian by:

$$i\mathcal{L}_{\text{RP}} = \sum_{n \in \mathcal{M}} \frac{\Pi_n}{m} \frac{\partial}{\partial Q_n} - \left[m\tilde{\omega}_n^2 Q_n + \frac{\partial U_M(Q)}{\partial Q_n} \right] \frac{\partial}{\partial \Pi_n} \tag{3.38}$$

The RPMD approximation to the Kubo-transformed TCF thus reads:

$$K_{AB}^{\text{RP}}(t) = \lim_{\substack{M \to \infty \\ M \ll \nu}} \int \mathrm{d}Q\mathrm{d}\Pi \; \rho_{\text{RP}}(Q,\Pi) A_M(Q) \; e^{i\mathcal{L}_{\text{RP}} t} B_M(Q) \tag{3.39}$$

RPMD is most commonly expressed in terms of real-space coordinates. Using (3.24), the ring-polymer density is then given by:

$$\rho_{\text{RP}}(q,p) = \frac{e^{-\frac{\beta}{\nu} \sum_{l=1}^{\nu} \left[\frac{p_l^2}{2m} + \frac{1}{2} m\omega_\nu^2 (q_l - q_{l-1})^2 + V(q_l) \right]}}{\int \mathrm{d}q\mathrm{d}p \; e^{-\frac{\beta}{\nu} \sum_{l=1}^{\nu} \left[\frac{p_l^2}{2m} + \frac{1}{2} m\omega_\nu^2 (q_l - q_{l-1})^2 + V(q_l) \right]}} \tag{3.40}$$

with $\omega_\nu = \nu/\beta\hbar$. The RPMD Liouvillian is given by:

$$i\mathcal{L}_{\text{RP}} = \sum_{l=1}^{\nu} \frac{p_l}{m} \frac{\partial}{\partial q_l} - \left[m\omega_\nu^2 (2q_l - q_{l+1} - q_{l-1}) + \frac{\partial V(q_l)}{\partial q_l} \right] \frac{\partial}{\partial p_l} \tag{3.41}$$

Finally, the RPMD approximation to the Kubo-transformed TCF in real-space coordinates is:

$$K_{AB}^{\text{RP}}(t) = \lim_{\nu \to \infty} \int \mathrm{d}q\mathrm{d}p \; \rho_{\text{RP}}(q,p) \left(\frac{1}{\nu} \sum_{l=1}^{\nu} A(q_l) \right) \; e^{i\mathcal{L}_{\text{RP}} t} \left(\frac{1}{\nu} \sum_{l=1}^{\nu} B(q_l) \right) \tag{3.42}$$

Therefore, in practice, RPMD simulations consist in performing standard PI molecular dynamics, as used for the sampling of static observables[1] and computing TCFs from the average (over the beads) observables A and B. In the case of momentum ATCF, on which we will focus more specifically, the Kubo-transformed TCF is simply approached by the centroid ATCF. Furthermore, since the RPMD dynamics conserves ρ_{RP}, the TCF obtained automatically verify detailed balance and the Wiener-Khinchin theorem can be used to reduce the numerical cost of the TCF calculation.

RPMD is exact in the same limits as Matsubara dynamics (i.e. short time, harmonic and classical limits). The main effect of approximating Matsubara dynamics with RPMD is that the frequencies of the Matsubara fluctuations are shifted to the ring-

[1] with the constraint that the mass of the beads, that can in principle be chosen arbitrarily, should be fixed to the actual atomic masses.

polymer frequencies. This leads to the apparition of the so-called "spurious peaks" in RPMD spectra corresponding to the unphysical ring-polymer frequencies. As we will see in chapter 5, it also leads to incorrect results for the amplitudes of anharmonic spectral features. Despite these difficulties, RPMD is one of the most efficient methods for computing quantum TCFs of high-dimensional systems and is routinely used to compute infrared spectra [59, 24, 83].

For linear observables (which depend on the centroid Q_0 only), it is possible to suppress the spurious peaks by applying a strong Langevin thermostat on the fluctuation modes $(Q_n)_{n\neq 0}$ (see ref. [84]). This is the so-called Thermostatted RPMD (TRPMD) method. The thermostat tends to overdamp the dynamics of the fluctuation modes thereby strongly broadening their spectrum and suppressing the associated spurious peaks. The thermostat also tends to broaden the physical peaks of the centroid spectrum, especially at low temperature.

3.2.3 Centroid Molecular Dynamics

For observables $\hat{A}$ and $\hat{B}$ depending only on the centroid position Q_0 (i.e. linear operators of position), one can focus on the centroid of the ring polymer and integrate out the other Matsubara modes (the fluctuation modes) in a mean-field approximation. This is the so-called Centroid MD approximation [40, 41, 42, 43, 44].

In CMD, the force $-\frac{\partial U_M(Q)}{\partial Q_0}$ acting on the centroid (which depends on all the Matsubara modes) is replaced by the mean-field force $F_{\mathrm{c}}(Q_0)$ depending only on the centroid position:

$$F_{\mathrm{c}}(Q_0) = -\lim_{M\to\infty} \int \Big(\prod_{\substack{n\,\in\,\mathcal{M}\\ n\,\neq\,0}} \mathrm{d}Q_n\Big)\, \frac{e^{-\beta\left(U_M(Q)+\sum_{n\in\mathcal{M}}\frac{1}{2}m\tilde{\omega}_2^2 Q_n^2\right)}}{\mathcal{Z}(Q_0)}\, \frac{\partial U_M(Q)}{\partial Q_0} \tag{3.43}$$

where $\mathcal{Z}(Q_0)$ is the centroid-conditional partition function (which normalizes the exponential factor at fixed centroid position). By this approximation, one obtains a dynamics that effectively depends on the centroid only. Once the mean-field average has been performed, the analytic continuation procedure described in the previous section can then be performed, since the higher order Matsubara modes appear only in the initial distribution. The CMD approximation to the Kubo-transformed TCF is then:

$$K^{\mathrm{c}}_{AB}(t) = \int \mathrm{d}Q_0\mathrm{d}P_0\; \rho_{\mathrm{c}}(Q_0,P_0)\; A(Q_0)e^{i\mathcal{L}_{\mathrm{c}}t}B(Q_0) \tag{3.44}$$

with $\rho_{\text{C}}(Q_0, P_0)$ the centroid distribution:

$$\rho_{\text{C}}(Q_0, P_0) = \int \Big(\prod_{\substack{n \in \mathcal{M} \\ n \neq 0}} \mathrm{d}Q_n \mathrm{d}P_n \Big) \, \rho_{\text{RP}}(Q, P) \tag{3.45}$$

and the mean-field centroid Liouvillian:

$$i\mathcal{L}_{\text{C}} = \frac{P_0}{m} \frac{\partial}{\partial Q_0} + F_{\text{C}}(Q_0) \frac{\partial}{\partial P_0} \tag{3.46}$$

An important note is that the mean-field centroid Liouvillian conserves the centroid-marginal distribution so that the CMD satisfies detailed balance.

For linear observables, CMD is exact in the same limits as Matsubara dynamics (i.e. short time, harmonic and classical limits) and it does not suffer from the sign problem. As we will see in chapter 5, averaging out the dynamics of the fluctuation modes leads to incorrect results for the amplitudes of anharmonic spectral features. Indeed, for anharmonic systems, the centroid is coupled to the dynamics of the fluctuation modes so that the mean-field approximation cannot properly describe the centroid dynamics. One of the most important difficulties of CMD is the so-called "curvature problem": for systems with rotating atomic bonds , the CMD displays strong red-shifts in the vibrational spectra at low temperature. Refs. [85, 86, 87] analyze the curvature problem in details. Recently, new attempts have been made to correct this inaccuracy of CMD by either including more and more fluctuation modes in the dynamics and generalizing the mean-field approach [87] or by recasting the description in terms of a quasi-centroid in curvilinear coordinates [88] instead of cartesian coordinates.

In practice, one must compute the mean-field force $F_{\text{C}}(Q_0)$ at each step of the centroid dynamics in order to propagate the motion described by (3.46). This can be done using an auxiliary sampling of the fluctuation modes at fixed Q_0 (via constrained Monte Carlo or Langevin dynamics for instance). An efficient approximation to bypass the auxiliary simulation is to consider the dynamics of the whole ring-polymer but to assign very light masses to the fluctuation modes so that their characteristic frequencies are adiabatically separated from the motion of the centroid. This adiabatic CMD allows to effectively apply the mean-field approximation on the fly [89, 90, 91].

3.2.4 Comparison on the Morse potential

We now compare the results of the TRPMD and CMD approximations for the Kubo-transformed momentum autocorrelation functions on the Morse potential (3.1). Figure 3.4 shows the Kubo-transformed momentum autocorrelation spectrum obtained using TRPMD and CMD compared to the LSC-LGA spectrum, the classical spectrum and the spectrum obtained by solving the Schrödinger equation. At 1200K, the TRPMD and CMD spectra are close to the LSC-LGA spectra described in the previous section. At 300K however, the TRPMD and CMD give very different results than LSC-IVR. The main spectral peak is much sharper in CMD and TRPMD (the TRPMD peak is broader than the CMD peak because of the strong thermostat applied to the fluctuation modes, as discussed in section 3.2.2) and located roughly halfway between the classical and quantum peaks. The same analysis can be done for the shape and position of the overtone at around 3100 cm^{-1}. We note, however, that the intensity of the overtone is very similar to that of the classical overtone and therefore much smaller than the actual quantum result (more details in chapter 5).

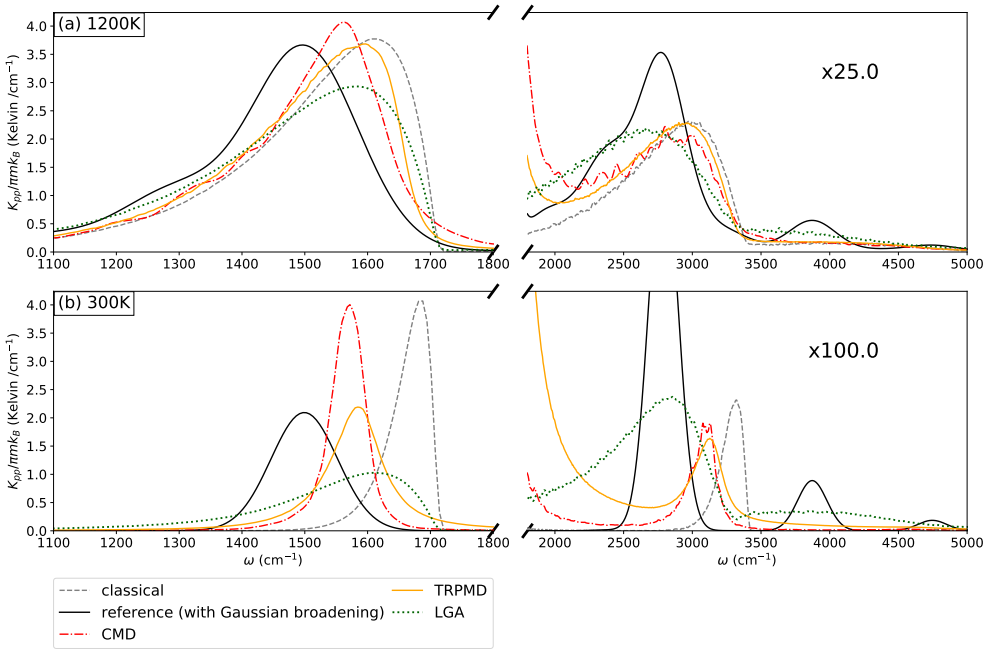

Fig. 3.4.: Kubo-transformed momentum autocorrelation spectrum for LGA+LSC-IVR (dotted green), CMD (dash-dotted red),TRPMD (solid orange), exact (solid black) and classical (dashed grey) at 1200K (panel a) and 300K (panel b) for the Morse potential of equation (3.1) (with $D = 20$ kcal/mol and $\alpha = 2.5$ Å^{-1}). The reference spectrum is broadened by convolution with a Gaussian function to approximately match the heights of the other spectra (the spectral weight of the peaks is not modified).

3.3 The Adaptive Quantum Thermal Bath

In this section we present a completely different approach that can be used to approximate both static and dynamical nuclear quantum effects: the Quantum Thermal Bath (QTB). A heuristic approach to the QTB may start by considering that the most relevant nuclear quantum effect in many cases is the fact that the quantum thermal distribution of energy differs from the classical rule of equipartition of energy, in particular due to zero-point fluctuations. The QTB approach then uses a Generalized Langevin Equation (GLE) to impose the quantum distribution of energy to an otherwise classical dynamics. The hybrid quantum-classical dynamics obtained in this way samples an approximation of the quantum phase space distribution (which is in principle given by the Wigner thermal distribution). Furthermore, if the coupling with the GLE thermostat remains weak enough, the short-term dynamics remains close to the classical NVE dynamics so that approximate dynamical spectra can also be obtained. Similarly to the LSC-IVR approach, the QTB combines (almost) classical dynamics with approximate quantum phase-space sampling. However, the QTB equations cannot be formally derived as the limit of the quantum statistical formalism under a well-defined approximation. Nevertheless, we will see that it still provides some interesting results often qualitatively correct, with the advantage of low-cost calculations compared to PI approaches.

The QTB approach is very close to the Quantum Thermostat method, although its formal implementation is significantly different. In this thesis we will focus on the QTB formalism. A comprehensive description of the Quantum Thermostat can be found in refs. [92, 93, 94].

3.3.1 The Fluctuation-Dissipation Theorem

Linear response theory provides a general relation, the fluctuation dissipation theorem, that relates the response of a system to an external perturbation to its internal dynamical properties, for any system at thermal equilibrium. The fluctuation-dissipation theorem (FDT) can be expressed for any pair of observables and in this section, we exploit the response of the momentum to a perturbation described by a time-dependent potential term proportional to position [95]. In this case, the FDT reads:

$$\frac{c_{pp}(\omega)}{2m} = \mathrm{Re}[\chi_{px}(\omega)] k_B T \Phi_\beta(\omega) \tag{3.47}$$

where $c_{pp}(\omega)$ is the Fourier transform of the momentum-momentum TCF (we use the convention that the ω dependence denotes a Fourier transform) and $\Phi_\beta(\omega)$ gives

the thermal energy distribution as a function of frequency. For a classical system where equipartition of energy holds, $\Phi_\beta(\omega) = 1$. For a quantum system, the average thermal energy depends on ω and is distributed as $\Phi_\beta(\omega) = (\beta\hbar\omega/2)/\tanh(\beta\hbar\omega/2)$ and $c_{pp}(\omega)$ is obtained as the Fourier transform of the real part of the standard quantum TCF. The term $\chi_{px}(\omega)$ (using the notations of ref. [95]) in expression (3.47) is the linear susceptibility which characterizes the response of momentum $\Delta p(t)$ to a small perturbative force $\Delta F(t)$ through the relation in the frequency domain:

$$\Delta p(\omega) = \chi_{px}(\omega)\Delta F(\omega) \tag{3.48}$$

Furthermore, for a harmonic system, $2\,\mathrm{Re}[\chi_{px}(\omega)]$ is the vibrational density of states and the FDT (3.47) characterizes the distribution of energy : it states that a vibrational mode at frequency ω is thermalized with an average kinetic energy $\frac{kT}{2}\Phi(\omega)$ (in the classical case, this corresponds simply to the equipartition of energy).

In classical simulations, one can impose the FDT using the Generalized Langevin Equation (GLE) which adds a frequency-dependent stochastic thermostat to Newton's equations of motion. The GLE for a unidimensional system reads:

$$\begin{cases} \dot{q}(t) = p(t)/m \\ \dot{p}(t) = -\dfrac{\partial V}{\partial q} - \displaystyle\int_0^\infty \mathrm{d}\tau\ \gamma(\tau)p(t-\tau) + F(t) \end{cases} \tag{3.49}$$

where $\gamma(\tau)$ is the memory kernel and $F(t)$ is a stationary Gaussian stochastic force defined by:

$$\langle F(t)\rangle = 0 \tag{3.50}$$

$$c_{FF}(\omega) = 2mk_BT\gamma(\omega) \tag{3.51}$$

Relation (3.51) is derived from the classical FDT and allows to enforce the equipartition of energy at k_BT (and to ensure that the correct Boltzmann distribution is sampled). This relation thus leaves freedom to choose different analytical forms for $\gamma(\omega)$. The properties of the GLE have been extensively investigated [96, 97, 98] and this freedom of choice has been exploited to optimize the sampling efficiency [99, 100]. In the standard Langevin equation, the friction is Markovian *i.e.* without memory: $\gamma(\tau) = \gamma\delta(\tau)$ where $\delta(\tau)$ is the Dirac delta function. This choice imposes that $F(t)$ is a white noise with an amplitude given by $c_{FF}(\omega) = 2mk_BT\gamma$.

As any thermostat, the Langevin equation affects the dynamics of the system. For example, for a harmonic system, the standard Langevin thermostat broadens the spectral peaks by convolution with a Lorentzian kernel of width γ. Using a small fric-

tion coefficient γ minimizes the effect of the thermostat on the dynamical properties, although it might also reduce the efficiency of the sampling.

3.3.2 The Standard Quantum Thermal Bath

The Quantum Thermal Bath [31] (QTB) uses a modified GLE to impose the quantum FDT to a classical system in order to sample an approximate Wigner distribution [101] and to obtain an approximate quantum dynamics [4, 5]. It uses the standard form of the Langevin equation with a Markovian friction but replaces relation (3.51) by:

$$c_{FF}(\omega) = 2mk_BT\Phi_\beta(\omega)\gamma \tag{3.52}$$

with $\Phi_\beta(\omega)$ the quantum distribution of energy. This relation aims at thermalizing the system with an energy corresponding to the quantum distribution of energy including ZPE and thermal fluctuations. For a harmonic system, adding a thermostat with relation (3.52) to the classical equations of motion allows to enforce the quantum FDT (3.47). In this case, in the limit of small friction $\gamma \to 0$, each harmonic mode is thermalized at the correct energy and the classical harmonic dynamics is equivalent to the true quantum dynamics. Thus, the QTB is exact for harmonic systems both for computing dynamical quantities and to sample the Wigner distribution.

Figure 3.5 show the Wigner distribution approximated by the QTB for the Morse potential of equation (3.1) at 1200K (panel a) and 300K (panel b). We see that the QTB is able to capture the broadening of the distribution due to zero-point energy, especially at 300K where the classical Boltzmann distribution is very narrow. The position of the maximum of probability of the QTB distribution corresponds to the classical one and thus the QTB is not able to capture the quantum shift of the equilibrium position (we will see in chapter 6 that this feature can be relevant, for example to describe the fine details of the structure of liquid water). Finally, as shown in ref. [101], the QTB distribution does not capture the position-momentum correlations of the Wigner distribution.

Figure 3.6 shows the Kubo-transformed momentum autocorrelation spectrum approximated using the QTB at 1200K (top panel) and 300K (bottom panel). We see that at both temperatures, the main spectral feature obtained using the QTB is very close to the LSC-IVR result. The overtone (around 3000 cm^{-1} however displays a shift (towards the classical overtone) and is roughly half as intense compared to the LSC-LGA result.

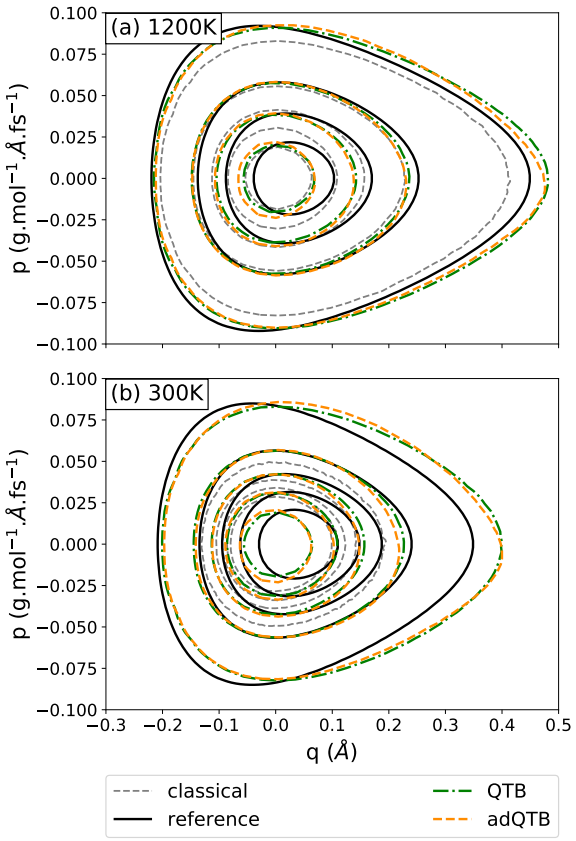

Fig. 3.5.: Wigner thermal distribution for the Morse potential of equation (3.1) (with $D = 20$ kcal/mol and $\alpha = 2.5$ Å^{-1}) approximated using the standard QTB (dash-dotted green) and adaptive QTB (dashed orange) at 1200K (panel a) and 300K (panel b). Contour levels are 1.5, 10, 20, 30, 40 fs.Å^{-2}.(g/mol)$^{-1}$.

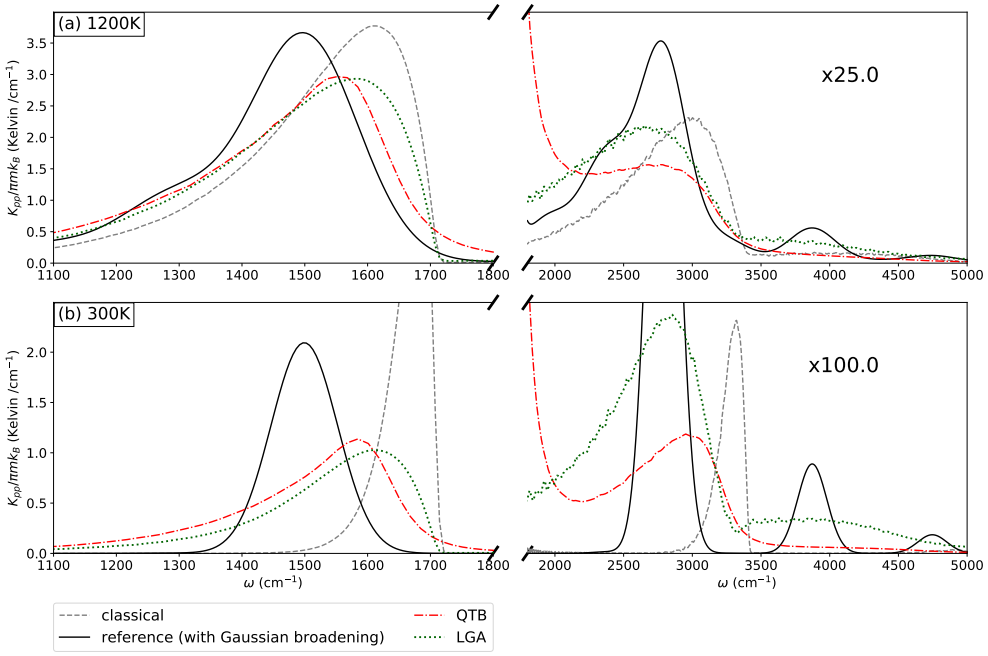

Fig. 3.6.: Kubo-transformed momentum autocorrelation spectrum for the QTB (dotted-dashed red) compared to the LSC-LGA (dotted green), exact (solid black) and classical (dashed grey) results at 1200K (panel a) and 300K (panel b) for the Morse potential of equation (3.1) (with $D = 20$ kcal/mol and $\alpha = 2.5$ Å^{-1}). The reference spectrum is broadened by convolution with a Gaussian function to approximately match the heights of the other spectra (the spectral weight of the peaks is not modified). The QTB spectra are obtained with a friction coefficient $\gamma = 10$THz and its effect on the width of the peaks have been reduced using the deconvolution procedure described in ref. [62].

3.3.3 The Quantum FDT: a diagnosis for zero-point energy leakage

In general, using a thermostat with the random force spectrum of (3.52) is not sufficient to enforce the quantum FDT of equation (3.47). It can lead to unphysical phenomena for anharmonic systems, such as Zero-Point Energy Leakage [57] which is an energy flow from high to low frequencies. ZPEL can have ravaging effects on a system and completely change its structure, for example leading to the melt down of solids even for temperatures close to zero [57, 102, 103] (see also the destructuration of liquid water in chapter 6). This unphysical effect in the QTB comes from the competition between the classical Newtonian evolution that drives the system towards equipartition of energy and the thermostat that tries to impose the quantum distribution of energy.

To illustrate this effect, let us consider a simple system involving two harmonic modes (of frequencies ω_1 and ω_2) with an anharmonic coupling. We can write the potential for this system as:

$$V(x_1, x_2) = \frac{1}{2}\omega_1^2 x_1^2 + \frac{1}{2}\omega_2^2 x_2^2 + c_3(x_1 - x_2)^3 \tag{3.53}$$

where the degrees of freedom x_1 and x_2 are mass-normalized. This potential allows to tune the anharmonicity through the coefficient c_3 and can be tuned to obtain large ZPEL. For this example, we use natural units with $\hbar = 1$ and $k_B = 1$ and consider a low temperature $T << \omega_1, \omega_2$ so that the energy in each degree of freedom consists mainly of zero-point energy. Figure 3.7 shows the average total energy in each mode as a function of the coupling parameter c_3 for different values of γ (with $\omega_1 = 1$ and $\omega_2 = 0.5$). The reference energies were obtained via an exact resolution of the two dimensional Schrödinger equation. In a classical simulation at thermal equilibrium, both modes would have the same average total energy $k_B T$. However, in the quantum reference, the modes have different energies, mostly given by their ZPE $\hbar\omega_1/2$ and $\hbar\omega_2/2$ and nearly independent of the coupling parameter in this range of values. With a small coupling parameter c_3, the QTB (blue lines in figure 3.7) is able to thermalize each mode at the correct energy as the ZPEL is slow compared to the thermostat's characteristic time γ^{-1}. As the anharmonicity is increased, the energy in the high frequency mode decreases while the energy in the low frequency mode increases, getting closer to equipartition of energy. Thus, ZPE "leaks" from the high frequency mode to the low frequency mode. We can see that this effect can be substantially reduced but not totally suppressed when using a larger value of γ.

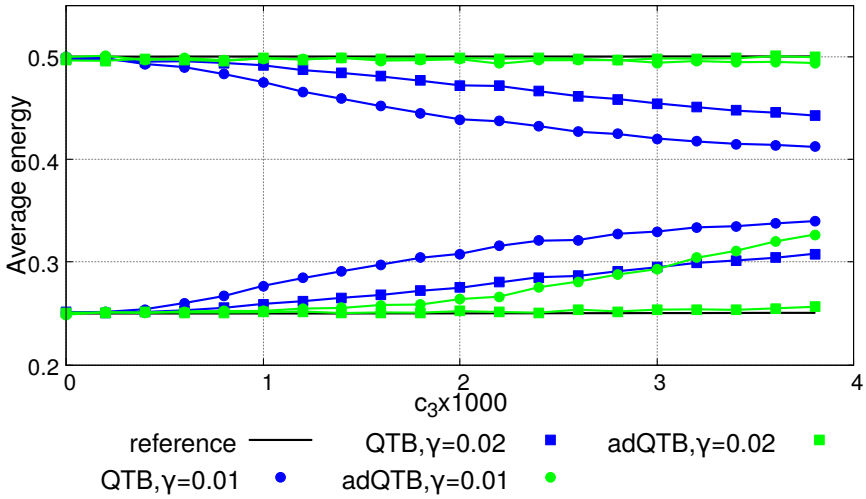

Fig. 3.7.: Average total energy in each harmonic oscillator of the model of equation (3.53), as a function of the coupling coefficients c_3. Blue curves: standard QTB. Green curves: adaptive QTB. The different dot shapes correspond to different values of the friction coefficient γ and the black lines show the exact result obtained through a numerical solution of the Schrödinger equation

Zero-point energy leakage can cause large errors in both static and dynamical properties of a system simulated with QTB. Therefore, until recently, it was very difficult to assess the accuracy of QTB simulations for large and complex systems, where no exact reference was available. In our group, we developed in ref. [58] a quantitative diagnosis for ZPEL, based on the measurement of deviations from the quantum FDT (3.47). In order to monitor these deviations during a QTB simulation, one has to translate equation (3.47) in a form that can be computed from the QTB trajectory. In the QTB framework, one approximates the real part of the quantum TCF $c_{pp}(t)$ using the TCF computed along a QTB trajectory. The main difficulty is then to estimate the linear susceptibility $\chi_{px}(\omega)$ and we show in ref. [58] that its real part can be expressed as a ratio of two correlation functions that can also be evaluated along a QTB trajectory:

$$\mathrm{Re}[\chi_{px}(\omega)] = \frac{\mathrm{Re}[c_{pF}(\omega)]}{c_{FF}(\omega)} \tag{3.54}$$

where F is the stochastic force of the GLE. This relation is obtained by using the property that the frequency components of F are statistically independent from one another ($\langle F(\omega)F(\omega')\rangle = 0$ if $\omega \neq \omega'$). This allows to treat the random force component at each particular frequency as a small perturbative force and use it as a probe to compute the linear response $\chi_{px}(\omega)$ using equation (3.48). By definition

of the QTB thermostat, $c_{FF}(\omega)$ is given explicitly by equation (3.52). Thus, the quantum FDT can be rewritten in the QTB framework as:

$$\mathrm{Re}[c_{pF}(\omega)] = \gamma c_{pp}(\omega) \tag{3.55}$$

Relation (3.55) thus links the response in momentum to the stochastic force $\mathrm{Re}[c_{pF}(\omega)]$ and the internal dynamical properties (*i.e.* the momentum power spectrum $c_{pp}(\omega)$). For a multidimensional system, this relation is valid independently for each degree of freedom. When relation (3.55) is met, it ensures that the equilibrium distribution of energy follows the quantum FDT. This is the case for harmonic potentials but, as shown for the coupled oscillators, the equality is not in general fulfilled for anharmonic system. Therefore, we use equation (3.55) as a criterion to quantify, for each frequency, the deviations from the quantum FDT. These deviations are quantified via the function:

$$\Delta_{\text{FDT}}(\omega) = \mathrm{Re}[c_{pF}(\omega)] - \gamma c_{pp}(\omega) \tag{3.56}$$

Equation (3.56) can also be given a simple physical interpretation: $\mathrm{Re}[c_{pF}(\omega)]$ is proportional to the power injected by the thermostat at frequency ω and $\gamma c_{pp}(\omega)$ describes the dissipated power. When the quantum FDT is enforced $\Delta_{\text{FDT}}(\omega) = 0$, the dissipated power balances the injected power. However, when the system is subject to ZPEL, energy flows from high frequency modes to low frequency modes so that the high frequency modes dissipate less energy than they are injected ($\Delta_{\text{FDT}} > 0$) and conversely for the low frequency modes ($\Delta_{\text{FDT}} < 0$).

The dashed purple curve in the top panel of figure 3.8 shows the deviation from the FDT, $\Delta_{\text{FDT}}(\omega)$, computed during a QTB simulation of the two oscillators (3.53) with coupling parameter $c_3 = 4 \times 10^{-3}$ and friction coefficient $\gamma = 0.02$. We can see that with the chosen parameters, the system is subject to ZPEL and Δ_{FDT} is not null at every frequency. More precisely, $\Delta_{\text{FDT}} > 0$ for the high-frequency mode and $\Delta_{\text{FDT}} < 0$ for the low-frequency mode, consistently with the intuition developed above.

3.3.4 The Adaptive QTB to cure zero-point energy leakage

The adaptive QTB (adQTB) was introduced in ref. [58] in order to enforce the quantum FDT in QTB simulations by adjusting on-the-fly the parameters of the thermostat. In the adQTB, the power spectrum of the stochastic force (3.52) is replaced with:

$$c_{FF}(\omega) = 2mk_BT\Phi_\beta(\omega)\gamma_r(\omega) \tag{3.57}$$

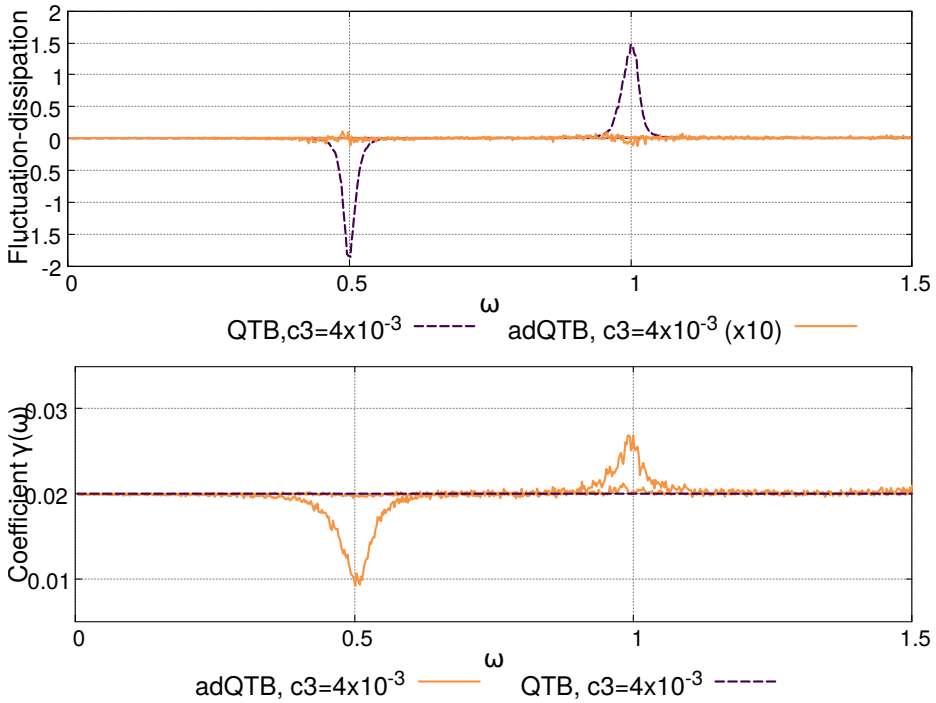

Fig. 3.8.: Top panel: deviation from the quantum FDT as defined in equation (3.56) during a QTB simulation (purple dashed curve) and after adaptation (orange curve) for the two oscillators model (3.53) with the coupling parameter $c_3 = 4 \times 10^{-3}$ and the friction coefficient $\gamma = 0.02$. The adQTB curve is multiplied by 10 for visualization purposes. Bottom panel: the orange curve is the coefficient $\gamma_r(\omega)$ as defined in equation (3.57) after adaptation. The purple dashed curve is the constant coefficient γ used in a standard QTB simulation.

where γ_r is an adjustable function of frequency that is adapted to enforce the quantum FDT, *i.e.* to have $\Delta_{\text{FDT}}(\omega) = 0$ for all ω. Note that the friction parameter γ in the GLE is kept constant. The quantum FDT for this modified power spectrum thus reads:

$$\text{Re}[c_{pF}(\omega)] = \gamma_r(\omega) c_{pp}(\omega) \tag{3.58}$$

and the deviation from the quantum FDT is:

$$\Delta_{\text{FDT}}(\omega) = \text{Re}[c_{pF}(\omega)] - \gamma_r(\omega) c_{pp}(\omega) \tag{3.59}$$

The aim of $\gamma_r(\omega)$ is to compensate for the lack or excess of energy at each frequency that could be introduced by the ZPEL for example. If $\gamma_r(\omega) > \gamma$ the thermostat introduces more energy at frequency ω than it dissipates. Conversely, if $\gamma_r(\omega) < \gamma$, it dissipates more energy than it injects. Thus, when the system is subject to ZPEL, γ_r should increase at high frequency and decrease at low frequency.

In practice, one starts the simulation with $\gamma_r(\omega) = \gamma$ (as in standard QTB) and computes Δ_{FDT} periodically via eq. (3.59). At each evaluation, γ_r is automatically adjusted on a grid of frequencies in order to match the FDT: if $\Delta_{\text{FDT}}(\omega) < 0$, $\gamma_r(\omega)$ is decreased by a small amount and conversely, if $\Delta_{\text{FDT}}(\omega) > 0$, $\gamma_r(\omega)$ is increased (a more precise suggestion of implementation of the adaptation procedure is provided in ref. [58]).

The bottom panel of figure 3.8 shows the coefficient $\gamma_r(\omega)$ after adaptation (with a friction coefficient $\gamma = 0.02$) for the two oscillators model (3.53). As expected, γ_r is larger than γ for the high-frequency mode in order to compensate for the energy that leaked into the low-frequency mode. Symmetrically, γ_r is lower than γ for the low-frequency mode. We can see on the top panel of figure 3.8 that Δ_{FDT} is indeed reduced to almost zero in adQTB (orange curve). As shown in figure 3.7 (green squares), the adaptation of $\gamma_r(\omega)$ allows to keep the average energy in each mode very close to the exact value in an adQTB simulation: the ZPEL is thus effectively compensated.

One should note that the coefficient $\gamma_r(\omega)$ must be positive in order for $c_{FF}(\omega)$ to be well defined. Thus, if the ZPEL is too large, one could reach the point where at a certain frequency ω_0, even if $\gamma_r(\omega_0)$ is null (i.e. no energy is injected), the deviation from the FDT is still negative. In this case, the friction term of the Langevin equation is not able to dissipate enough energy, even if no external energy is injected at this frequency: the amount of ZPEL is just too large. Thus, it might not be possible to enforce the quantum FDT for any friction γ and this parameter should be chosen large enough. This effect can be seen with the two oscillators model with a small

friction coefficient $\gamma = 0.01$ (green circles of figure 3.7). While the energy of the high frequency mode remains close to the exact value for all coupling c_3 , the energy of the low frequency mode remains too large for large values of c_3, even after the adaptation procedure. This indicates that γ_r is null around the low frequency mode so that the adaptation procedure cannot totally compensate the ZPEL.

In this example, each degree of freedom has a specific $\gamma_r(\omega)$. In practice, in the simulations of more complex systems, the same coefficient γ_r can be used for different degrees of freedom (it is then adapted from averaged Δ_{FDT}, as in chapter 6). This allows to average on fluctuations and to converge faster on the coefficients γ_r, and, in some cases, it is necessary to avoid them to diverge (in particular when rotation degrees of freedom are involved).

Ref. [58] showed that the adQTB greatly improved over the QTB for anharmonic systems. For example, in the case of small Neon clusters, the standard QTB is subject to large ZPEL that destabilizes the structure and causes the cluster to melt even at temperature close to zero. On the contrary, using the adQTB, the obtained radial pair distributions are very close to the path integrals reference, indicating that the adaptation procedure successfully compensated the ZPEL and allowed to recover the correct structure. In chapter 6, we apply the adQTB to liquid phase water and compare it to standard QTB and RPMD in order to assess the ability of the adQTB to correct for the ZPEL in a very anharmonic setting.

Ref. [58] also introduced another variant of adQTB in which the friction is non-Markovian and adapted on the fly to set Δ_{FDT} to zero. This other variant, which is technically more involved, is not discussed here.

To conclude this section, we apply the adQTB to the Morse potential of equation (3.1). Panel (a) of Figure 3.9 shows the two spectra involved in the FDT criterion (3.55) as well as the deviation to the quantum FDT (3.56) obtained in standard QTB. We can see that Δ_{FDT} is slightly negative on the tail of the main peak and positive around the overtone. This indicates that the overtone lacks energy according to the FDT and agrees with the observation made above that the QTB overtone is less intense than the reference (about half the intensity). Unexpectedly, the criterion (3.55) is thus able to detect this inaccuracy: although this kind of deviations from the FDT are manifestations of the (strong) anharmonicity of the Morse potential, they are of a different nature from ZPE leakage, which we defined as an energy flow between vibration modes, while the overtone is not, strictly speaking, such a mode. Nonetheless, we may try to correct it with the adQTB. Panel (b) of Figure 3.9 shows the coefficient γ_r obtained after the adaptation procedure. As expected, it is lower than γ (=10THz here) where $\Delta_{\text{FDT}} < 0$ and greater than γ where $\Delta_{\text{FDT}} > 0$. We can

see that γ_r takes very large values around the overtone. The adQTB thus injects a lot of energy at these frequencies but one can see in fig. 3.5 that it does not significantly affect the distribution sampled by the adQTB. The convergence of γ_r in this region is slow as the overtone is a purely anharmonic spectral feature and increasing γ_r has only limited impact. Nonetheless, γ_r converges after a long period of adaptation and is able to nullify Δ_{FDT} in the overtone region. We can see in the panel (c) of Figure 3.9 that the intensity of the overtone in the adQTB spectrum is much larger than for the standard QTB and is almost as intense as in LSC-LGA. Thus, the adaptation procedure, despite being designed initially for ZPEL between harmonic modes, also seems to be able to correct the intensity of the overtone in the Morse potential. This point will be analyzed more quantitatively in chapter 5.

The examples provided in this section, as well as others presented in ref. [58], clearly show that the criterion (3.55) is a very useful tool that allows to monitor and compensate for ZPEL in QTB simulations. In chapter 6, we will apply the adQTB to liquid-phase water and show that it is able to effectively correct ZPEL, even for this extremely anharmonic system.

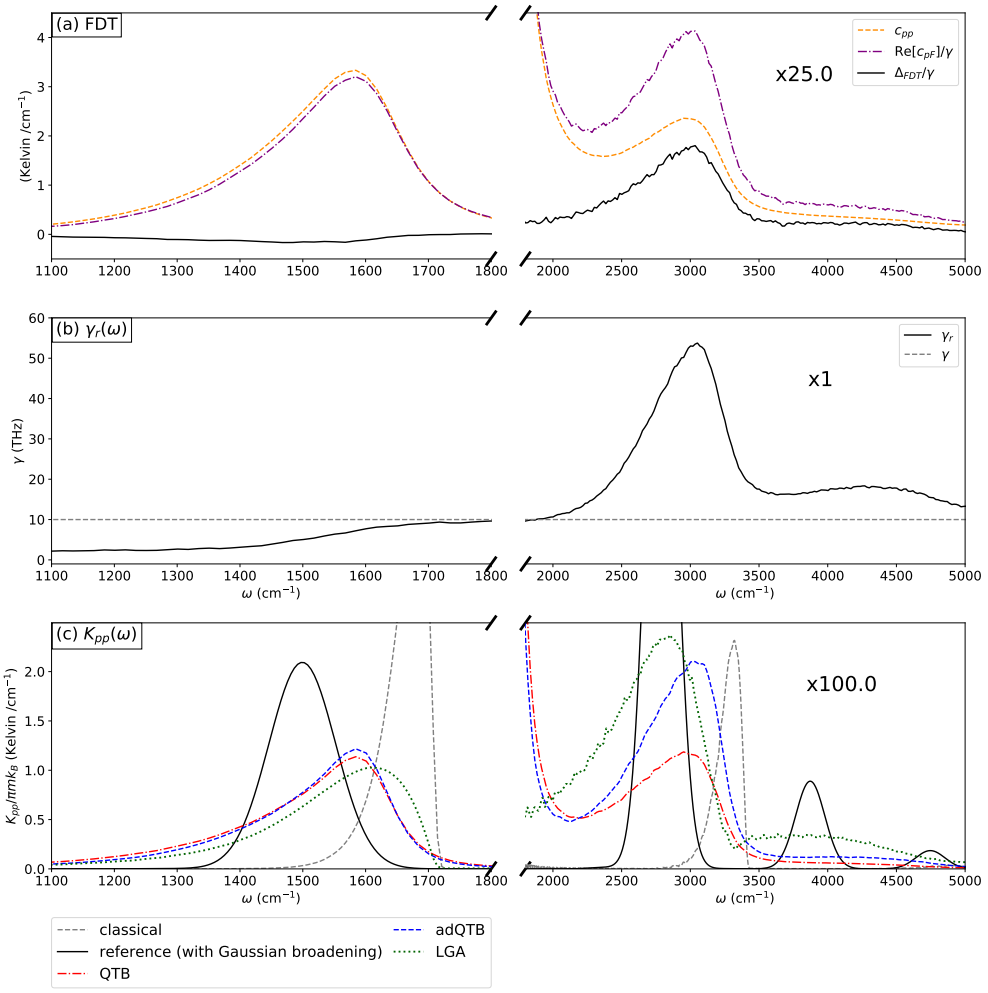

Fig. 3.9.: panel (a): fluctuation-dissipation criterion obtained using standard QTB (with friction $\gamma = 10$ THz) for the Morse potential. The momentum autocorrelation spectrum c_{pp} (dashed orange) is compared to $\mathrm{Re}[c_{pF}]$ (dash-dotted purple) in order to monitor deviations to the QTB version of the quantum FDT (3.55). The difference between the two spectra $\Delta_{\mathrm{FDT}}(\omega)$ (black curve) quantifies the deviations to the quantum FDT. panel (b): $\gamma_r(\omega)$ obtained after the adaptation procedure in order to minimize $\Delta_{\mathrm{FDT}}(\omega)$. panel (c): same as figure 3.6 with the adQTB spectrum superimposed (dashed blue curve).

4

Approximate quantum dynamics with the Edgeworth expansion of the Wigner distribution

In sections 2.2 and 3.1, we highlighted the role of the Wigner distribution in the computation of static and dynamical quantum statistical properties and we underlined some of the limitations of the most common sampling methods. In this chapter, we present a new approximation to the Wigner density that relies on an Edgeworth expansion of the momentum distribution and two differents ways of exploiting this approximation in order to compute approximate quantum time correlation functions.

Here and in most of the following we use one-dimensional notations. The multidimensional expressions for our developments are technically more involved and are presented in section 4.5. We start by recalling the definition of the Wigner thermal distribution:

$$\rho_{\mathrm{w}}(q,p) = \frac{1}{2\pi\hbar\mathcal{Z}} \int \mathrm{d}\Delta \; e^{\frac{ip}{\hbar}\Delta} \left\langle q - \frac{\Delta}{2} \middle| e^{-\beta\hat{H}} \middle| q + \frac{\Delta}{2} \right\rangle \tag{4.1}$$

with $\mathcal{Z}$ the partition function, $\beta = 1/k_B T$ the inverse thermal energy and $\hat{H} = \hat{p}^2/2m + V(\hat{q})$ the Hamiltonian of the system of mass m. As stated in section 2.2, the practical computation of the Wigner distribution presents notable difficulties. In fact, the Wigner density defined in eq. (4.1) is, in general, not positive, which prevents its immediate interpretation as a probability density. Furthermore, since the analytic form of this function is generally unknown, one must rely on numerical methods to estimate it. This calculation, however, is highly non-trivial because brute force schemes suffer from a numerical sign problem due to the oscillating phase factor $e^{\frac{ip}{\hbar}\Delta}$, which becomes rapidly unmanageable for generic high-dimensional systems. Several strategies (such as LGA, FK-LPI and QTB presented in sections 3.1 and 3.3), have been suggested to sample approximations of eq. (4.1). All of these strategies consider only the positive part of the Wigner function and introduce approximations that often cannot be assessed systematically from the theory or in the

implementations. Recently, an alternative approach was proposed [52], relying on an Edgeworth expansion to control the phase factor in eq.(4.1): the Phase Integration Method (PIM). This approach, that we briefly review in appendix A, was shown to capture interesting quantum effects, such as the correct correlations between different degrees of freedom (including coordinate-momentum and momentum-momentum correlations) and to provide reliable indications of the existence of negative parts of the Wigner density.

In this chapter, we derive a different and formally simpler Edgeworth expansion of the Wigner density. As for PIM, the new approximation is not subject to the sign problem, allows to recover negative parts of the distribution and its convergence can be systematically tested. We then consider two methods to exploit this approximation in order to compute approximate quantum TCFs. The first method is similar in spirit to the LGA and uses the Edgeworth expansion to approximate the conditional momentum distribution of the Wigner density. Time correlation functions are then computed in the LSC-IVR framework. We will see in the following that this approximation, namely the Edgeworth Conditional Momentum Approximation (ECMA), is systematically more accurate for sampling the distribution than LGA on the models we tested and that it results in better approximations of the TCFs. The second method is based on a generalized Langevin dynamics that rigorously samples the approximate Wigner distribution. This method, that we shall refer to as Wigner-Langevin dynamics (WiLD), is numerically less efficient than ECMA for sampling the Wigner distribution but we explore the possibility of exploiting the conservation of the density along the dynamics to directly compute quantum TCFs.

In the first section of this chapter, we derive the new Edgeworth expansion of the Wigner density and comment on its formal properties. We then derive the equations of motion of the WiLD and show that the dynamics is exact in the classical and harmonic limits in order to justify its use to compute approximate TCFs. In the third section, we present the formalism of the Edgeworth conditional momentum approximation. We then apply the methods to unidimensional models and compare the results to state-of-the-art methods. Finally, we present the multidimensional generalization of the formalism and show its application to two-dimensional systems that display interesting quantum properties.

4.1 The Edgeworth expansion of the Wigner distribution

In this section, we derive the Edgeworth expansion of the Wigner density in order to obtain an optimal Gaussian approximation of the momentum distribution. We also obtain a correction term, in the form of an infinite series, that allows to recover the negative parts of the Wigner distribution.

Let us begin by rewriting eq.(4.1) as

$$\rho_{\mathrm{w}}(q,p) = \frac{1}{2\pi\hbar\mathcal{Z}}\, e^{-\beta U(q)} e^{-\kappa_2(q)\frac{p^2}{2\hbar^2}} \int \mathrm{d}\Delta e^{\frac{ip}{\hbar}\Delta + \kappa_2(q)\frac{p^2}{2\hbar^2}} \rho_c(\Delta|q) \tag{4.2}$$

where

$$e^{-\beta U(q)} = \int \mathrm{d}\Delta \left\langle q - \frac{\Delta}{2}\middle| e^{-\beta\hat{H}} \middle| q + \frac{\Delta}{2}\right\rangle, \tag{4.3}$$

$$\rho_c(\Delta|q) = \frac{\left\langle q - \frac{\Delta}{2}\middle| e^{-\beta\hat{H}} \middle| q + \frac{\Delta}{2}\right\rangle}{\int \mathrm{d}\Delta \left\langle q - \frac{\Delta}{2}\middle| e^{-\beta\hat{H}} \middle| q + \frac{\Delta}{2}\right\rangle} \tag{4.4}$$

and $\kappa_2(q)$ is an arbitrary function of position.

Expanding $e^{\frac{ip}{\hbar}\Delta + \frac{\kappa_2 p^2}{2\hbar^2}}$ as a power series with respect to p, and choosing κ_2 as the second cumulant of the probability density ρ_c,

$$\kappa_2(q) = \int \mathrm{d}\Delta\ \Delta^2 \rho_{\mathrm{c}}(\Delta|q) = \left\langle \Delta^2 \right\rangle_{\rho_c|q} \tag{4.5}$$

yields the so-called Edgeworth approximation of the Wigner distribution:

$$\rho_{\mathrm{EWn}}(q,p) = \frac{1}{2\pi\hbar\mathcal{Z}}\, e^{-\beta U(q)} e^{-\kappa_2(q)\frac{p^2}{2\hbar^2}} \left[1 + \underbrace{\sum_{m=4,\mathrm{even}}^{n} \frac{\kappa_m(q)}{m!}\left(\frac{ip}{\hbar}\right)^m}_{C_{\mathrm{EWn}}(q,p)}\right] \tag{4.6}$$

where $\kappa_m(q)$ is the m-th order cumulant of ρ_c, for example, $\kappa_4(q) = \left\langle \Delta^4 \right\rangle_{\rho_c|q} - 3\left\langle \Delta^2 \right\rangle^2_{\rho_c|q}$. In equation (4.6), $\rho_{\mathrm{w}}(q,p)$ is approximated as the product of a positive function times the Edgeworth correction factor $1 + C_{\mathrm{EWn}}(q,p)$, that takes the form of an expansion in powers of p truncated at order n. The coefficients of this expansion, the cumulants of ρ_c, can be computed numerically without facing a sign problem. Note that the odd orders of $C_{\mathrm{EWn}}(q,p)$ vanish by parity of ρ_c with respect to Δ. Appendix A discusses the differences between the Edgeworth expansion described here and the one used in the PIM. In the following, we will indicate as EWn the Edgeworth approximation

to the Wigner density obtained by including terms up to order n in (4.6). Therefore EW0 designates the positive exponential factor alone.

The choice of $\kappa_2(q)$ as the second cumulant of ρ_c cancels the second order term in the Edgeworth correction so that the distribution $e^{-\kappa_2(q)\frac{p^2}{2\hbar^2}}$ is an optimal Gaussian approximation to the momentum distribution (in the sense of the Edgeworth expansion). In particular, this ensures that the approximation is exact when the true momentum distribution is Gaussian, for example for the harmonic potential (in this case, all of the terms in C_{EWn} are null) or in the classical limit.

Note that the Edgeworth correction can take negative values and allows in principle to recover negative parts of the Wigner density. Moreover, the expression 4.6 is exact in the limit $n \to \infty$ if the series C_{EWn} converges. The convergence is not ensured in general but C_{EWn} has the properties of an asymptotic series [104, 105] which means that the error is at most of the order of the last term considered in the truncated sum. In particular, we typically observe that the properties computed from the EWn approximation initially get closer to the exact quantum result with increasing n, before eventually diverging when $n \to \infty$. The consequences of this property as well as the way to choose the optimal order n are discussed in more details in paragraph 4.4.2. In practice the quality of the convergence may vary depending on the specific problem, but so far experience on relevant model systems shows that only few terms are needed to reach satisfactory convergence and that in many cases, even the zero order ρ_{EW0} provides a very good approximation to ρ_{w}. Our calculations also indicate that deviations from this form are not substantial for the model systems considered in this work with the notable exception of the quartic potential at low temperature.

In the following sections, we derive the two new methods obtained from the Edgeworth expansion. We will start with the Wigner-Langevin Dynamics (WiLD) that directly samples equation (4.6) using a generalized Langevin equation. We will then introduce the Edgeworth Conditional Momentum Approximation (ECMA) that slightly modifies equation (4.6) to allow for a more efficient sampling algorithm. The two methods mostly differ by their approach for computing quantum TCFs: the WiLD exploits the conservation of the approximate distribution by the Langevin dynamics to directly compute dynamical properties while the ECMA focuses on efficient sampling of the Wigner distribution in order to compute LSC-IVR approximations to the TCFs.

4.2 The Wigner-Langevin Dynamics

The WiLD uses a generalized Langevin dynamics to sample the EW0 distribution of equation (4.6) which is given by:

$$\rho_{\text{EW0}}(q,p) = \frac{\exp\left\{-\beta\left(U(q) + \frac{\kappa_2(q)}{\lambda_{th}^2}\frac{p^2}{2m}\right)\right\}}{\int \mathrm{d}q\mathrm{d}p\ \exp\left\{-\beta\left(U(q) + \frac{\kappa_2(q)}{\lambda_{th}^2}\frac{p^2}{2m}\right)\right\}} \tag{4.7}$$

with $\lambda_{th}^2 = \hbar^2\beta/m$ the thermal De Broglie wavelength. The EWn approximation is then obtained by reweighting the samples by the factor $1 + C_{\text{EWn}}(q,p)$. The density ρ_{EW0} resembles a standard Boltzmann thermal probability distribution but with an effective potential (or quantum free energy) $U(q)$ which is not the physical potential $V(q)$ and instead is given by expression (4.3), and incorporates nuclear quantum effects. Furthermore, the kinetic energy is multiplied by the quantum correction factor $\kappa_2(q)/\lambda_{th}^2$ which accounts for such effects as ZPE. This factor is also position-dependent, which allows for position-momentum correlation in the Wigner density. The quantum correction factor $\kappa_2(q)/\lambda_{th}^2$ and the effective potential (or free energy) $U(q)$ are given by expressions (4.3) and (4.5). These are not closed analytic expressions but averages over the density ρ_c and they have to be evaluated via an auxiliary path integral calculation (see section 4.2.2 for details).

In this section we start by deriving the Langevin equations of motion of the WiLD. We then derive numerically computable estimators for $U(q)$ and $\kappa_2(q)$ using open-chain path integrals in order to evaluate the WiLD forces. Finally, we investigate the classical and harmonic limits of the WiLD in order to motivate its use for computing approximate time-dependent properties.

4.2.1 Langevin equations of motion

In this section we derive the WiLD equations of motion and show that they sample the EW0 distribution $\rho_{\text{EW0}}(q,p)$. Our proof takes place as follows: (1) we postulate a form for the generalized Langevin equation containing an unknown force depending on position and momentum that contains some unspecified functions. (2) we write the Fokker-Planck equation that describes the time evolution of the distribution under the postulated Langevin dynamics. (3) we enforce stationarity of the probability density ρ_{EW0} in the Fokker-Planck equation and determine the previously unspecified

functions in the force. More in detail, let us consider the following generalized Langevin equations:

$$\begin{cases} \dot{q} = p/m \\ \dot{p} = F(q,p) - \gamma(q)p + \sigma(q)R(t) \end{cases} \tag{4.8}$$

where $R(t)$ is a white noise, and the generalized force $F(q,p)$ is of the form,

$$F(q,p) = A(q) + C(q)p^2 \tag{4.9}$$

A and C are functions of the position that we will determine below. Note that we imposed the relation $\dot{q} = p/m$ which is essential to obtain a meaningful dynamics from which we directly compute approximate TCFs (more details in the following). The Fokker-Planck equation describes the time-evolution of the phase-space probability distribution $\rho(q,p,t)$ under the stochastic dynamics (4.8):

$$\frac{\partial \rho}{\partial t} = -\frac{p}{m}\frac{\partial \rho}{\partial q} - \frac{\partial}{\partial p}\Big[\Big(F(q,p) - \gamma(q)p\Big)\rho\Big] + \frac{\sigma^2(q)}{2}\frac{\partial^2 \rho}{\partial p^2} \tag{4.10}$$

We then apply (4.10) to ρ_{EW0} and impose its stationarity (*i.e.* $\frac{\partial \rho_{\text{EW0}}(q,p)}{\partial t} = 0$) in order to determine the expressions of the functions A and C and the relation betwen $\gamma(q)$ and $\sigma(q)$. The Fokker-Planck equation yields (we omit the dependence on position to simplify the notations):

$$\begin{aligned} &\frac{\beta p}{m}\left(\frac{p^2}{2m\lambda_{th}^2}\frac{\partial \kappa_2}{\partial q} + \frac{\partial U}{\partial q}\right) + \frac{\beta \kappa_2}{m\lambda_{th}^2}p(A - \gamma p + Cp^2) \\ &- (-\gamma + 2Cp) + \frac{\sigma^2}{2}\left(-\frac{\beta\kappa_2}{m\lambda_{th}^2} + \left(\frac{\beta\kappa_2}{m\lambda_{th}^2}p\right)^2\right) = 0 \end{aligned} \tag{4.11}$$

The equation above is satisfied by setting to zero the position-dependent coefficient for each power of p. This leads to the following expressions for the unknown functions in eq. (4.9):

$$C(q) = -\frac{1}{2m\kappa_2(q)}\frac{\partial \kappa_2}{\partial q} \tag{4.12}$$

$$\gamma(q) = \frac{\beta\sigma^2(q)}{2m}\frac{\kappa_2(q)}{\lambda_{th}^2} \tag{4.13}$$

$$A(q) = -\frac{\lambda_{th}^2}{\kappa_2(q)}\frac{\partial U}{\partial q} - \frac{\lambda_{th}^2}{\beta\kappa_2^2(q)}\frac{\partial \kappa_2}{\partial q} \tag{4.14}$$

Inserting these expressions into (4.9) gives the generalized force of the WiLD:

$$F(q,p) = -\frac{\lambda_{th}^2}{\kappa_2(q)}\frac{\partial U}{\partial q} - \left(\frac{\lambda_{th}^2}{\beta\kappa_2(q)} + \frac{p^2}{2m}\right)\frac{1}{\kappa_2(q)}\frac{\partial \kappa_2}{\partial q}, \tag{4.15}$$

The discussion above shows that the EW0 probability density ρ_{EW0} is stationary under the stochastic dynamics (4.8) when the force is given by (4.15). Equation (4.13) is the fluctuation-dissipation relation of the WiLD. As in standard Langevin dynamics, either γ or σ is a free parameter. It is simpler in the case of the WiLD to choose a position-independent friction coefficient γ and deduce σ as:

$$\sigma^2(q) = 2mk_BT\gamma\frac{\lambda_{th}^2}{\kappa_2(q)} \tag{4.16}$$

The WiLD equations (4.8) with the force given by eq. (4.15) have three main non-standard features. Firstly, the force $F(q,p)$ depends on both position and momentum. This unusual dependence on momentum originates from the position-dependent factor $\kappa_2(q)/\lambda_{th}^2$ that renormalizes the kinetic energy. Secondly, the thermostat itself depends on position as the fluctuation-dissipation relation of the WiLD (4.16) is position-dependent. This fact too is a consequence of the renormalization of the kinetic energy. Thirdly, as discussed in more detail in the next subsection, both the force $F(q,p)$ and the noise amplitude $\sigma(q)$ are not known analytically and must be estimated via an auxiliary path integral calculations at each time step of the WiLD trajectory. In order to ensure the stability and the accuracy of the evolution, these non-analytic terms must be estimated with enough precision so that the dynamics is not altered.

4.2.2 Estimating the generalized forces using path integrals

Three terms that do not have a known analytical expression ($\frac{\partial U}{\partial q}$, $\kappa_2(q)$ and $\frac{\partial \kappa_2}{\partial q}$) appear in the WiLD equations of motion. In order to be able to compute the WiLD forces derived in the previous section, one has to compute these terms that are integrals over the off-diagonal elements of the density operator. In particular, we have:

$$U(q) = -k_BT\ln\left[\int \mathrm{d}\Delta \left\langle q - \frac{\Delta}{2}\middle| e^{-\beta\hat{H}} \middle| q + \frac{\Delta}{2}\right\rangle\right] \tag{4.17}$$

and

$$\kappa_2(q) = \frac{\int \mathrm{d}\Delta\ \Delta^2 \left\langle q - \frac{\Delta}{2}\middle| e^{-\beta\hat{H}} \middle| q + \frac{\Delta}{2}\right\rangle}{\int \mathrm{d}\Delta \left\langle q - \frac{\Delta}{2}\middle| e^{-\beta\hat{H}} \middle| q + \frac{\Delta}{2}\right\rangle} \tag{4.18}$$

From the solution of the Schrödinger equation, these expressions are easily computed using the wavefunction representation of the density operator (2.7)[1]. When the solution to the Schrödinger equation is not accessible, one can express the density operator using path integrals. The path integral representation of the conditional density $\rho_c(\Delta|q)$ defined in equation (4.4) takes the form:

$$\rho_c(\Delta|q) = \lim_{\nu\to\infty} \int \mathrm{d}x_1 \ldots \mathrm{d}x_{\nu-1}\ \rho_\nu(\Delta, x_1, x_{\nu-1}|q) \tag{4.19}$$

with

$$\rho_\nu(\Delta, x_1, \ldots, x_{\nu-1}|q) = \frac{\exp\left\{-\beta\tilde{V}_q(\Delta, x_1, \ldots, x_{\nu-1})\right\}}{\int \mathrm{d}\Delta\mathrm{d}x_1 \ldots \mathrm{d}x_{\nu-1} \exp\left\{-\beta\tilde{V}_q(\Delta, x_1, \ldots, x_{\nu-1})\right\}} \tag{4.20}$$

and the q-constrained open chain path integral potential

$$\begin{aligned}\tilde{V}_q(\Delta, x_1, \ldots, x_{\nu-1}) = &\frac{1}{2\nu}V(q+\frac{\Delta}{2}) + \frac{1}{2\nu}V(q-\frac{\Delta}{2}) + \frac{1}{\nu}\sum_{l=1}^{\nu-1}V(x_l) \\ &+ \frac{1}{2}\frac{m\nu}{\beta^2\hbar^2}\left[(q-\frac{\Delta}{2}-x_{\nu-1})^2 + (q+\frac{\Delta}{2}-x_1)^2 + \sum_{l=1}^{\nu-2}(x_{l+1}-x_l)^2\right]\end{aligned} \tag{4.21}$$

The density $\rho_\nu(\Delta, x_1, \ldots, x_{\nu-1}|q)$ corresponds to the thermal density for an open-chain of beads. The middle point between the two ends of the chain is fixed at q (see figure 4.1). The end points are symmetrically distributed around q and the end-to-end distance is equal to the variable Δ. The distribution $\rho_c(\Delta|q)$ is thus the marginal density of the end-to-end distance around the position q when integrating over all open chain configurations.

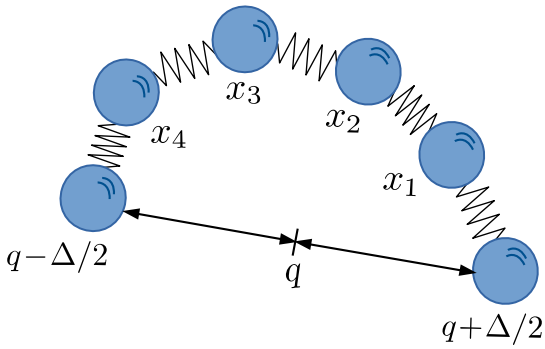

Fig. 4.1.: Schematic representation of the open chain used in the auxiliary calculation for WiLD simulations for $\nu = 5$. The middle between the two ends of the chain is fixed at q and the opening of the chain is labeled Δ.

[1] We use this strategy in chapter 5 for 1D and 2D systems for which precise estimations of κ_2 were necessary.

We now write the path integral estimators of the WiLD non-analytical terms. First, $\kappa_2(q)$ is equal to the variance of the end-to-end distribution:

$$\kappa_2(q) = \lim_{\nu\to\infty} \left\langle \Delta^2 \right\rangle_{\rho_\nu|q} \tag{4.22}$$

where $\langle \cdot \rangle_{\rho_\nu|q}$ denotes the expectation value over the path integral density constrained at q. The higher order cumulants $\kappa_m(q)$ appearing in the Edgeworth correction can also be computed using similar expressions. In the following, we will drop the explicit limit $\nu \to \infty$ but it is implied for all ν-dependent quantities.

The derivative of the WiLD effective potential $\frac{\partial U}{\partial q}$ is obtained as follows. First, we rewrite:

$$\begin{aligned}\frac{\partial U}{\partial q} &= -k_B T \frac{\partial}{\partial q} \ln\left[\int \mathrm{d}\Delta \mathrm{d}x_1 \dots \mathrm{d}x_{\nu-1}\; e^{-\beta \tilde{V}_q(\Delta, x_1, \dots, x_{\nu-1})}\right] \\ &= \frac{\int \mathrm{d}\Delta \mathrm{d}x_1 \dots \mathrm{d}x_{\nu-1}\; e^{-\beta \tilde{V}_q(\Delta, x_1, \dots, x_{\nu-1})} \frac{\partial}{\partial q} \tilde{V}_q(\Delta, x_1, \dots, x_{\nu-1})}{\int \mathrm{d}\Delta \mathrm{d}x_1 \dots \mathrm{d}x_{\nu-1}\; e^{-\beta \tilde{V}_q(\Delta, x_1, \dots, x_{\nu-1})}}\end{aligned} \tag{4.23}$$

We then recognize an expectation value over ρ_ν and obtain:

$$\frac{\partial U}{\partial q} = \left\langle \frac{\partial}{\partial q} \tilde{V}_q(\Delta, x_1, \dots, x_{\nu-1}) \right\rangle_{\rho_\nu|q} \tag{4.24}$$

which is a mean-field force averaged over the path integral distribution. Two different expressions can be obtained for the derivative of the path integral potential with respect to q. The first one is to directly differentiate expression (4.21) with respect to q. The second is obtained by first performing the change of variable $x_l = q + \delta_l$ (which cancels q from the spring terms), differentiating the new path integral potential with respect to q and then revert back to x_l. These estimators read:

$$\frac{\partial U}{\partial q} = \left\langle \frac{1}{2\nu}\frac{\partial}{\partial q} V(q + \frac{\Delta}{2}) + \frac{1}{2\nu}\frac{\partial}{\partial q} V(q - \frac{\Delta}{2}) + \frac{m\nu}{\beta^2\hbar^2}(2q - x_1 - x_{\nu-1}) \right\rangle_{\rho_\nu|q} \tag{4.25}$$

$$= \left\langle \frac{1}{\nu}\left[\frac{1}{2}\frac{\partial}{\partial q} V(q + \frac{\Delta}{2}) + \frac{1}{2}\frac{\partial}{\partial q} V(q - \frac{\Delta}{2}) + \sum_{l=1}^{\nu-1} \frac{\partial}{\partial x_l} V(x_l)\right] \right\rangle_{\rho_\nu|q} \tag{4.26}$$

Both estimators give the same result but their numerical convergence properties may differ depending on the system potential energy surface, on the position q and on the temperature. In the following examples, we mostly used the second estimator. It should be possible to work out an optimal estimator based on the average of the two expressions, with weights adjusted depending on the variance of each estimator (this is not done in this work).

Similarly, we obtain the estimator for the derivative of κ_2 by differentiating equation (4.22) with respect to q:

$$\frac{\partial \kappa_2}{\partial q} = \beta \Bigg[\left\langle \Delta^2 \right\rangle_{\rho_\nu|q} \left\langle \frac{\partial}{\partial q} \tilde{V}_q(\Delta, x_1, \ldots, x_{\nu-1}) \right\rangle_{\rho_\nu|q} - \left\langle \Delta^2 \frac{\partial}{\partial q} \tilde{V}_q(\Delta, x_1, \ldots, x_{\nu-1}) \right\rangle_{\rho_\nu|q} \Bigg] \tag{4.27}$$

which can also be expressed using either one of the two different estimators for the derivative of the path integral potential.

At each step of the Wigner-Langevin dynamics, the expectation values in equations (4.22),(4.24) and (4.27) must be numerically evaluated in order to propagate the WiLD equations of motion (4.8). One thus samples configurations of the open chain distributed as ρ_ν and approximates the expectation values by empirical averages. In this work, the sampling of the open chain is done using an auxiliary path integral Langevin dynamics (see ref. [106] for technical details).

This auxiliary calculation is mainly responsible for the high numerical cost of the method. Indeed, to ensure the stability and the accuracy of the propagation, the variance of the estimators of the forces has to be small. For simplicity in this work, we only use brute force reduction of the variance by using long auxiliary Langevin dynamics. Two routes might be pursued in future work to circumvent this requirement. A first strategy would consist in adapting to our method the interesting schemes recently proposed to accommodate noisy terms in classical Langevin equations[107, 108]. This would allow to relax the current requirement on the accuracy of the estimates and reduce the numerical cost of our dynamics considerably. We experimented with this strategy for unidimensional systems with encouraging results. The generalization to multidimensional systems is technically involved but can in principle be done. A second strategy might be to compute the averages with high accuracy on a fixed set of points in the q space and then use these values to obtain noiseless estimates in the whole space via interpolation schemes. We have tested this approach with excellent results for the 1-d models presented in this work. Generalizations to higher dimensional systems would be possible adapting methods currently used to fit energy and/or forces via machine learning techniques, based on accurate quantum chemical calculations of the Born-Oppenheimer potential energy surface at a few reference geometries. In this spirit, one could use machine learning approaches, such as artificial neural networks [18, 19] or Gaussian process regression[20, 21, 22], to train a model for the Wigner forces on selected points in position space.

Figure 4.2 shows a sketch of the complete procedure to perform a WiLD simulation and compute approximate TCFs. In the next section, we show that the WiLD is exact in the classical and harmonic limits in order to motivate its use for computing approximate quantum TCFs.

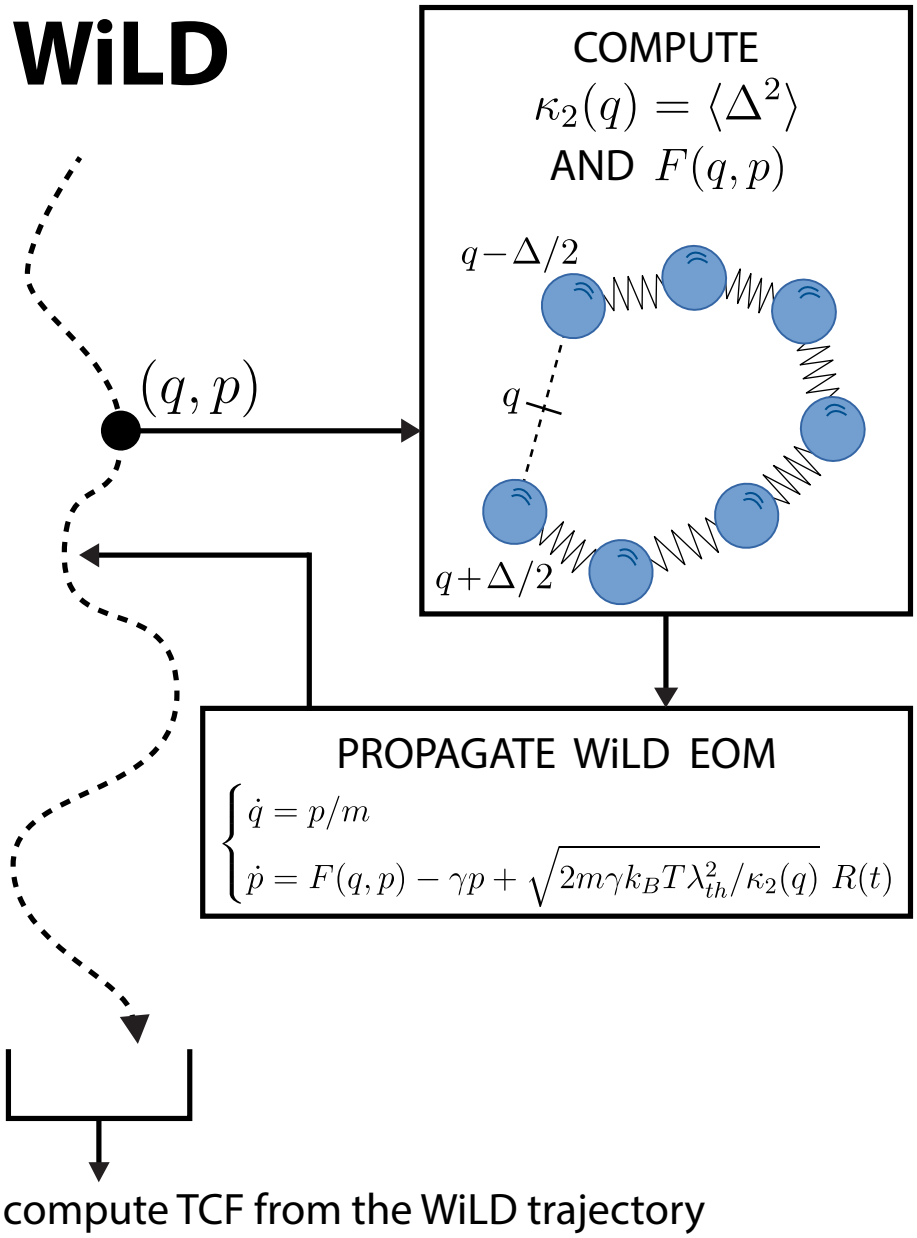

Fig. 4.2.: Sketch of the WiLD algorithm for computing TCFs

4.2.3 Using WiLD for dynamical properties

By construction, the WiLD is a stationary dynamics that conserves the EW0 approximation to the Wigner distribution. It is therefore tempting to use it not only as a sampling tool, but to compute time correlation functions directly from the WiLD trajectories. With respect to the LSC-IVR approach (*i.e.* sampling according to EW0 then computing dynamical properties along classical NVE trajectories), this offers two advantages. The first is conceptual: since the EW0 distribution is conserved, it avoids spurious effects related to non-stationarity and particularly zero-point energy leakage. The second is computational: the stationarity of the dynamics allows using the Wiener-Khinchin theorem to compute time correlation functions more efficiently.

We will demonstrate in this section that the particular equations of motion chosen for the WiLD give the exact quantum dynamics in the classical and harmonic limits (which are the two limits usually invoked when designing approximate schemes for quantum dynamics) at least in the limit of small γ. We will show in chapter 5 that the WiLD is also able to better reproduce some anharmonic features (such as overtones and combination bands) than most approximate methods for quantum dynamics.

To simplify the notations in this section, we define:

$$w(q,\Delta) \equiv \left\langle q - \frac{\Delta}{2}\middle| e^{-\beta\hat{H}} \middle| q + \frac{\Delta}{2}\right\rangle \tag{4.28}$$

and rewrite the auxiliary sampling density ρ_c as:

$$\rho_c(\Delta|q) = \frac{w(q,\Delta)}{\int d\Delta\, w(q,\Delta)} \tag{4.29}$$

Classical limit

In the classical limit, the operator $e^{-\beta\hat{H}}$ can be broken up via the Trotter formula as:

$$\begin{aligned} e^{-\beta\hat{H}} &= e^{-\frac{m\lambda_{th}^2}{\hbar^2}\hat{H}} \\ &= e^{-\frac{m\lambda_{th}^2}{2\hbar^2}V(\hat{q})} e^{-\frac{\lambda_{th}^2\hat{p}^2}{2\hbar^2}} e^{-\frac{m\lambda_{th}^2}{2\hbar^2}V(\hat{q})} + \mathcal{O}\left(\lambda_{th}^6\right) \end{aligned} \tag{4.30}$$

In the equation above, we chose to use the thermal De Broglie wavelength $\lambda_{th}^2 = \hbar^2\beta/m$ as a more suitable control parameter than the temperature for the classical limit (see below). Eq. (4.28) then becomes:

$$w(q,\Delta) \propto \exp\left\{-\frac{m\lambda_{th}^2}{2\hbar^2}\left(V(q-\frac{\Delta}{2})+V(q+\frac{\Delta}{2})\right)-\frac{\Delta^2}{2\lambda_{th}^2}\right\} \tag{4.31}$$

Due to the Gaussian factor in this expression, only values of Δ at most of the order of the De Broglie wavelength will lead to significant contributions to the Wigner density. Let us now consider the different terms appearing in the WiLD equations of motion. We begin by performing the change of variable $X = \Delta/\lambda_{th}$ to obtain:

$$\begin{aligned}\kappa_2(q) &= \frac{\int \mathrm{d}X\ \lambda_{th}^2 X^2 w(q,\lambda_{th}X)}{\int \mathrm{d}X\ w(q,\lambda_{th}X)} \\ \frac{\partial U}{\partial q} &= \frac{\int \mathrm{d}X\ \frac{1}{2}\left[V^{(1)}(q-\frac{\lambda_{th}X}{2})+V^{(1)}(q+\frac{\lambda_{th}X}{2})\right]w(q,\lambda_{th}X)}{\int \mathrm{d}X\ w(q,\lambda_{th}X)}\end{aligned} \tag{4.32}$$

where $V^{(1)}$ is the first derivative of the physical potential V. The expressions above are integrals over the density $w(q,\lambda_{th}X)/\int \mathrm{d}X w(q,\lambda_{th}X)$ that we can rewrite via a Taylor expansion in powers of λ_{th}:

$$\frac{w(q,\lambda_{th}X)}{\int \mathrm{d}X w(q,\lambda_{th}X)} = \frac{e^{-X^2/2}}{\int \mathrm{d}X\ e^{-X^2/2}}\left(1+\frac{m\lambda_{th}^4}{8\hbar^2}V^{(2)}(q)(1-X^2)+\mathcal{O}\left(\lambda_{th}^6\right)\right) \tag{4.33}$$

where $V^{(n)}$ denotes n-th order derivative of the physical potential V. Substituting (4.33) in eq. (4.32) and performing the integrals, we obtain:

$$\kappa_2(q) = \lambda_{th}^2 + \mathcal{O}\left(\lambda_{th}^6\right) \tag{4.34}$$

$$\frac{\partial U}{\partial q} = V^{(1)}(q) + \frac{\lambda_{th}^2}{8}V^{(3)}(q) + \frac{\lambda_{th}^4}{128}V^{(5)}(q) + \mathcal{O}\left(\lambda_{th}^6\right) \tag{4.35}$$

and we see that the kinetic correction factor κ_2/λ_{th}^2 tends to unity in the classical limit. Note that the definition of $U(q)$ (eq. (4.3)) has some analogies with the definition of a quantum free energy at position q. Its derivative can then be interpreted as a potential of mean force incorporating non-local contributions via the integral over the displacement Δ. Eq. (4.35) shows that in the classical limit, this mean force reduces to $-V^{(1)}(q)$, the standard force. Higher order terms in the λ_{th} expansion denote the quantum delocalization by implicitly exploring broader regions of the potential via higher order derivatives.

To complete the classical limit of the WiLD, we observe that p is distributed according to $e^{-\frac{\kappa_2(q)p^2}{2\hbar^2}}$, so that we can assign the order of magnitude $p^2 \sim \hbar^2/\lambda_{th}^2$. This, together with (4.34) and (4.35), yields:

$$F(q,p) \sim -V^{(1)}(q) + \mathcal{O}\Big(\lambda_{th}^2\Big) \tag{4.36}$$

and

$$\sigma^2(q) = \gamma 2mk_BT + \mathcal{O}\Big(\lambda_{th}^6\Big) \tag{4.37}$$

In summary, in the high-temperature limit $\lambda_{th} \to 0$, the WiLD equations of motion (4.8) become:

$$\begin{cases} \dot{q} = p/m \\ \dot{p} = -V^{(1)}(q) - \gamma p + \sqrt{\gamma 2mk_BT}R(t) \end{cases} \tag{4.38}$$

Thus, we retrieve the standard classical Langevin equation for a system subject to potential V at inverse temperature β. The Edgeworth expansion terms can be estimated with the same approach. In particular, we find that $\kappa_4(q) = \mathcal{O}(\lambda_{th}^6)$ and, using $p^4 \sim \hbar^4/\lambda_{th}^4$, $C_{\text{EWn}}(q,p) = \mathcal{O}(\lambda_{th}^2)$. In the classical limit $\lambda_{th} \to 0$, the Wigner density approaches the classical Boltzmann density, which is a Gaussian function of p. Therefore the Edgeworth expansion tends to converge already at the lowest lorder EW0. Indeed, as we showed for the 4th order, although p^n tends to take large values in the high-temperature limit, the high-order cumulants κ_n vanish even faster, so that the EWn terms tend to zero for $\lambda_{th} \to 0$.

Harmonic limit

We now consider the case of the harmonic potential $V(q) = \frac{m\omega^2}{2}q^2$. For this system, the density matrix elements in the coordinate representation are known analytically (see for example ref. [60]), and we have:

$$w(q,\Delta) \propto \exp\Big\{-\frac{m\omega}{4\hbar\tanh(\beta\hbar\omega/2)}\Delta^2 - \frac{m\omega}{\hbar}\tanh(\beta\hbar\omega/2)q^2\Big\} \tag{4.39}$$

so that

$$\begin{aligned} \kappa_2(q) &= \frac{\int \mathrm{d}\Delta\ \Delta^2 \exp\Big\{-\frac{m\omega}{4\hbar}\tanh^{-1}(\beta\hbar\omega/2)\Delta^2\Big\}}{\int \mathrm{d}\Delta\ \exp\Big\{-\frac{m\omega}{4\hbar}\tanh^{-1}(\beta\hbar\omega/2)\Delta^2\Big\}} \\ &= \frac{\tanh(\beta\hbar\omega/2)}{\beta\hbar\omega/2}\ \lambda_{th}^2 \end{aligned} \tag{4.40}$$

Note that κ_2 is in this case independent of q and $\frac{\partial \kappa_2}{\partial q} = 0$. We can also write an analytical expression for $\frac{\partial U}{\partial q}$ via:

$$\begin{aligned}\frac{\partial U}{\partial q} &= -\frac{1}{\beta}\frac{\int \mathrm{d}\Delta\ \frac{\partial w}{\partial q}}{\int \mathrm{d}\Delta\ w(q,\Delta)} \\ &= \frac{\tanh(\beta\hbar\omega/2)}{\beta\hbar\omega/2}\, m\omega^2 q\end{aligned} \tag{4.41}$$

Thus, for a harmonic system, the WiLD equations of motion are given by:

$$\begin{cases} \dot{q} = p/m \\ \dot{p} = -\, m\omega^2 q - \gamma p + \sqrt{\gamma 2m\Theta(\omega,\beta)}R(t) \end{cases} \tag{4.42}$$

where $\Theta(\omega,\beta) = \frac{\hbar\omega}{2}\coth(\beta\hbar\omega/2)$ is the average thermal energy of the quantum harmonic oscillator. Therefore, the Wigner-Langevin dynamics reduces to the classical evolution for its deterministic part (*i.e.* $F(q,p)$ in eq. (4.8) is simply the classical force), combined with a Langevin thermostat at an effective temperature $\Theta(\omega,\beta)/k_B$. Therefore, the WiLD is exact, in the limit of small γ, for the harmonic potential. In passing, we note that (4.42) takes a similar form as the Quantum Thermal Bath in which the dynamics is classical and the thermostat is responsible for the quantum thermal effects.

Finally, one should note that, in the harmonic case, $\rho_c(\Delta|q) \propto w(q,\Delta)$ is Gaussian and thus all cumulants of order higher than two are zero and $C_{\text{EWn}}(q,p) = 0$.

4.3 The Edgeworth Conditional Momentum Approximation

The WiLD rigorously samples the EW0 approximation to the Wigner distribution but is computationally very intensive as it requires to perform an auxiliary path integral calculation at *each step* of the dynamics in order to propagate the equations of motion. Furthermore, one should also notice that the EW0 approximation does not ensure that the marginal position distribution is exact. In this section, we slightly modify the Edgeworth approximation (4.6) in order to enforce the exact marginal position distribution that can efficiently be sampled using standard PIMD. The conditional momentum distribution is given by the Edgeworth expansion and this rewriting allows for a more efficient sampling of the approximate Wigner distribution in order to compute approximate TCFs using LSC-IVR.

We start by rewriting the exact Wigner density eq. (4.1) as the position marginal density times the conditional momentum density

$$\rho_{\mathrm{w}}(q,p) = \rho_{\mathrm{w}}^{m}(q)\rho_{\mathrm{w}}^{c}(p|q) \tag{4.43}$$

where

$$\rho_{\mathrm{w}}^{m}(q) = \langle q|\hat{\rho}|q\rangle \tag{4.44}$$

can be efficiently sampled using its path integrals representation given by eqs. (2.13),(2.14) and

$$\begin{aligned}\rho_{\mathrm{w}}^{c}(p|q) &= \frac{\int \mathrm{d}\Delta\; e^{\frac{ip}{\hbar}\Delta}\left\langle q-\frac{\Delta}{2}\middle|e^{-\beta\hat{H}}\middle|q+\frac{\Delta}{2}\right\rangle}{2\pi\hbar\,\langle q|e^{-\beta\hat{H}}|q\rangle} \\ &= \frac{\int \mathrm{d}\Delta\; e^{\frac{ip}{\hbar}\Delta}\left\langle q-\frac{\Delta}{2}\middle|e^{-\beta\hat{H}}\middle|q+\frac{\Delta}{2}\right\rangle}{\int \mathrm{d}\Delta\; 2\pi\hbar\delta(\Delta)\left\langle q-\frac{\Delta}{2}\middle|e^{-\beta\hat{H}}\middle|q+\frac{\Delta}{2}\right\rangle}\end{aligned} \tag{4.45}$$

with δ the Dirac function. We then insert the relation $2\pi\hbar\delta(\Delta) = \int \mathrm{d}p\; e^{i\frac{p\Delta}{\hbar}}$ to obtain:

$$\rho_{\mathrm{w}}^{c}(p|q) = \frac{\int \mathrm{d}\Delta\; e^{\frac{ip}{\hbar}\Delta}\left\langle q-\frac{\Delta}{2}\middle|e^{-\beta\hat{H}}\middle|q+\frac{\Delta}{2}\right\rangle}{\int \mathrm{d}p\;\int \mathrm{d}\Delta\; e^{\frac{ip}{\hbar}\Delta}\left\langle q-\frac{\Delta}{2}\middle|e^{-\beta\hat{H}}\middle|q+\frac{\Delta}{2}\right\rangle} \tag{4.46}$$

thus making clear the normalization of the conditional momentum distribution. We now use the same Edgeworth expansion as in section 4.1 for both Δ integrals in $\rho_{\mathrm{w}}^{c}(p|q)$ to obtain the Edgeworth Conditional Momentum Approximation (ECMA) to the Wigner distribution:

$$\rho_{\mathrm{ECMAn}}(q,p) = \rho_{\mathrm{w}}^{m}(q)\rho_{\kappa_2}(p|q)\frac{1+C_{\mathrm{EWn}}(q,p)}{1+\overline{C_{\mathrm{EWn}}}(q)} \tag{4.47}$$

with

$$\overline{C_{\mathrm{EWn}}}(q) = \int \mathrm{d}p\;\rho_{\kappa_2}(p|q)\;C_{\mathrm{EWn}}(q,p) \tag{4.48}$$

and

$$\rho_{\kappa_2}(p|q) = \frac{e^{-\kappa_2(q)\frac{p^2}{2\hbar^2}}}{\int \mathrm{d}p\; e^{-\kappa_2(q)\frac{p^2}{2\hbar^2}}} = \frac{e^{-\beta\frac{p^2}{2m}\Phi_{\mathrm{EW0}}^{-1}(q)}}{\int \mathrm{d}p\; e^{-\beta\frac{p^2}{2m}\Phi_{\mathrm{EW0}}^{-1}(q)}} \tag{4.49}$$

where we introduced the Quantum Correction Factor (EW0-QCF)

$$\Phi_{\mathrm{EW0}}(q) = \frac{\hbar^2\beta}{m\kappa_2(q)} \tag{4.50}$$

in analogy with the momentum distribution of LGA (eq. (3.9)).

The natural procedure to sample the ECMA is similar to the LGA. First, sample the marginal position distribution $\rho_{\text{w}}^{m}(q)$ using standard path integral techniques. Then, compute $\kappa_2(q)$ using equation (4.22) and potentially higher order cumulants to obtain $C_{\text{EWn}}(q,p)$ (and $\overline{C_{\text{EWn}}}(q)$ by a simple Gaussian integration). Finally sample the momentum using the conditional Gaussian distribution $\rho_{\kappa_2}(p|q)$. In order to correct the distribution and obtain negative parts of the Wigner distribution, one must multiply the observables by the ratio $\frac{1+C_{\text{EWn}}(q,p)}{1+\overline{C_{\text{EWn}}}(q)}$. Approximate quantum TCFs are then obtained in the LSC-IVR framework by propagating the sampled phase space point using classical dynamics.

Since $\kappa_2(q)$ is non-analytical and estimated numerically (see section 4.2.2), it is subject to statistical noise. This statistical noise can then induce biases on the conditional momentum distribution, which in turn can affect the estimation of momentum-dependent observables. In practice, the noise tends to broaden the momentum distribution and leads to an overestimation of the kinetic energy. One can correct this effect by reweighting the distribution with a factor depending on the variance σ^2 of the numerically estimated κ_2 (see appendix B). For the EW0 momentum distribution, the noise correction factor is given, up to second order in σ, by:

$$C_{\text{noise}}^{\text{EW0}}(p\ ;\ \kappa_2,\sigma) = 1 - \sigma^2\left(\frac{p^4}{8\hbar^4} - \frac{p^2}{4\hbar^2\kappa_2} - \frac{1}{8\kappa_2^2}\right) \tag{4.51}$$

Appendix B demonstrates the effect of the noise correction on the estimation of the kinetic energy of the unidimensional Morse potential of equation 3.1. It also shows the multidimensional version of equation (4.51).

This approximation has two major advantages over LHA and the FK approximation. First, it allows to correct the conditional Gaussian approximation by including successive orders of C_{EWn} and to recover negative parts of the Wigner distribution. Second, the conditional Gaussian approximation is well defined for any system since, by construction, $\kappa_2(q)$ and the EW0-QCF are always positive. In particular, one does not need an ansatz to treat systems with barriers (in cases of strong barriers, the C_{EWn} correction should provide significant contribution) which lead to imaginary frequencies and ill-defined terms in LHA or FK-LPI. For all the examples considered in this thesis, the ECMA yields a much better approximation to the Wigner distribution than LGA and FK-LPI, in particular at low temperature.

As a final comment, one should note that sampling the ECMA0 distribution did not yield significant differences compared to the EW0 distribution sampled by the WiLD for the examples provided in this thesis. It allowed, however, for a much more efficient sampling. Thus, if one is only interested in sampling the Wigner density

(in order to perform a LSC-IVR calculation for example), the ECMA seems to be a more favourable approximation than the WiLD. Moreover, since Φ_{EW0} is not needed to sample the marginal position distribution of ECMA, the auxiliary calculation can be performed on only a subset of independent positions and multiple values of the momentum can be sampled at each position. Figure 4.3 shows a sketch of the complete procedure to compute approximate TCFs in the LSC-IVR framework using ECMA initial conditions.

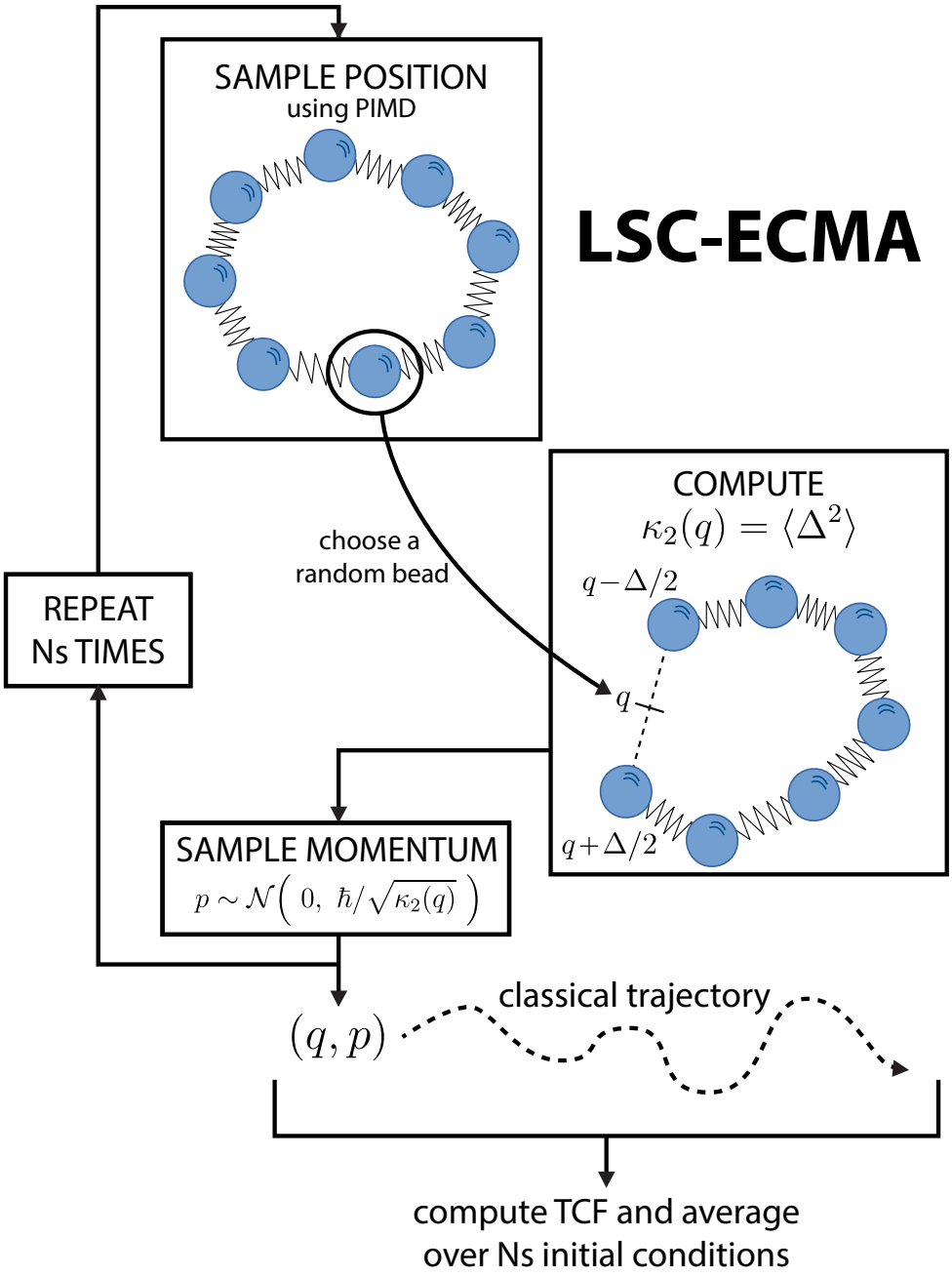

Fig. 4.3.: Sketch of the LSC-ECMA algorithm for computing TCFs

4.4 Application to unidimensional model systems

In this section we present applications of the ECMA and WiLD to two unidimensional model systems closely related to those used in ref. [52]: the Morse and quartic potentials. For each test case, we study two aspects: the static sampling of the Wigner density and the computation of the approximate momentum autocorrelation spectrum.

For the sampling problem, we compute the positive approximation to the Wigner density (EW0) and analyze the effect of the Edgeworth correction[2]. The results are compared to the classical Boltzmann distribution (always shown as a dashed gray curve) and to the quantum reference (always shown as a black continuous curve) obtained via a numerical resolution of the Schrödinger equation. We also compare the distributions to the LGA and FK approximations.

We then present approximations to the momentum autocorrelation spectrum for each model using WiLD, TRPMD, QTB and LSC-IVR with initial conditions given by ECMA, LGA and FK (that we will denote respectively LSC-ECMA, LSC-LGA and LSC-FK). This will allow us to compare directly the effect of the different approximations both on initial distribution and dynamics.

The number of beads ν employed in the path integral calculations is indicated in the figure captions.

4.4.1 Morse potential

Let us start by considering the one-dimensional Morse potential:

$$V(q) = D\left[e^{-2\alpha q} - 2e^{-\alpha q}\right] + D\zeta(q) \tag{4.52}$$

with $D = 20$ kcal/mol, $\alpha = 2.5$ Å^{-1} (same as ref. [52] and chapter 3), and for a particle with the mass of a proton. The term $\zeta(q)$ is introduced to prevent dissociation of the system: $\zeta(q) = 1$ for $q \leq q_{max}$ and $\zeta(q) = e^{\eta(q-q_{max})}$ for $q > q_{max}$ with $q_{max} = 2.5$ Å and $\eta = 2$ Å^{-1}.

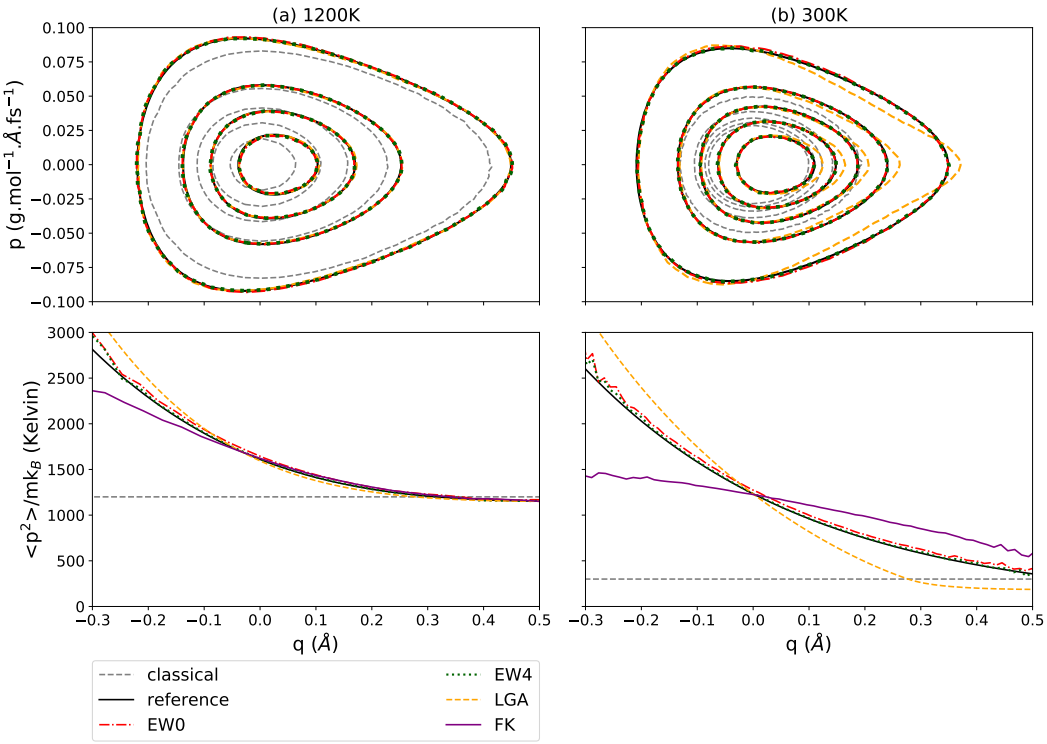

Fig. 4.4.: top panels: Wigner thermal distribution for the Morse potential approximated using EW0 (dash-dotted red), EW4 (dotted green) compared to LGA (dashed orange). Contour levels are 1.5, 10, 20, 30, 40 fs.Å^{-2}.(g/mol)$^{-1}$. FK is not shown in order to keep the curves more visible but the corresponding results can be found in chapter 3. bottom panels: mean square momentum as a function of q. This graph corresponds to the average of p^2 over a vertical slice of the top panel, renormalized by mk_B to obtain a temperature. The EW approximations are compared to the classical Boltzmann distribution (dashed grey), to the exact result (solid black) obtained from solving the Schrödinger equation on a grid and to LGA (dashed orange) and FK (solid purple). Left panels: 1200K, 8 beads. Right panels: 300K, 32 beads.

Sampling of the Wigner distribution

The top panels of figure 4.4 show contour plots of the Wigner density at 1200K (upper left panel) and 300 K (upper right panel), as obtained with the positive approximation EW0 (dashed-dotted red curves) and including terms up to 4th-order in the Edgeworth expansion (EW4: dotted green curve). EW0 and EW4 results are very close, indicating convergence of the expansion already at order 0 at both temperatures. In particular, for this system, the Wigner density does not present significant negative regions. The bottom panels of figure 4.4 show the variance of the conditional momentum distribution as a function of q (*i.e.* the average value of p^2 on each vertical slice of the corresponding distribution in the top panel). We can see that, at both temperatures, the EW approximation is close to the exact result (a slightly better agreement can be seen with EW4 at 300K).

At 1200K, the thermal energy k_BT is of the same order as the zero-point energy for the system, so quantum effects are not very pronounced. The numerically exact Wigner density is similar to the classical Boltzmann distribution, with only a slight broadening and a small shift of the maximum of probability, due to zero-point motion. These effects are perfectly captured by the EW0 approximation and also well described by the LGA.

At 300K, k_BT is significantly smaller than the zero-point energy, and quantum effects are much more significant. The classical Boltzmann distribution is considerably narrower than the Wigner density, and their respective maxima are clearly shifted from one another. The EW0 results are in very good agreement with the exact distribution also in this more challenging situation. Even at 300K, the effect of the Edgeworth correction terms remains small: the 4th order is responsible only for a slight narrowing of the momentum distribution (barely distinguishable on the top panels of Fig. 4.4).

One should note that the Wigner distribution displays position-momentum correlations which is a purely quantum effect since such correlations are completely absent from the classical Boltzmann distribution. This can easily be seen in the bottom panels of figure 4.4. We can see that in the classical case, the mean square momentum does not depend on position while it does for the quantum system, and most notably at low temperature. These figures also show that EW clearly provides a better approximation to the Wigner density than both LGA and FK approaches, which tend to overestimate (resp. underestimate) the dependence on q of the mean

[2] In this thesis, we use ECMA to sample the Wigner distribution. The distributions sampled using WiLD can be found in ref. [106] but do not display significant differences

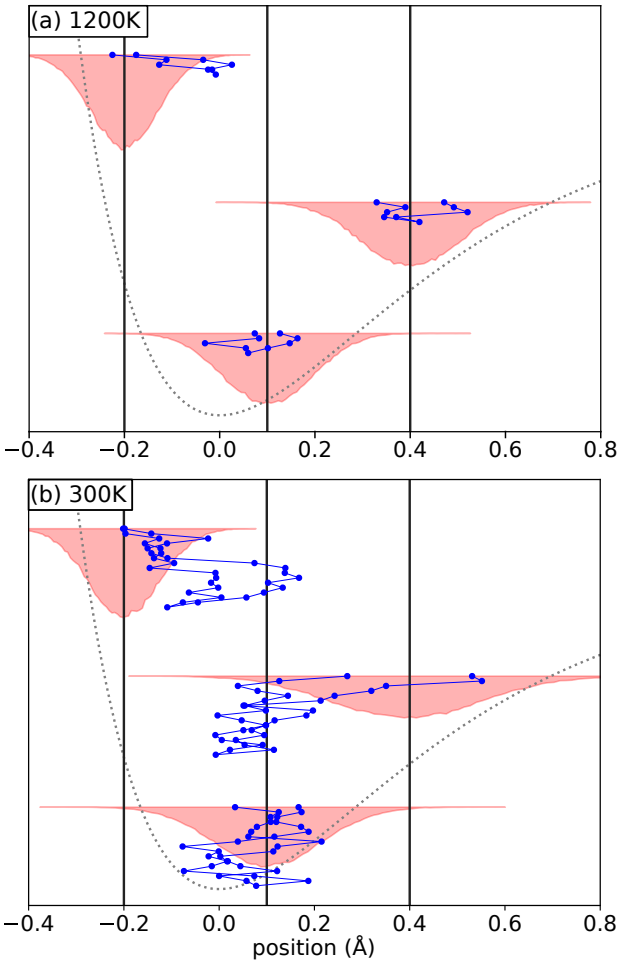

Fig. 4.5.: Snapshots of typical open chain configurations sampled in the auxiliary Langevin dynamics for the Morse potential at 1200 K (a) and 300 K (b). The position of the different beads is indicated with a blue dot (the position of the dots along the vertical axis is arbitrary and just for visualization purposes). Successive beads in the chain are connected with a blue line. The black vertical lines indicate the value of q for which the auxiliary calculation is performed (*i.e.* the middle between the two endpoints of the chain): -0.2 Å, 0.1 Å and 0.4 Å. The figure also shows in red the histogram of the positions of the two endpoints of the open chain, $q - \frac{\Delta}{2}$ and $q + \frac{\Delta}{2}$, sampled during the auxiliary dynamics. The variance of this distribution is directly related to $\kappa_2(q)$. On each panel, the potential is superimposed (gray dotted line) with a suitable scale.

square momentum. At order EW0, the mean square momentum is directly related to the quantum correction factor $\Phi_{\text{EW0}}(q) = \lambda_{th}^2/\kappa_2(q)$. From the definition of κ_2 in equation (4.22), we clearly see that Φ_{EW0} is a non-local quantity. This can be visualized in figure 4.5 which shows typical configurations of the open chain extracted from the auxiliary calculation used to compute κ_2 at different positions and at both temperatures. We see that the beads of the open chain explore a wide area around q where the potential varies and, at 300K, most of the beads fluctuate close to the minimum of the potential. This non-locality allows the EW approximation to correctly capture the q-dependence of the quantum correction factor and thus of the mean square momentum. By contrast, the LGA-QCF is purely local and overestimates the q-dependence of the mean square momentum. The position dependence of the FK-QCF is more subtle as it depends on the centroid position and not directly on q. Like the EW-QCF, it is a non-local quantity but it only considers fluctuations around the centroid which tends to be localized close to the minimum of the potential at low temperature. This results in the underestimation of the q-dependence of the mean square momentum in the FK approximation.

Momentum autocorrelation spectrum

We now focus on the computation of dynamical properties using the WiLD and LSC-ECMA. Figure 4.6 shows the Kubo-transformed momentum autocorrelation spectrum for the different approximate methods, compared to the exact spectrum and to the classical result at 1200K (top panel) and 300K (bottom panel).

At 1200K, the main spectral feature (around 1500 cm^{-1}) exhibits a slight shift between the classical and quantum spectra. The quantum spectrum of a finite dimension system consist in a series of Dirac delta-functions, centered at the difference frequencies between the eigenmodes of the system (see section 2.2.2). Here for visualization purposes, these delta-peaks are artificially replaced with Gaussian functions (of the same width, chosen so that the height of the features approximately matches the classical one). Therefore the asymmetric shape of the main peak actually arises from a series of peaks with decreasing intensities. In the classical case, the broadening of the peak is due to anharmonic effects (the softening of the Morse potential at large q). The position and shape of this main spectral feature mostly agree between the different approximate methods: the shape is close to the classical spectrum and the peak is shifted roughly halfway between the quantum and classical peaks. The same observations can be made for the overtones (zoom on the overtones region on the right side of figure 4.6) with slightly larger variations of the peaks positions.

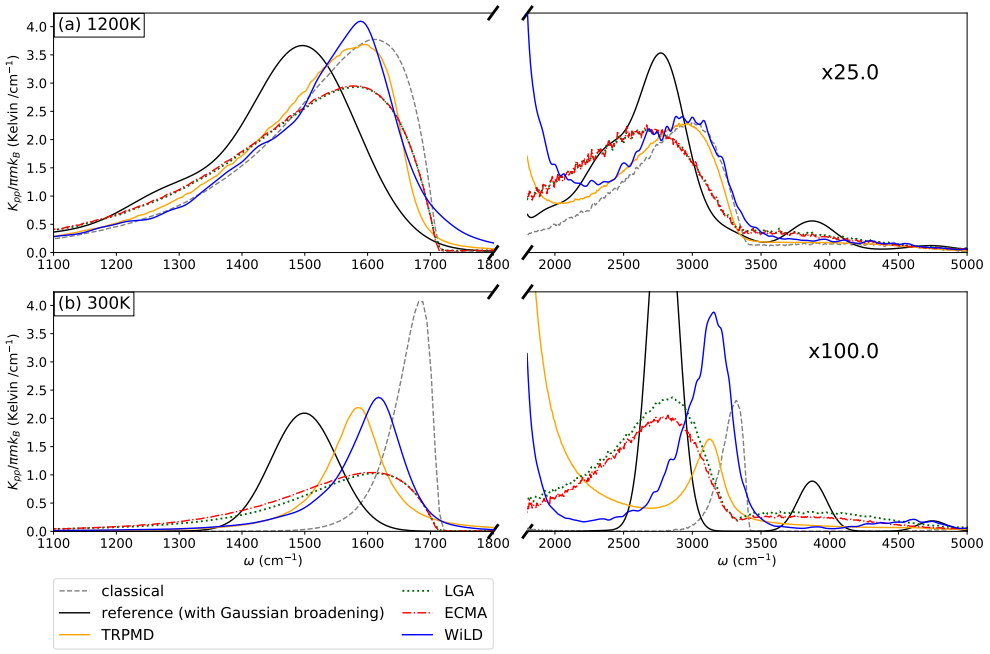

Fig. 4.6.: Kubo-transformed momentum autocorrelation spectrum for WiLD (solid blue), LSC-ECMA (dash-dotted red), LSC-LGA (dotted green), TRPMD (solid orange), exact (solid black) and classical (dashed grey) at 1200K (panel a) and 300K (panel b) for the Morse potential. The reference spectrum is broadened by convolution with a Gaussian function to match the heights of the other spectra (the spectral weight of the peaks is not modified).

At 300K, the shift between the classical and quantum spectra is larger and the classical peaks are narrower and less asymmetric (less exploration of the anharmonic regions of the Morse potential). At this lower temperature, differences between the approximate methods are more visible. For the main spectral feature, the LSC-ECMA is almost identical to the LSC-LGA and the WiLD gives a nearly symmetric peak halfway between the classical and TRPMD peaks. TRPMD and WiLD both place the first overtone between the classical (3300 cm^{-1}) and the quantum (2750 cm^{-1}) overtones. However, they strongly differ by their intensities: the intensity of the overtone for the TRPMD is closer to the classical one while for the WiLD, it is closer to the quantum one. The LSC-IVR seems to better capture both position and intensity of the overtone but with a larger broadening of the peaks. It is interesting to notice that, while the dynamics and the position distribution are the same for LSC-ECMA and LSC-LGA, the spectra differ in the overtone region. These differences mostly come from the position-momentum correlations in the initial approximations to the Wigner distribution that are treated differently in ECMA and LGA. An in-depth analysis of the effect of position-momentum correlations on overtones and resonances is provided in chapter 5. In chapter 5 we examine the case of a slightly anharmonic potential, in order to analyze the different methods analytically via perturbation theory, but our main conclusions remain qualitatively valid for the Morse potential and explain all the trends that we pointed out in the above.

4.4.2 Quartic potential

In this section we consider the case of the one-dimensional quartic potential:

$$V(q) = aq^4 \tag{4.53}$$

with $a = 800$ Å^{-4}.kcal/mol. The mass of the system was again chosen to be the proton's mass.

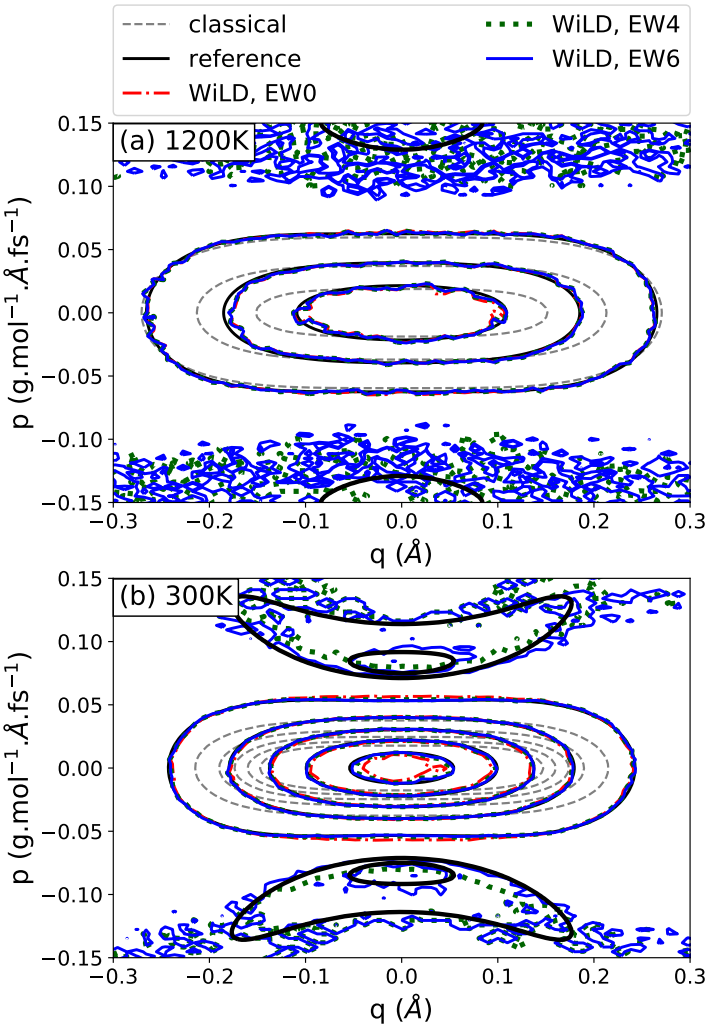

Fig. 4.7.: Contour plot of the Wigner density for the 1D quartic potential. Panel a: 1200K ($\nu = 8$). Panel b: 300K ($\nu = 32$). Contour levels are -0.25, -0.0002, 5, 15, 25, 35, 45 fs.Å^{-2}.(g/mol)$^{-1}$.

Figure 4.7 shows the results for the Wigner density at 1200K (panel (a)) and 300K (panel (b)). At 1200K, the main feature in the quantum and classical densities, the symmetrical oblong peak centered around zero, is quite similar, only the quantum distribution is slightly sharper around $q = 0$. The specific shape of the central peak of the Wigner distribution is very well reproduced by the Edgeworth approximation at order EW0 (dashed dotted red curve), EW4 (green dotted curve) and EW6 (blue curve). However, even at this relatively high temperature, the numerically exact quantum solution shows symmetrically placed features at large momentum that are

absent in the classical and EW0 approximations. These are negative parts of the Wigner density. They have a very small relative amplitude compared to the main peak (less than 10^{-4}) and are therefore difficult to capture accurately. Encouragingly, however, high order terms in the Edgeworth expansion display some signal in the correct regions.

As expected, the difference between quantum and classical results becomes more significant at 300K. The main feature in the Wigner density is significantly broadened by zero-point motion and, more strikingly, wide regions of negative $\rho_{\text{w}}(q,p)$ now appear for large values of p. The zero-order EW0 approximation already captures the central (positive) peak of the distribution accurately, with only slight discrepancies with respect to the exact result, that are corrected by the EW4 term. The high-order terms of the Edgeworth expansion also allow describing the negative parts of $\rho_{\text{w}}(q,p)$: at order EW4, negative regions appear in the approximate distribution but are slightly underestimated, an error that is corrected when the EW6 term is included. For very large momenta, the distribution becomes noisy because these regions of phase space are seldom explored. In spite of this, the inclusion of the first terms in the C_{EW} series systematically improves the estimate of negative regions of the Wigner density, even when their relative amplitude remains small compared to the positive peak: for instance, here, the (negative) minimum of $\rho_{\text{w}}(q,p)$ corresponds to approximately 1% of its maximum. Note that the EW4 and EW6 terms in the Edgeworth expansion require longer auxiliary calculations to converge than the terms in the EW0 approximation. Moreover, the full evaluation of the high-order Edgeworth terms becomes cumbersome for systems with many degrees of freedom (see section 4.5 for details), so that further work may be needed to treat complex systems that display large negative values of $\rho_{\text{w}}(q,p)$.

In spite of these numerical difficulties, higher order terms in the Edgeworth expansion can significantly impact the accuracy of calculated physical observables. In table 4.1, we report the relative error in the estimate of the mean square momentum for the quartic potential with respect to the numerically exact reference at 300K as a function of the truncation order. The EW0 approximation for the density results in a substantial overestimation of the mean square momentum, which is strongly reduced by including the fourth order term and essentially eliminated at order EW6. Note that the convergence to the exact result is systematically improved at low order (up to order EW6) before degrading slowly at higher orders and finally diverging at very high orders. This is a consequence of the asymptotic character of the Edgeworth series. The divergence of the Edgeworth series can be detected by monitoring the contribution of each EWn term on the estimated squared momentum (third column in table 4.1): we observe that this contribution first decreases, then

	Relative error on $\langle p^2 \rangle$	relative EWn contribution
EW0	16%	
EW4	4%	-11%
EW6	-2%	-6%
EW8	-7%	-5%
EW10	-12%	-6%
EW12	-20%	-10%
EW14	-33%	-17%
EW16	-61%	-41%

Tab. 4.1.: Relative error on the global mean square momentum $\langle p^2 \rangle$ (averaged over both p and q) compared to exact quantum results for the quartic potential at 300K. Higher order terms in the Edgeworth expansion are computed by solving the 1D Schrödinger equation and computing ρ_c using the wavefunction expression of the thermal density operator. The third column shows the relative contribution of the EWn order term, measured by the relative difference: $\left(\langle p^2 \rangle_{EWn} - \langle p^2 \rangle_{EWn-2}\right) / \langle p^2 \rangle_{EWn}$.

reaches a plateau with a relative value around 5%, before increasing beyond order EW12, as the Edgeworth series begins to diverge. Experience indicates that the optimal approximation of the full Wigner density is obtained at order EW6, when this plateau begins, although the general validity of this criterion should be investigated further for other systems with strongly non-Gaussian momentum distributions.

The Wigner density also displays significant position-momentum correlations, as evidenced by the q-dependence of the mean square momentum, as shown in the bottom panel of Fig. 4.8. The results for the EWn approximations are consistent with the previous observations: EW0 globally overestimates the mean square momentum and the agreement with the exact result is improved up to order EW6 which captures the correct position-dependence of the square momentum. Consistently with the discussion on the Morse potential, we see that the LGA overestimates the variations of $\langle p^2 \rangle$ with q while the FK approximation underestimates them. Most notably, the mean square momentum of the LGA at $q = 0$ is the classical value since the local frequency is null at this position (*i.e.* the harmonic approximation is not valid close to $q = 0$ for the quartic potential).

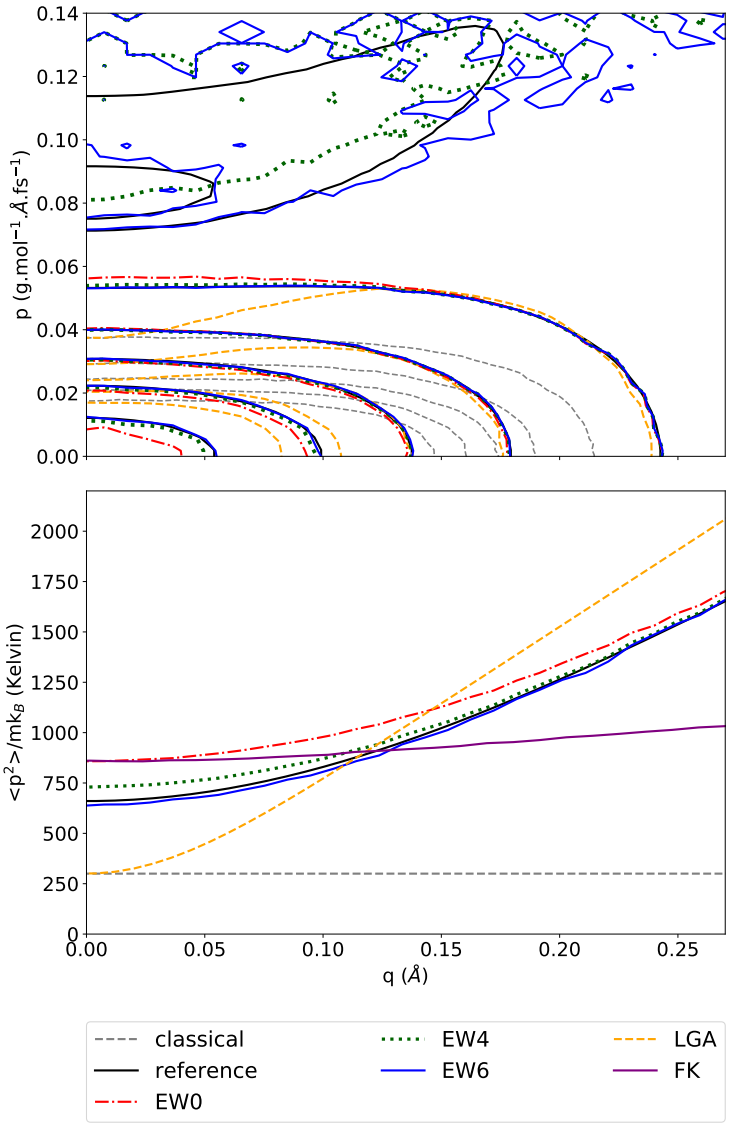

Fig. 4.8.: top panel: Wigner thermal distribution for the quartic potential at 300K approximated using EW0 (dash-dotted red), EW4 (dotted green) and EW6 (solid blue) compared to LGA (dashed orange). Contour levels are -0.25, -0.0002, 5, 15, 25, 35, 45 fs.Å^{-2}.(g/mol)$^{-1}$. Since the distribution is even with respect to position and momentum, only the positive quadrant is displayed. bottom panel: mean square momentum as a function of q. This graph corresponds to the average of p^2 over a vertical slice of the top panel, renormalized by mk_B to obtain a temperature. The EW approximations are compared to the classical Boltzmann distribution (dashed grey), to the exact result (solid black) obtained from solving the Schrödinger on a grid equation and to LGA (dashed orange) and FK (solid purple).

Momentum autocorrelation spectrum

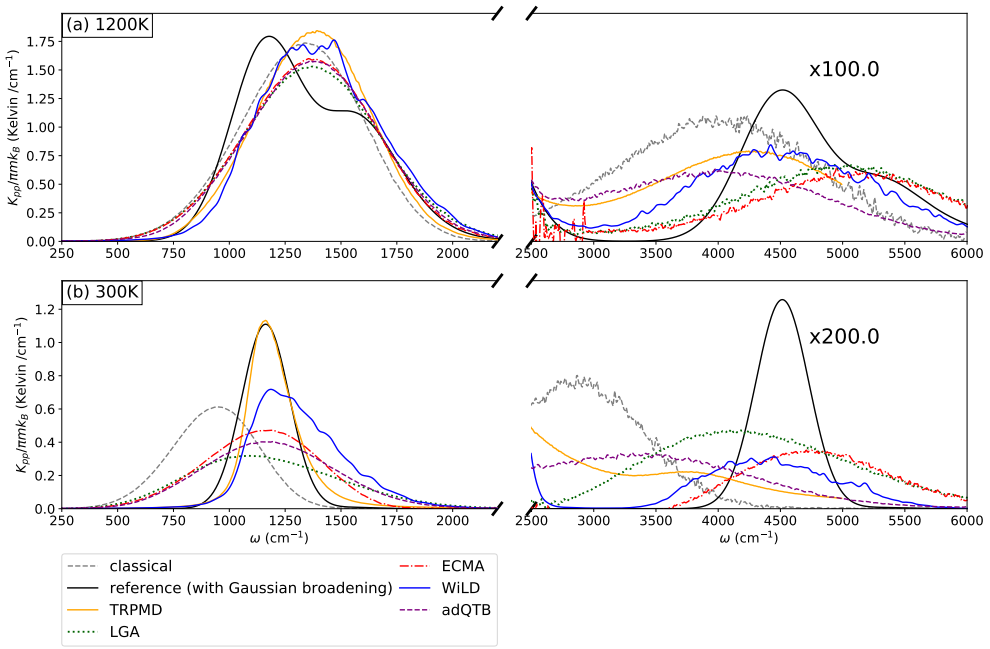

Fig. 4.9.: Kubo-transformed momentum autocorrelation spectrum for WiLD (solid blue), LSC-ECMA+EW6 (dash-dotted red), LSC-LGA (dotted green), TRPMD (solid orange), exact (solid black) and classical (dashed grey) at 1200K (panel a) and 300K (panel b) for the quartic potential. The reference spectrum is broadened by convolution with a Gaussian function to match the heights of the other spectra.

Figure 4.9 shows the momentum autocorrelation spectrum approximated using the WiLD and LSC-ECMA+EW6 compared to TRPMD, QTB and LSC-LGA. At high temperature, all the approximate methods give similar results which are close to the classical spectrum. At 300K however, the different methods yield quite different spectra. For the main spectral peak (around 1200 cm^{-1}), TRPMD best captures the position with the most limited broadening. The position of the main peak for the other methods is also close to the quantum result but within a too broad lineshape. For the high frequency resonance (at around 4500 cm^{-1}), the best agreement with the quantum result is obtained by LSC-ECMA, WiLD and LSC-LGA (although none of them captures the exact position and they all broaden the peak). The resonance intensity is approximately correct for adQTB but its position is closer to the classical result. The TRPMD approximation largely underestimates the resonance at 300K, as in the previously considered example of the Morse potential.

Note that, at 300K, the EW4 and EW6 corrections to ECMA influence the shape and position of the peaks and improve the agreement with the reference result as can

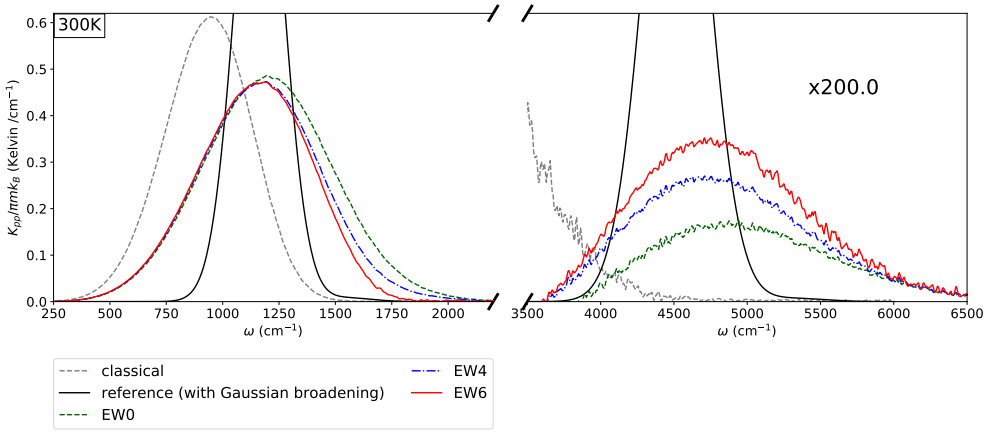

Fig. 4.10.: Kubo-transformed momentum autocorrelation spectrum for LSC-ECMA at order EW0 (dashed green), EW4 (dotted-dashed blue) and EW6 (solid red) compared to the exact (solid black) and classical (dashed grey) spectra at 300K for the quartic potential. The reference spectrum is broadened by convolution with a Gaussian function to match the heights of the other spectra.

be seen in figure 4.10. This is due to the very anharmonic nature of the quartic potential (and thus cannot be described by the perturbative approach developed in chapter 5). For the quartic potential, the approximation to the initial Wigner distribution is critical for the result of the linearized dynamics. This can be seen with the LSC-LGA spectrum which is significantly different from the LSC-ECMA spectrum and reflects the differences in the approximations of the Wigner density (as shown in the top panel of figure 4.8).

4.5 Generalization to multiple degrees of freedom

4.5.1 Multidimensional formalism

The generalization of the ECMA and WiLD formalism to N degrees of freedom is non-trivial. In the multidimensional case, κ_2 and the EW0-QCF become $N \times N$ matrices and care is required when deriving the Edgeworth expansion and the expressions for the generalized forces.

Edgeworth expansion

Introducing the notation $\mathbf{q}$, $\mathbf{p}$ and $\mathbf{\Delta}$ to indicate N-dimensional vectors and taking into account the fact that κ_2 is now a matrix, equation (4.2) becomes:

$$\rho_{\text{w}}(\mathbf{q},\mathbf{p}) = \frac{1}{(2\pi\hbar)^N \mathcal{Z}} \exp\left\{-\frac{\mathbf{p}^T\kappa_2(\mathbf{q})\mathbf{p}}{2\hbar^2} - \beta U(\mathbf{q})\right\} \tag{4.54}$$

$$\times \int \mathrm{d}\mathbf{\Delta}\ \exp\left\{\left[\frac{1}{2\hbar^2}\mathbf{p}^T\kappa_2(\mathbf{q}) + \frac{i}{\hbar}\mathbf{\Delta}\right].\,\mathbf{p}\right\}\rho_c(\mathbf{\Delta}|\mathbf{q}) \tag{4.55}$$

where $U(\mathbf{q})$ and $\rho_c(\mathbf{\Delta}|\mathbf{q})$ are defined in analogy with eqs. (4.3) and (4.4). Introducing the notation:

$$h(\mathbf{p}) = \exp\left\{\left[\frac{1}{2\hbar^2}\mathbf{p}^T\kappa_2(\mathbf{q}) + \frac{i}{\hbar}\mathbf{\Delta}\right].\,\mathbf{p}\right\} \tag{4.56}$$

and considering the expansion of the exponential in h gives:

$$\begin{aligned} h(\mathbf{p}) = 1 &+ \sum_i p_i \frac{\partial h}{\partial p_i}\bigg|_{\mathbf{p}=0} + \frac{1}{2!}\sum_{i,j} p_i p_j \frac{\partial^2 h}{\partial p_i \partial p_j}\bigg|_{\mathbf{p}=0} \\ &+ \frac{1}{3!}\sum_{i,j,k} p_i p_j p_k \frac{\partial^3 h}{\partial p_i \partial p_j \partial p_k}\bigg|_{\mathbf{p}=0} \\ &+ \frac{1}{4!}\sum_{i,j,k,l} p_i p_j p_k p_l \frac{\partial^4 h}{\partial p_i \partial p_j \partial p_k \partial p_l}\bigg|_{\mathbf{p}=0} + \cdots \end{aligned} \tag{4.57}$$

where all the sum indices run from 1 to N.

Explicit calculation of the derivatives shows that odd orders in the expansion above contain only odd powers of the components of $\mathbf{\Delta}$ and, as in the 1D case, they vanish when integrated, by parity of ρ_c. Similarly to the 1D case, we choose:

$$[\kappa_2(\mathbf{q})]_{ij} = \int \mathrm{d}\mathbf{\Delta}\ \Delta_i\Delta_j\ \rho_c(\mathbf{\Delta}|\mathbf{q}) = \langle \Delta_i\Delta_j \rangle_{\rho_c|\mathbf{q}} \tag{4.58}$$

With this choice of κ_2, the second order in the Taylor expansion cancels and we obtain:

$$\rho_{\text{EWn}}(\mathbf{q},\mathbf{p}) = \frac{1}{(2\pi\hbar)^N \mathcal{Z}}\, e^{-\frac{\mathbf{p}^T\kappa_2(q)\mathbf{p}}{2\hbar^2} - \beta U(\mathbf{q})}\left[1 + \left(\frac{i}{\hbar}\right)^4 \sum_{j,k,l,m} \frac{[\kappa_4(\mathbf{q})]_{jklm}}{4!} p_j p_k p_l p_m + \cdots\right] \tag{4.59}$$

where κ_4 is the fourth order cumulant tensor of ρ_c defined by:

$$[\kappa_4(\mathbf{q})]_{ijkl} = \langle \Delta_i \Delta_j \Delta_k \Delta_l \rangle_{\rho_c|\mathbf{q}} - \langle \Delta_i \Delta_j \rangle_{\rho_c|\mathbf{q}} \langle \Delta_k \Delta_l \rangle_{\rho_c|\mathbf{q}} - \langle \Delta_i \Delta_k \rangle_{\rho_c|\mathbf{q}} \langle \Delta_j \Delta_l \rangle_{\rho_c|\mathbf{q}} - \langle \Delta_i \Delta_l \rangle_{\rho_c|\mathbf{q}} \langle \Delta_j \Delta_k \rangle_{\rho_c|\mathbf{q}} \quad (4.60)$$

The higher orders of the Edgeworth expansion involve cumulants of increasing order which may be difficult to compute for high dimensional systems. However, as we saw in the previous section, only few terms of the Edgeworth correction are necessary for most systems and the EW0 approximation will often be sufficient. Including only the fourth order of the Edgeworth expansion already gives a good idea of negative parts of the Wigner distribution and of the validity of the EW0 approximation. Furthermore, in large multiatomic systems, all terms in the expansion will not be physically relevant so that reasonable approximations can be derived depending on the system under study (for example by setting to zero terms that couple atoms that are far apart). These difficulties notwithstanding, the control on convergence available via the expansion is an important conceptual advantage compared to alternative methods.

Multidimensional WiLD equations of motion

In analogy to the unidimensional case, the EW0 approximation to the joint Wigner distribution is given by:

$$\rho_{\text{EW0}}(\mathbf{q},\mathbf{p}) = \frac{\exp\left\{-\beta U(\mathbf{q}) - \frac{1}{2\hbar^2}\mathbf{p}^T\kappa_2(\mathbf{q})\mathbf{p}\right\}}{\int \mathrm{d}\mathbf{q}\mathrm{d}\mathbf{p}\ \exp\left\{-\beta U(\mathbf{q}) - \frac{1}{2\hbar^2}\mathbf{p}^T\kappa_2(\mathbf{q})\mathbf{p}\right\}} \quad (4.61)$$

The WiLD equations of motion are determined similarly to the one-dimensional case. They read:

$$\begin{cases} \dot{\mathbf{q}} = M^{-1}\mathbf{p} \\ \dot{\mathbf{p}} = \mathbf{F}(\mathbf{q},\mathbf{p}) - \gamma\mathbf{p} + \sigma(\mathbf{q})\mathbf{R}(t) \end{cases} \quad (4.62)$$

where M is the mass matrix of the system, $\sigma(\mathbf{q})$ is a $N \times N$ matrix and $\mathbf{R}(t)$ is a vector of N independent Gaussian white noises. The forces $F_i(\mathbf{q},\mathbf{p})$ are given for $i = 1,\ldots,N$ by:

$$F_i(\mathbf{q},\mathbf{p}) = -\sum_{j=1}^{N}[\kappa_2^{-1}(\mathbf{q})]_{ij}\left(\frac{\hbar^2\beta}{m_j}\frac{\partial U}{\partial q_j} + \sum_{k=1}^{N}[C_k(\mathbf{q})]_{kj}\right) - \frac{1}{2\hbar^2}\mathbf{p}^T C_i(\mathbf{q})\mathbf{p} \quad (4.63)$$

We use the multidimensional Fokker-Planck equation to determine the expressions for the $N \times N$ matrices $C_i(\mathbf{q})$ $(i = 1 \ldots N)$ and the fluctuation-dissipation relation

in order for the probability density (4.61) to be stationary. We obtain for all $i = 1, \ldots, N$:

$$C_i(\mathbf{q}) = \sum_{j=1}^{N} \frac{\hbar^2}{m_j} [\kappa_2^{-1}(\mathbf{q})]_{ij} \frac{\partial \kappa_2}{\partial q_j} \tag{4.64}$$

The fluctuation dissipation relation is given by:

$$\sigma^2(\mathbf{q}) = 2\gamma\hbar^2\kappa_2^{-1}(\mathbf{q}) \tag{4.65}$$

Path integral estimators of $\kappa_2(\mathbf{q})$, $\nabla U(\mathbf{q})$ and $\nabla\kappa_2(\mathbf{q})$ can be obtained similarly as in the unidimensional case. Note that $\kappa_2(\mathbf{q})$ must be inverted in order to propagate the WiLD equations of motion. This inversion is always possible since $\kappa_2(\mathbf{q})$ is positive definite by construction (because it is defined as the covariance matrix of the density $\rho_c(\mathbf{\Delta}|\mathbf{q})$).

Edgeworth Conditional Momentum Approximation

In analogy with equation (**??**), we obtain the multidimensional ECMA as:

$$\rho_{\text{ECMA}}(\mathbf{q}, \mathbf{p}) = \langle \mathbf{q}|\hat{\rho}|\mathbf{q}\rangle \, \rho_{\kappa_2}(\mathbf{p}|\mathbf{q}) \frac{1 + C_{\text{EWn}}(\mathbf{q}, \mathbf{p})}{1 + \overline{C_{\text{EWn}}}(\mathbf{q})} \tag{4.66}$$

where $\rho_{\kappa_2}(\mathbf{p}|\mathbf{q})$ is the conditional EW0 momentum distribution:

$$\rho_{\kappa_2}(\mathbf{p}|\mathbf{q}) = \frac{\exp\left\{-\frac{\beta}{2}\mathbf{p}^T M^{-\frac{1}{2}} \Phi_{\text{EW0}}^{-1}(\mathbf{q}) M^{-\frac{1}{2}} \mathbf{p}\right\}}{\int \mathrm{d}\mathbf{p} \, \exp\left\{-\frac{\beta}{2}\mathbf{p}^T M^{-\frac{1}{2}} \Phi_{\text{EW0}}^{-1}(\mathbf{q}) M^{-\frac{1}{2}} \mathbf{p}\right\}} \tag{4.67}$$

with M the diagonal mass matrix and $\Phi_{\text{EW0}}(\mathbf{q})$ the $N \times N$ EW0-QCF matrix defined as:

$$\Phi_{\text{EW0}}^{-1}(\mathbf{q}) = \frac{M^{\frac{1}{2}} \kappa_2(\mathbf{q}) M^{\frac{1}{2}}}{\hbar^2 \beta} \tag{4.68}$$

Similarly to LHA, the Quantum Correction factor transforms the independent momenta of the classical Boltzmann distribution into a generalized Gaussian distribution where all momenta are in principle correlated. Contrary to LHA however, the EW0-QCF is not tied to a normal modes analysis of the Hessian of the potential at configuration $\mathbf{q}$ and is always well defined (*i.e.* positive definite by construction), even for configurations where a harmonic analysis would give imaginary frequencies (on barriers of potential energy for example). We can push the interpretation further and consider the eigenvectors of $\Phi_{\text{EW0}}(\mathbf{q})$ which give characteristic modes of the system that, contrary to the local normal modes used in LHA, account for anharmonicity and quantum thermal motion.

4.5.2 A simple 2D Hydrogen bonding model

In order to test the multidimensional generalization of our formalism, we performed WiLD and ECMA simulations on the following two-dimensional potential[52]:

$$\begin{aligned} V(q,Q) =& D\left[e^{-2\alpha(\frac{Q}{2}+q-d)} - 2e^{-\alpha(\frac{Q}{2}+q-d)} + 1\right] \\ &+ D\xi^2\left[e^{-2\frac{\alpha}{\xi}(\frac{Q}{2}+q-d)} - 2e^{-\frac{\alpha}{\xi}(\frac{Q}{2}+q-d)}\right] \\ &+ Ae^{-BQ} - \frac{C}{Q^6} \end{aligned} \tag{4.69}$$

$V(q,Q)$ represents an asymmetric A-H-B hydrogen bond, between two different anions A and B. The coordinate Q is the A-B distance while q is the distance of the proton to the center of the A-B bond. We denote P and p the associated momenta, respectively. The parameters are chosen as in ref. [52]: $D = 60$ kcal/mol, $\alpha = 2.52$ Å^{-1}, $d = 0.95$ Å, $A = 2.32 \times 10^5$ kcal/mol, $B = 3.15$ Å^{-1}, $C = 2.31 \times 10^4$ (kcal/mol).Å^6 and the asymmetry factor $\xi = 0.707$.

Figure 4.11 shows the position (panel a) and momentum (panel b) probability distributions at 300K. These are obtained by integration of the Wigner density with respect to momentum (resp. position):

$$\mathcal{P}_{\mathrm{a}}(q,Q) = \int \mathrm{d}p\, \mathrm{d}P\, \rho_{\mathrm{w}}(q,p,Q,P) \tag{4.70}$$

$$\mathcal{P}_{\mathrm{b}}(p,P) = \int \mathrm{d}q\, \mathrm{d}Q\, \rho_{\mathrm{w}}(q,p,Q,P) \tag{4.71}$$

The figures show that, for these quantities, the zero-order EW0 approximation sampled by the WiLD very accurately reproduces the reference probability distributions. In this case, the WiLD simulation is able to capture a variety of nuclear quantum effects. First, we note that, at fixed Q the quantum distribution in Fig. 4.11.a is much wider than the classical one because of the high zero-point energy of the light degree of freedom (q,p). Moreover, the zero-point motion is responsible for a large shift of the equilibrium position: quantum effects shorten the bond length and shift the Hydrogen mean position towards the center of the bond.

In addition, in this 2D system, the p and P momenta are correlated, as it appears in Fig. 4.11.b. The classical Boltzmann momentum distribution is separable and can be written as a product of non-correlated Gaussian factors. However, in quantum mechanics, this distribution is not necessarily separable due to the non-commutation of the position and momentum operators, and momenta associated with different degrees of freedom can be correlated. This is the case for the asymmetric hydrogen bond model, as can be seen from the tilt of the 2D momentum distribution in figure

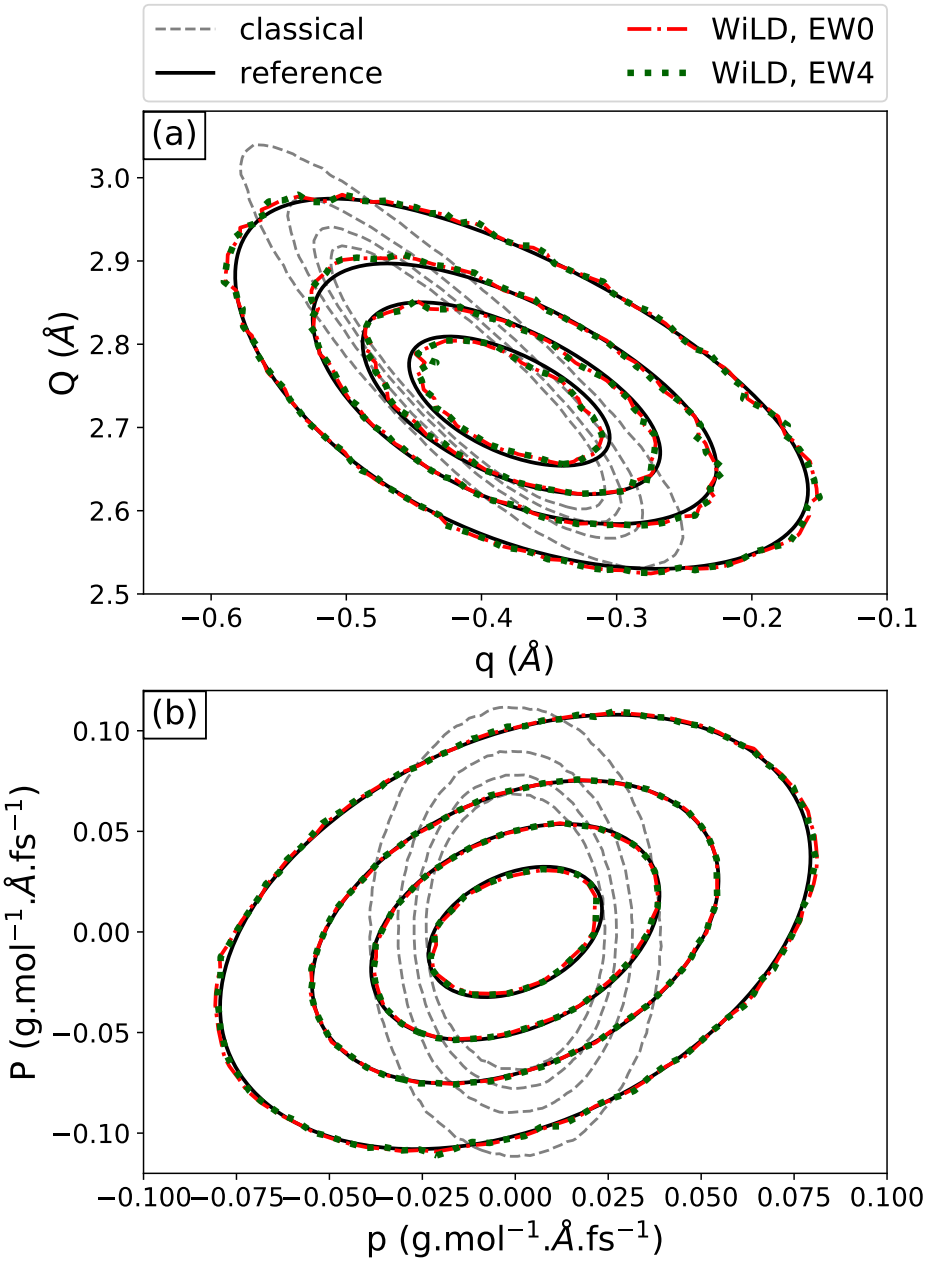

Fig. 4.11.: Contour plot of the position (eq. (4.70), panel a) and momentum (eq. (4.71), panel b) probability distributions for the asymmetric hydrogen bond model in equation (4.69), at 300K ($\nu = 64$). The reference is obtained from a direct numerical solution of the two-dimensional Schrödinger equation.

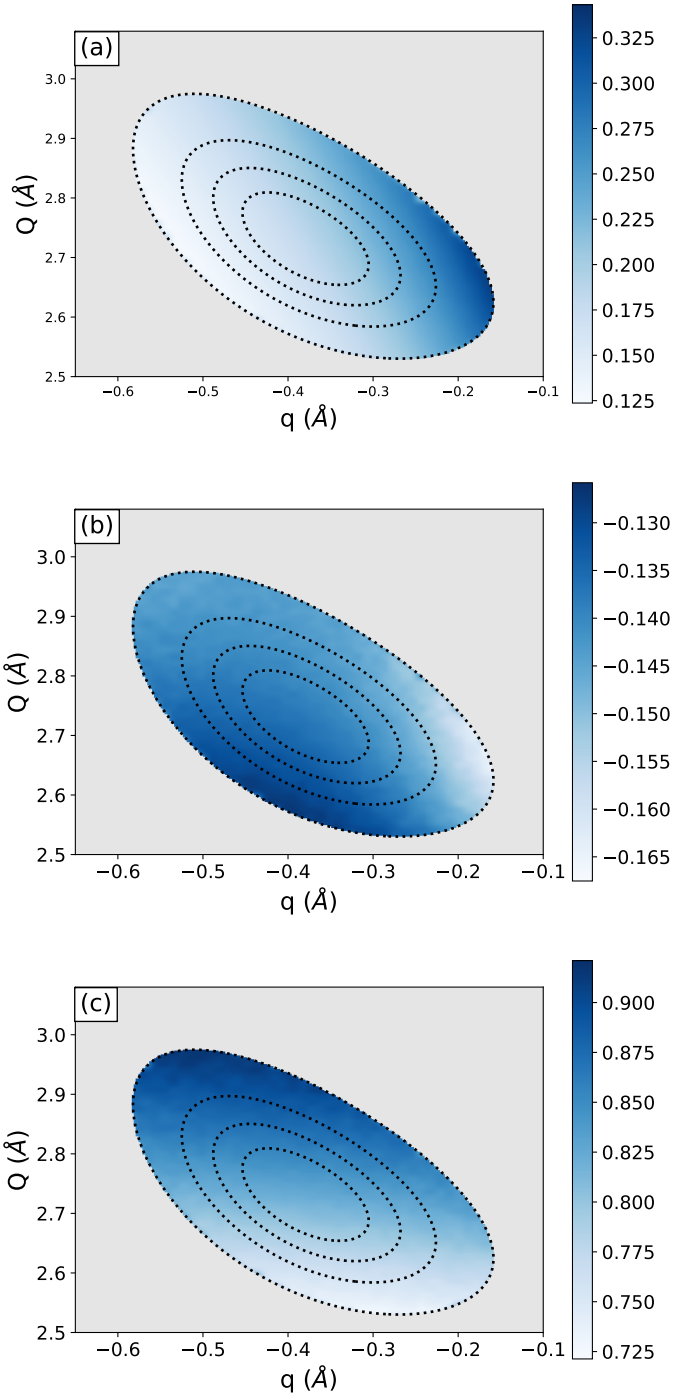

Fig. 4.12.: Color map of the matrix elements of $\Phi^{-1}_{\mathrm{EW0}}(q, Q)$ for the asymmetric hydrogen bond model at 300K. Panels (a) and (c) represent the diagonal elements corresponding respectively to the light and heavy degrees of freedom. Panel (b) shows the off-diagonal matrix element. The contour plots of the probability density are superimposed (dotted black curve). The gray area outside of the lowest probability contour is not statistically relevant and it was thus excluded.

4.11.b. The correlation in momentum space is indeed captured in the 2×2 matrix $\kappa_2(q, Q)$ and it is therefore perfectly accounted for by the WiLD simulations, even at the zero-order of the Edgeworth expansion. Fig. 4.12 shows the matrix elements of $\Phi^{-1}_{\text{EW0}}(q, Q)$ obtained from κ_2 using equation (4.68). In the classical limit, the diagonal elements are constant and equal to one while the off-diagonal element is null. In contrast, in Fig. 4.12.a, the diagonal element for the light degree of freedom goes down as low as 0.125, indicating large quantum effects. It also displays a marked dependence on position, with almost a factor of 3 between its lowest and its highest value, revealing a high degree of non-classical position-momentum correlation. As expected, the diagonal element for the heavy degree of freedom, Fig. 4.12.c, is closer to one but it still deviates from its classical value and varies with position (although more weakly). Finally, the off-diagonal element in Fig. 4.12.b is non-zero and causes the correlation in momentum space mentioned above.

4.5.3 Mexican hat potential: the curvature problem

We now consider the following two-dimensional potential:

$$V(x, y) = D\left[\left(\frac{r - r_0}{\sigma}\right)^2 - \left(\frac{r - r_0}{\sigma}\right)^3 + \frac{7}{12}\left(\frac{r - r_0}{\sigma}\right)^3\right] \tag{4.72}$$

with $r = \sqrt{x^2 + y^2}$ the distance from the origin, $D = 116$ kcal/mol, $r_0 = 0.94$ Å the equilibrium radius and $\sigma = 0.437$ Å. The potential in the radial direction is a Morse potential (truncated at fourth order to avoid dissociation) and the system is free to rotate in one direction. Figure 4.13 shows a colormap of the bidimensional potential energy surface where we can see its rotational symmetry.

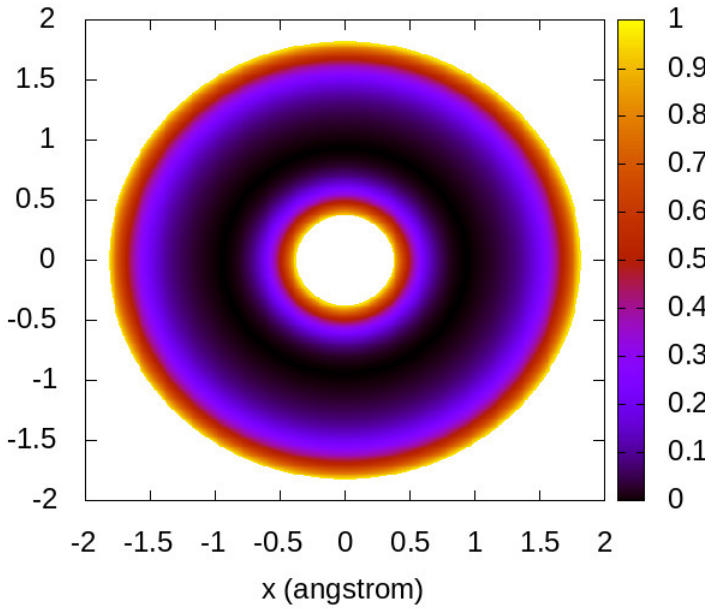

Fig. 4.13.: Color map of the potential of equation (4.72) with $D = 116$ kcal/mol, $r_0 = 0.94$ Å and $\sigma = 0.437$. The energy values are expressed in Hartree.

Potential (4.72) is built to highlight the so-called "curvature problem" that affects some approximate quantum dynamics methods such as CMD (and, as we will show, WiLD) and that is present in simulations of more realistic systems (for example water). For CMD, the curvature problem occurs at low temperature when the ring polymer distribution around the centroid is very delocalized. This delocalization in the curve of the potential causes the centroid potential to flatten at low temperature, leading to an artificially red-shifted and broadened peak [86, 87].

A similar effect can be observed for WiLD simulations. Figure 4.14 shows the momentum autocorrelation spectrum obtained with WiLD at different temperatures. The spectrum obtained by solving the Schrödinger equation (black curve in fig. 4.14) displays a peak at around 3700 cm^{-1} which position does not depend on temperature (the reference spectrum has been artificially broadened in fig. 4.14 in order to match the height of the WiLD peaks). We can see that at 600K, the peak given by WiLD is quite sharp and close to the reference. For lower temperatures, we notice a gradual red-shift and a broadening of the peak that are typical of the curvature problem. As for CMD, this effect hinders the use of the WiLD for computing spectra of systems that are subject to this type of curvature, for example the rovirational spectra of O-H bonds in water. It would be interesting to explore if this problem could be alleviated

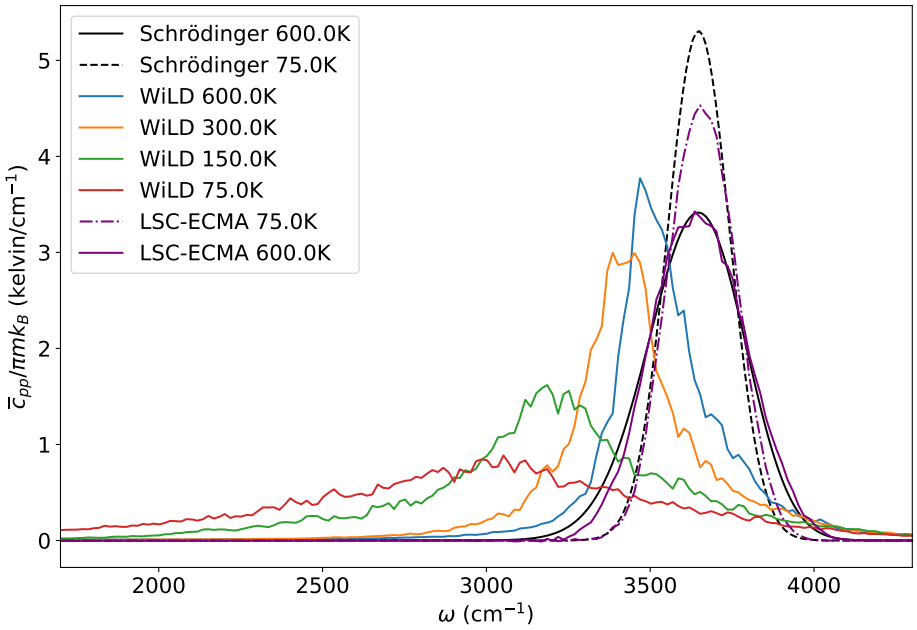

Fig. 4.14.: Momentum autocorrelation spectrum obtained from WiLD and LSC-ECMA at different temperatures for the mexican hat potential (4.72). The results are compared to the exact spectra at 75K and 600K (with a Gaussian broadening of width 16THz) obtained via the solution of the bidimensional Schrödinger equation.

by using curvilinear path integrals to compute the WiLD forces, as it has recently been done in the case of QCMD (see ref. [88]).

Note that the curvature problem only affects the *dynamics* of the WiLD so that static properties can still be computed (within the EW approximation). The curvature problem does not affect LSC-ECMA as shown in figure 4.14: the position of the peak does not depend on temperature and is very close to the reference. However, the classical dynamics induces ZPEL in that case (especially at low temperature) so that the intensity of the main peak is slightly understimated and that of the low-frequency rotational peak (not shown in the figure) is overestimated.

5 Nuclear Quantum Dynamics: a step beyond the harmonic oscillator

In the previous chapters, we have pointed out that a minimum criterion to design a novel approximate quantum dynamics method is that it must be exact for the harmonic potential since it is the lowest order approximation of any system close to an equilibrium configuration. For the harmonic potential, one can analytically show that all the methods presented in above are exact. The harmonic dynamics thus constitutes a "common minimum denominator", and allows to discard some approximations that would not describe it satisfactorily. However, it does not allow to differentiate the approximations that fulfill this criterion.

It is thus desirable to obtain similar analytical, or at least rational, arguments to compare the different methods on physically relevant anharmonic systems. Throughout the previous chapters, we used the Morse potential of eq. (3.1), which is a strongly anharmonic potential, in order to qualitatively compare several methods in a case where an exact solution is available. In particular, we pointed out that the momentum autocorrelation spectrum of the Morse potential displays an overtone that is reproduced with different levels of accuracy by the different approximations: RPMD and CMD strongly understimate the overtone at low temperature while LSC-IVR, WiLD and adQTB show only small discrepancies compared to the exact result.

In this chapter, we take the comparison of the different methods one step further and make it quantitative by considering simple model potentials, obtained by adding anharmonic perturbations to a harmonic potential, that display typical anharmonic effects such as overtones and combination bands. For these models we can derive analytical results within the different approximations using perturbation theory. This analysis is interesting for two main reasons. Firstly, it enables to put on mathematical grounds the different characteristics (and to some extent the reliability) of these approaches when interpreting computed spectral features. Secondly, it illustrates that the lack of coherence effects in the dynamics cannot always be invoked to explain missing features in approximate spectra. Indeed, all the methods considered share the characteristic of coupling a sampling of the quantum thermal distribution

92

with a (generalized) classical dynamics and yet perform very differently. This indicates that the interplay between sampling and propagation is more delicate than usually assumed and qualitative statements on this topic should be carefully considered (note that similar analysis start appearing in the literature, e.g. ref. [59]). Our results explain all the trends observed for the overtone of the Morse potential and allow to trace them back to the treatment of position-momentum correlations, rather than coherence effects to which they are often associated. Beyond the Morse potential, our perturbative analysis provides some keys to examine anharmonic resonances occurring in more complex systems such as the water molecule that we present in section 5.4 and liquid and solid water in chapter 6.

In the first section, we introduce the simplest possible model for an overtone consisting in a unidimensional harmonic potential subject to a cubic perturbation. We then present a perturbative framework within which we derive analytical expressions of the overtone intensity obtained in each of the approximate methods presented in chapters 3 and 4. In the second section, we investigate the issue of combination bands by applying the same perturbative analysis to a system of two weakly coupled harmonic oscillators. In the third section, we focus on the Fermi resonance and use the model and the perturbative results presented in ref. [109]. For all the model potentials, we compare numerically the performance of the different approximate methods in order to validate the perturbative approach. Finally, we shall extend the investigation – numerically – to the more challenging case of gas-phase water in the last section of this chapter. In order to perform these comparisons, we implementated the various methods in a common framework for trajectory-based quantum dynamics[1].

5.1 Overtones: the perturbed harmonic oscillator

The simplest model for investigating overtones is given by the following potential:

$$V(q) = \frac{1}{2} m\omega_0^2 q^2 + \frac{\lambda}{3} q^3 \tag{5.1}$$

which consists of a harmonic oscillator at frequency ω_0 and a cubic term that we will consider to be a perturbation to the harmonic potential. The parameter λ gives the amplitude of the anharmonicity and acts as a control parameter. In practice, the

[1] The Fortran package we developed is available at `https://gitlab.com/nqe-insp/QDPack`

cubic term can be treated perturbatively if we choose λ such that the ratio of the two components of the energy is small for all relevant positions:

$$\frac{|\lambda| \langle |q^3| \rangle}{m\omega_0^2 \langle q^2 \rangle} \ll 1 \tag{5.2}$$

where $\langle \cdot \rangle$ refers to the expectation value over the thermal equilibrium distribution at inverse temperature β. At first order in λ, we can replace $\langle \cdot \rangle$ by $\langle \cdot \rangle_0$ which is the expectation value over the unperturbed (harmonic) distribution:

$$\rho^m_{\mathrm{w},0}(q) \propto \exp\left\{ -\frac{m\omega_0^2 q^2}{2\Theta(\omega_0, \beta)} \right\} \tag{5.3}$$

where

$$\Theta(\omega_0, \beta) = \frac{\hbar\omega_0/2}{\tanh(\beta\hbar\omega_0/2)} \tag{5.4}$$

is the harmonic average quantum thermal energy. With this distribution, we have:

$$\left\langle q^2 \right\rangle_{0,\beta} = \frac{\Theta(\omega_0, \beta)}{m\omega_0^2} \tag{5.5}$$

$$\left\langle \left| q^3 \right| \right\rangle_{0,\beta} = \frac{1}{\sqrt{\pi}} \left(\frac{2\Theta(\omega_0, \beta)}{m\omega_0^2} \right)^{3/2} \tag{5.6}$$

Thus, to consider the anharmonic contribution as perturbative, we must have:

$$|\lambda| \ll \sqrt{\frac{m^3\omega_0^6}{\Theta(\omega_0, \beta)}} \tag{5.7}$$

Under condition (5.7), the dynamics of the system is mainly harmonic with a small overtone contribution at frequency $2\omega_0$. Moreover, under this condition, the region where the potential diverges to $-\infty$ for $q \to -\infty$ is not explored (if the dynamics is initialized at a position close to $q = 0$, the probability that it escapes from this local minimum is negligible).

We will measure the intensity of the overtone at inverse temperature β by its contribution $\eta(\beta)$ to the (generalized) vibrational density of states:

$$\eta(\beta) = \int_{2\omega_0 - \Delta\omega}^{2\omega_0 + \Delta\omega} \frac{\beta}{m} K_{pp}(\omega; \beta) \mathrm{d}\omega \tag{5.8}$$

with $K_{pp}(\omega; \beta)$ the (Kubo-transformed) momentum autocorrelation function at inverse temperature β and $\Delta\omega$ a frequency interval chosen in a way to encompass

the whole overtone region. Note that, according to the fluctuation-dissipation theorem of equation (3.47) (and using eq. (2.38)), we have the relation:

$$\frac{\beta}{m} K_{pp}(\omega) = 2\,\mathrm{Re}[\chi_{px}(\omega)] \tag{5.9}$$

with $\chi_{px}(\omega)$ the linear susceptibility defined in chapter 3.3. For a harmonic system, $2\,\mathrm{Re}[\chi_{px}(\omega)]$ is the vibrational density of states (VDOS) and, in this chapter, we will use this denomination even for anharmonic systems. Using the definitions provided here, the classical and quantum VDOS coincide in the harmonic case ($\lambda = 0$) for all temperatures. However, we will show in the following that, in the anharmonic case ($\lambda \neq 0$), the quantum and classical temperature-dependence of η are very different: the overtone contribution to the VDOS goes to zero at low temperature in the classical case while it saturates at a non-zero value in the quantum case.

In the following sections we will derive analytical expressions for η (by treating the cubic potential as a small perturbation), within the different approximate quantum dynamics frameworks presented in the previous chapters and compare them to the classical and the exact quantum reference. We also check the analytical expressions against numerical simulations. We use $\omega_0 = 1500\mathrm{cm}^{-1}$, $\lambda = 21\ \mathrm{kcal\,mol}^{-1}\,\mathrm{\AA}^{-3}$ and m as the proton mass for all numerical applications. We performed simulations of the different methods for temperatures between 0K and 3000K. The momentum autocorrelation spectrum is extracted from the simulated trajectories and the overtone contribution to the VDOS is obtained by integrating the spectrum on an interval $\Delta\omega$ appropriately chosen around $2\omega_0$.

5.1.1 Classical correlation function

We recall the definition of the classical momentum-momentum time correlation function:

$$K_{pp}(t) = \int \mathrm{d}q\mathrm{d}p\ \rho_{\mathrm{cl}}(q,p)\ p\ e^{i\mathcal{L}_{\mathrm{cl}}t} p \tag{5.10}$$

where $\rho_{\mathrm{cl}}(q,p)$ is the classical Boltzmann density defined in equation (2.1) and $i\mathcal{L}_{\mathrm{cl}}$ is the classical Liouville operator defined in equation (2.4). Note that we switched the notation of the classical TCF from c_{pp} to K_{pp} in order to emphasize the analogy with the Kubo-transformed quantum TCF.

The methodology that we use to compute η in the classical case goes as follows: (1) we expand the density ρ_{cl} in powers of the anharmonicity parameter λ. (2) We write the Dyson expansion of the time propagator $e^{i\mathcal{L}_{\mathrm{cl}}t}$ at second order in λ (the order at which the overtone contribution appears, as we will see in the following) and

compute the propagated momentum $e^{i\mathcal{L}_{\text{cl}}t}p$. (3) we combine the two previous results by averaging the second-order expansion of $pe^{i\mathcal{L}_{\text{cl}}t}p$ on the distribution ρ_{cl}. This will give $K_{pp}(t)$ at second order in λ. (4) Finally, we compute the Fourier transform of $K_{pp}(t)$ to obtain the overtone contribution to the VDOS η using eq. (5.8).
Note that for simplicity, we will only show here the key elements of the derivation and will not detail all the calculations which are quite technical but only involve elementary operations. Most of the developments for the approximate quantum methods use essentially the same methodology. Therefore, the derivation is presented in more details for the classical case, which we refer to in the following sections.

Let us begin by splitting the Hamiltonian into a harmonic part and a perturbation $H(q,p) = H_0(q,p) + \frac{\lambda}{3}q^3$. The perturbed Boltzmann density, expanded to second order in λ, is then given by:

$$\rho_{\text{cl}}(q,p) = \frac{e^{-\beta H(q,p)}}{\mathcal{Z}} = \rho_{\text{cl},0}(q,p)\left[1 - \frac{\lambda\beta q^3}{3} + \frac{\lambda^2\beta^2}{18}\left(q^6 - \left\langle q^6\right\rangle_0\right)\right] + \mathcal{O}\left(\lambda^3\right) \quad (5.11)$$

where $\rho_{\text{cl},0}(q,p)$ is the unperturbed harmonic Boltzmann density and $\langle\cdot\rangle_0$ denotes the expectation value over $\rho_{\text{cl},0}$. The term in $\langle q^6\rangle_0$ comes from the expansion of the partition function (a first-order term in $\langle q^3\rangle_0$ should also appears but it is equal to zero by parity).

The classical Liouville operator of the system can be written as:

$$i\mathcal{L}_{\text{cl}} = i\mathcal{L}_0 - \lambda q^2\frac{\partial}{\partial p} \quad (5.12)$$

where $i\mathcal{L}_0$ is the harmonic Liouville operator. We use the Dyson expansion of the classical time propagator to rewrite the perturbed propagator $e^{i\mathcal{L}_{\text{cl}}t}$ as a series of harmonic propagations (that are represented by the operator $e^{i\mathcal{L}_0 t}$ and can be computed analytically) with intermediate applications of the perturbation Liouvillan $-\lambda q^2\frac{\partial}{\partial p}$ at different times. The Dyson series of the classical time propagator truncated at second order is given by:

$$\begin{aligned} e^{i\mathcal{L}_{\text{cl}}t} = e^{i\mathcal{L}_0 t} &- \lambda\int_0^t \mathrm{d}s\; e^{i\mathcal{L}_0(t-s)}q^2\frac{\partial}{\partial p}\; e^{i\mathcal{L}_0 s} \\ &+ \lambda^2\int_0^t \mathrm{d}s_1\int_0^{s_1}\mathrm{d}s_2\; e^{i\mathcal{L}_0(t-s_1)}\; q^2\frac{\partial}{\partial p}\; e^{i\mathcal{L}_0(s_1-s_2)}\; q^2\frac{\partial}{\partial p}\; e^{i\mathcal{L}_0 s_2} + \mathcal{O}\left(\lambda^3\right) \end{aligned} \quad (5.13)$$

The zeroth order of the expansion corresponds to a purely harmonic propagation. The first order corresponds to a single application of the perturbation at a time s between 0 and t with harmonic propagations from time 0 to s and s to t. The second

order corresponds to two applications of the perturbation at different times and so on for the higher orders. The effect of the harmonic time propagator $e^{i\mathcal{L}_0 s}$ on q and p is:

$$e^{i\mathcal{L}_0 s} q = q\cos(\omega_0 s) + \frac{p}{m\omega_0}\sin(\omega_0 s) \tag{5.14}$$

$$e^{i\mathcal{L}_0 s} p = p\cos(\omega_0 s) - m\omega_0 q\sin(\omega_0 s) \tag{5.15}$$

Using (5.11) and (5.13), we can compute the TCF of the perturbed system using only properties of the harmonic density and time propagator. In the following, we will denote $K_{pp}^{(ij)}(t)$ the contribution at order i of the density expansion and order j of the Dyson series. At second order in λ, we thus have:

$$K_{pp}(t) = \sum_{i,j}^{i+j\leq 2} K_{pp}^{(ij)}(t) + \mathcal{O}\left(\lambda^3\right) \tag{5.16}$$

Note that since the unperturbed Liouvillian (*i.e.* the harmonic dynamics) does not produce overtones, none of the $K_{pp}^{(i0)}$ contribute to the intensity of the overtone (and thus do not appear in the calculation of η). In particular, since $K_{pp}^{(20)}$ does not contribute, one does not need the second order of the expansion of the distribution to compute $\eta(\beta)$. In this section, we nonetheless compute all of the $K_{pp}^{(ij)}$ in order to show the expression of the full TCF at second order in λ, for completeness sake.

The unperturbed contribution is given by the standard result for the classical harmonic oscillator:

$$K_{pp}^{(00)}(t) = \frac{m}{\beta}\cos(\omega_0 t) \tag{5.17}$$

Using the parity and separability of the harmonic Boltzmann density, one can easily show that:

$$K_{pp}^{(01)} = K_{pp}^{(10)} = K_{pp}^{(20)} = 0 \tag{5.18}$$

The first anharmonic contribution to the correlation function is thus of second order in λ and comes from the two contributions $K_{pp}^{(11)}$ and $K_{pp}^{(02)}$. Using first orders of both (5.11) and (5.13), we obtain:

$$K_{pp}^{(11)}(t) = \frac{\lambda^2\beta}{3}\int \mathrm{d}q\mathrm{d}p\ \rho_{\mathrm{cl},0}(q,p)\ q^3 p\ \int_0^t \mathrm{d}s\ e^{i\mathcal{L}_0(t-s)} q^2 \frac{\partial}{\partial p}\ e^{i\mathcal{L}_0 s} p \tag{5.19}$$

After applying the time propagators and using symmetries of the density again, this term is given by:

$$K_{pp}^{(11)}(t) = \frac{2\lambda^2\beta}{3m\omega_0}\left\langle q^4\right\rangle_0\left\langle p^2\right\rangle_0\int_0^t \mathrm{d}s\ \cos(\omega_0 s)\cos(\omega_0(t-s))\sin(\omega_0(t-s))$$
$$= \frac{2\lambda^2}{3m^2\omega_0^6\beta^2}[\cos(\omega_0 t) - \cos(2\omega_0 t)] \tag{5.20}$$

Finally, the second order of the Dyson series gives:

$$K_{pp}^{(02)}(t) = \lambda^2\int \mathrm{d}q\mathrm{d}p\,\rho_{\mathrm{cl},0}(q,p)\,p\int_0^t \mathrm{d}s_1\int_0^{s_1}\mathrm{d}s_2\,e^{i\mathcal{L}_0(t-s_1)}\,q^2\frac{\partial}{\partial p}\,e^{i\mathcal{L}_0(s_1-s_2)}\,q^2\frac{\partial}{\partial p}\,e^{i\mathcal{L}_0 s_2}p \tag{5.21}$$

After applying all the propagators, averaging over the harmonic density, computing the time integrals and simplifying the expression, we obtain:

$$K_{pp}^{(02)}(t) = \frac{10\lambda^2}{9m^2\omega_0^6\beta^2}[\cos(2\omega_0 t) - \cos(\omega_0 t) + \frac{3}{2}\omega_0 t\sin(\omega_0 t)] \tag{5.22}$$

The full expression of $K_{pp}(t)$ at second order in λ is then:

$$K_{pp}(t) = \frac{m}{\beta}\cos(\omega_0 t) + \frac{\lambda^2}{m^2\omega_0^6\beta^2}\left(\frac{4}{9}[\cos(2\omega_0 t) - \cos(\omega_0 t)] + \frac{5}{3}\omega_0 t\sin(\omega_0 t)\right) + \mathcal{O}\left(\lambda^3\right) \tag{5.23}$$

Finally, we use equation (5.8) to obtain the overtone contribution to the classical VDOS, at second order in λ, as:

$$\eta_{\mathrm{cl}}(\beta) = \frac{4\lambda^2}{9m^3\omega_0^6}\beta^{-1} + \mathcal{O}\left(\lambda^3\right) \tag{5.24}$$

We can already note that this quantity tends to zero linearly with T at low temperature: the system freezes close to the potential minimum where the anharmonicity is negligible and the (classical) overtone disappears.[2]

[2]Equation (5.22) contains a term proportional to $\omega_0 t\sin(\omega_0 t)$ which diverges when $t\to\infty$. This term, called a secular term, is a well known artefact of this type of Dyson series (see refs. [110, 111]) and can be removed using multiple-scale perturbation [112, 113], resummation techniques [114, 115] or by using an appropriate change of variables (for example action-angle variables as in ref. [116]). As this term does not affect the overtone intensity (as confirmed by numerical tests), we simply chose to discard it and to discard similar terms appearing in the perturbative calculation for the approximate quantum methods.

5.1.2 Quantum case: exact and linearized dynamics

We now move on to the quantum case. In appendix C.1 we show, using perturbation theory on the eigenstates of the harmonic oscillator, that the contribution of the overtone to the quantum VDOS is given by:

$$\eta_{\mathrm{Q}}(\beta) = \frac{4\lambda^2}{9m^3\omega_0^6}\Theta(\omega_0, \beta) + \mathcal{O}\left(\lambda^3\right) \tag{5.25}$$

As expected, in the high temperature limit, the classical and quantum results coincide. However, at low temperature, $\Theta(\omega_0, \beta) \to \hbar\omega_0/2$ and thus, as shown in figure 5.1, η_{Q} tends to a constant while its classical counterpart tends linearly to 0. Quantum perturbation theory shows that, at low temperature, the overtone is produced by the transition from the fundamental energy level to the second excited state. Since the fundamental energy level is always populated, this transition is possible even at temperatures close to zero and thus the intensity of the overtone tends to a constant.

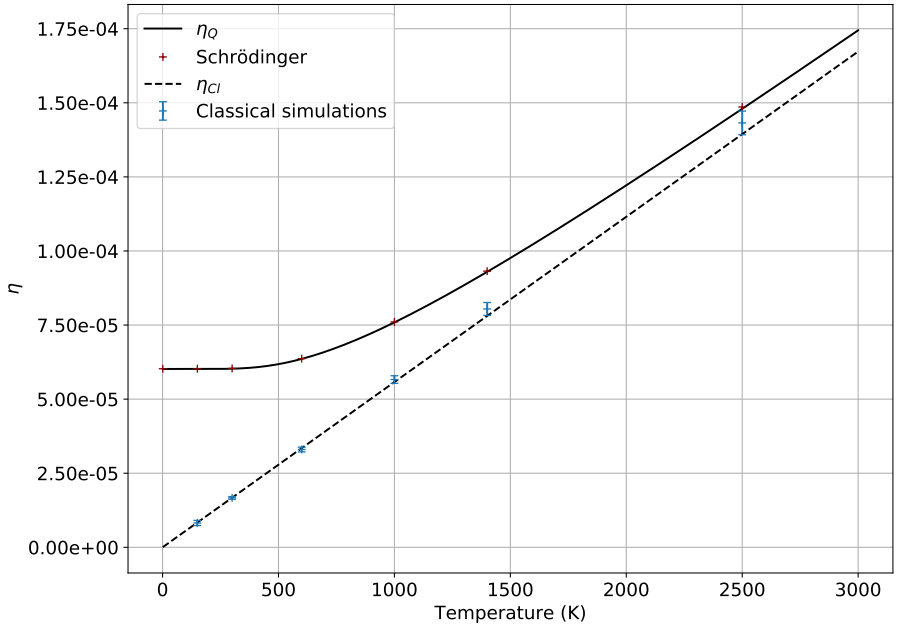

Fig. 5.1.: Intensity of the overtone quantified by η_{cl} (eq. (5.24)) in the classical case (dashed line) and η_{Q} (eq. (5.25)) in the quantum case (solide line) for the potential (5.1) with $\omega_0 = 1500\mathrm{cm}^{-1}$ and $\lambda = 21\ \mathrm{kcal\,mol}^{-1}\,\mathrm{Å}^{-3}$. The perturbative expressions are compared to numerical results obtained from classical MD (blue points) and from the resolution of the Schrödinger equation on a grid (red points).

In order to set the stage for the different LSC-IVR approximations, we propose here another derivation of equation (5.25) in the IVR framework. We recall the expression of the real part of the standard momentum-momentum TCF (see section 2.2.2):

$$\bar{c}_{pp}(t) = \int \mathrm{d}q\mathrm{d}p\ \rho_{\mathrm{w}}(q,p)\ p\ e^{i\mathcal{L}_Q t}p \tag{5.26}$$

with ρ_{w} the Wigner distribution defined in equation (2.16) and $i\mathcal{L}_Q$ the quantum Liouvillian defined in equation (2.30). The perturbative calculation of $\bar{c}_{pp}(t)$ requires to expand the Wigner distribution (or its approximation as we will see later) in powers of λ and to compute the Dyson expansion of $e^{i\mathcal{L}_Q t}p$. As discussed in the previous section, since the harmonic dynamics does not produce overtones, only the first order of the expansion of the distribution is needed to compute η. The Wigner density expanded to first order in λ is given by (see the derivation in appendix C.2):

$$\rho_{\mathrm{w}}(q,p) = \rho_{\mathrm{w},0}(q,p)\Bigg[1 - \frac{\lambda q}{m\omega_0^2}\left(\frac{\Theta(2\omega_0,\beta)}{\Theta(\omega_0,\beta)} - 1\right) - \frac{2\lambda q^3}{9\Theta(\omega_0,\beta)}\left(\frac{5}{2} - \frac{\Theta(2\omega_0,\beta)}{\Theta(\omega_0,\beta)}\right) + \frac{\lambda q p^2}{3m^2\omega_0^2\Theta(\omega_0,\beta)}\left(\frac{\Theta(2\omega_0,\beta)}{\Theta(\omega_0,\beta)} - 1\right)\Bigg] + \mathcal{O}\left(\lambda^2\right) \tag{5.27}$$

where the unperturbed (harmonic) Wigner distribution is given by:

$$\rho_{\mathrm{w},0}(q,p) = \frac{e^{-\frac{1}{\Theta(\omega_0,\beta)}\left(\frac{p^2}{2m} + \frac{1}{2}m\omega_0^2 q^2\right)}}{\int \mathrm{d}q\mathrm{d}p\ e^{-\frac{1}{\Theta(\omega_0,\beta)}\left(\frac{p^2}{2m} + \frac{1}{2}m\omega_0^2 q^2\right)}} \tag{5.28}$$

which is simply the classical harmonic Boltzmann distribution with β^{-1} replaced by the harmonic average thermal energy $\Theta(\omega_0,\beta) = \frac{\hbar\omega_0/2}{\tanh(\beta\hbar\omega_0/2)}$. It is easy to show (by replacing every Θ by their classical limit β^{-1}) that the classical limit of the distribution (5.27) yields the first-order expansion of equation (5.11). As for the classical Boltzmann distribution, the harmonic Wigner distribution does not display position-momentum correlations. However, position-momentum correlations appear in the perturbed distribution through the term proportional to qp^2 in equation (5.27).

We now show that the LSC-IVR approximation, *i.e.* replacing the quantum Liouvillian by the classical one in equation (5.26), is exact for the potential (5.1) at least up

to second order in the anharmonicity parameter λ. Due to the simple form of the potential, the quantum Liouvillian of eq. 2.30 can be written explicitly as:

$$i\mathcal{L}_{\text{Q}} = i\mathcal{L}_{\text{cl}} + \frac{\lambda\hbar^2}{12}\frac{\partial^3}{\partial p^3} \tag{5.29}$$

where $i\mathcal{L}_{\text{cl}}$ is the classical Liouville operator (5.12). A Dyson expansion of the quantum Liouville time propagator gives the following propagation of p:

$$\begin{aligned} e^{i\mathcal{L}_{\text{Q}}t}p =& e^{i\mathcal{L}_{\text{cl}}t}p + \frac{\lambda\hbar^2}{12}\int_0^t \mathrm{d}s e^{i\mathcal{L}_0(t-s)}\frac{\partial^3}{\partial p^3}e^{i\mathcal{L}_0 s}p \\ &+ \frac{\lambda^2\hbar^4}{144}\int_0^t \mathrm{d}s_1\int_0^{s_1}\mathrm{d}s_2 e^{i\mathcal{L}_0(t-s_1)}\frac{\partial^3}{\partial p^3}e^{i\mathcal{L}_0(s_1-s_2)}\frac{\partial^3}{\partial p^3}e^{i\mathcal{L}_0 s_2}p \\ &- \frac{\lambda^2\hbar^2}{12}\int_0^t \mathrm{d}s_1\int_0^{s_1}\mathrm{d}s_2 e^{i\mathcal{L}_0(t-s_1)}q^2\frac{\partial}{\partial p}e^{i\mathcal{L}_0(s_1-s_2)}\frac{\partial^3}{\partial p^3}e^{i\mathcal{L}_0 s_2}p \\ &- \frac{\lambda^2\hbar^2}{12}\int_0^t \mathrm{d}s_1\int_0^{s_1}\mathrm{d}s_2 e^{i\mathcal{L}_0(t-s_1)}\frac{\partial^3}{\partial p^3}e^{i\mathcal{L}_0(s_1-s_2)}q^2\frac{\partial}{\partial p}e^{i\mathcal{L}_0 s_2}p \\ &+ \mathcal{O}\left(\lambda^3\right) \end{aligned} \tag{5.30}$$

Since $\frac{\partial^3}{\partial p^3}e^{i\mathcal{L}_0 s}p = \frac{\partial^3}{\partial p^3}\left(p\cos(\omega_0 s) - m\omega_0 q\sin(\omega_0 s)\right) = 0$, the first three perturbation terms are null. Moreover, since $\frac{\partial^3}{\partial p^3}e^{i\mathcal{L}_0 s}q^2 = \frac{\partial^3}{\partial p^3}\left(q\cos(\omega_0 s) - \frac{p}{m\omega_0}\sin(\omega_0 s)\right)^2 = 0$, the last perturbation also cancels and thus:

$$e^{i\mathcal{L}_{\text{Q}}t}p = e^{i\mathcal{L}_{\text{cl}}t}p + \mathcal{O}\left(\lambda^3\right) \tag{5.31}$$

A classical propagation of p then gives the same result as a quantum propagation at least up to second order in λ. Thus, the LSC-IVR approximation to $\bar{c}_{pp}$ is exact up to this order. In this situation, all the quantum effects involved in the computation of $\bar{c}_{pp}$ for this potential are thus contained in the initial Wigner distribution $\rho_{\text{w}}(q,p)$ and quantum dynamical effects, such as real-time quantum coherence, play no role in the intensity of the overtone. Note that this result applies to any linear combination of p and q but does not apply to nonlinear observables. This suggests that, in general, LSC-IVR might be more reliable for linear observables than nonlinear one.

Using the exact Wigner distribution expanded to first order in λ (5.27) and the Dyson series of the classical time propagator (5.13), one can follow the same steps as for the classical case to compute the different orders of $\bar{c}_{pp}(t)$. One can then use relation (2.38) to obtain the contribution of the overtone to the VDOS at second order in λ which is, as expected, given by equation (5.25). Note, however, the following subtlety: even if the effect of the classical propagation on p is the same as the quantum propagation (at second order in λ, see eq. 5.31), it does not mean that the Wigner distribution is conserved by the classical dynamics (one can

indeed show that $i\mathcal{L}_{cl}\rho_{\text{w}}(q,p)$ is not null at first order in λ). It is therefore very interesting to remark that the correct $\bar{c}_{pp}$ spectrum can be obtained even if the initial distribution is not conserved by the dynamics. It should be investigated further how this particular result can be generalized to more complex systems but the accuracy of the TCFs obtained with LSC-IVR (with well distributed initial conditions) is somewhat strengthened by this observation, at least for linear observables.

In the following, we will compare the approximation to $\eta(\beta)$ obtained with ECMA, the global harmonic approximation, LHA and FK-LPI and show that an accurate description of the initial Wigner distribution is of the utmost importance to properly reproduce the overtone intensity.

Edgeworth Conditional Momentum Approximation

The ECMA uses the exact marginal position distribution $\rho_{\text{w}}^{m}(q)$ and approximates the conditional momentum distribution $\rho_{\text{w}}^{c}(p|q)$ with a Gaussian distribution characterized by the EW0-QCF of equation (4.50). The exact marginal position distribution and conditional momentum distribution obtained from equation (5.27) are given by:

$$\rho_{\text{w}}^{m}(q) = \frac{e^{-\frac{m\omega_0^2 q^2}{2\Theta(\omega_0,\beta)}}}{\sqrt{2\pi\Theta(\omega_0,\beta)/m\omega_0^2}}\Big[1 - \frac{2\lambda q}{3m\omega_0^2}\left(\frac{\Theta(2\omega_0,\beta)}{\Theta(\omega_0,\beta)} - 1\right) - \frac{2\lambda q^3}{9\Theta(\omega_0,\beta)}\left(\frac{5}{2} - \frac{\Theta(2\omega_0,\beta)}{\Theta(\omega_0,\beta)}\right)\Big] + \mathcal{O}\left(\lambda^2\right) \tag{5.32}$$

$$\rho_{\text{w}}^{c}(p|q) = \frac{e^{-\frac{p^2}{2m\Theta(\omega_0,\beta)}}}{\sqrt{2\pi m\Theta(\omega_0,\beta)}}\left[1 + \frac{\lambda q}{3m\omega_0^2}\left(\frac{\Theta(2\omega_0,\beta)}{\Theta(\omega_0,\beta)} - 1\right)\left(\frac{p^2}{m\Theta(\omega_0,\beta)} - 1\right)\right] + \mathcal{O}\left(\lambda^2\right) \tag{5.33}$$

One can show (see appendix C.2) that the EW0-QCF is given, at first order in λ, by:

$$\Phi_{\text{EW0}}(q) = \beta\Theta(\omega_0,\beta)\left[1 + \frac{2\lambda q}{3m\omega_0^2}\left(\frac{\Theta(2\omega_0,\beta)}{\Theta(\omega_0,\beta)} - 1\right)\right] + \mathcal{O}\left(\lambda^2\right) \tag{5.34}$$

The EW0 conditional momentum distribution is then:

$$\begin{aligned}\rho_{\kappa_2}(p|q) &= \frac{e^{-\frac{\beta p^2}{2m\Phi_{\text{EW0}}(q)}}}{\sqrt{2\pi\Phi_{\text{EW0}}(q)m/\beta}} \\ &= \frac{e^{-\frac{p^2}{2m\Theta(\omega_0,\beta)}}}{\sqrt{2\pi m\Theta(\omega_0,\beta)}}\left[1+\frac{\lambda q}{3m\omega_0^2}\left(\frac{\Theta(2\omega_0,\beta)}{\Theta(\omega_0,\beta)}-1\right)\left(\frac{p^2}{m\Theta(\omega_0,\beta)}-1\right)\right]+\mathcal{O}\left(\lambda^2\right)\end{aligned} \tag{5.35}$$

which is equal to the exact conditional momentum distribution (5.33) at first order in λ. Since ECMA uses the exact marginal position distribution, the ECMA approximation to the Wigner distribution is exact at first order in λ. Furthermore, since classical dynamics gives the exact result at second order in perturbation, LSC-ECMA gives the correct overtone intensity and thus

$$\eta_{\text{ECMA}}(\beta) = \eta_{\text{Q}}(\beta) + \mathcal{O}\left(\lambda^3\right) \tag{5.36}$$

Global Harmonic Approximation

In order to emphasize the importance of the correct position-dependence in the conditional momentum distribution, we consider a global harmonic approximation to the Wigner distribution that we will denote IVR0. We define the IVR0 approximation as the exact marginal position distribution (5.32) times the harmonic momentum distribution of equation (5.28). The IVR0 distribution thus does not feature position-momentum correlations. We compute $\eta_{\text{IVR0}}(\beta)$ using the same reasoning as in the previous subsection, substituting the ECMA with the IVR0 distribution, and obtain:

$$\eta_{\text{IVR0}}(\beta) = \frac{4\lambda^2}{9m^3\omega_0^6}\frac{\Theta^2(\omega_0,\beta)}{\Theta(2\omega_0,\beta)} + \mathcal{O}\left(\lambda^3\right) = \eta_{\text{Q}}(\beta)\frac{\Theta(\omega_0,\beta)}{\Theta(2\omega_0,\beta)} + \mathcal{O}\left(\lambda^3\right) \tag{5.37}$$

which is the exact value of η multiplied by the factor $\Theta(\omega_0,\beta)/\Theta(2\omega_0,\beta)$. This factor equals 1 in the classical limit ($\beta \to 0$) and $1/2$ in the zero-temperature limit ($\beta \to \infty$). It is interesting to see that neglecting position-momentum correlations results in an underestimation of the overtone intensity by a half. Note that the same result can be obtained with a classical MD simulation thermostatted at temperature $\Theta(\omega_0,\beta)/k_B$ instead of the physical temperature. As we will see later, this is strongly related to the QTB approximation to $\eta(\beta)$.

Local Harmonic Approximation

The LHA uses the exact marginal position distribution (5.32) and approximates the conditional momentum distribution using the local frequency (obtained from the curvature of the potential, see equation (3.7)). The local frequency for the potential (5.1) is given by:

$$\Omega^2(q) = \omega_0^2 + \frac{2\lambda}{m}q \tag{5.38}$$

If condition (5.7) is enforced so that the cubic potential is a small perturbation, $\Omega^2(q)$ should be positive for all relevant positions and thus the LHA approximation is stable (see section 3.1).

The LHA-QCF is then given, at second order in λ, by:

$$\Phi_{\text{LHA}}(q) = \beta\Theta(\omega_0,\beta)\left(1 + \frac{\lambda q}{m\omega_0^2}(1 + \beta\Theta(2\omega_0,\beta) - 2\beta\Theta(\omega_0,\beta))\right) + \mathcal{O}\left(\lambda^2\right) \tag{5.39}$$

and the LHA conditional momentum distribution is:

$$\rho_{\text{LHA}}(p|q) = \frac{e^{-\frac{p^2}{2m\Theta(\omega_0,\beta)}}}{\sqrt{2\pi m\Theta(\omega_0,\beta)}}\left[1 + \frac{\lambda q}{2m\omega_0^2}(1 + \beta\Theta(2\omega_0,\beta) - 2\beta\Theta(\omega_0,\beta))\left(\frac{p^2}{m\Theta(\omega_0,\beta)} - 1\right)\right] + \mathcal{O}\left(\lambda^2\right) \tag{5.40}$$

We compute $\eta_{\text{LHA}}(\beta)$ using the same reasoning as above with the LHA distribution and obtain:

$$\eta_{\text{LHA}}(\beta) = \eta_{\text{Q}}(\beta)\frac{\Theta(\omega_0,\beta)}{\Theta(2\omega_0,\beta)}\left[\frac{5}{2} + \frac{3}{2}\beta(\Theta(2\omega_0,\beta) - 2\Theta(\omega_0,\beta))\right] + \mathcal{O}\left(\lambda^3\right) \tag{5.41}$$

The LSC-LHA thus gives the correct result in the classical limit (as the factor that multiplies η_{Q} tends to one) and $\eta_{\text{LHA}} \to \frac{5}{4}\eta_{\text{Q}}$ in the zero-temperature limit. The overtone contribution to the VDOS is thus slightly overestimated.

Feynman-Kleinert Linearized Path Integrals

The derivation of the momentum ATCF in the LSC-FKLPI approximation is quite cumbersome and goes as follows: we start by writing the perturbative expression of the FK optimal frequency and of the frequency of the fluctuations (respectively defined in equations (3.18) and (3.17)). We then expand the distribution of the fluctuations and compute the TCF at fixed centroid position. Finally, we average

over the centroid position (using the perturbative centroid distribution obtained in section 5.1.5).

Due to the parity of the fluctuation distribution in equation (3.18) and the linear dependence in position of the local frequency (5.38), it can be shown that the FK optimal frequency is equal to the local frequency:

$$\Omega^2_{\text{FK}}(x_c) = \omega_0^2 + \frac{2\lambda}{m} x_c \tag{5.42}$$

We then obtain from equation (3.17) that

$$\theta^2(x_c) = \frac{\omega_0^2}{\frac{u_0}{\tanh(u0)} - 1}\left[1 + x_c \frac{2\lambda}{m\omega_0^2}\left(1 - \frac{u_0}{2}\frac{1 - u_0 + u_0\tanh^2(u_0)}{u_0 - \tanh(u_0)}\right)\right] + \mathcal{O}\left(\lambda^2\right) \tag{5.43}$$

with $u_0 = \beta\hbar\omega_0/2$. Since Ω^2_{FK} is the local frequency, the FK-QCF is equal to the LHA-QCF, see eq. (5.39), at first order in λ, evaluated at the centroid position x_c. One can then expand the fluctuation distribution to first order in λ and compute the TCF at fixed centroid position. Integration over the perturbed centroid distribution (obtained in section 5.1.5) then yields LSC-FKLPI approximation to $\eta(\beta)$ which reads:

$$\eta_{\text{FK}}(\beta) = \eta_{\text{Q}}(\beta)\left[\frac{3}{2} + \frac{3}{2\beta\Theta(2\omega_0,\beta)} - \frac{2\Theta(\omega_0,\beta)}{\Theta(2\omega_0,\beta)}\right] + \mathcal{O}\left(\lambda^3\right) \tag{5.44}$$

The LSC-FKLPI then gives the correct result in the classical limit (as the factor multiplying η_{Q} tends to 1 when $\beta \to 0$) where the fluctuations around the centroid are negligible and the centroid behaves classically. In the zero-temperature limit, $\eta_{\text{FK}} \to \eta_{\text{Q}}/2$. The overtone contribution is thus globally underestimated. The zero-temperature limit is the same as IVR0, which can be understood in the following way: at $k_BT = 0$, the centroid is frozen at the minimum of the potential and thus the fluctuations are purely Gaussian without position-momentum correlations, similarly as IVR0.

5.1.3 Matsubara dynamics

We now turn to path integrals methods. In this section, we show that Matsubara dynamics yields the exact result, at second order in λ, for the overtone intensity. We will also show in the next sections that RPMD and CMD yield the classical result for η, thus losing the correct distribution of energy when approximating Matsubara dynamics.

We recall the Matsubara dynamics approximation to the Kubo-transformed momentum-momentum TCF:

$$K_{pp}^{\text{Mats}}(t) = \lim_{M\to\infty} \int \mathrm{d}Q\mathrm{d}P\; \rho_{\text{M}}(Q,P)\; P_0\; e^{i\mathcal{L}_M t}\; P_0 \tag{5.45}$$

where $Q = (Q_n)_{n\in\mathcal{M}}$ and $P = (P_n)_{n\in\mathcal{M}}$ are the M first Matsubara modes (with the notation $n \in \mathcal{M}$ denoting $n = -(M-1)/2, \ldots, (M-1)/2$) among which (Q_0, P_0) is the centroid, $\rho_{\text{M}}(Q,P)$ is the Matsubara quasi-density defined in equation (3.33) and $i\mathcal{L}_M$ is the Matsubara Liouvillian defined in equation (3.30). For the potential (5.1), the Matsubara potential is given by:

$$U_M(Q) = \frac{1}{2}m\omega_0^2 \sum_{n\in\mathcal{M}} Q_n^2 + \frac{\lambda}{3} \sum_{i,j,k\in\mathcal{M}} A_{ijk} Q_i Q_j Q_k \tag{5.46}$$

where

$$A_{ijk} = \lim_{N\to\infty} \sqrt{N} \sum_{l=1}^{N} T_{li} T_{lj} T_{lk} \tag{5.47}$$

with (T_{ij}) the transfer matrix between the normal modes and the spatial ring-polymer coordinates defined in equation (3.26).

The Matsubara Hamiltonian and Liouville operator can be split into a harmonic part and a perturbation:

$$H_M(Q,P) = \sum_{n\in\mathcal{M}} H_0(Q_n,P_n) + \frac{\lambda}{3} \sum_{i,j,k\in\mathcal{M}} A_{ijk} Q_i Q_j Q_k \tag{5.48}$$

$$i\mathcal{L}_M(Q,P) = \sum_{n\in\mathcal{M}} i\mathcal{L}_0(Q_n,P_n) - \lambda \sum_{i,j,k\in\mathcal{M}} A_{ijk} Q_i Q_j \frac{\partial}{\partial P_k} \tag{5.49}$$

where H_0 and $i\mathcal{L}_0$ are the classical harmonic Hamiltonian and Liouville operator, respectively. Note that, for a harmonic system, the Matsubara modes evolve independently from each other with the classical harmonic equations of motion (propagated using equations (5.14) and (5.15)). In particular, all the fluctuation modes are decoupled from the centroid so that coupling only occurs through the perturbation. We denote the unperturbed Matsubara distribution as:

$$\rho_{\text{M},0}(Q,P) = e^{i\beta\theta_M(Q,P)} \prod_{n\in\mathcal{M}} \frac{e^{-\beta H_0(Q_n,P_n)}}{\mathcal{Z}_{n,0}} \tag{5.50}$$

with $\mathcal{Z}_{n,0} = \int \mathrm{d}Q_n \mathrm{d}P_n e^{-\beta(H_0(Q_n,P_n)+\frac{1}{2}m\tilde{\omega}_n^2 Q_n^2)}$ and $\tilde{\omega}_n = 2n\pi/\beta\hbar$. Normalization of $\rho_{\mathrm{M},0}$ can be verified by performing the momentum integrals by analytic continuation (see ref. [44])

$$\int \mathrm{d}P \; \rho_{\mathrm{M},0}(Q,P) = \prod_{n\in\mathcal{M}} \frac{e^{-\beta\frac{1}{2}m(\omega_0^2+\tilde{\omega}_n^2)Q_n^2}}{\int \mathrm{d}Q_n e^{-\beta\frac{1}{2}m(\omega_0^2+\tilde{\omega}_n^2)Q_n^2}} \tag{5.51}$$

and finding that the position marginal density (5.51) is the standard imaginary-time path-integrals harmonic density for the Matsubara modes. We now use the same method as for the classical case in the extended Matsubara phase-space. The Matsubara distribution is expanded as:

$$\begin{aligned}\rho_{\mathrm{M}}(Q,P) = \rho_{\mathrm{M},0}(Q,P)\Bigg[1 - \frac{\beta\lambda}{3}\sum_{i,j,k\in\mathcal{M}} A_{ijk}Q_iQ_jQ_k \\ + \frac{\beta^2\lambda^2}{18}\left(\left(\sum_{i,j,k\in\mathcal{M}} A_{ijk}Q_iQ_jQ_k\right)^2 - \left\langle\left(\sum_{i,j,k\in\mathcal{M}} A_{ijk}Q_iQ_jQ_k\right)^2\right\rangle_0\right)\Bigg] + \mathcal{O}\left(\lambda^3\right)\end{aligned} \tag{5.52}$$

The time propagator can be expanded at second order using the same Dyson series as (5.13) with the perturbed Matsubara Liouvillian (5.49). As in the classical case, we decompose the Matsubara time correlation function (5.45) as:

$$K_{pp}^M(t) = \sum_{i,j}^{i+j\leq 2} K_{pp}^{M(ij)}(t) + \mathcal{O}\left(\lambda^3\right) \tag{5.53}$$

Since all the Matsubara modes are decoupled from the centroid for the unperturbed dynamics, it is relatively easy to show that:

$$K_{pp}^{M(00)}(t) = \frac{m}{\beta}\cos(\omega_0 t) \tag{5.54}$$

which is the standard result for the harmonic oscillator. One can also show, using the parity of the harmonic distribution that:

$$K_{pp}^{M(10)} = K_{pp}^{M(01)} = 0 \tag{5.55}$$

The first non trivial term in this perturbative analysis arises from the second order of the distribution combined with the unperturbed dynamics and is given by:

$$K_{pp}^{M(20)}(t) = \frac{\beta^2\lambda^2}{18}\int \mathrm{d}Q\mathrm{d}P\ \rho_{\mathrm{M},0}(Q,P)\ P_0^2\cos(\omega_0 t) \\ \times\left(\left(\sum_{i,j,k\in\mathcal{M}} A_{ijk}Q_iQ_jQ_k\right)^2 - \left\langle\left(\sum_{i,j,k\in\mathcal{M}} A_{ijk}Q_iQ_jQ_k\right)^2\right\rangle_0\right) \quad (5.56)$$

This term too, however, leads to a null contribution. Since the phase factor $e^{i\beta\theta_M(Q,P)}$ in (5.50) does not couple P_0 to the other modes, the integrals in P_0 and Q can be performed independently so that the difference in the second line cancels and thus $K_{pp}^{M(20)} = 0$.

Moving on to the following terms, and using the same reasoning as in the classical case, one can also show that:

$$K_{pp}^{M(11)}(t) = \frac{2\lambda^2\beta}{3m\omega_0^2}[\cos(\omega_0 t) - \cos(2\omega_0 t)]\int \mathrm{d}Q\mathrm{d}P\ \rho_{\mathrm{M},0}(Q,P)P_0^2\left(Q_0^2\sum_{i\neq 0}Q_i^2 + \frac{Q_0^4}{3}\right) \quad (5.57)$$

Since the integrand does not involve $P_{i\ (i\neq 0)}$, one can integrate out the momenta first to recover the marginal position density (5.51) and obtain:

$$K_{pp}^{M(11)}(t) = \frac{2\lambda^2}{3\omega_0^2}[\cos(\omega_0 t) - \cos(2\omega_0 t)]\left(\left\langle Q_0^2\right\rangle_0\sum_{i\neq 0}\left\langle Q_i^2\right\rangle_0 + \frac{\langle Q_0^4\rangle_0}{3}\right) \quad (5.58)$$

Since the density for Q_0 is Gaussian, we have $\langle Q_0^4\rangle_0 = 3\langle Q_0^2\rangle_0^2$ and thus $K_{pp}^{M(11)}$ simplifies to:

$$K_{pp}^{M(11)}(t) = \frac{2\lambda^2}{3m\omega_0^4\beta}[\cos(\omega_0 t) - \cos(2\omega_0 t)]\sum_{n\in\mathcal{M}}\left\langle Q_n^2\right\rangle_0 \quad (5.59)$$

When the number of Matsubara modes tends to infinity, the sum appearing in equation (5.59) can be expressed, recognising that in the limit $M\to\infty$ it is related to the average harmonic potential energy by:

$$\lim_{M\to\infty}\sum_{n\in\mathcal{M}}\frac{1}{2}m\omega_0^2\left\langle Q_n^2\right\rangle_0 = \frac{1}{2}\Theta(\omega_0,\beta) \quad (5.60)$$

so that we can rewrite

$$\lim_{M\to\infty} K_{pp}^{M(11)}(t) = \frac{2\lambda^2}{3m^2\omega_0^6\beta}\Theta(\omega_0,\beta)[\cos(\omega_0 t) - \cos(2\omega_0 t)] \tag{5.61}$$

Finally, using the same reasoning as above, and after quite cumbersome calculations, it can be shown that the remaining second order term in the expansion of the TCF is:

$$\lim_{M\to\infty} K_{pp}^{M(02)}(t) = \frac{\lambda^2}{m^2\omega_0^6\beta}\Theta(\omega_0,\beta)\left(\frac{10}{9}[\cos(2\omega_0 t) - \cos(\omega_0 t)] + \frac{5}{3}\omega_0 t\sin(\omega_0 t)\right) \tag{5.62}$$

Combining the results above, the Matsubara TCF is thus given, at second order in λ, by:

$$K_{pp}^{\text{Mats}} = \frac{m}{\beta}\cos(\omega_0 t) + \frac{\lambda^2\Theta(\omega_0,\beta)}{m^2\omega_0^6\beta}\left(\frac{4}{9}[\cos(2\omega_0 t) - \cos(\omega_0 t)] + \frac{5}{3}\omega_0 t\sin(\omega_0 t)\right) + \mathcal{O}\left(\lambda^3\right) \tag{5.63}$$

The contribution of the overtone to the VDOS, approximated using Matsubara dynamics, is then:

$$\eta_{\text{Mats}}(\beta) = \frac{4\lambda^2}{9m^3\omega_0^6}\Theta(\omega_0,\beta) + \mathcal{O}\left(\lambda^3\right) = \eta_{\text{Q}}(\beta) + \mathcal{O}\left(\lambda^3\right) \tag{5.64}$$

which is the exact result[3]. It is interesting to note that, while the zero-order term in equation (5.63) is purely classical and only involves the centroid dynamics, the term that constitutes the overtone is produced from the anharmonic interactions between the centroid and the fluctuation modes.

In the following paragraphs, we will investigate the most common approximations to Matsubara dynamics, which are Centroid Molecular Dynamics (CMD) and Ring-Polymer Molecular Dynamics (RPMD). Both methods are exact in the harmonic case but, in contrast with Matsubara dynamics, display a classical behavior of the overtone intensity.

5.1.4 Ring-Polymer Molecular Dynamics

The RPMD approximation to the Kubo-transformed momentum ATCF is similar to the Matsubara expression except that the analytic continuation for the momentum is performed also in the dynamics to integrate out the phase (see section 3.2.2). This

[3] Like in the classical case, equation (5.63) contains a term proportional to t. As in the previous case, we are going to discard it, based on similar motivations.

does not change the time evolution of the centroid but results in a modification of the frequency for the fluctuation modes. The derivation of the perturbative RPMD approximation to K_{pp} is very similar to the one for Matsubara dynamics. We perform the same steps as in section 5.1.3 and replace ρ_{M} and $i\mathcal{L}_M$ by ρ_{RP} (equation (3.37)) and $i\mathcal{L}_{\text{RP}}$ (equation (3.38)) respectively. After setting the number of Matsubara modes to infinity, the final result is given by:

$$\begin{aligned} K_{pp}^{\text{RPMD}}(t) =& \frac{m}{\beta}\cos(\omega_0 t) + \frac{4\lambda^2}{9m^2\omega_0^6\beta^2}[\cos(2\omega_0 t) - \cos(\omega_0 t)] \\ &+ \frac{\lambda^2}{m^2\omega_0^6\beta}(\Theta(\omega_0, t) + \frac{2}{3}\beta^{-1})\omega_0 t\sin(\omega_0 t) \\ &+ \frac{2\lambda^2}{m^2\omega_0^6\beta^2}\sum_{n=1}^{\infty}\frac{\omega_0^4}{(\omega_0^2+\tilde{\omega}_n^2)(3\omega_0^2+4\tilde{\omega}_n^2)}\Big(\omega_0 t\sin(\omega_0 t) \\ &\qquad + \frac{2\omega_0^2}{3\omega_0^2+4\tilde{\omega}_n^2}\left[\cos\left(2\sqrt{\omega_0^2+\tilde{\omega}_n^2}t\right) - \cos(\omega_0 t)\right]\Big) + \mathcal{O}\left(\lambda^3\right) \end{aligned} \tag{5.65}$$

And thus the RPMD approximation to η is:

$$\eta_{\text{RPMD}}(\beta) = \frac{4\lambda^2}{9m^3\omega_0^6}\beta^{-1} + \mathcal{O}\left(\lambda^3\right) = \eta_{\text{cl}}(\beta) + \mathcal{O}\left(\lambda^3\right) \tag{5.66}$$

which is the classical result. As explained in ref. [44], when approximating Matsubara dynamics with RPMD, energy is transferred from the physical frequencies to the internal modes of the ring-polymer. These spurious frequencies appear in the last line of (5.65) and come from the anharmonic interaction between the centroid and the fluctuation modes. In the original Matsubara Liouvillian, the fluctuation modes all evolve at frequency ω_0 and interact anharmonically with the centroid so that each fluctuation mode contributes to the overtone at $2\omega_0$. In the RPMD Liouvillian, the fluctuation modes evolve at different frequencies and interact with the centroid to give contributions at $2\sqrt{\omega_0^2+\tilde{\omega}_n^2}$ instead of $2\omega_0$. Thus, the only contribution to the overtone intensity is the classical centroid overtone.

5.1.5 Centroid Molecular Dynamics

The CMD approximation to the Kubo-transformed momentum autocorrelation function is similar to the classical momentum ATCF, except that the potential V (and the corresponding Liouville operator) is replaced by the centroid potential V_{c} defined through the centroid mean-field force F_{c} of equation (3.43). To obtain a perturbative expression of the CMD force, we expand the Matsubara distribution (at fixed cen-

troid position) at second order in λ. Using symmetries of the harmonic Matsubara density, we obtain the following perturbative expression for the CMD force:

$$F_{\mathrm{c}}(Q_0) = -m\omega_0^2 Q_0 - \lambda Q_0^2 - \lambda \frac{\beta\Theta(\omega_0,\beta) - 1}{\beta m \omega_0^2} - 2\lambda^2 Q_0 \frac{\alpha_{\mathrm{c}}(\omega_0,\beta)}{\beta m^2 \omega_0^4} + \mathcal{O}\left(\lambda^3\right) \quad (5.67)$$

with the adimensional parameter

$$\alpha_{\mathrm{c}}(\omega_0,\beta) = 1 + \frac{\beta\Theta(\omega_0,\beta)}{2}[\beta\Theta(2\omega_0,\beta) - 2\beta\Theta(\omega_0,\beta) - 1] \quad (5.68)$$

After integration with respect to Q_0, we obtain the following centroid potential:

$$V_{\mathrm{c}}(Q_0) = V(Q_0) + \lambda Q_0 \frac{\beta\Theta(\omega_0,\beta) - 1}{\beta m \omega_0^2} + \lambda^2 Q_0^2 \frac{\alpha_{\mathrm{c}}(\omega_0,\beta)}{\beta m^2 \omega_0^4} + \mathcal{O}\left(\lambda^3\right) \quad (5.69)$$

If we proceed exactly as in the classical case by treating all terms of order λ and higher in the potential as perturbative, we obtain the following expression for the CMD approximation to the TCF:

$$K_{pp}^{\mathrm{CMD}}(t) = \frac{m}{\beta}\cos(\omega_0 t) + \frac{\lambda^2}{m^2\omega_0^6\beta^2}\left[\frac{2}{3} + \beta\Theta(\omega_0,\beta) - \alpha_{\mathrm{c}}(\omega_0,\beta)\right]\omega_0 t \sin(\omega_0 t) + \frac{4\lambda^2}{9m^2\omega_0^6\beta^2}[\cos(2\omega_0 t) - \cos(\omega_0 t)] + \mathcal{O}\left(\lambda^3\right) \quad (5.70)$$

The CMD approximation to η is then:

$$\eta_{\mathrm{CMD}}(\beta) = \frac{4\lambda^2}{9m^3\omega_0^6}\beta^{-1} + \mathcal{O}\left(\lambda^3\right) = \eta_{\mathrm{cl}}(\beta) \quad (5.71)$$

which is the classical result. The quantum behavior of the overtone is thus lost when integrating out the fluctuation modes in the mean-field approximation used to obtain the CMD approximation to Matsubara dynamics. Indeed, as we noted in the previous paragraph, the dynamical coupling between the centroid and the fluctuation modes, which is neglected in the mean-field approximation, reinforces the centroid overtone in order to give the correct amplitude in the full Matsubara dynamics.

5.1.6 Comparison and conclusions

For the numerical application of our results, we used $\omega_0 = 1500\mathrm{cm}^{-1}$ and $\lambda = 21\ \mathrm{kcal\,mol}^{-1}\,\text{Å}^{-3}$. Figure 5.2 shows the overtone contribution to the VDOS η as

a function of temperature computed with the different methods. For all methods analysed in the previous sections, we show both the reported analytic results and the data from numerical simulations of the system. As expected, since in the numerical experiments we ensured that we are in the correct perturbative regime, the two sets are in excellent agreement.

In addition, the figure reports results of simulations for two more methods considered in this thesis: QTB and WiLD propagation. Unfortunately, the perturbative analysis for these approaches is considerably more complicated than those reported and obtaining analytical results proved too difficult. Some insights can, however, be gained from a qualitative discussion of the numerical evidence.

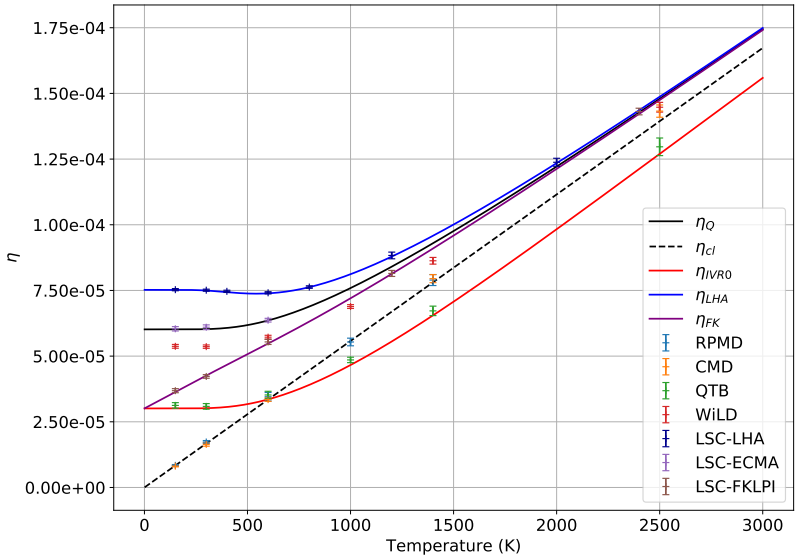

Fig. 5.2.: Contribution η of the overtone to the VDOS as function of temperature for the potential (5.1) computed using different methods. Lines are perturbative expressions, points are simulation results.

We show in appendix C.2 that the WiLD samples the exact Wigner distribution up to first order in λ. Thus, propagating classical trajectories from initial positions sampled using WiLD, in the IVR spirit, gives the exact result for the overtone (as for LSC-ECMA). However, the figures show that computing η directly from the WiLD trajectories yields a slightly underestimated value at low temperature. It is not trivial to examine the origin of this inaccuracy in the WiLD propagation and we leave this task for future work. Still, the WiLD gives the correct qualitative result and is closer to the exact result at low temperature than the other approximate methods (except for LSC-ECMA and Matsubara dynamics).

Fig. 5.2 also shows QTB simulations results obtained from the QTB approximation to K_{pp}. These results are strikingly close to the IVR0 results and thus yield a qualitatively correct temperature-dependence of the overtone (the saturation at low temperature) but underestimate the overtone intensity by a factor two at low temperature. This can be understood noting that the short-term QTB propagation corresponds to the classical propagation (on time scales shorter than γ^{-1}) but the thermalization is quantum in the sense that it includes zero-point energy, but without any position-momentum correlation, as it was noted in ref. [101].
We showed in section 3.3 that the (generalized) vibrational density of states $2\,\mathrm{Re}[\chi_{px}(\omega)]$ can also be estimated in a QTB simulation using the cross correlation function of the momentum and stochastic force $\mathrm{Re}[C_{pF}(\omega)]$ via eq. (3.54). For anharmonic systems, we noted that the two QTB estimators of the VDOS might differ. Figure 5.3 shows the QTB approximations to η obtained using the two different estimators of the VDOS. One can see that the two estimators are indeed different and that the estimator obtained from C_{pF} is much closer to the exact value (with larger error bars due to a noisier behavior of the spectrum) than the one obtained from C_{pp}. One could use the adaptive QTB scheme described in section 3.3.4 in order to compensate this difference and obtain the correct VDOS from C_{pp}. It is however difficult to correctly adapt the γ_r coefficients as the overtone intensity is very low compared to the main peak. It is however encouraging that the FDT criterion is able to detect the discrepancy between the two estimators of the VDOS. This result is consistent with the observations made on the Morse potential in section 3.3 and, for this particular system, we were able to correct this mismatch for the overtone using the adQTB.

For this perturbative model, both CMD (not shown in figure 5.3) and RPMD yield the classical result for the overtone which linearly goes to zero at low temperature. On the other hand, Matsubara dynamics yields the exact result (at least at second order in perturbation) so that the quantum behavior of the overtone is lost in the approximations inherent to CMD or RPMD.

Finally, it is interesting to compare the different flavors of LSC-IVR stemming from different methods for sampling initial conditions. For this particular model and for linear observables, we showed that the classical dynamics correctly describes the time propagation at second order in perturbation. Thus, only statistical effects (*i.e.* the approximation to the Wigner thermal density) influence the result and quantum coherence is not responsible for the differences between the LSC-IVR and the exact results. Here, we see that ECMA allows to sample the exact Wigner density (at first order in λ) so that LSC-ECMA yields the correct overtone intensity. Moreover, it is surprising to see that the LSC-LHA and LSC-FKLPI, which are designed to behave

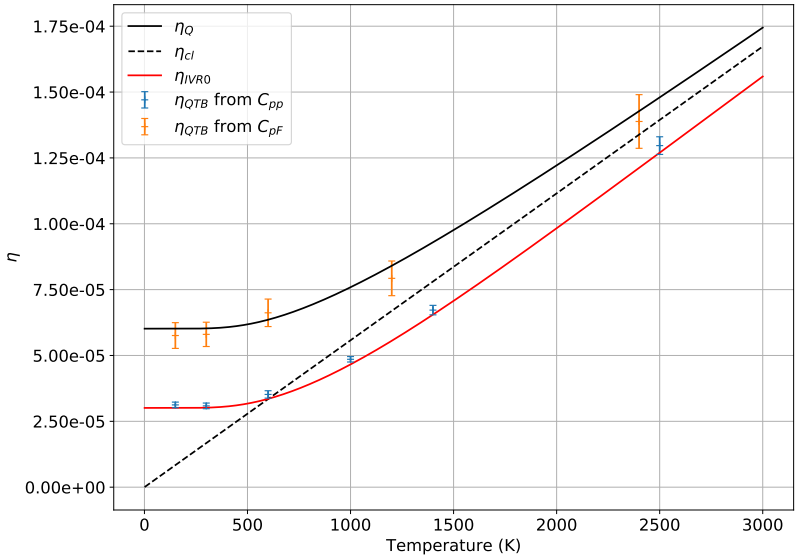

Fig. 5.3.: Contribution η of the overtone to the VDOS as function of temperature for the potential (5.1) computed with the two different QTB estimators for the VDOS.

well for nearly harmonic potentials, are not able to capture the correct behavior of the overtone: LSC-LHA systematically overestimates its intensity and LSC-FKLPI underestimates it. This is consistent with the observations made on the Morse potential in chapter 3 and can be related to the ability of the different methods to reproduce the position-momentum correlations of the Wigner distribution.

In conclusion, the analytical results obtained are consistent with the observations made earlier for the Morse potential of chapters 3 and 4, in particular the fact that CMD and RPMD miss the quantum effects on the overtone and predict the same amplitude as classical MD. The precise quantitative comparison of the different linearized methods and with the exact quantum result is difficult to extend to this particular Morse potential because it is so anharmonic that the main peak and the overtone obtained in LSC-IVR partly overlap. However, we verified that for a Morse potential with parameters typically used for the O-H bond of water (see section 5.4), the amplitude of the overtone obtained with the different methods agrees quantitatively with the perturbative results above.

5.2 Combination bands: weakly coupled harmonic oscillators

In the previous section, we treated a simple 1D overtone model, but in molecular or solid state systems, anharmonic resonances also arise from the coupling between different modes. In particular, when two modes are coupled, combination bands (CB), corresponding to the sum and the differences of the harmonic frequencies, appear in the spectrum. This behavior can be modeled by using the following two-dimensional potential:

$$V(q_1, q_2) = \frac{1}{2} m_1 \omega_1 q_1^2 + \frac{1}{2} m_2 \omega_2 q_2^2 + \lambda q_1 q_2^2 \tag{5.72}$$

$V(q_1, q_2)$ consists of two harmonic oscillators at frequencies ω_1 and ω_2 with a cubic coupling with amplitude controlled by the parameter λ. As in section 5.1, one can choose λ so that the coupling can be treated as a perturbation. Moreover, in order to avoid the special case of a resonant configuration, we choose frequencies ω_1 and ω_2 that are not multiple of one another and, more precisely, we impose $\omega_1 > 2\omega_2$. For numerical applications in this section, we use $\omega_1 = 2.5\omega_2 = 1500 \text{ cm}^{-1}$ and $\lambda = 8.5 \text{ kcal mol}^{-1} \text{ Å}^{-3}$. The particular case $\omega_1 = 2\omega_2$ corresponds to the Fermi resonance and is treated numerically in section 5.3.

As we show in the following, three resonances appear in the momentum autocorrelation spectrum for the potential (5.72): an overtone at $2\omega_2$ and combination bands at $\omega_1 + \omega_2$ and $\omega_1 - \omega_2$. As in the previous section, we characterize the contribution of the different resonances by their contribution η to the vibrational density of states. For example, for the CB at $\omega_1 + \omega_2$ we have:

$$\eta(\beta; \omega_1 + \omega_2) = \frac{1}{2} \int_{\omega_1+\omega_2-\Delta\omega}^{\omega_1+\omega_2+\Delta\omega} \left(\frac{\beta}{m_1} K_{p_1 p_1}(\omega; \beta) + \frac{\beta}{m_2} K_{p_2 p_2}(\omega; \beta) \right) \mathrm{d}\omega \tag{5.73}$$

and similarly for $\eta(\beta; \omega_1 - \omega_2)$ and $\eta(\beta; 2\omega_2)$. The integration window $\Delta\omega$ is chosen for each method and each resonance so that it encompasses the peak but does not integrate contributions from other peaks.

The perturbative approach, although more technically involved, is conceptually very similar to the one developed in section 5.1. Therefore, we will only provide the key calculation steps and the final results.

5.2.1 Classical correlation functions

To compute each autocorrelation function in the classical case, we perform the same steps as in section 5.1.1 by expanding the classical Boltzmann distribution and the Liouville operator of the bidimensional system at second order in λ. The classical Liouville operator is given by:

$$i\mathcal{L} = i\mathcal{L}_0 - \lambda\left(q_2^2\frac{\partial}{\partial p_1} + 2q_1q_2\frac{\partial}{\partial p_2}\right) \tag{5.74}$$

where $i\mathcal{L}_0$ is the Liouville operator of the bidimensional (separable) harmonic system. For each degree of freedom, the effect of the harmonic time propagator $e^{i\mathcal{L}_0 t}$ is independently given by equations (5.14) and (5.15) and the Dyson expansion of $e^{i\mathcal{L}t}$ has the same form as (5.13) where we replace the perturbation by $-\lambda\left(q_2^2\frac{\partial}{\partial p_1} + 2q_1q_2\frac{\partial}{\partial p2}\right)$.

The full expressions of the correlation functions are quite involved so that we give here only the final results for the contributions to the VDOS at the resonance frequencies $\omega_1+\omega_2$, $\omega_1-\omega_2$ and $2\omega_2$ (note that at second order in λ, the overtone contribution at $2\omega_1$ is zero for this form of the potential). The classical contributions are given by:

$$\eta_{\text{cl}}(\beta;\omega_1+\omega_2) = \frac{\lambda^2(\omega_1+\omega_2)^2\beta^{-1}}{m_1m_2^2(\omega_1+2\,\omega_2)^2{\omega_1}^4{\omega_2}^2} + \mathcal{O}\left(\lambda^3\right) \tag{5.75}$$

$$\eta_{\text{cl}}(\beta;\omega_1-\omega_2) = \frac{\lambda^2(\omega_1-\omega_2)^2\beta^{-1}}{m_1m_2^2(\omega_1-2\,\omega_2)^2{\omega_1}^4{\omega_2}^2} + \mathcal{O}\left(\lambda^3\right) \tag{5.76}$$

$$\eta_{\text{cl}}(\beta;2\omega_2) = \frac{2\,\lambda^2\beta^{-1}}{m_1m_2^2(\omega_1+2\,\omega_2)^2(\omega_1-2\,\omega_2)^2{\omega_2}^2} + \mathcal{O}\left(\lambda^3\right) \tag{5.77}$$

As in the case of the overtone in the previous section, the amplitudes of the combination bands are of second order in λ and go linearly to zero at low temperature. Moreover, the configuration $\omega_1 = 2\omega_2$ appears clearly as a special case (the Fermi resonance) where this perturbation method does not apply since the intensity of the resonances would diverge. This particular case is addressed in section 5.3.

5.2.2 Quantum perturbation theory

As for the overtone model of section 5.1, two different methods can be used to derive a quantum perturbative expression for the CB amplitudes: the first one uses an expansion of the harmonic eigenstates and is summarized in appendix C.1. The

second one implies a perturbative expansion of the Wigner density of the system using path integral methods, similarly to what is presented in appendix C.2 for the overtone model, and a Dyson expansion of the quantum Liouvillian. This method is not presented in this work. The quantum contributions to the VDOS of the resonances at frequencies $\omega_1 + \omega_2$, $\omega_1 - \omega_2$ and $2\omega_2$ are given by:

$$\eta_{\mathrm{Q}}(\beta;\omega_1+\omega_2) = \frac{(\omega_1\Theta\left(\omega_2,\beta\right)+\omega_2\Theta\left(\omega_1,\beta\right))\lambda^2(\omega_1+\omega_2)}{m_1 m_2^2(\omega_1+2\,\omega_2)^2{\omega_1}^4{\omega_2}^2} + \mathcal{O}\Big(\lambda^3\Big) \tag{5.78}$$

$$\eta_{\mathrm{Q}}(\beta;\omega_1-\omega_2) = \frac{(\omega_1\Theta\left(\omega_2,\beta\right)-\omega_2\Theta\left(\omega_1,\beta\right))\lambda^2(\omega_1-\omega_2)}{m_1 m_2^2(\omega_1-2\,\omega_2)^2{\omega_1}^4{\omega_2}^2} + \mathcal{O}\Big(\lambda^3\Big) \tag{5.79}$$

$$\eta_{\mathrm{Q}}(\beta;2\omega_2) = \frac{2\,\lambda^2\Theta\left(\omega_2,\beta\right)}{m_1 m_2^2(\omega_1+2\,\omega_2)^2(\omega_1-2\,\omega_2)^2{\omega_2}^2} + \mathcal{O}\Big(\lambda^3\Big) \tag{5.80}$$

These expressions are very similar to the classical ones, except that the factor β^{-1} at the numerator is replaced with weighted combinations of $\Theta(\omega_1,\beta)$ and $\Theta(\omega_2,\beta)$. Indeed, contrary to the classical case where equipartition of energy holds, in the quantum case, the different amounts of ZPE present in each mode affects the combination bands amplitude.

Figure 5.4 shows the three ratios for the classical and quantum dynamics as a function of temperature. In classical mechanics, the three contributions have similar linear behaviors with temperature. However, in the quantum case, we clearly observe two different behaviors: $\eta_{\mathrm{Q}}(\omega_1+\omega_2)$ and $\eta_{\mathrm{Q}}(2\omega_2)$ saturate at a non-zero value at low temperature due to zero-point energy contributions, similarly to the overtone in the previous section. On the other hand, $\eta_{\mathrm{Q}}(\omega_1-\omega_2)$ goes to zero at low temperature faster than for the classical system. Indeed, this frequency corresponds necessarily to a transition, starting from an excited state. Therefore, at low temperature where only the ground state is populated, these transitions are suppressed and the corresponding resonance vanishes (even much faster than in the classical case).

We now move to the perturbative analysis of the different trajectory-based methods. Results for these methods are summarized in figure 5.5.

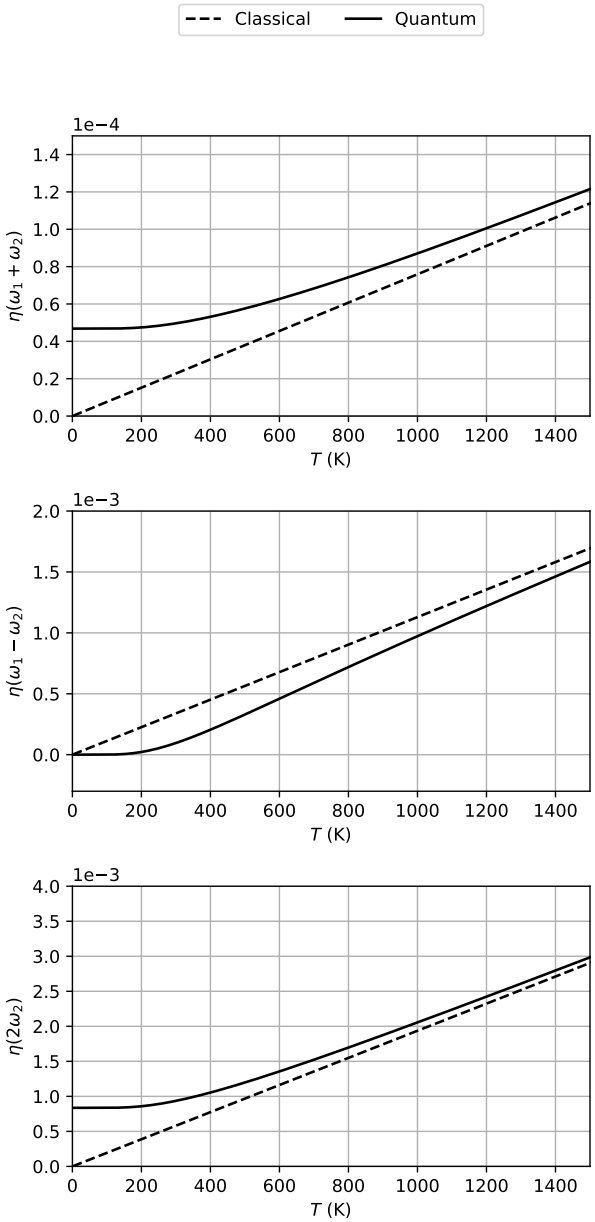

Fig. 5.4.: Contributions of the three resonances to the VDOS for the potential (5.72) as a function of temperature in the classical (dashed line) and quantum (solid line) cases.

5.2.3 Matsubara Dynamics

For this system, the Matsubara potential is given by:

$$U_M(Q_1, Q_2) = \frac{1}{2} \sum_{n \in \mathcal{M}} m_1 \omega_1^2 Q_{1,n}^2 + m_2 \omega_2^2 Q_{2,n}^2 + \lambda \sum_{i,j,k \in \mathcal{M}} A_{ijk} Q_{1,i} Q_{2,j} Q_{2,k} \quad (5.81)$$

with A_{ijk} defined in equation (5.47), and the Liouville operator is:

$$\begin{aligned} i\mathcal{L}_M(Q_1, Q_2, P_1, P_2) = &\sum_{n \in \mathcal{M}} i\mathcal{L}_0(Q_{1,n}, Q_{2,n}, P_{1,n}, P_{2,n}) \\ &- \lambda \sum_{i,j,k \in \mathcal{M}} A_{ijk} \left(Q_{2,i} Q_{2,j} \frac{\partial}{\partial P_{1,k}} + 2 Q_{1,i} Q_{2,j} \frac{\partial}{\partial P_{2,k}} \right) \end{aligned} \quad (5.82)$$

where $i\mathcal{L}_0$ is the classical harmonic Liouville operator of the bidimensional system. As for the overtone, we can expand the density and time propagator at second order in λ and perform the same steps as in section 5.1.3 to compute the Kubo-transformed ATCFs. The detailed calculations are not reported since they are lengthy and do not provide insight for the analysis. The final expressions for the contributions of the different resonances to the VDOS (in the limit of infinite number of Matsubara modes) are:

$$\lim_{M \to \infty} \eta_{\mathrm{M}}(\omega_1 + \omega_2) = \eta_{\mathrm{Q}}(\omega_1 + \omega_2) + \mathcal{O}\left(\lambda^3\right) \quad (5.83)$$

$$\lim_{M \to \infty} \eta_{\mathrm{M}}(\omega_1 - \omega_2) = \eta_{\mathrm{Q}}(\omega_1 - \omega_2) + \mathcal{O}\left(\lambda^3\right) \quad (5.84)$$

$$\lim_{M \to \infty} \eta_{\mathrm{M}}(2\omega_2) = \eta_{\mathrm{Q}}(2\omega_2) + \mathcal{O}\left(\lambda^3\right) \quad (5.85)$$

Therefore, similarly to the previously considered overtone model, Matsubara dynamics yields the exact result at second order in perturbation for the CB intensities.

Using the same methodology as in sections 5.1.4 and 5.1.5, it would be possible to write perturbative expressions for RPMD and CMD. However, these developments are quite involved and we only present here the results of numerical simulations for RPMD (see figure 5.5) which, as for the overtone model, yield the same results as classical MD for the amplitude of the resonances.

5.2.4 Linearized dynamics

We now compare the different LSC-IVR approximations. For the IVR0, LHA and ECMA, we use the exact position distribution given by the marginal Matsubara

distribution (in the limit $M \to \infty$), expanded to first order in λ. The conditional momentum distribution is then approximated using a bidimensional Gaussian distribution. The covariance matrix of this Gaussian distribution is characterized by the quantum correction matrix (QCM) Φ as:

$$\rho_c(p_1, p_2|q_1, q_2) \propto \exp\left\{-\frac{1}{2} P^T M^{-\frac{1}{2}} \Phi^{-1}(q_1, q_2) M^{-\frac{1}{2}} P\right\} \tag{5.86}$$

with $P = (p_1, p_2)$ and M the diagonal mass matrix. The IVR0-QCM is position-independent and diagonal, thus neglecting position-momentum and momentum-momentum correlations. For LHA and ECMA, the coefficients of the QCM are position-dependent and contain off-diagonal terms that couple the momenta of the two degrees of freedom. For all the methods, we expand the momentum distribution to first order in λ and use the Dyson expansion of the classical Liouvillian to compute the resonance contributions to $\bar{c}_{p_1 p_1}$ and $\bar{c}_{p_2 p_2}$ at second order in λ. We will not detail the expansion of the different distributions as the expressions are quite involved and thus only provide the QCM and the final result for the CB amplitudes for each method.

Global Harmonic approximation

The global harmonic approximation uses the harmonic momentum distribution which is position-independent and characterized by the following diagonal IVR0-QCM:

$$\Phi_{\text{IVR0}} = \begin{pmatrix} \beta\Theta(\omega_1, \beta) & 0 \\ 0 & \beta\Theta(\omega_2, \beta) \end{pmatrix} \tag{5.87}$$

The resulting momentum distribution is then a product of (independent) Gaussian distributions. The contributions of the resonances to the LSC-IVR0 VDOS are:

$$\eta_{\text{IVR0}}(\beta; \omega_1 + \omega_2) = \frac{\Theta(\omega_2, \beta)}{\Theta(\omega_1 + \omega_2, \beta)} \eta_{\text{Q}}(\beta; \omega_1 + \omega_2) \tag{5.88}$$

$$\eta_{\text{IVR0}}(\beta; \omega_1 - \omega_2) = \frac{\Theta(\omega_2, \beta)}{\Theta(\omega_1 - \omega_2, \beta)} \eta_{\text{Q}}(\beta; \omega_1 - \omega_2) \tag{5.89}$$

$$\eta_{\text{IVR0}}(\beta; 2\omega_2) = \frac{\Theta(\omega_1, \beta)}{\Theta(2\omega_2, \beta)} \eta_{\text{Q}}(\beta; 2\omega_2) \tag{5.90}$$

Similarly to the overtone case, LSC-IVR0 yields the exact quantum result η_Q multiplied by a factor which corresponds to the ratio between the harmonic thermal energy Θ at the frequency ω_2 (or ω_1 for eq. (5.90)) and at the frequency of the combination band considered. The qualitative behavior of the resonances as a function of

temperature is thus correct as can be seen on figure 5.5. However, the contributions at $\omega_1 + \omega_2$ and $2\omega_2$ do not tend to the correct value at low temperature.

Local Harmonic approximation

The LHA-QCM is obtained from the local frequency matrix which is given by:

$$\Omega^2(q_1, q_2) = \begin{pmatrix} \omega_1^2 & \frac{2\lambda q_2}{\sqrt{m_1 m_2}} \\ \frac{2\lambda q_2}{\sqrt{m_1 m_2}} & \omega_2^2 + \frac{2\lambda q_1}{m_2} \end{pmatrix} \tag{5.91}$$

At first order in λ, the eigenvalues of $\Omega^2(q)$ are simply ω_1^2 and $\tilde{\omega}_2^2 = \omega_2^2 + 2\lambda q_1/m_2$. In the basis where $\Omega^2(q)$ is diagonal, the QCM is, by definition, also diagonal with eigenvalues given by equation (3.9) with $\Omega(q)$ replaced by ω_1 and $\tilde{\omega}_2$. Furthermore, the unitary transfer matrix is, at first order in λ:

$$T(q_1, q_2) = \begin{pmatrix} 1 & -\frac{2\lambda q_2}{\sqrt{m_1 m_2}(\omega_1^2 - \omega_2^2)} \\ \frac{2\lambda q_2}{\sqrt{m_1 m_2}(\omega_1^2 - \omega_2^2)} & 1 \end{pmatrix} + \mathcal{O}\left(\lambda^2\right) \tag{5.92}$$

The first order expansion to the LHA-QCM in the original basis thus reads:

$$\Phi_{\text{LHA}}^{-1}(q_1, q_2) = \Phi_{\text{IVR0}}^{-1} - \frac{\lambda}{\beta} \begin{pmatrix} 0 & \frac{2q_2}{\sqrt{m_1 m_2}} \frac{\Theta^{-1}(\omega_2,\beta) - \Theta^{-1}(\omega_1,\beta)}{\omega_1^2 - \omega_2^2} \\ \frac{2q_2}{\sqrt{m_1 m_2}} \frac{\Theta^{-1}(\omega_2,\beta) - \Theta^{-1}(\omega_1,\beta)}{\omega_1^2 - \omega_2^2} & \frac{q_1}{m_2 \omega_2^2}\left[\Theta^{-1}(\omega_2,\beta) + \frac{\hbar^2\omega_2^2}{4\Theta^2(\omega_2,\beta)} - \beta\right] \end{pmatrix} + \mathcal{O}\left(\lambda^2\right) \tag{5.93}$$

The contributions of the resonances to the LSC-LHA VDOS are:

$$\eta_{\text{LHA}}(\beta; \omega_1 + \omega_2) = \eta_{\text{Q}}(\beta; \omega_1 + \omega_2)\ \gamma^{\text{LHA}}_{\omega_1+\omega_2} \tag{5.94}$$

$$\eta_{\text{LHA}}(\beta; \omega_1 - \omega_2) = \eta_{\text{Q}}(\beta; \omega_1 - \omega_2)\ \gamma^{\text{LHA}}_{\omega_1-\omega_2} \tag{5.95}$$

$$\eta_{\text{LHA}}(\beta; 2\omega_2) = \eta_{\text{Q}}(\beta; 2\omega_2)\ \gamma^{\text{LHA}}_{2\omega_2} \tag{5.96}$$

where $\gamma^{\text{LHA}}_{\omega_1+\omega_2}$, $\gamma^{\text{LHA}}_{\omega_1-\omega_2}$ and $\gamma^{\text{LHA}}_{2\omega_2}$ are functions of ω_1, ω_2 and β whose expressions are quite involved and given in appendix C.3. Figure 5.5 shows the three contributions as a function of temperature for IVR0 and LHA (the analytical perturbation approach is confirmed by comparison with numerical simulation results). The most surprising behavior is for $\eta_{\text{LHA}}(\omega_1 - \omega_2)$ since it becomes negative at low temperature. Indeed, the momentum autocorrelation spectrum computed with LHA is not positive for every frequency and displays a peak of negative intensity at $\omega_1 - \omega_2$. According to the Wiener-Khinchin theorem, for a stationary dynamics, the momentum autocorrelation

spectrum is positive everywhere. Thus, this negative peak is a clear manifestation that the classical dynamics does not conserve the initial distribution. For this particular form of the potential, the local harmonic approximation thus gives an unphysical result at low temperature.

Edgeworth conditional momentum approximation

Using a similar procedure as in appendix C.2, we obtain the EW0-QCM, at first order in λ, as:

$$\Phi^{-1}_{\text{EW0}}(q_1,q_2) = \Phi^{-1}_{\text{IVR0}} - \frac{2\lambda}{\beta}\begin{pmatrix} 0 & \frac{q_2\ \alpha_{12}}{\sqrt{m_1 m_2}} \\ \frac{q_2\ \alpha_{12}}{\sqrt{m_1 m_2}} & \frac{q_1 \alpha_{22}}{m_2} \end{pmatrix} + \mathcal{O}\left(\lambda^2\right) \tag{5.97}$$

with

$$\alpha_{12} = \frac{\Theta(\omega_1,\beta) - \Theta(\omega_2,\beta) - \hbar^2\omega_2^2/4\Theta(\omega_2,\beta)}{\Theta(\omega_1,\beta)\Theta(\omega_2,\beta)(\omega_1^2 - 4\omega_2^2)} \tag{5.98}$$

$$\alpha_{22} = \frac{2\Theta(\omega_2,\beta) - 2\Theta(\omega_1,\beta) + \hbar^2(\omega_1^2 - 2\omega_2^2)/4\Theta(\omega_2,\beta)}{\Theta(\omega_1,\beta)\Theta(\omega_2,\beta)(\omega_1^2 - 4\omega_2^2)} \tag{5.99}$$

We found that the three contributions of the resonances to the LSC-ECMA VDOS are exactly the ratios $\eta_{\text{Q}}(\omega_1+\omega_2)$, $\eta_{\text{Q}}(\omega_1-\omega_2)$ and $\eta_{\text{Q}}(2\omega_2)$ given by the quantum perturbation theory, at second order in λ.

5.2.5 QTB results and summary

Figure 5.5 summarizes the results obtained for the CB model. It also presents the CB intensities obtained in QTB simulations using the two different estimators for the VDOS. Using the C_{pp} estimator, the QTB underestimates the contributions at $\omega_1+\omega_2$ and $2\omega_2$ and largely overestimates the contribution at $\omega_1-\omega_2$ (which does not go to zero at low temperature, contrary to the exact result). Interestingly, as it was noted already in the overtone case, the VDOS estimator obtained from the C_{pF} spectrum yields CB intensities that are much closer to the quantum result. This again suggests that the adQTB approach might be interesting to explore as an approximate dynamics method for computing vibrational spectra. Surprisingly, even for the case of the difference-frequency CB, which is strongly suppressed by NQE at low temperatures, the C_{pF} spectrum yields the correct (almost zero) amplitude. This indicates that the fluctuation-dissipation relation proposed in section 3.3 exceeds the simple ZPEL diagnosis and has more far-reaching consequences (even though in

that particular case, simply adapting the γ_r coefficients is probably not an efficient cure to restore the correct amplitude of the difference-frequency CB).

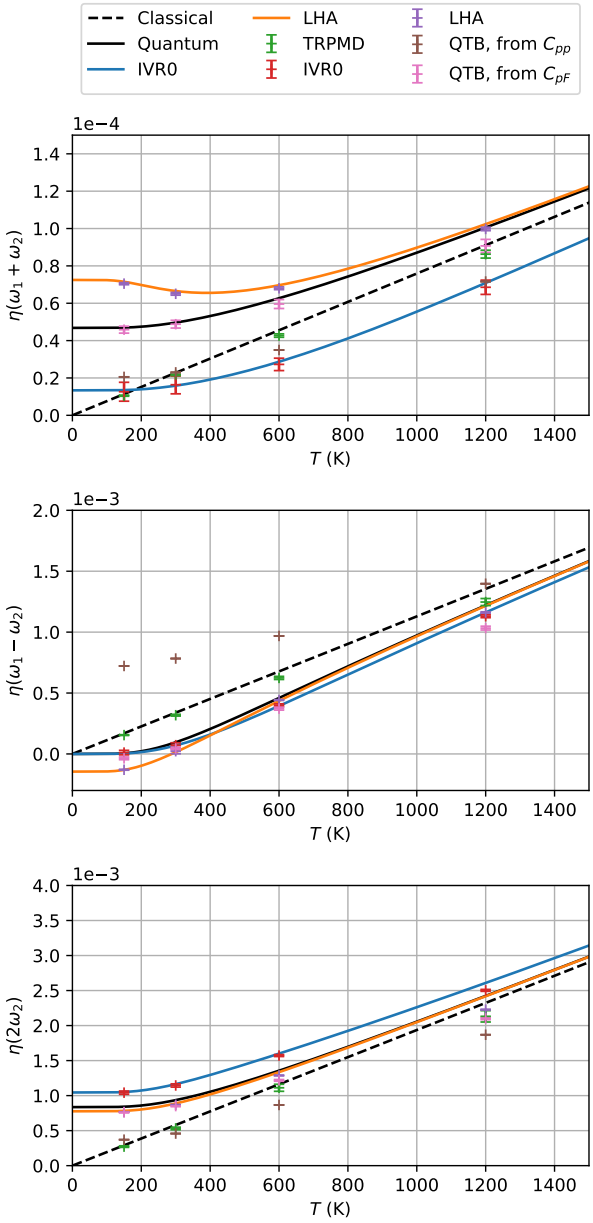

Fig. 5.5.: Contributions of the three resonances to the VDOS for the potential (5.72) as a function of temperature for the different methods. Lines are analytical expressions and crosses are simulation results.

In summary, the results obtained in this section confirm and extend the trends already observed in section 5.1 for the simple overtone model: among the linearized methods, the Edgeworth approximation of the Wigner density provides the most

accurate description and it allows to precisely recover the correct amplitudes for the different CB. On the other hand, the most common PI-based methods, CMD and RPMD completely miss the NQEs and yield CB amplitudes similar to that obtained in classical MD. This limitation however is not present in the Matsubara dynamics which yields the exact quantum result. For this model, we did not treat the LSC-FKLPI and WiLD approximations yet. We do not expect significant qualitative differences from the overtone model for the contributions at $\omega_1 + \omega_2$ and $2\omega_2$ but it would be interesting to see how they perform for the difference-frequency CB.

5.3 The Fermi resonance

In section 5.2, we noted that the configuration $\omega_1 \approx 2\omega_2$ appears as a particular case of combination bands, the Fermi resonance (FR), that the perturbative approach that we developed fails to describe. In this configuration, the interaction between the modes causes the high-frequency peak in the vibration spectrum to split. The width of the splitting is temperature-dependent, and, as shown in ref. [109] its low-temperature behavior is qualitatively different if the system is treated classicaly or using quantum mechanics. Indeed, the Fermi splitting for the classical system goes to zero at low temperature while it saturates at a non-zero value for the quantum system due to zero-point energy. This behavior is reminiscent of that of the overtone amplitude in section 5.1 and indeed, FR arises from the coupling between the mode at ω_1 and the overtone of the mode at ω_2. To study the Fermi resonance, we use the 3-dimensional model for the CO_2 molecule in gas phase – the historic example for which Fermi provided the theoretical explanation of this phenomenon [117] – also adopted in ref. [109]. This model describes the normal modes of the CO_2 molecule using the following potential:

$$V(x, y_1, y_2) = \frac{1}{2} m_1 \omega_1^2 x^2 + \frac{1}{2} m_2 \omega_2^2 (y_1^2 + y_2^2) + \frac{1}{2} \chi_{12} x (y_1^2 + y_2^2) \sqrt{m_1} m_2 \quad (5.100)$$

where x is the coordinate associated to the symmetric stretching and $y_1,\ y_2$ are the coordinates associated to the degenerate bending modes. We work under the assumption that the antisymmetric streching mode, which is on a different frequency range, does not interact with the other modes; it is thus not included in the model. The masses m_1 and m_2 are chosen as the reduced masses of CO_2 and the harmonic frequencies are $\omega_1 = 1261$ cm^{-1} and $\omega_2 = 634$ cm^{-1}. The anharmonic coupling parameter is taken equal to $\chi_{12} = 1.479 \times 10^{-7}$ a.u..

This model has a similar structure to the previous one for studying combination bands except that it includes two degenerate low-frequency modes and, most importantly, the high and low-frequency modes are in a Fermi resonant configuration with $\omega_1 \approx 2\omega_2$. In this configuration, one cannot use the same perturbative approach as in section 5.2 because of the terms in $1/(\omega_1 - 2\omega_2)^2$ that appear in the expressions for η_{cl} and η_{Q} and would diverge in the FR configuration. In ref. [109], Basire et al. used a different perturbative method that allows to compute the Fermi splitting as a function of temperature for this model of CO_2. The results of this perturbative approach are shown as the solid and dashed lines in the center panel of figure 5.6, corresponding to the quantum and classical cases, respectively. One can see that the behavior of the Fermi splitting as a function of temperature is very different for the classical and quantum systems. For the classical system, the splitting goes to zero at low temperature as the overtone of the low frequency mode is less and less intense (and the interaction with the high frequency mode vanishes). For the quantum system, the overtone of the low frequency mode is still present at zero temperature (as we saw in section 5.1) and thus still interacts with the high-frequency mode, yielding a finite value of the splitting at low temperature.

Figure 5.6 shows the Fermi splitting obtained using TRPMD, LSC-ECMA and WiLD. As in ref. [109], the splitting is measured as the distance between the center of mass of the two spectral peaks that constitute the Fermi dyad. This gives a good agreement between the perturbative approach and the exact result obtained by solving the Schrödinger equation on a basis of harmonic wavefunctions (black diamond shapes on the center panel of figure 5.6).

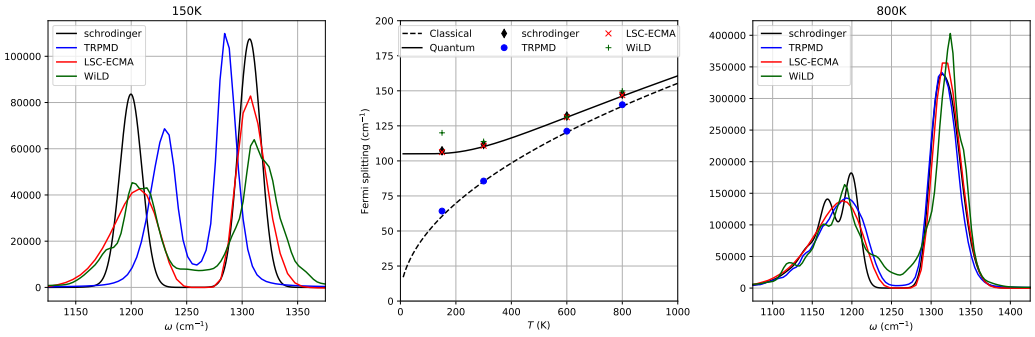

Fig. 5.6.: Center panel: Fermi splitting as a function of temperature approximated with TRPMD, LSC-ECMA and WiLD. Left and right panels: Kubo-transformed momentum autocorrelation spectrum at 150K (left) and 800K (right) in the region of the Fermi dyad for TRPMD, LSC-ECMA and WiLD, compared to the exact results. The exact spectra are obtained by solving the Schrödinger equation on a basis of harmonic wavefunctions and are artificially broadened by convolution with a Gaussian function so that the height of the peaks approximately match the other methods.

The TRPMD and CMD (not presented on the figure) methods precisely follow the classical result with a vanishing splitting at low temperature. This can again be related to the lowering intensity of the overtone of the low frequency mode which we attributed in section 5.1 to the displacement of spectral intensity towards spurious peaks for TRPMD or by averaging out the dynamics of fluctuation modes for CMD.

The FR splitting approximated by the WiLD agrees well with the exact result at 300K and higher temperatures but the splitting is slightly overestimated at 150K. This inaccuracy may be due to increased numerical noise in the estimated WiLD forces at low temperature which results in an overestimation of the overall energy and thus yields a larger Fermi splitting. More converged results are thus necessary to really conclude on the accuracy of the WiLD at low temperature. Note however that the precision necessary for the estimation of the WiLD forces in order to obtain a stable and well thermalized dynamics implies a large computational cost, even for this low-dimensional system. Further efforts to improve the numerical efficiency of the method might be needed to tackle larger systems.

The LSC-IVR yields a Fermi splitting that is close to the exact result when using initial conditions given either by LGA, FK or ECMA (thus only ECMA is represented on the figure). However, due to the classical dynamics, the peaks are unphysically broadened even at low temperature. We can see this effect on figure 5.6 where we show the spectra at high (right panel) and low (left panel) temperature.
It is rather surprising that the different methods yield almost identical results concerning the FR splitting, even though they displayed significant differences in the overtone intensity. This seems to indicate that position-momentum correlations, although determinant in the overtone and in the combination bands intensities, plays only a minor role in the amplitude of the FR splitting. Indeed, combining a sampling that well captures the ZPE in each mode, with a classical dynamics, seems to be enough to describe the FR splitting accurately.

Consistently with this observation, the QTB method also yields rather satisfactory results for the FR splitting that is only slightly overestimated (fig. 5.7, center). This effect arises from the significant ZPEL occurring in this system, which results in a too small intensity of the Fermi dyad at low temperature (left panel of fig. 5.7) and an overestimation of the low-frequency mode intensity (not shown). This error is efficiently corrected in the adaptive QTB simulations which yield a splitting in almost perfect agreement with the exact quantum results.

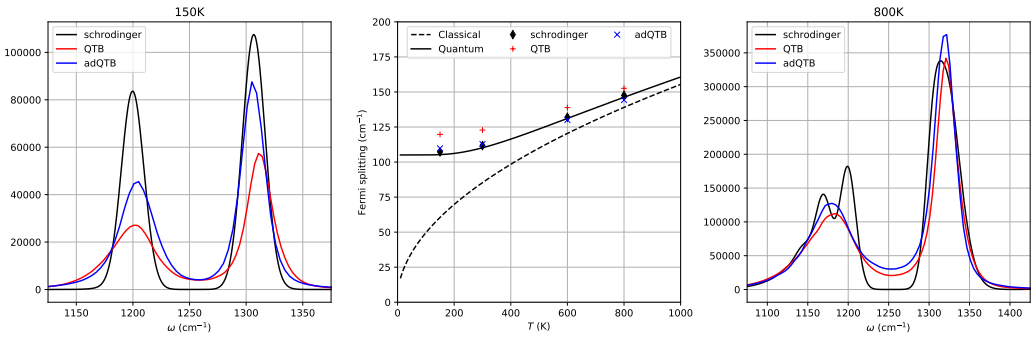

Fig. 5.7.: Center panel: Fermi splitting as a function of temperature approximated with QTB and adQTB. Left and right panels: Kubo-transformed momentum autocorrelation spectrum at 150K (left) and 800K (right) in the region of the Fermi dyad for the QTB and adQTB, compared to the exact results.

5.4 Gas-phase water

To conclude this chapter, we move one step up in complexity, and closer to realistic models for physical systems, and compare the performance of the various methods on the simulation of the IR spectrum of a water molecule in gas-phase. We model the interactions using the accurate potential energy surface due to Partridge and Schwenke (see ref. [118]). This system is of particular interest for our study since the coupling between the bending and stretching modes of the molecule naturally gives rise to overtones and combination bands in the vibration spectrum. Furthermore, at room temperature, the quantum ZPE of these high-frequency modes strongly dominates over their thermal energy $k_B T$. This corresponds to a quantum regime in which, according to the analysis in the previous sections, we expect the various trajectory-based methods to perform very differently. This system has already been considered for a similar analyis: in ref. [59], Benson *et al.* numerically compared the IR absorption spectra obtained for this model using PI-based methods (TRPMD, CMD and the most recent QCMD), LSC-LGA and a quasi-exact wavefunction-based resolution (using the DVR [119]). They pointed out interesting effects concerning overtones and combination bands. They showed that the PI approaches do not reproduce the correct amplitudes of these anharmonic resonances while the LSC-LGA is in much better agreement with the quasi-exact reference (although with broadened spectral lineshapes). These findings are consistent with our analytical perturbative results and gives hope that they remain correct, at least qualitatively, for more complex systems. In this section, we explore the performance of the LSC-ECMA and the adQTB with the double goal of investigating how they perform on this more

challenging system, and of extending the set of methods considered by Benson *et al*.

As in ref. [59], we compute the Kubo-transformed dipole-derivative autocorrelation spectrum $K_{\dot{\mu}\dot{\mu}}(\omega)$ which is proportional to the infrared spectrum of the molecule. However, contrary to ref. [59] we compute the spectrum using the qTIP4p-f linear dipole moment [120] instead of the non-linear Partridge-Schwenke dipole moment [121]. In the linear case, the real part of the standard dipole-derivative ATCF can be expressed exactly as:

$$C_{\dot{\mu}\dot{\mu}} = \int \mathrm{d}q\mathrm{d}p \; \rho_{\mathrm{w}}(q,p) \; \dot{\mu} \; e^{i\mathcal{L}_Q t}\dot{\mu} \tag{5.101}$$

while a similar expression would introduce an approximation for a non-linear dipole moment which would directly impact the LSC-IVR results.

The calculations were performed at 300K and we used 64 beads for all PI calculations (including the open-chain auxiliary calculation of ECMA). For both LSC-ECMA and LSC-LGA, we used the same parameters as in ref. [59], *i.e.* we sampled 10^5 initial positions using thermostatted PIMD and for each position we sampled 5 momenta from the LGA and ECMA conditional momentum distribution. We then propagated classical trajectories of 1 ps (with a time step of 0.125 fs) to compute the TCF. For each sampled configuration, the EW0-QCF of eq. (4.68) was computed using 8 independent auxiliary path-integral Langevin simulations of 500 fs each and the effect of statistical noise on the momentum distribution was corrected using the scheme described in appendix B.

For the adQTB simulations, the adaptation of $\gamma_r(\omega)$ was done separately for the different species H and O. More precisely, Δ_{FDT} was averaged on the three directions (and the two atoms for H) to obtain $\Delta_{\mathrm{FDT,H}}$ and $\Delta_{\mathrm{FDT,O}}$. We then adjusted $\gamma_{r,H}(\omega)$ and $\gamma_{r,O}(\omega)$ over 100 ns of adQTB simulation in order to nullify both Δ_{FDT}. We intentionally ran a very long adaptation period to make sure that the γ_r coefficients were fully converged, in particular at the resonance frequencies[4]. We then computed the IR spectra over a trajectory of 10 ns and used the deconvolution procedure of ref. [62] to reduce the effect of the thermostat on the spectrum. Figure. 5.8 shows the kinetic energy spectrum for each species computed via adQTB (top panel) and the final sets of γ_r (bottom panel). We can see that only limited adjustments of γ_r were necessary to compensate the ZPEL in the region of the main vibrational peaks (from 0 to 4000 cm^{-1}). Note that $\gamma_{r,H}$ requires more adjustments than $\gamma_{r,O}$ which only deviates significantly from γ close to the stretching peak. We observe more

[4]We used a particularly slow adaptation, in order to reduce the statistical noise on the γ_r coefficients but faster convergence could be obtained with a more optimized set-up.

significant variations in the region of the overtone of the stretching peak at around 7000 cm^{-1}. Consistently with the analysis on the Morse potential in section 3.3, the FDT criterion detects that this resonance lacks intensity and γ_r increases strongly to compensate it.

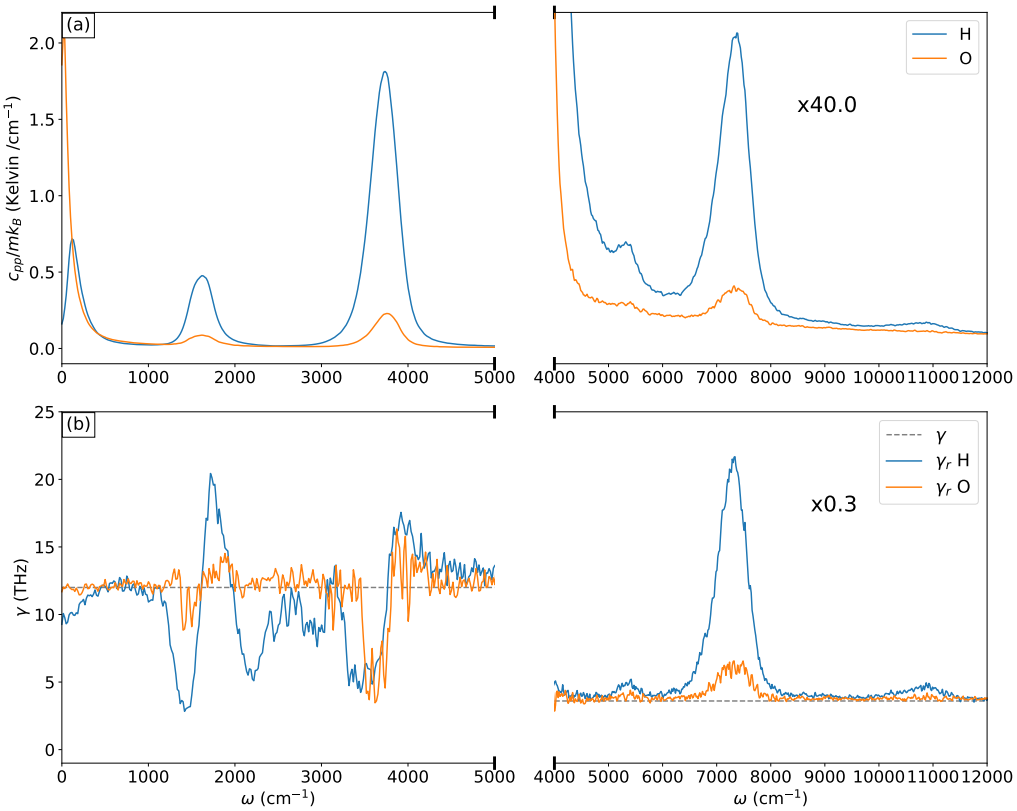

Fig. 5.8.: Top panel: kinetic energy spectrum of H and O for gas-phase water computed using adQTB. Bottom panel: adjusted γ_r for H and O.

The top panel Figure 5.9 shows the three main peaks of the IR absorption spectrum simulated using classical MD (dashed grey), TRPMD (solid blue), adQTB (dashed yellow), LSC-LGA (dotted blue) and LSC-ECMA at order EW0 (dotted dashed red) and EW4 (dotted dashed green). The spectra are also compared to the numerically exact DVR results (filled curve). Note that the lineshape of the DVR spectrum has been artificially broadened for visualization purposes (by damping the TCF with a Hann window of length 750 fs, consistently with ref. [59]). All approximate quantum methods yield similar results in this spectral region and agree reasonably well with the DVR spectrum, although none of the methods is able to capture the fine structure of the stretching band ($\approx 3700 cm^{-1}$). A closer inspection of the rotational feature ($\approx 300 cm^{-1}$) shows that the LSC-ECMA0, yields a slightly broader, more

intense peak. The EW4 correction decreases its intensity towards the correct result. It is interesting that the Edgeworth correction has a more pronounced effect on the low-frequency rotation region than on the higher-frequency modes. This effect is counter-intuitive since these modes are more "quantum" in the sense that their ZPE is very large compared to that of the, supposedly classical, rotational motion. It would therefore be interesting to investigate in further works on what conditions such low-frequency effects of the EW4 correction might appear, and whether it is a particularity of free-rotating molecules. The LSC-LGA spectrum is very similar to LSC-ECMA, except that the rotational peak is slightly smaller (and close to the correct result), at the condition that the free rotation modes are treated classically (*i.e.* the three eigenvalues of the local frequency corresponding to free rotations are set to zero, see ref. [59]).

The bottom panel of Figure 5.9 shows the anharmonic resonances that appear in the high-frequency region of the spectrum (from 4500cm^{-1} to 8500cm^{-1}). They consist in two main features around 5100-5500cm^{-1} (sum of the bending and stretching frequencies, which we will label as combination band) and 7000-7400cm^{-1} (twice the stretching frequency, which we will label as overtone). Consistently with the perturbative analysis, TRPMD strongly underestimates these resonances, with intensities comparable to the classical results (although an accurate estimation of the combination band intensity is difficult due to the strong broadening of the stretching peak). LSC-IVR and adQTB methods, on the other hand, yield more intense peaks, closer to the exact result (though with broader lineshapes) and satisfactory agreement with the perturbative results for combination bands. Indeed, despite this strong anharmonicity, the adaptive QTB only slightly underestimates the combination band ($\sim -5\%$, although difficult to estimate accurately due to the broadening of the stretching peak) and is able to accurately capture the overtone intensity (less than 1% discrepancy). For LSC-LGA, both resonances intensities are overestimated by approximately 40%. The LSC-ECMA0 slightly underestimates the combination band ($\sim -7\%$) and underestimates more significantly the overtone ($\sim -25\%$). Contrary to the perturbative case, the Edgeworth correction plays an important role in this more anharmonic case: weighting the samples with the first term in the Edgeworth correction (ECMA4) increases the resonance intensities which are both slightly overestimated ($\sim 10\%$). The inclusion of higher orders of the Edgeworth correction, although more computationally demanding, might further improve the results and their effect should be investigated in more details in future work. This impact of the Edgeworth correction is a strong signal that the perturbative approach does not hold quantitatively for this very anharmonic potential.

To further investigate this point, we also computed separately the spectrum of the unidimensional Morse potential used in this model for the O-H stretching to check if the perturbative results remain quantitatively valid for the overtone in this case. Indeed, the LSC-LGA overestimates the overtone intensity by approximately 23%, which is in good agreement with the $\sim$25% overestimation predicted in the perturbative model of section 5.1. The LSC-ECMA0 overestimates this intensity by roughly 7% but the EW4 correction brings this relative error close to 1%. This effect of the EW4 correction is interesting since it is absent of the perturbative models, however, it is less significant than in the water molecule and has the opposite effect, *i.e.* it tends to decrease the overtone intensity of the Morse potential while it increases the anharmonic resonances of the water molecule. The influence of the EW4 correction on the IR spectrum of the water molecule is therefore subtle: it originates from the interactions between the different modes and should be investigated in more details in future work.

In summary, the analysis of the anharmonic resonances of this realistic system generally confirms the perturbative results derived for the model potentials of the previous sections. In particular the strong differences in intensity between TRPMD (and the other PI-based methods) on the one hand, and LSC-IVR and adQTB on the other hand are also present in the more complex case of the water molecule. The anharmonic interplay between the different modes is however more complex than in the simple combination bands model that we investigated in section 5.2 so that the predictions of the perturbative analysis for the different LSC-IVR variants do not apply quantitatively. In particular, the effect of the Edgeworth correction on the LSC-ECMA spectrum needs to be further investigated. Future works could shed light on the origin of these differences by considering a more complete perturbative model that would include all the internal modes of the water molecule: the bending, symmetric and antisymmetric stretching modes and their interactions.

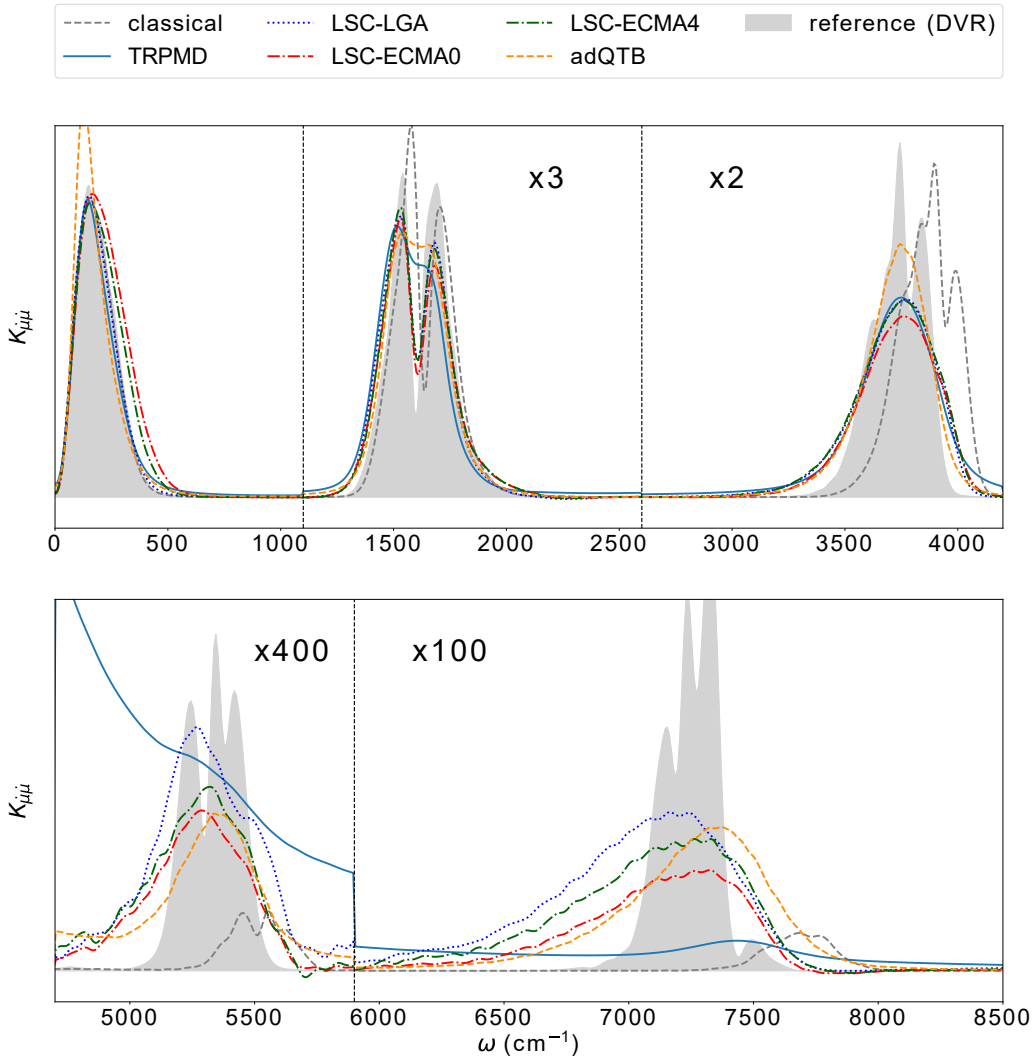

Fig. 5.9.: IR absorption spectrum for gas-phase water (Partridge-Schwenke potential energy and qTIP4P-f linear dipole moment) at 300K approximated using TRPMD (solid blue), adQTB (dashed yellow), LSC-LGA (dotted blue), LSC-ECMA0 (dotted-dashed red) and LSC-ECMA4 (dotted-dashed green) compared to the classical spectrum (dashed grey) and the DVR quantum reference (filled grey). The effect of the coupling with the thermostat in the adQTB spectrum has been deconvoluted using the procedure described in ref. [62]. Arbitrary units are used for the peak intensities.

6 Simulating condensed-phase water using the adaptive QTB

Condensed-phase water, and in particular liquid water, is ubiquitous in systems of chemical and biological interest. Its many structures are complex, in particular due to the intricate network of hydrogen bonds [122, 123], and its properties are strongly affected by NQEs, even at room temperature [7]. Liquid water is also the most common solvent for chemical reactions and its accurate theoretical description – and simulation – is thus crucial, although very challenging. Assessing the performance of approximate methods for nuclear quantum dynamics on condensed-phase water is therefore an active and important area of research (see for example refs. [59, 81, 120, 124]).

Condensed-phase water is a particularly interesting system also for the analysis developed in this work, and particularly in chapter 5, since the anharmonic atomic interactions give rise to multiple anharmonic resonances and combination bands. The Wigner-Langevin dynamics presented in section 4.2 is too computationally expensive in its current implementation and further work on the algorithm is necessary to apply it to condensed-phase systems. On the other hand, the LSC-ECMA presented in section 4.3 is more efficient and its application to liquid-phase water is currently under study and will be presented in future works.

In view of its novelty and computational convenience, we investigate in this section the performance of the adQTB for simulating liquid water at 300K and hexagonal ice at 150K. These two systems are very anharmonic and pose a serious challenge to the method. Indeed, interactions between water molecules involve modes of very different frequencies, which leads to massive ZPEL, as was already shown in LSC-IVR simulations [59, 76] and in the quantum thermostat framework [92]. In particular, the low-frequency inter-molecular vibrations pick up large amounts of ZPE from the high-frequency intra-molecular modes, leading to an increase of their effective temperature and causing a destructuration of the liquid and even melting of the ice as shown in ref. [59].

In the following, we show that, using the FDT criterion and the adaptation procedure presented in section 3.3, we can correct the ZPEL in QTB simulations and recover

133

accurate results for static properties and IR spectra that are similar to the LSC-LGA results of ref. [59].

For both solid and liquid phases, we use the q-TIP4P/F potential energy surface [120]. This is a flexible water model, parametrized to reproduce experimental data when simulated with path integrals. This potential is commonly used to benchmark methods for nuclear quantum dynamics [59] since it is cheap and realistic enough to indicate how the different methods would perform on more accurate models.

As in section 5.4, we follow ref. [59] and compare the IR spectra (given by the dipole-derivative Kubo-transformed spectrum) obtained in adQTB and TRPMD simulations. The dipole-moment derivative for the q-TIP4P/F model is linear and given by:

$$\dot{\mu} = \sum_{i=1}^{N_{\text{mol}}} \left(q_{\text{O}} v_{\text{O,i}} + q_{\text{H}} (v_{\text{H1,i}} + v_{\text{H2,i}}) \right) \tag{6.1}$$

with N_{mol} the number of water molecules, $q_{\text{O}} = -0.8192e$ and $q_{\text{H}} = 0.4096e$ the effective charges fixed on the Oxygen and Hydrogen nuclei respectively and $v_{\text{O,i}}$, $v_{\text{H1,i}}$ and $v_{\text{H2,i}}$ the velocities of the Oxygen and the two Hydrogen nuclei of molecule i, respectively.

All the simulations were performed using the Tinker-HP package [17] in which we implemented the adQTB and TRPMD methods, in collaboration with N. Mauger, PhD student co-supervized by J.P. Piquemal, S. Huppert and L. Lagardère at the *Laboratoire de Chimie Théorique* at Sorbonne Université.

6.1 Liquid phase

Liquid-phase water simulations were performed at 300K, using 32 beads for the PI calculations (consistently with ref. [59]). The QTB and adQTB simulations were performed using a friction coefficient $\gamma = 16$ THz. This friction coefficient is large enough to allow for a complete compensation of the ZPEL in adQTB but small enough so that the effect of the thermostat on the spectra can be efficiently corrected using the deconvolution procedure of ref. [62]. The cubic simulation box of length 31.1 Å contains 1000 water molecules, resulting in a density of 994.5 kg.m^{-3}. We used 70ps of TRPMD simulation and 700ps of adQTB simulation (after adaptation of the γ_r coefficients) to produce the results of this section.

As for the gas phase in section 5.4, we slowly adapted the γ_r coefficients of the adQTB separately for the Oxygen an Hydrogen atoms over 1 ns of simulation (this

adaptation time could be drastically reduced – at least by a factor 10 – by using a more agressive adaptation procedure). The top panel of figure 6.1 shows the Δ_{FDT} for each species obtained with a standard QTB simulation and an adQTB simulation with the adapted γ_r shown in the bottom panel of figure 6.1. We can see that the adaptation procedure is able to completely nullify Δ_{FDT} (within small fluctuations which are not visible at this scale). Since ZPEL is more important in the liquid-phase than in the gas-phase – due to the anharmonic coupling between the high-frequency intra-molecular modes and the low-frequency inter-molecular vibrations –, larger adjustments of the γ_r are necessary, in particular for the low-frequency part of the Hydrogen spectrum. The lack of energy in the stretching overtone, on the other hand, is compensated in part by a small increase of $\gamma_{r,H}$ at the stretching frequency ($\sim$ 3500 cm^{-1}), and more importantly by the large increase of γ_r in the overtone region ($\sim$7000 cm^{-1}).

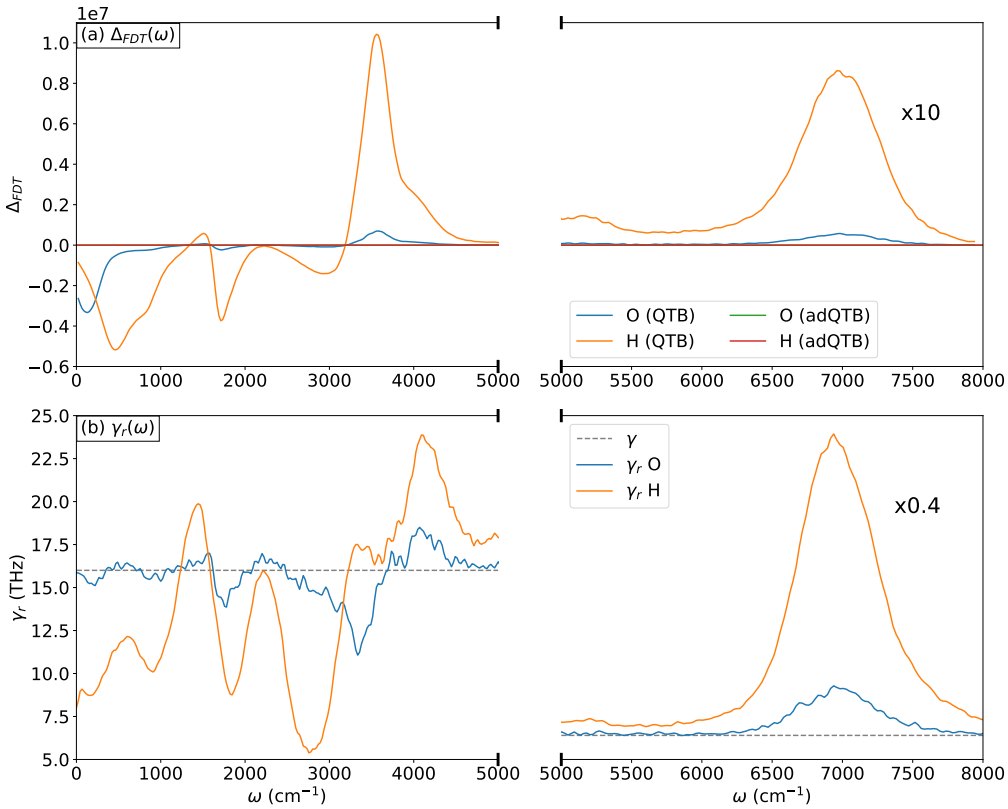

Fig. 6.1.: Top panel: $\Delta_{\text{FDT,H}}$ and $\Delta_{\text{FDT,O}}$ for liquid-phase water computed using QTB and adQTB. Bottom panel: adjusted γ_r for H and O.

The correction of the ZPEL greatly improves the description of the structural properties of water in the adQTB simulations. For example, figure 6.2 shows the radial

distribution functions (RDFs) between each pair of species. Panel (a) shows the OO RDF which describes the inter-molecular structure of the liquid. Due to competing NQEs [7], this quantity is similar for classical MD and PIMD, with only a slight broadening in the quantum case. The standard QTB, however, displays a very broadened RDF, indicating that the ZPEL completely destructures the liquid. Finally, the adQTB results are very close to the PIMD, with only a slight broadening. Thus, the compensation of the ZPEL allows to correctly recover the structure of liquid water.

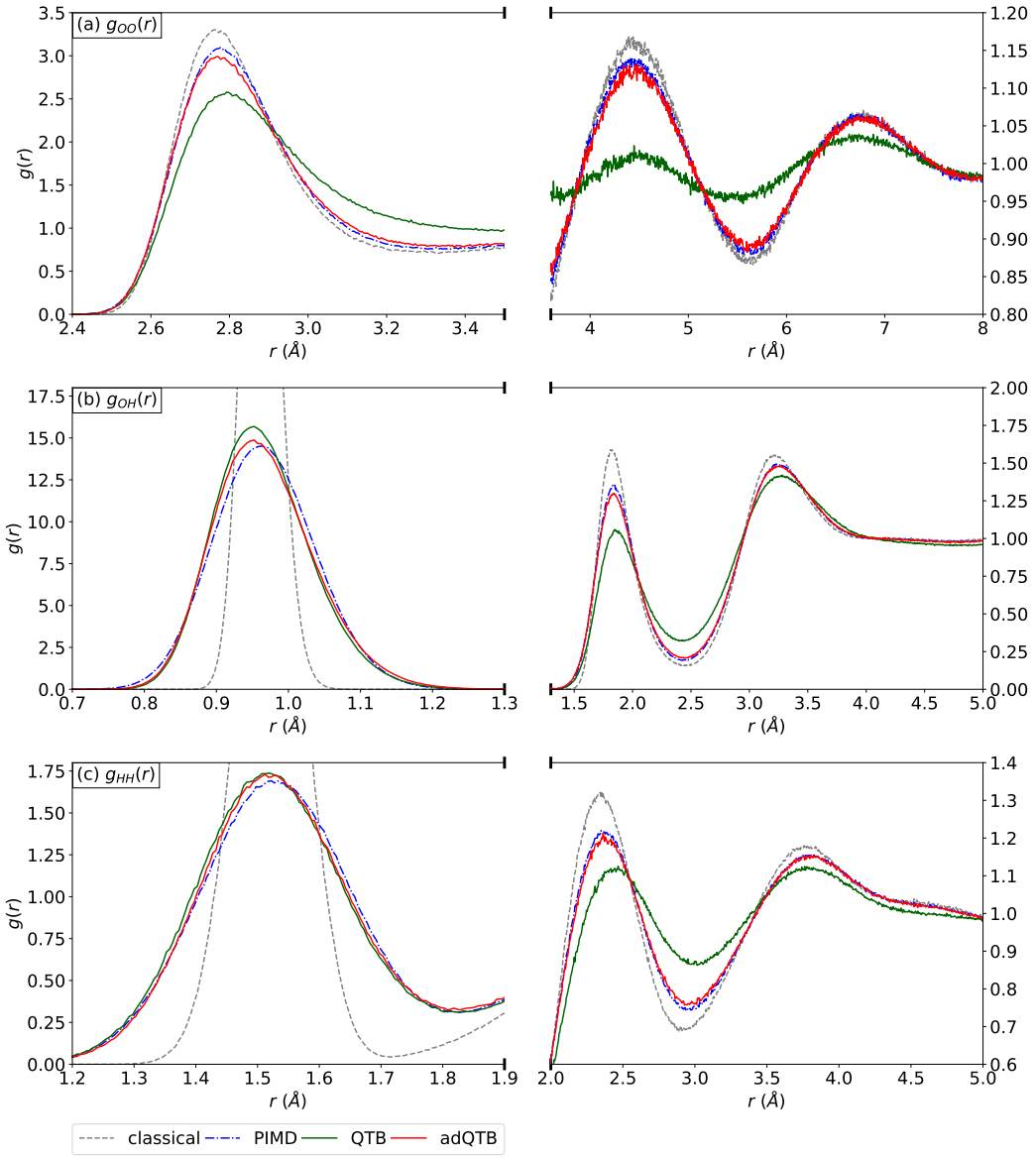

Fig. 6.2.: Radial distribution functions of liquid-phase water at 300K obtained with classical MD (dashed grey), PIMD (dotted-dashed blue), QTB (solid green) and adQTB (solid red). Panel (a): OO. Panel (b): OH. Panel (c): HH.

Nuclear quantum effects have a larger impact on the OH and HH RDFs, in particular for the intra-molecular peak which is much narrower in classical MD than in PIMD. The QTB and adQTB capture this effect very well, with only slightly narrower peaks than the PI results, in particular for the standard QTB (due to ZPEL). We note that the maximum of probability in the OH distribution of QTB and adQTB is slightly shifted with respect to the PIMD reference. This effect is reminiscent of that observed for the unidimensional Morse potential of section 3.3 and it is an intrinsic limitation of (ad)QTB simulations that cannot recover the exact probability distribution in such an anharmonic potential energy landscape. The inter-molecular part of the OH and HH RDFs are very broadened in the standard QTB simulations while they are close to the PI result for the adQTB, indicating again that the adaptation scheme successfully corrected the ZPEL.

We now move on to the analysis of the dynamical properties. Figure 6.3 shows the IR spectra obtained using classical MD, TRPMD and adQTB. We refer to ref. [59] for the comparison with CMD, QCMD and LSC-LGA. The overall performance of adQTB is very satisfactory. First, we see that the position of the stretching peak obtained with adQTB (center panel of fig. 6.3) coincides with the TRPMD result, but with a narrower lineshape. The low-frequency part of the adQTB spectrum is slightly broadened compared to TRPMD and is very similar to the LSC-LGA spectrum presented in ref. [59]. Here we use the deconvolution procedure of ref. [62] to minimize the effect of the coupling with the adQTB thermostat (Figure 6.4 shows the effect of the deconvolution on the adQTB spectrum). This procedure is not fully reliable at low frequencies ($\omega \lesssim \gamma$) and causes an unphysical increase of the IR intensity towards zero-frequency. Finally, consistently with the observations of the previous chapters, the adQTB predicts a much larger intensity of the stretching overtone (right panel of fig. 6.3) than TRPMD (which yields a similar intensity as classical MD). This agrees with the LSC-LGA results of ref. [59] and, although no exact reference is available for this system, we expect this more intense resonance to be a more accurate description of the overtone.

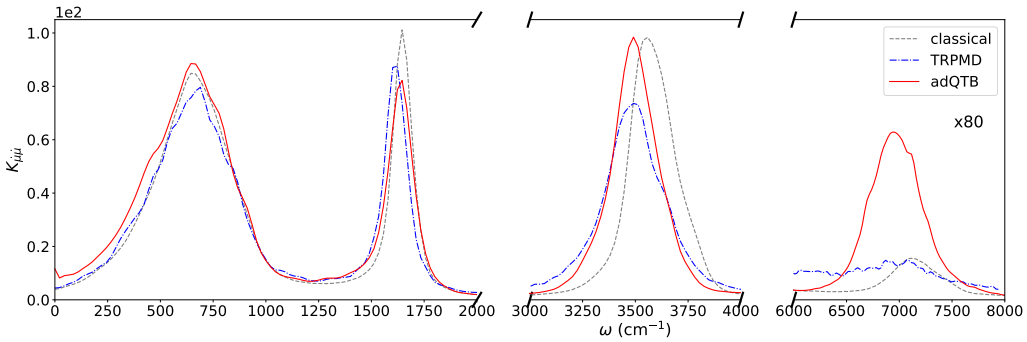

Fig. 6.3.: IR absorption spectrum of liquid-phase water at 300K approximated using TRPMD (dotted-dashed blue) and adQTB (solid red) compared to the classical spectrum (dashed grey). The effect of the coupling with the thermostat in the adQTB spectrum has been deconvoluted using the procedure described in ref. [62].

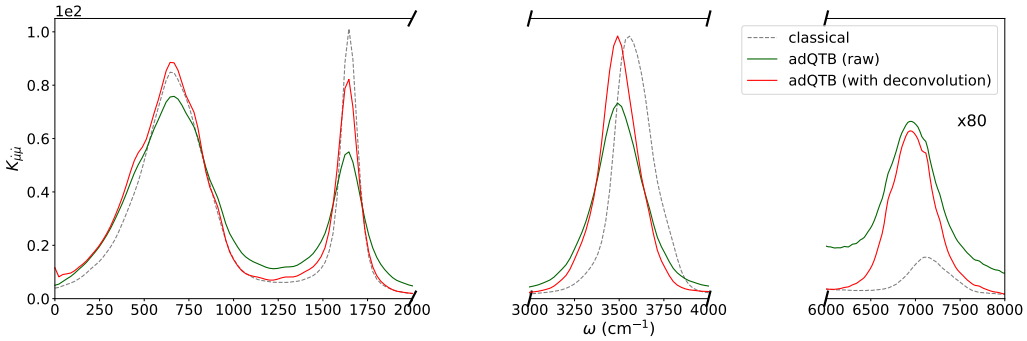

Fig. 6.4.: Effect of the deconvolution procedure (ref. [62]) on the IR absorption spectrum of liquid-phase water at 300K simulated using adQTB with a friction coefficient $\gamma = 16$ THz.

6.2 Solid phase

We performed simulations of ice at 150K starting from an ordered ice XI configuration, using 64 beads for the PI calculations (consistently with ref. [59]). The QTB and adQTB simulations were performed using a friction coefficient $\gamma = 12$ THz. The simulation box of size $35.45 \times 31.09 \times 29.08$ Å^3 contains 1024 water molecules, resulting in a density of 955.7 kg.m^{-3}. We used 70ps of TRPMD simulation and 700ps of adQTB simulation (after adaptation of the γ_r coefficients) to produce the results of this section.

Zero-point energy leakage has a massive impact on the structure of ice, making it a very challenging system for LSC-IVR or QTB simulations. Indeed, ref. [59]

showed that in LSC-IVR, the ice melts and completely loses its crystal structure within one picosecond of evolution. The mechanism is similar to that occurring in liquid water: low-frequency phonons pick up a large amount of ZPE from the high-frequency intra-molecular bending and stretching modes, which destabilizes the structure and makes the ice melt. Figure 6.5 shows the OO RDF calculated at different times during a standard QTB simulation. We can see that the first RDF is only slightly broader than the PIMD reference and that the structure is gradually lost within a few hundreds of picoseconds. We note that the melting time is longer in QTB compared to LSC-IVR because of the coupling to the thermal bath which continuously tries to impose the quantum energy distribution but fails due to large ZPEL. The equilibrium structural properties of ice computed with the standard QTB are therefore not reliable.

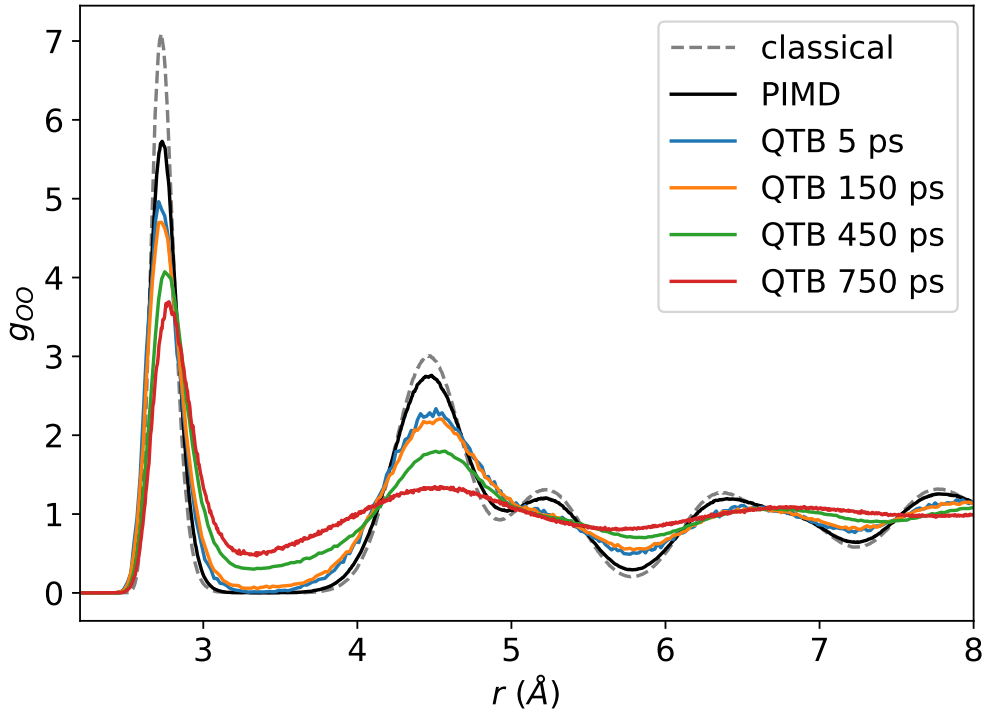

Fig. 6.5.: Oxygen-Oxygen Radial distribution function of ice at 150K computed at different times of a standard QTB simulation starting from an ordered Ice XI configuration. The results are compared to the equilibrium classical RDF (dashed grey) and the path integrals RDF (solid black)

As in the previous section, we adapted the γ_r of the adQTB separately for the Hydrogen and Oxygen atoms over 1 ns of simulation. The adaptation procedure was fast enough so that the ZPEL was compensated before the crystal structure was lost.

The final γ_r coefficients (not shown) are quite similar to those obtained for the liquid phase. Figure 6.6 shows the different equilibrium RDFs computed using adQTB, PIMD and classical MD. We can see for all RDFs that the adQTB reproduces well the structure of ice and is in good agreement with the PI results, with only slight shifts of the intra-molecular peaks. The adaptation procedure thus successfully prevents the adQTB-simulated ice from melting and allows recovering accurate structural properties.

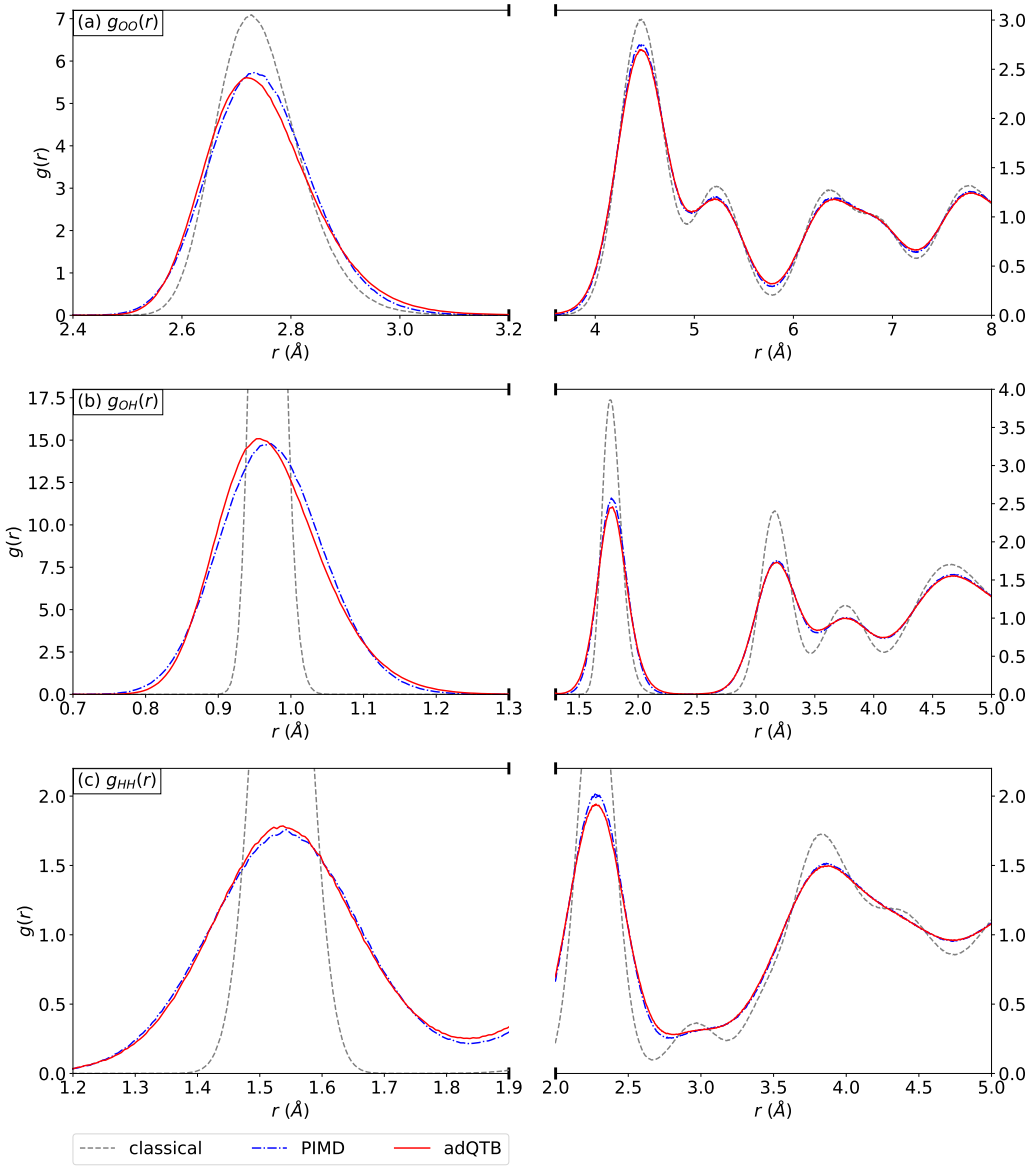

Fig. 6.6.: Radial distribution functions of solid-phase water at 150K obtained with classical MD (dashed grey), PIMD (dotted-dashed blue) and adQTB (solid red). Panel (a): OO. Panel (b): OH. Panel (c): HH.

Finally, figure 6.7 shows the IR spectra of ice at 150K simulated with classical MD, TRPMD and adQTB. Note that the classical and TRPMD spectra are different from ref. [59], indicating differences in the system under consideration (probably in the simulation-box shape and/or the ice structure, with ordered ice XI in our case) so that a direct comparison is not possible. Using the TRPMD and classical spectra as reference, we note the same trends as in the liquid phase. Indeed, the adQTB result is very close to the TRPMD for the stretching peak (with a slighlty narrower lineshape) and yields slightly broader and more intense peaks at low frequencies. The overtone of the stretching mode is again more intense in adQTB than in TRPMD and classical MD. These trends are similar to what is reported for LSC-LGA in ref. [59], which is consistent with the previous observations concerning the proximity of the two methods.

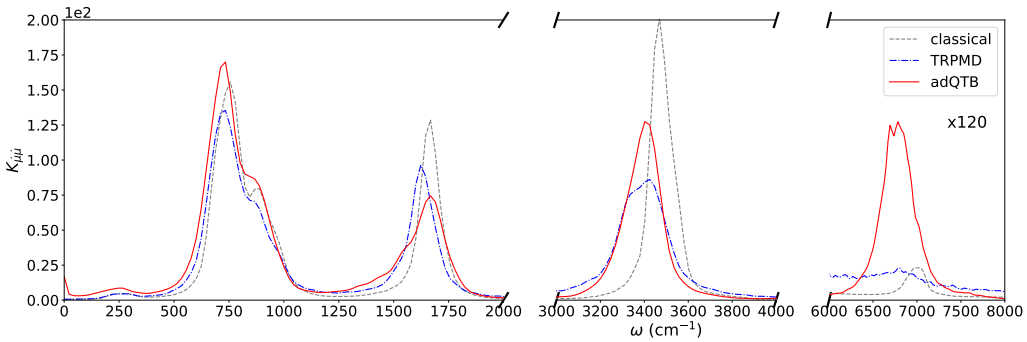

Fig. 6.7.: IR absorption spectrum of solid-phase water at 150K approximated using TRPMD (dotted-dashed blue) and adQTB (dashed red), compared to the classical spectrum (dashed grey). The effect of the coupling with the thermostat in the adQTB spectrum has been deconvoluted using the procedure described in ref. [62].

In summary, we showed in this chapter that the adQTB scheme proposed in ref. [58] and described in section 3.3 provides very significant improvements over the standard QTB for computing properties of condensed-phase water. Indeed, ZPEL has a massive impact on the properties of water obtained in standard QTB simulations, especially in the solid phase for which the crystal structure is completely lost. The adQTB allows to recover distributions that are in strikingly close agreement with the path-integrals distributions, even for the ice at 150K. We also showed that the adQTB performs similarly to more conventional trajectory-based methods for computing the IR spectra of water and we underlined the close resemblance with the LSC-IVR results reported in ref. [59]. In particular, the intensity of the stretching overtone obtained with the adQTB is similar to the LSC-IVR one and much more intense than the TRPMD which is perfectly consistent with the analysis of chapter 5. The good performance of the adQTB for both static and dynamical properties should be

confirmed by further studies on different systems and its computational cost should be assessed more systematically in comparison to other methods. Still, the results presented in this work provide promising indications in favor of its use as a low-cost but accurate simulation method for NQEs.

7 Conclusion

In this thesis, we explored and compared different trajectory-based methods for nuclear quantum dynamics, proposing two original approaches and focusing on the calculation of approximate quantum time correlation functions at thermal equilibrium. This broad family of methods allows to model mildly quantum particles, such as light atomic nuclei in most conditions of temperature and pressure, in a computationally efficient way. Methods based on generalized classical trajectories cannot capture highly quantum effects, such as deep tunnelling or quantum coherence, but they provide good approximations of zero-point energy (ZPE) effects, which are often the main quantum contributions for large condensed phase systems in which decoherence is generally very fast.

In chapter 3, we reviewed some of the most well-established trajectory-based methods, namely RPMD, CMD and LSC-IVR, as well as more recent ones that bring new perspectives into the field from a theoretical or practical viewpoint: Matsubara dynamics and the adaptive Quantum Thermal Bath. The adQTB, in particular, is a relatively recent addition to the set of approximate methods and, so far, it had not been thoroughly investigated with regards to its ability to capture time-dependent properties. Although the use of the adQTB dynamics cannot be rigorously justified, it is considerably cheaper than most alternatives. This motivates the investigation of its performances, in particular in view of combining it with first-principles forces. The results presented here, that illustrate a somewhat surprising competitiveness of this approach, are the first attempt to do so, to the best of our knowledge. We used the unidimensional Morse potential as a common benchmark to thoroughly compare the methods. This comparison highlighted some important differences in the treatment of anharmonic resonances (in this case, the overtone). In particular, we pointed out that RPMD and CMD strongly underestimate the intensity of the overtone whereas the QTB only slightly underestimates it. We also showed that the fluctuation-dissipation criterion, initially designed to correct zero-point energy leakage (ZPEL) in QTB simulations, is also able to detect and quantify this inaccuracy. Finally, we found that in LSC-IVR, the choice of the approximation to the initial Wigner distribution largely influences the overtone intensity. As discussed also below, this observation might be of some value to assess the relative merits of different

143

LSC-IVRs, that differ mainly in the choice of the approximate scheme for sampling the Wigner thermal density.

In chapter 4, we presented a new approach to perform such sampling that generalizes and makes more flexible the recently introduced Phase Integration Method [52]. We used the so-called Edgeworth expansion to obtain an accurate approximation of the Wigner thermal density which is not subject to the oscillating sign problem. The new approximation has two important features. Firstly, it provides an optimal – in the sense of the Edgeworth expansion – Gaussian approximation to the momentum distribution. Secondly, the quality of the approximation can be systematically checked via a correction term that allows, in principle, to recover the negative parts of the Wigner density. These two features constitute an important conceptual advantage over the more common approaches that often rely on various harmonic approximations, as the LGA or FK-LPI. We designed an efficient sampling method, the Edgeworth Conditional Momentum Approximation (ECMA) and showed on the Morse and quartic potentials that it captures the quantum features of the distribution much better than the other methods that we considered here. In particular, position-momentum correlations are very well reproduced by our zero-order Gaussian approximation and nearly perfectly match the exact results when including the first terms of the Edgeworth correction. This new sampling scheme is of relevance also when computing time correlation functions in the LSC-IVR framework. In fact, we also showed, by comparing LSC-IVR spectra obtained with ECMA, LGA and FK-LPI, that position-momentum correlation is of particular importance to correctly reproduce the overtone intensity of the Morse potential.

We also introduced an original generalized stochastic propagation, the Wigner-Langevin Dynamics (WiLD), that rigorously samples the new zero-order Edgeworth approximation to the Wigner density. The conservation of the quantum distribution is a very attractive feature for an approximate quantum dynamics that the WiLD shares with RPMD and CMD and that LSC-IVR lacks. Motivated by the RPMD and CMD approaches, we investigated the performance of WiLD for computing TCFs. We showed that the WiLD yields the exact dynamical properties for the harmonic potential as well as in the classical limit and that it performs well for the very anharmonic Morse and quartic potentials. In particular, it is able to satisfactorily reproduce the overtone intensities. The numerical cost of the WiLD is considerably higher than that of its counterparts, but this scheme has provided a number of useful insights paving the way for the comparisons presented in chapter 5.

The family of trajectory-based schemes features a variety of methods with different levels of complexity and numerical cost. However, the community lacks quantitative

arguments to distinguish their accuracy. Indeed, all the methods presented in this work are exact in the harmonic case but yield very different results for anharmonic potentials and none of them particularly stand out as more accurate in every case and for all of the relevant spectral features. This observation motivated the quantitative comparison that we presented in chapter 5 through analytic calculations and numerical simulations. We focused on overtones and combination bands as simple, quantifiable, anharmonic effects that appear in the vibrational spectra when adding a small anharmonic perturbation to a harmonic potential. Our analytical results, obtained via the perturbation theory, allow to assess the accuracy of the different approximations, in particular at low temperatures. They confirm that RPMD and CMD are not able to model anharmonic resonance effects correctly, yielding identical results as classical MD. By applying the perturbative approach to Matsubara dynamics, we showed that it correctly predicts the intensities of these resonances and we used this analysis to shed some light on the origin of the inaccuracies of CMD and RPMD. We also showed that, in the perturbative regime, the classical dynamics involved in the LSC-IVR approximation is not responsible for the inaccuracies of the method. Indeed, we demonstrated that an accurate description of the initial Wigner distribution, and in particular of the position-momentum correlations, is critical to correctly capture the anharmonic features. For the perturbative models that we presented, the Edgeworth approximation provides, at first order in perturbation, the exact Wigner distribution so that LSC-ECMA yields the correct resonance intensities. We also noted that the QTB tends to underestimate the intensity of the resonances (probably due to the absence of position-momentum correlations). Surprisingly, the fluctuation-dissipation criterion, that was introduced to quantify the ZPEL, is also able to detect and quantitatively measure the inaccuracies of the QTB concerning the intensity of these resonances. This motivates further exploration of the adQTB as a method for quantum dynamics simulations.

We explored the generalizability of our results and compared the different methods on the more realistic case of gas-phase water. The results on this system follow the main trends that we derived from the perturbative analysis: RPMD and CMD (and even its more accurate variant QCMD [59]) do not correctly reproduce the combination bands in the spectrum of water. We also confirmed that the LSC-IVR approach is able to better reproduce these resonances. However, the distinction between the different methods for the sampling of the initial Wigner density appears to be subtle. We applied the LSC-ECMA to compute the IR spectrum of the water molecule and found that the results are close to LSC-LGA, but interestingly, the Edgeworth correction seems to influence the intensities of the combination bands of water, which is not the case in the perturbative regime. It might be interesting

to explore further the details of this correction and of the negative parts of the Wigner distribution it may produce, and their effect on vibrational spectra. Finally, we showed that the adaptive QTB is able to effectively compensate for the ZPEL in the water molecule and yields a IR spectrum that is very close to that of the LSC-IVR approach, even at the combination bands frequencies. These very encouraging results motivated the study of liquid and solid-phase water of chapter 6.

Multiple aspects should be considered concerning the perspectives of this work. On the one hand, the new approximation that we introduced for sampling the Wigner density has proved to be more accurate than the most commonly used alternatives. This improved accuracy, however, comes with an increased computational cost. We expect that ECMA could be applied to similar systems as LGA and FK-LPI with a manageable numerical overhead. In contrast, the WiLD in its current form is significantly more expansive and further improvements of the algorithm are required in order to tackle larger systems (some were suggested in section 4.2.2). The Edgeworth approximation may also be particularly relevant when combined with more advanced time propagators [125, 126] or in the context of non-adiabatic quantum dynamics [127, 128, 129].
On the other hand, the adQTB proved to be surprisingly accurate, even for very anharmonic systems. Due to its low computational cost, it is thus a very promising candidate for including NQEs in large condensed-phase systems. In this context, we recently implemented the adQTB in the Tinker-HP package [17], in collaboration with the *Laboratoire de Chimie Théorique* at Sorbonne Université, with the aim of exploring its use for the study of systems of biological relevance, modeled with accurate polarizable potentials fitted on first-principles electronic calculations.
Finally, it would be interesting to apply the perturbative approach of chapter 5 to a larger variety of approximate methods and, in particular, to test the performance of the new approximations to Matsubara dynamics proposed in refs. [55, 56] and assess the convergence of the mean-field Matsubara dynamics of ref. [87]. Furthermore, the valuable insights provided by the perturbative models on overtones and combination bands, should motivate a generalization of this approach to other relevant anharmonic effects.

Feasible yet accurate simulations of nuclear quantum dynamics for large condensed-phase systems are still an open issue. In this context, this work aims at giving new analytical and numerical insights on the accuracy of the current methods and at providing information for designing new accurate approximations for treating the nuclear quantum dynamics of highly anharmonic systems.

Bibliography

[1] I. R. Sims, "Tunnelling in space", Nature Chemistry **5**, 734–736 (2013) (cit. on p. 1).

[2] K. M. Hickson, J.-C. Loison, D. Nuñez-Reyes, and R. Méreau, "Quantum tunneling enhancement of the C+ H2O and C+ D2O reactions at low temperature", The Journal of Physical Chemistry Letters **7**, 3641–3646 (2016) (cit. on p. 1).

[3] M. Benoit, D. Marx, and M. Parrinello, "Tunnelling and zero-point motion in high-pressure ice", Nature **392**, 258–261 (1998) (cit. on p. 1).

[4] Y. Bronstein, P. Depondt, F. Finocchi, and A. M. Saitta, "Quantum-driven phase transition in ice described via an efficient Langevin approach", Physical Review B **89**, 214101 (2014) (cit. on pp. 1, 3, 4, 40).

[5] Y. Bronstein, P. Depondt, L. E. Bove, et al., "Quantum versus classical protons in pure and salty ice under pressure", Physical Review B **93**, 024104 (2016) (cit. on pp. 1, 3, 40).

[6] S. D. Ivanov, I. M. Grant, and D. Marx, "Quantum free energy landscapes from ab initio path integral metadynamics: double proton transfer in the formic acid dimer is concerted but not correlated", The Journal of Chemical Physics **143**, 124304 (2015) (cit. on p. 1).

[7] M. Ceriotti, W. Fang, P. G. Kusalik, et al., "Nuclear quantum effects in water and aqueous systems: experiment, theory, and current challenges", Chemical reviews **116**, 7529–7550 (2016) (cit. on pp. 1, 133, 136).

[8] B. S. El'Kin, "Solid NaOH and KOH as superionic proton conductors: conductivity and its isotope effect", Solid State Ionics **37**, 139–148 (1990) (cit. on p. 1).

[9] P. W. Bessonette and M. A. White, "Why is there no low-temperature phase transition in NaOH?", The Journal of chemical physics **110**, 3919–3925 (1999) (cit. on p. 1).

[10] R. G. Snyder and J. A. Ibers, "O–H–O and O–D–O potential energy curves for chromous acid", The Journal of Chemical Physics **36**, 1356–1360 (1962) (cit. on p. 1).

[11] F. S. Bates and G. D. Wignall, "Isotope-induced quantum-phase transitions in the liquid state", Physical Review Letters **57**, 1429 (1986) (cit. on p. 1).

[12] A. Sano-Furukawa, H. Kagi, T. Nagai, et al., "Change in compressibility of δ-AlOOH and δ-AlOOD at high pressure: a study of isotope effect and hydrogen-bond symmetrization", American Mineralogist **94**, 1255–1261 (2009) (cit. on p. 1).

[13] Y. Bronstein, P. Depondt, and F. Finocchi, "Thermal and nuclear quantum effects in the hydrogen bond dynamical symmetrization phase transition of δ-AlOOH", European Journal of Mineralogy **29**, 385–395 (2017) (cit. on p. 1).

[14]G. S. Fanourgakis and S. S. Xantheas, "Development of transferable interaction potentials for water. v. extension of the flexible, polarizable, thole-type model potential (TTM3-F, v. 3.0) to describe the vibrational spectra of water clusters and liquid water", The Journal of chemical physics **128**, 074506 (2008) (cit. on p. 2).

[15]J. W. Ponder, C. Wu, P. Ren, et al., "Current status of the AMOEBA polarizable force field", The journal of physical chemistry B **114**, 2549–2564 (2010) (cit. on p. 2).

[16]M. Devereux, N. Gresh, J.-P. Piquemal, and M. Meuwly, "A supervised fitting approach to force field parametrization with application to the SIBFA polarizable force field", Journal of computational chemistry **35**, 1577–1591 (2014) (cit. on p. 2).

[17]L. Lagardère, L.-H. Jolly, F. Lipparini, et al., "Tinker-HP: a massively parallel molecular dynamics package for multiscale simulations of large complex systems with advanced point dipole polarizable force fields", Chemical science **9**, 956–972 (2018) (cit. on pp. 2, 134, 146).

[18]J. Behler and M. Parrinello, "Generalized neural-network representation of high-dimensional potential-energy surfaces", Physical Review Letters **98** (2007) (cit. on pp. 2, 60).

[19]J. Behler, "First principles neural network potentials for reactive simulations of large molecular and condensed systems", Angewandte Chemie International Edition **56**, 12828–12840 (2017) (cit. on pp. 2, 60).

[20]A. P. Bartók, M. C. Payne, R. Kondor, and G. Csányi, "Gaussian approximation potentials: the accuracy of quantum mechanics, without the electrons", Physical Review Letters **104** (2010) (cit. on pp. 2, 60).

[21]A. P. Bartók, S. De, C. Poelking, et al., "Machine learning unifies the modeling of materials and molecules", Science Advances **3**, e1701816 (2017) (cit. on pp. 2, 60).

[22]J. P. Alborzpour, D. P. Tew, and S. Habershon, "Efficient and accurate evaluation of potential energy matrix elements for quantum dynamics using Gaussian process regression", J. Chem. Phys. **145**, 174112 (2016) (cit. on pp. 2, 60).

[23]T. T. Nguyen, E. Székely, G. Imbalzano, et al., "Comparison of permutationally invariant polynomials, neural networks, and gaussian approximation potentials in representing water interactions through many-body expansions", The Journal of chemical physics **148**, 241725 (2018) (cit. on p. 2).

[24]Y. Litman, J. Behler, and M. Rossi, "Temperature dependence of the vibrational spectrum of porphycene: a qualitative failure of classical-nuclei molecular dynamics", Faraday Discussions **221**, 526–546 (2019) (cit. on pp. 2, 35).

[25]L. Pereyaslavets, I. Kurnikov, G. Kamath, et al., "On the importance of accounting for nuclear quantum effects in ab initio calibrated force fields in biological simulations", Proceedings of the National Academy of Sciences **115**, 8878–8882 (2018) (cit. on p. 2).

[26]R. P. Feynman, A. R. Hibbs, and D. F. Styer, *Quantum mechanics and path integrals* (Courier Corporation, 2010) (cit. on p. 2).

[27]D. Chandler and P. G. Wolynes, "Exploiting the isomorphism between quantum theory and classical statistical mechanics of polyatomic fluids", J. Chem. Phys. **74**, 4078–4095 (1981) (cit. on p. 2).

[28]D. M. Ceperley, "Path integrals in the theory of condensed helium", Rev. Mod. Phys. **67**, 279–355 (1995) (cit. on p. 2).

[29]M. Parrinello and A. Rahman, "Study of an F center in molten KCl", J. Chem. Phys. **80**, 860–867 (1984) (cit. on p. 2).

[30]M. Ceriotti, G. Bussi, and M. Parrinello, "Nuclear quantum effects in solids using a colored-noise thermostat", Phys. Rev. Lett. **103**, 030603 (2009) (cit. on p. 3).

[31]H. Dammak, Y. Chalopin, M. Laroche, M. Hayoun, and J.-J. Greffet, "Quantum thermal bath for molecular dynamics simulation", Physical Review Letters **103**, 190601 (2009) (cit. on pp. 3, 40).

[32]H. Dammak, E. Antoshchenkova, M. Hayoun, and F. Finocchi, "Isotope effects in lithium hydride and lithium deuteride crystals by molecular dynamics simulations", J. Phys. Condens. Matter **24**, 435402 (2012) (cit. on p. 3).

[33]M. Ceriotti, G. Miceli, A. Pietropaolo, et al., "Nuclear quantum effects in ab initio dynamics: theory and experiments for lithium imide", Phys. Rev. B **82**, 174306 (2010) (cit. on p. 3).

[34]K. Druzbicki, M. Krzystyniak, D. Hollas, et al., "Hydrogen dynamics in solid formic acid: insights from simulations with quantum colored-noise thermostats", in Journal of physics: conference series, Vol. 1055 (2018), p. 012003 (cit. on p. 3).

[35]T. Qi and E. J. Reed, "Simulations of shocked methane including self-consistent semiclassical quantum nuclear effects", The Journal of Physical Chemistry A **116**, 10451–10459 (2012) (cit. on p. 3).

[36]M. H. Beck, A. Jäckle, G. A. Worth, and H.-D. Meyer, "The multiconfiguration time-dependent hartree (MCTDH) method: a highly efficient algorithm for propagating wavepackets", Physics reports **324**, 1–105 (2000) (cit. on p. 3).

[37]J. C. Light and T. Carrington Jr, "Discrete-variable representations and their utilization", Advances in Chemical Physics **114**, 263–310 (2000) (cit. on p. 3).

[38]N. Makri, "Quantum dissipative dynamics: a numerically exact methodology", The Journal of Physical Chemistry A **102**, 4414–4427 (1998) (cit. on p. 3).

[39]J. Shao and N. Makri, "Iterative path integral formulation of equilibrium correlation functions for quantum dissipative systems", The Journal of chemical physics **116**, 507–514 (2002) (cit. on p. 3).

[40]J. Cao and G. A. Voth, "A new perspective on quantum time correlation functions", J. Chem. Phys. **99**, 10070–10073 (1993) (cit. on pp. 4, 30, 35).

[41]J. Cao and G. A. Voth, "The formulation of quantum statistical mechanics based on the Feynman path centroid density. I. Equilibrium properties", J. Chem. Phys. **100**, 5093–5105 (1994) (cit. on pp. 4, 30, 35).

[42]S. Jang and G. A. Voth, "Path integral centroid variables and the formulation of their exact real time dynamics", J. Chem. Phys. **111**, 2357–2370 (1999) (cit. on pp. 4, 25, 30, 35).

[43]S. Jang and G. A. Voth, "A derivation of centroid molecular dynamics and other approximate time evolution methods for path integral centroid variables", J. Chem. Phys. **111**, 2371–2384 (1999) (cit. on pp. 4, 30, 35).

[44]T. J. H. Hele, M. J. Willatt, A. Muolo, and S. C. Althorpe, "Communication: relation of centroid molecular dynamics and ring-polymer molecular dynamics to exact quantum dynamics", The Journal of Chemical Physics **142**, 191101 (2015) (cit. on pp. 4, 30, 33, 35, 107, 110).

[45]I. R. Craig and D. E. Manolopoulos, "Quantum statistics and classical mechanics: real time correlation functions from ring polymer molecular dynamics", J. Chem. Phys. **121**, 3368–3373 (2004) (cit. on pp. 4, 30).

[46]W. H. Miller, "The semiclassical initial value representation: a potentially practical way for adding quantum effects to classical molecular dynamics simulations", The Journal of Physical Chemistry A **105**, 2942–2955 (2001) (cit. on p. 4).

[47]Q. Shi and E. Geva, "Semiclassical theory of vibrational energy relaxation in the condensed phase", The Journal of Physical Chemistry A **107**, 9059–9069 (2003) (cit. on pp. 4, 21, 22).

[48]J. Liu and W. H. Miller, "Using the thermal Gaussian approximation for the Boltzmann operator in semiclassical initial value time correlation functions", J.Chem. Phys. **125**, 224104 (2006) (cit. on p. 4).

[49]J. Liu and W. H. Miller, "A simple model for the treatment of imaginary frequencies in chemical reaction rates and molecular liquids", J. Chem. Phys. **131**, 074113 (2009) (cit. on pp. 4, 21–23).

[50]R. P. Feynman and H. Kleinert, "Effective classical partition functions", Physical Review A **34**, 5080–5084 (1986) (cit. on pp. 4, 25).

[51]J. A. Poulsen, G. Nyman, and P. J. Rossky, "Practical evaluation of condensed phase quantum correlation functions: a Feynman–Kleinert variational linearized path integral method", The Journal of chemical physics **119**, 12179–12193 (2003) (cit. on pp. 4, 21, 25, 26).

[52]J. Beutier, D. Borgis, R. Vuilleumier, and S. Bonella, "Computing thermal Wigner densities with the phase integration method", J. Chem. Phys. **141**, 084102 (2014) (cit. on pp. 4, 21, 29, 52, 70, 86, 144, 157–159).

[53]J. Liu, "Path integral Liouville dynamics for thermal equilibrium systems", J. Chem. Phys. **140**, 224107 (2014) (cit. on p. 4).

[54]K. K. G. Smith, J. A. Poulsen, G. Nyman, and P. J. Rossky, "A new class of ensemble conserving algorithms for approximate quantum dynamics: theoretical formulation and model problems", J. Chem. Phys. **142**, 244112 (2015) (cit. on p. 4).

[55]M. J. Willatt, M. Ceriotti, and S. C. Althorpe, "Approximating Matsubara dynamics using the planetary model: tests on liquid water and ice", The Journal of chemical physics **148**, 102336 (2018) (cit. on pp. 4, 33, 146).

[56]S. Karsten, S. D. Ivanov, S. I. Bokarev, and O. Kühn, "Simulating vibronic spectra via Matsubara-like dynamics: coping with the sign problem", The Journal of chemical physics **149**, 194103 (2018) (cit. on pp. 4, 33, 146).

[57]F. Brieuc, Y. Bronstein, H. Dammak, et al., "Zero-point energy leakage in quantum thermal bath molecular dynamics simulations", J. Chem. Theory Comput. **12**, 5688–5697 (2016) (cit. on pp. 4, 42).

[58]E. Mangaud, S. Huppert, T. Plé, et al., "The fluctuation–dissipation theorem as a diagnosis and cure for zero-point energy leakage in quantum thermal bath simulations", Journal of chemical theory and computation **15**, 2863–2880 (2019) (cit. on pp. 4, 44, 45, 47–49, 141).

[59]R. L. Benson, G. Trenins, and S. C. Althorpe, "Which quantum statistics–classical dynamics method is best for water?", Faraday Discussions **221**, 350–366 (2019) (cit. on pp. 5, 24, 35, 93, 127–130, 133, 134, 137, 138, 141, 145).

[60]M. E. Tuckerman, *Statistical mechanics: theory and molecular simulation* (Oxford University Press, 2010) Chap. 12.4.1 (cit. on pp. 7, 11, 18, 64, 168, 169).

[61]*The analysis of time series* (Chapman and Hall/CRC, Mar. 2016) (cit. on p. 8).

[62]M. Rossi, V. Kapil, and M. Ceriotti, "Fine tuning classical and quantum molecular dynamics using a generalized Langevin equation", J. Chem. Phys. **148**, 102301 (2018) (cit. on pp. 9, 42, 128, 132, 134, 137, 138, 141).

[63]E. Wigner, "On the quantum correction for thermodynamic equilibrium", Physical Review **40**, 749–759 (1932) (cit. on p. 12).

[64]T. J. Hele, "Thermal quantum time-correlation functions from classical-like dynamics", Molecular Physics **115**, 1435–1462 (2017) (cit. on p. 14).

[65]M. Hillery, R. O'Connell, M. Scully, and E. Wigner, "Distribution functions in physics: fundamentals", Physics Reports **106**, 121–167 (1984) (cit. on p. 16).

[66]T. J. Hele, M. J. Willatt, A. Muolo, and S. C. Althorpe, "Boltzmann-conserving classical dynamics in quantum time-correlation functions:"Matsubara dynamics"", The Journal of chemical physics **142**, 134103 (2015) (cit. on pp. 16, 30, 33).

[67]H. J. Groenewold, "On the principles of elementary quantum mechanics", in *On the principles of elementary quantum mechanics* (Springer, 1946), pp. 1–56 (cit. on p. 16).

[68]J. E. Moyal, "Quantum mechanics as a statistical theory", in Mathematical proceedings of the cambridge philosophical society, Vol. 45, 1 (Cambridge University Press, 1949), pp. 99–124 (cit. on p. 16).

[69]T. L. Curtright and C. K. Zachos, "Quantum mechanics in phase space", Asia Pacific Physics Newsletter **1**, 37–46 (2012) (cit. on p. 16).

[70]S. Bonella and G. Ciccotti, "Approximating time-dependent quantum statistical properties", Entropy **16**, 86–109 (2014) (cit. on pp. 18, 159).

[71]J. R. Cendagorta, Z. Bačić, and M. E. Tuckerman, "An open-chain imaginary-time path-integral sampling approach to the calculation of approximate symmetrized quantum time correlation functions", The Journal of chemical physics **148**, 102340 (2018) (cit. on p. 18).

[72]P. Johannsen, "Vibrational states and optical transitions in hydrogen bonds", Journal of Physics: Condensed Matter **10**, 2241 (1998) (cit. on p. 19).

[73]J. Liu and W. H. Miller, "Real time correlation function in a single phase space integral beyond the linearized semiclassical initial value representation", The Journal of chemical physics **126**, 234110 (2007) (cit. on p. 20).

[74]H. Wang, X. Sun, and W. H. Miller, "Semiclassical approximations for the calculation of thermal rate constants for chemical reactions in complex molecular systems", J. Chem. Phys. **108**, 9726 (1998) (cit. on p. 20).

[75]Q. Shi and E. Geva, "A relationship between semiclassical and centroid correlation functions", The Journal of chemical physics **118**, 8173–8184 (2003) (cit. on p. 20).

[76]S. Habershon and D. E. Manolopoulos, "Zero point energy leakage in condensed phase dynamics: an assessment of quantum simulation methods for liquid water", The Journal of chemical physics **131**, 244518 (2009) (cit. on pp. 21, 133).

[77]J. Liu, "Recent advances in the linearized semiclassical initial value representation/classical Wigner model for the thermal correlation function", International Journal of Quantum Chemistry **115**, 657–670 (2015) (cit. on p. 21).

[78]Q. Shi and E. Geva, "Vibrational energy relaxation in liquid oxygen from a semiclassical molecular dynamics simulation", The Journal of Physical Chemistry A **107**, 9070–9078 (2003) (cit. on p. 24).

[79]J. Liu, W. H. Miller, G. S. Fanourgakis, et al., "Insights in quantum dynamical effects in the infrared spectroscopy of liquid water from a semiclassical study with an ab initio-based flexible and polarizable force field", The Journal of chemical physics **135**, 244503 (2011) (cit. on p. 24).

[80]J. Liu and W. H. Miller, "An approach for generating trajectory-based dynamics which conserves the canonical distribution in the phase space formulation of quantum mechanics. II. Thermal correlation functions", The Journal of chemical physics **134**, 104102 (2011) (cit. on p. 25).

[81]J. A. Poulsen, G. Nyman, and P. J. Rossky, "Feynman-Kleinert linearized path integral (FK-LPI) algorithms for quantum molecular dynamics, with application to water and he(4)", Journal of chemical theory and computation **2**, 1482–1491 (2006) (cit. on pp. 26, 133).

[82]J. A. Poulsen, G. Nyman, and P. J. Rossky, "Quantum diffusion in liquid para-hydrogen: an application of the Feynman- Kleinert linearized path integral approximation", The Journal of Physical Chemistry B **108**, 19799–19808 (2004) (cit. on p. 26).

[83]Q. Yu and J. M. Bowman, "Classical, thermostated ring polymer, and quantum VSCF/VCI calculations of IR spectra of H7O3+ and H9O4+ (eigen) and comparison with experiment", The Journal of Physical Chemistry A **123**, 1399–1409 (2019) (cit. on p. 35).

[84]M. Rossi, M. Ceriotti, and D. E. Manolopoulos, "How to remove the spurious resonances from ring polymer molecular dynamics", J. Chem. Phys. **140**, 234116 (2014) (cit. on p. 35).

[85]A. Witt, S. D. Ivanov, M. Shiga, H. Forbert, and D. Marx, "On the applicability of centroid and ring polymer path integral molecular dynamics for vibrational spectroscopy", The Journal of chemical physics **130**, 194510 (2009) (cit. on p. 36).

[86]S. Ivanov, A. Witt, M. Shiga, and D. Marx, "Communications: on artificial frequency shifts in infrared spectra obtained from centroid molecular dynamics: quantum liquid water", Journal of Chemical Physics **132**, 031101–4 (2010) (cit. on pp. 36, 90).

[87]G. Trenins and S. C. Althorpe, "Mean-field Matsubara dynamics: analysis of path-integral curvature effects in rovibrational spectra", The Journal of chemical physics **149**, 014102 (2018) (cit. on pp. 36, 90, 146).

[88]G. Trenins, M. J. Willatt, and S. C. Althorpe, "Path-integral dynamics of water using curvilinear centroids", The Journal of Chemical Physics **151**, 054109 (2019) (cit. on pp. 36, 91).

[89]J. Cao and G. A. Voth, "The formulation of quantum statistical mechanics based on the Feynman path centroid density. IV. Algorithms for centroid molecular dynamics", The Journal of chemical physics **101**, 6168–6183 (1994) (cit. on p. 36).

[90]T. D. Hone and G. A. Voth, "A centroid molecular dynamics study of liquid para-hydrogen and ortho-deuterium", The Journal of chemical physics **121**, 6412–6422 (2004) (cit. on p. 36).

[91]T. D. Hone, P. J. Rossky, and G. A. Voth, "A comparative study of imaginary time path integral based methods for quantum dynamics", The Journal of chemical physics **124**, 154103 (2006) (cit. on p. 36).

[92]M. Ceriotti, "A novel framework for enhanced molecular dynamics based on the generalized Langevin equation", PhD thesis (ETH Zurich, 2010) (cit. on pp. 38, 133).

[93]M. Ceriotti, G. Bussi, and M. Parrinello, "Colored-noise thermostats à la carte", Journal of Chemical Theory and Computation **6**, 1170–1180 (2010) (cit. on p. 38).

[94]M. Ceriotti, D. E. Manolopoulos, and M. Parrinello, "Accelerating the convergence of path integral dynamics with a generalized Langevin equation", The Journal of chemical physics **134**, 084104 (2011) (cit. on p. 38).

[95]R. Kubo, "The fluctuation-dissipation theorem", Reports on progress in physics **29**, 255 (1966) (cit. on pp. 38, 39).

[96]H. Mori, "Transport, collective motion, and Brownian motion", Progress of theoretical physics **33**, 423–455 (1965) (cit. on p. 39).

[97]S. Nordholm and R. Zwanzig, "A systematic derivation of exact generalized Brownian motion theory", Journal of Statistical Physics **13**, 347–371 (1975) (cit. on p. 39).

[98]R. Zwanzig, *Nonequilibrium statistical mechanics* (Oxford University Press, 2001) (cit. on p. 39).

[99]M. Ceriotti, G. Bussi, and M. Parrinello, "Langevin equation with colored noise for constant-temperature molecular dynamics simulations", Physical review letters **102**, 020601 (2009) (cit. on p. 39).

[100]M. Ceriotti, M. Parrinello, T. E. Markland, and D. E. Manolopoulos, "Efficient stochastic thermostatting of path integral molecular dynamics", J. Chem. Phys. **133**, 124104 (2010) (cit. on p. 39).

[101]M. Basire, D. Borgis, and R. Vuilleumier, "Computing Wigner distributions and time correlation functions using the quantum thermal bath method: application to proton transfer spectroscopy", Physical Chemistry Chemical Physics **15**, 12591 (2013) (cit. on pp. 40, 113).

[102]O. Bedoya-Martinez, J.-L. Barrat, and D. Rodney, "Computation of the thermal conductivity using methods based on classical and quantum molecular dynamics", Physical Review B **89**, 014303 (2014) (cit. on p. 42).

[103]J. Hernández-Rojas, F. Calvo, and E. G. Noya, "Applicability of quantum thermal baths to complex many-body systems with various degrees of anharmonicity", Journal of chemical theory and computation **11**, 861–870 (2015) (cit. on p. 42).

[104]S. Blinnikov and R. Moessner, "Expansions for nearly Gaussian distributions", Astronomy and Astrophysics Supplement Series **130**, 193–205 (1998) (cit. on p. 54).

[105]P. Hall, *The bootstrap and Edgeworth expansion* (Springer Science & Business Media, 2013) (cit. on p. 54).

[106]T. Plé, S. Huppert, F. Finocchi, P. Depondt, and S. Bonella, "Sampling the thermal Wigner density via a generalized Langevin dynamics", The Journal of chemical physics **151**, 114114 (2019) (cit. on pp. 60, 72, 160).

[107]B. Leimkuhler and X. Shang, "Adaptive thermostats for noisy gradient systems", SIAM J. Sci. Comput. **38**, A712–A736 (2016) (cit. on p. 60).

[108]F. Mouhat, S. Sorella, R. Vuilleumier, A. M. Saitta, and M. Casula, "Fully quantum description of the Zundel ion: combining variational quantum Monte Carlo with path integral langevin dynamics", Journal of Chemical Theory and Computation **13**, 2400–2417 (2017) (cit. on p. 60).

[109]M. Basire, F. Mouhat, G. Fraux, et al., "Fermi resonance in CO2: mode assignment and quantum nuclear effects from first principles molecular dynamics", J. Chem. Phys. **146**, 134102 (2017) (cit. on pp. 93, 124, 125).

[110]C. M. Bender and S. A. Orszag, *Advanced mathematical methods for scientists and engineers i: asymptotic methods and perturbation theory* (Springer Science & Business Media, 2013) (cit. on p. 98).

[111]A. H. Nayfeh, *Introduction to perturbation techniques* (John Wiley & Sons, 2011) (cit. on p. 98).

[112]C. M. Bender and L. M. Bettencourt, "Multiple-scale analysis of the quantum anharmonic oscillator", Physical review letters **77**, 4114 (1996) (cit. on p. 98).

[113]C. M. Bender and L. M. Bettencourt, "Multiple-scale analysis of quantum systems", Physical Review D **54**, 7710 (1996) (cit. on p. 98).

[114]L.-Y. Chen, N. Goldenfeld, and Y. Oono, "Renormalization group and singular perturbations: multiple scales, boundary layers, and reductive perturbation theory", Physical Review E **54**, 376 (1996) (cit. on p. 98).

[115]S. Iso, H. Ohta, and T. Suyama, "Secular terms in dyson series to all orders of perturbation", Progress of Theoretical and Experimental Physics **2018**, 083A01 (2018) (cit. on p. 98).

[116]R. L. Benson and S. C. Althorpe, "On the 'Matsubara heating' of overtone intensities and fermi splittings", J. Chem. Phys. **X**, zzz (2021) (cit. on p. 98).

[117]E. Fermi, "Über den ramaneffekt des kohlendioxyds", Zeitschrift für Physik **71**, 250–259 (1931) (cit. on p. 124).

[118]H. Partridge and D. W. Schwenke, "The determination of an accurate isotope dependent potential energy surface for water from extensive ab initio calculations and experimental data", The Journal of Chemical Physics **106**, 4618–4639 (1997) (cit. on p. 127).

[119]J. Tennyson, M. A. Kostin, P. Barletta, et al., "DVR3D: a program suite for the calculation of rotation–vibration spectra of triatomic molecules", Computer physics communications **163**, 85–116 (2004) (cit. on p. 127).

[120]S. Habershon, T. E. Markland, and D. E. Manolopoulos, "Competing quantum effects in the dynamics of a flexible water model", The journal of chemical physics **131**, 024501 (2009) (cit. on pp. 128, 133, 134).

[121]D. W. Schwenke and H. Partridge, "Convergence testing of the analytic representation of an ab initio dipole moment function for water: improved fitting yields improved intensities", The Journal of Chemical Physics **113**, 6592–6597 (2000) (cit. on p. 128).

[122]F. H. Stillinger, "Water revisited", Science **209**, 451–457 (1980) (cit. on p. 133).

[123]J. Teixeira, "The physics of liquid water", Le Journal de Physique IV **3**, C1–163 (1993) (cit. on p. 133).

[124]B. Cheng, E. A. Engel, J. Behler, C. Dellago, and M. Ceriotti, "Ab initio thermodynamics of liquid and solid water", Proceedings of the National Academy of Sciences **116**, 1110–1115 (2019) (cit. on p. 133).

[125]S.-i. Koda, "Initial-value semiclassical propagators for the Wigner phase space representation: formulation based on the interpretation of the Moyal equation as a Schrödinger equation", The Journal of chemical physics **143**, 244110 (2015) (cit. on p. 146).

[126]M. Buchholz, E. Fallacara, F. Gottwald, et al., "Herman-Kluk propagator is free from zero-point energy leakage", Chemical Physics **515**, 231–235 (2018) (cit. on p. 146).

[127]M. A. Saller, A. Kelly, and J. O. Richardson, "On the identity of the identity operator in nonadiabatic linearized semiclassical dynamics", The Journal of chemical physics **150**, 071101 (2019) (cit. on p. 146).

[128]M. A. Saller, A. Kelly, and J. O. Richardson, "Improved population operators for multi-state nonadiabatic dynamics with the mixed quantum-classical mapping approach", Faraday Discussions **221**, 150–167 (2019) (cit. on p. 146).

[129]S. Bonella and D. Coker, "LAND-map, a linearized approach to nonadiabatic dynamics using the mapping formalism", The Journal of chemical physics **122**, 194102 (2005) (cit. on p. 146).

[130]J. Beutier, "Development of a quasi-classical method and application to the infrared spectroscopy", PhD thesis (Paris 6, 2016) (cit. on p. 157).

[131]J. Beutier, M. Monteferrante, S. Bonella, R. Vuilleumier, and G. Ciccotti, "Gas phase infrared spectra via the phase integration quasi-classical method", Molecular Simulation **40**, 196–207 (2014) (cit. on p. 159).

[132]M. Monteferrante, S. Bonella, and G. Ciccotti, "Quantum dynamical structure factor of liquid neon via a quasiclassical symmetrized method", The Journal of chemical physics **138**, 054118 (2013) (cit. on p. 159).

A Details on the Phase Integration Method

Ref. [52] recently introduced a controlled approximation for the Wigner density that allows to tame the phase factor without resorting to a harmonic approximation. Moreover, contrary to LGA or FK-LPI, it allows in principle to recover negative parts of the Wigner density. In this section, we will only sketch the procedure in the unidimensional case. The multidimensional generalization can be found in [130].

One starts by writing the off-diagonal matrix element of the density operator in path integral form using the symmetric Trotter break-up of equation (2.12) with 2ν slices:

$$\left\langle q-\frac{\Delta}{2}\middle|e^{-\beta\hat{H}}\middle|q+\frac{\Delta}{2}\right\rangle \propto \int \mathrm{d}x_1\ldots\mathrm{d}x_{2\nu-1}\; e^{-\frac{\beta}{2\nu}\left(\frac{1}{2}V(q-\frac{\Delta}{2})+\frac{1}{2}V(q+\frac{\Delta}{2})+\sum_{l=1}^{2\nu-1}V(x_l)\right)} \times \exp\left\{-\frac{\beta}{2\nu}\frac{1}{2}m\omega_{2\nu}^2\left((q-\frac{\Delta}{2}-x_1)^2+(q+\frac{\Delta}{2}-x_{2\nu-1})^2+\sum_{l=1}^{2\nu-2}(x_{l+1}-x_l)^2\right)\right\} \tag{A.1}$$

with $\omega_{2\nu}=2\nu/\beta\hbar$. This path integral forms an open chain with endpoints $q-\Delta/2$ and $q+\Delta/2$. We now split the chain in half and change variables to the center path and the fluctuation path as:

$$\begin{aligned} r_l &= (x_l+x_{2\nu-l})/2 \\ \Delta_l &= x_l-x_{2\nu-l} \end{aligned} \qquad l=0,\ldots,\nu \tag{A.2}$$

Using this definition, we denote $r_0=q$ and $\Delta_0=\Delta$. Moreover, we have $\Delta_\nu=0$. The Wigner density then reads:

$$\rho_w(q,p)\propto\lim_{\nu\to\infty}\int \mathrm{d}\mathbf{r}\;\mathrm{d}\boldsymbol{\Delta}\; e^{ip\Delta_0/\hbar}\rho(\mathbf{r},\boldsymbol{\Delta})\;\delta(q-r_0) \tag{A.3}$$

157

with $\mathbf{r} = (r_0, \ldots, r_\nu)$, $\mathbf{\Delta} = (\Delta_0, \ldots, \Delta_{\nu-1})$ and:

$$\rho(\mathbf{r}, \mathbf{\Delta}) = \frac{1}{N_\nu} e^{-\frac{\beta}{\nu}\left(\frac{1}{4}V(r_0 - \frac{\Delta}{2}) + \frac{1}{4}V(r_0 + \frac{\Delta}{2}) + V(r_\nu) + \sum_{l=1}^{\nu-1} \frac{V(r_l - \Delta_l/2) + V(r_l + \Delta_l/2)}{2}\right)} \times \exp\left\{-\frac{\beta}{\nu}\frac{1}{2}m\omega_{2\nu}^2\left(\sum_{l=0}^{\nu-1}(r_{l+1} - r_l)^2 + \frac{1}{4}(\Delta_{l+1} - \Delta_l)^2\right)\right\} \quad \text{(A.4)}$$

with N_ν a normalization constant. We now split the path integral density ρ into marginal $\rho_m(\mathbf{r}) = \int \mathrm{d}\mathbf{\Delta}\ \rho(\mathbf{r}, \mathbf{\Delta})$ times conditional $\rho_c(\mathbf{\Delta}|\mathbf{r}) = \rho(\mathbf{r}, \mathbf{\Delta})/\rho_m(\mathbf{r})$. We also multiply and divide by the Gaussian term $e^{-\kappa_2(\mathbf{r})p^2/2\hbar^2}$ with $\kappa_2(\mathbf{r})$ to be determined. The Wigner distribution is then (we now imply and drop the limit $\nu \to \infty$):

$$\rho_w(q,p) \propto \int \mathrm{d}\mathbf{r}\ \rho_m(\mathbf{r}) e^{-\kappa_2(\mathbf{r})p^2/2\hbar^2} \delta(q - r_0) \left[\int \mathrm{d}\mathbf{\Delta}\ e^{\kappa_2(\mathbf{r})p^2/2\hbar^2 + ip\Delta_0/\hbar} \rho_c(\mathbf{\Delta}|\mathbf{r})\right] \quad \text{(A.5)}$$

Expanding $e^{\kappa_2(\mathbf{r})p^2/2\hbar^2 + ip\Delta_0/\hbar}$ as a power series with respect to p and choosing κ_2 as the second order cumulant of the conditional distribution with respect to Δ_0

$$\kappa_2(\mathbf{r}) = \int \mathrm{d}\mathbf{\Delta}\ \Delta_0^2\ \rho_c(\mathbf{\Delta}|\mathbf{r}) = \left\langle \Delta_0^2 \right\rangle_{\rho_c} \quad \text{(A.6)}$$

we obtain:

$$\rho_w(q,p) \propto \int \mathrm{d}\mathbf{r}\ \rho_m(\mathbf{r}) e^{-\kappa_2(\mathbf{r})p^2/2\hbar^2} \delta(q - r_0) \left[1 + \frac{\kappa_4(\mathbf{r})}{4!}\left(\frac{ip}{\hbar}\right)^4 + \frac{\kappa_6(\mathbf{r})}{6!}\left(\frac{ip}{\hbar}\right)^6 + \ldots\right] \quad \text{(A.7)}$$

where $\kappa_n(\mathbf{r})$ is the n-th order cumulant with respect to Δ_0 of the distribution ρ_c. Note that, by parity of ρ_c, all odd orders in the expansion are null. We will refer to the power expansion in (A.7) as the Edgeworth correction.

Using the fact that the Wigner density is normalized, we obtain the full expression:

$$\rho_w(q,p) = \frac{\int \mathrm{d}\mathbf{r}\ \rho_m(\mathbf{r}) e^{-\kappa_2(\mathbf{r})p^2/2\hbar^2} \delta(q - r_0) \left[1 + \frac{\kappa_4(\mathbf{r})}{4!}\left(\frac{ip}{\hbar}\right)^4 + \frac{\kappa_6(\mathbf{r})}{6!}\left(\frac{ip}{\hbar}\right)^6 + \ldots\right]}{\int \mathrm{d}p\mathrm{d}\mathbf{r}\ \rho_m(\mathbf{r}) e^{-\kappa_2(\mathbf{r})p^2/2\hbar^2} \left[1 + \frac{\kappa_4(\mathbf{r})}{4!}\left(\frac{ip}{\hbar}\right)^4 + \frac{\kappa_6(\mathbf{r})}{6!}\left(\frac{ip}{\hbar}\right)^6 + \ldots\right]} \quad \text{(A.8)}$$

In ref. [52], the Wigner density is computed via a Monte Carlo algorithm that samples the density $\rho_m(\mathbf{r})e^{-\kappa_2(\mathbf{r})p^2/2\hbar^2}$. Averages over this density are then weighted by the Edgeworth correction (truncated at a certain order). The density sampled via Monte Carlo is positive so that negative parts of the Wigner density are recovered through the Edgeworth correction. This formulation of the Wigner density was shown to capture interesting quantum effects, such as the correct correlations between different degrees of freedom (including coordinate-momentum and momentum-

momentum correlations). As for the slightly different Edgeworth approximation introduced in chapter 4, the numerical convergence – or failure to converge – of the method can be systematically tested by computing successive terms of the Edgeworth correction. The main numerical difficulty of this approach is that $\rho_m(\mathbf{r})$, $\kappa_2(\mathbf{r})$ and the higher order cumulants are non analytical and need to be computed via an auxiliary path integral Monte Carlo.

Similar approximations have been used to compute the Kubo-transformed [131] and symmetrized [70, 132] correlation functions.

The Edgeworth expansion that we derive in chapter 4 differs from the one in the PIM mainly by the distribution it approximates. While our approximation considers the Edgeworth expansion of the full matrix element $\langle q - \Delta/2|e^{-\beta\hat{H}}|q + \Delta/2\rangle$, conditionally to q, the PIM starts by expanding this element in path-integral form and approximates the extended-space distribution $\rho_c(\mathbf{\Delta}|\mathbf{r})$ ($\mathbf{\Delta}$ and $\mathbf{r}$ are ν-dimensional vectors). The PIM is thus tied to path-integrals from the start and it is more difficult to derive from it a Langevin dynamics that allows to compute TCFs, as the WiLD. By contrast, the WiLD only involves the physical degrees of freedom (q, p) and uses path-integrals only in the auxiliary calculation, as a calculation tool for its generalized forces. The PIM version of the Edgeworth approximation and the one derived in chapter 4 yield equivalent accuracy on all the model systems tested. However, the new formulation is simpler and we expect the ECMA sampling scheme to be computationally more efficient than the generalized Monte Carlo procedure of ref. [52], although this point should be more systematically investigated for future works.

Noise correction of ECMA

B

In this appendix, we demonstrate that the factor of equation (4.51) allows to correct for the noise on the EW0 conditional momentum.

First, let us clarify the notations. We will denote κ_2 the exact second order cumulant matrix as given by equation (4.58) (we drop the dependence on $\mathbf{q}$ as we will consider the position fixed) and $\overline{\kappa}_2 = \kappa_2 + X$ an unbiased estimate of κ_2 (thus X is a random matrix of zero mean) obtained, for example, using an auxiliary Langevin equation (see ref. [106]).

The EW0 conditional momentum density for a N-dimensional system, obtained using $\overline{\kappa}_2$ is given by:

$$\rho_{\overline{\kappa}_2}(\mathbf{p}|\mathbf{q}) = \frac{e^{-\frac{\mathbf{p}^T(\kappa_2+X)\mathbf{p}}{2\hbar^2}}}{\sqrt{2\pi\hbar^2|\kappa_2|^{-1}}}\left|I + \kappa_2^{-1}X\right|^{1/2} \tag{B.1}$$

where $|\cdot|$ denotes the determinant and I is the $N \times N$ identity matrix.

We now expand the distribution at second order in X. As a first step, one can show that the determinant $|I+H|^{1/2}$ can be expanded at second order in H as:

$$|I+H|^{1/2} = 1 + \frac{1}{2}\sum_i H_{ii} + \frac{1}{2}\sum_i\sum_{j\neq i}(H_{ii}H_{jj} - H_{ij}H_{ji}) - \frac{1}{8}\left(\sum_i H_{ii}\right)^2 + \cdots \tag{B.2}$$

The distribution can then be expanded at second order in X as:

$$\rho_{\overline{\kappa}_2}(\mathbf{p}|\mathbf{q}) = \rho_{\kappa_2}(\mathbf{p}|\mathbf{q})\left[1 - \frac{\mathbf{p}^T X\mathbf{p}}{2\hbar^2} + \frac{(\mathbf{p}^T X\mathbf{p})^2}{8\hbar^4} + \frac{1}{2}\sum_i[\kappa_2^{-1}X]_{ii} - \frac{1}{8}\sum_i[\kappa_2^{-1}X]_{ii}^2\right.$$
$$\left. + \sum_i\sum_{j\neq i}\left(\frac{3}{8}[\kappa_2^{-1}X]_{ii}[\kappa_2^{-1}X]_{jj} - \frac{1}{2}[\kappa_2^{-1}X]_{ij}[\kappa_2^{-1}X]_{ji}\right) - \frac{\mathbf{p}^T X\mathbf{p}}{4\hbar^2}\sum_i[\kappa_2^{-1}X]_{ii} + \cdots\right] \tag{B.3}$$

160

The expectation value of this distribution over many realizations of $\overline{\kappa}_2$ is then:

$$\langle \rho_{\overline{\kappa}_2}(\mathbf{p}|\mathbf{q}) \rangle = \rho_{\kappa_2}(\mathbf{p}|\mathbf{q}) \Bigg[1 + \frac{\left\langle (\mathbf{p}^T X \mathbf{p})^2 \right\rangle}{8\hbar^4} - \frac{1}{8} \sum_i \left\langle [\kappa_2^{-1} X]_{ii}^2 \right\rangle - \left\langle \frac{\mathbf{p}^T X \mathbf{p}}{4\hbar^2} \sum_i [\kappa_2^{-1} X]_{ii} \right\rangle + \sum_i \sum_{j \neq i} \left\langle \frac{3}{8} [\kappa_2^{-1} X]_{ii} [\kappa_2^{-1} X]_{jj} - \frac{1}{2} [\kappa_2^{-1} X]_{ij} [\kappa_2^{-1} X]_{ji} \right\rangle + \cdots \Bigg] \quad \text{(B.4)}$$

where the first order terms cancel since X is of zero mean. One can then see that the expectation value $\langle \rho_{\overline{\kappa}_2} \rangle$ is biased by a multiplicative factor which depends on the fluctuations of the noise X (its variance for a unidimensional system). One can then construct an unbiased estimator (up to second order in X) for ρ_{κ_2} which reads:

$$\rho^{\text{corr}}_{\overline{\kappa}_2}(\mathbf{p}|\mathbf{q}) = \rho_{\overline{\kappa}_2}(\mathbf{p}|\mathbf{q}) \Bigg[1 - \frac{\left\langle (\mathbf{p}^T X \mathbf{p})^2 \right\rangle}{8\hbar^4} + \frac{1}{8} \sum_i \left\langle [\kappa_2^{-1} X]_{ii}^2 \right\rangle + \left\langle \frac{\mathbf{p}^T X \mathbf{p}}{4\hbar^2} \sum_i [\kappa_2^{-1} X]_{ii} \right\rangle - \sum_i \sum_{j \neq i} \left\langle \frac{3}{8} [\kappa_2^{-1} X]_{ii} [\kappa_2^{-1} X]_{jj} - \frac{1}{2} [\kappa_2^{-1} X]_{ij} [\kappa_2^{-1} X]_{ji} \right\rangle \Bigg] \quad \text{(B.5)}$$

and one can show, following the same procedure as above, that $\left\langle \rho^{\text{corr}}_{\overline{\kappa}_2} \right\rangle = \rho_{\kappa_2} + \mathcal{O}(X^3)$. For a unidimensional system, this expression reduces to:

$$\rho^{\text{corr}}_{\overline{\kappa}_2}(p|q) = \rho_{\overline{\kappa}_2}(p|q) \left[1 - \sigma^2 \left(\frac{p^4}{8\hbar^4} - \frac{p^2}{4\hbar^2 \overline{\kappa}_2} - \frac{1}{8\overline{\kappa}_2^2} \right) \right] \quad \text{(B.6)}$$

where $\sigma^2 = \langle X^2 \rangle$ is the variance on the estimated value of κ_2 and we recognize in this expression the correction factor of equation (4.51) of the main text.

In practice, in order to evaluate the expectation values in equation (B.5) (or the variance σ^2 in (B.6) for the unidimensional case), we perform N_{aux} independent evaluations of κ_2 that we will denote $\overline{\kappa}_2^{(i)}$ ($i = 1, \ldots, N_{\text{aux}}$). We use their average $\overline{\kappa}_2 = \sum_i \overline{\kappa}_2^{(i)} / N_{\text{aux}}$ as our closest estimate of κ_2 and the expectation values are estimated on the sample of $\overline{\kappa}_2^{(i)}$. For example, for a unidimensional system, the unbiased estimator of the variance of $\overline{\kappa}_2$ is:

$$\sigma^2 \approx \frac{\sum_i (\overline{\kappa}_2^{(i)} - \overline{\kappa}_2)^2}{N_{\text{aux}}(N_{\text{aux}} - 1)} \quad \text{(B.7)}$$

And similarly for a multidimensional system, for example:

$$\left\langle (\mathbf{p}^T X \mathbf{p})^2 \right\rangle \approx \frac{\sum_i \left[\mathbf{p}^T (\overline{\kappa}_2^{(i)} - \overline{\kappa}_2) \mathbf{p} \right]^2}{N_{\text{aux}}(N_{\text{aux}} - 1)} \quad \text{(B.8)}$$

The noise correction allows in principle to use very noisy estimates of κ_2 when sampling the conditional momentum distribution and thus to drastically reduce the numerical cost of ECMA. To illustrate the effect of the noise correction, we compute the kinetic energy of the Morse potential of equation (3.1) numerically estimated via ECMA with and without the correction factor. The reference energy is computed from the exact ECMA distribution given by the wavefunction expression of the density operator (2.7). The numerical estimations of $\kappa_2(q)$ were obtained using $N_{\text{aux}} = 16$ auxiliary open-chain path-integral Langevin simulations (with 128 beads) and the position distribution was sampled from standard PIMD. To avoid any correlations and biases on the estimation of the $\overline{\kappa}_2^{(i)}$, each auxiliary simulation is thermalized for 25 fs before accumulating the statistics. Figure B.1 shows the relative error on the kinetic energy with and without the noise correction as a function of the auxiliary simulation time. One can see that, even for very short auxiliary simulations, the noise correction is able to drastically reduce the error on the kinetic energy to less than 2%. Furthermore, the corrected kinetic energy converges to the exact value much before the uncorrected one.

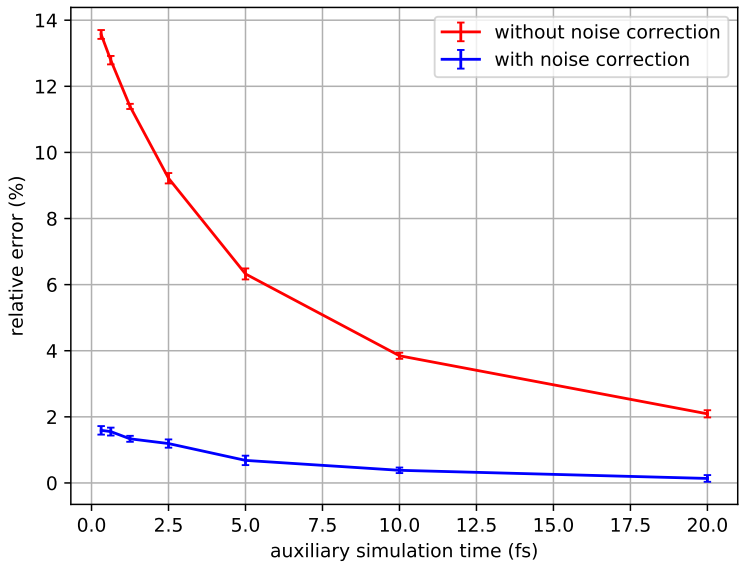

Fig. B.1.: Relative error on the kinetic energy for the Morse potential of equation (3.1) numerically estimated via ECMA with (blue curve) and without (red curve) noise correction as a function of the auxiliary simulation time. The reference energy is computed from the exact ECMA distribution given by the wavefunction expression of the density operator. The numerical estimations of κ_2 are averaged over 16 independent Langevin trajectories, each thermalized for 25 fs.

The top panel of figure B.2 shows the ECMA distribution (at order EW0) with and without noise correction with an auxiliary simulation time of 1.25 fs. One can see that without the correction, the conditional momentum distribution is broader than the reference and that the broadening depends on the position (see the lower panel of figure B.2). The corrected distribution is however very close to the exact distribution and the conditional momentum distribution is well reproduced for all positions.

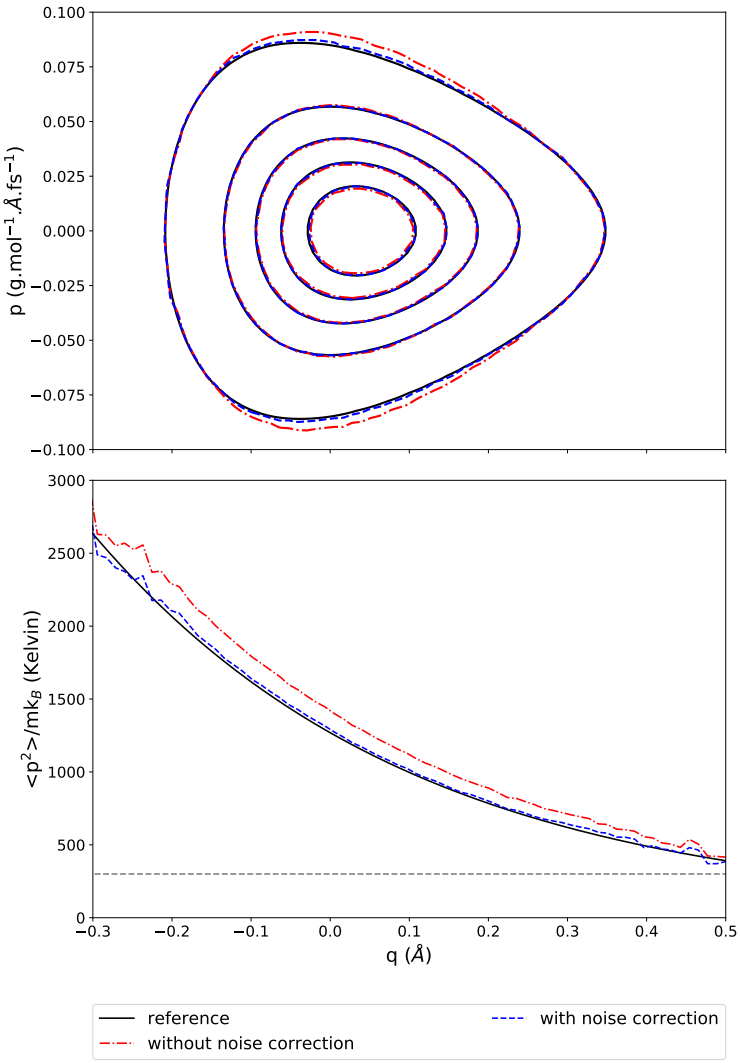

Fig. B.2.: top panel: ECMA-EW0 distribution for the Morse potential at 300K. Contour levels are 1.5, 10, 20, 30, 40 fs.Å^{-2}.(g/mol)$^{-1}$. bottom panel: variance of the conditional momentum distribution (renormalized by mk_B to obtain a temperature) as a function of q (*i.e.* the average value of p^2 on each vertical slice of the corresponding top panel). solid black curve: exact ECMA (from wavefunctions); red dotted-dashed curve: numerical estimation (128 beads, 1.25fs of auxiliary simulation, $N_{\text{aux}} = 16$) without noise correction; blue: numerical estimation with noise correction.

We confirm the multidimensional expression of the noise correction with the bidimensional model of section 4.5.2. We found similar resuls as in the 1D case (see figure B.3).

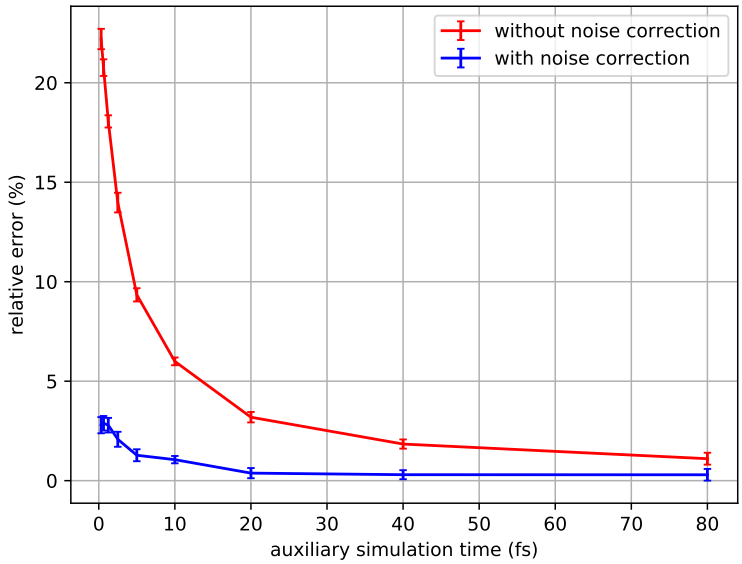

Fig. B.3.: Relative error on the kinetic energy for the bidimensional potential of equation (4.69) numerically estimated via ECMA with (blue curve) and without (red curve) noise correction as a function of the auxiliary simulation time. The reference energy is computed from the exact ECMA distribution given by the wavefunction expression of the density operator. The numerical estimations of κ_2 are averaged over 16 independent Langevin trajectories, each thermalized for 25 fs.

C

Quantum perturbation theory applied to the mildly anharmonic oscillator

C.1 overtone intensity by perturbation of the harmonic eigenstates

In this appendix, we use quantum perturbation theory to derive the intensity of the overtone of equation (5.25) for the perturbative model of equation (5.1). The Hamiltonian operator of the system under the potential (5.1) can be split as:

$$\hat{H} = \hat{H}_0 + \frac{\lambda}{3}\hat{q}^3 \tag{C.1}$$

where $\hat{H}_0$ is the Hamiltonian of the harmonic system. The unperturbed eigenstates are given by the time-independent Schrödinger equation:

$$\hat{H}_0 \left|n\right\rangle = \epsilon_n \left|n\right\rangle \quad (n \geq 0) \tag{C.2}$$

where $|n\rangle$ is the n^{th} wavefunction of the harmonic oscillator and $\epsilon_n = \frac{\hbar\omega_0}{2}(2n+1)$. We also remind the following relations involving the standard creation $\hat{a}^\dagger$ and annihilation $\hat{a}$ operators:

$$\hat{a}^\dagger \left|n\right\rangle = \sqrt{n+1}\left|n+1\right\rangle \tag{C.3}$$

$$\hat{a} \left|n\right\rangle = \sqrt{n}\left|n-1\right\rangle \tag{C.4}$$

and

$$\hat{q} = \sqrt{\frac{\hbar}{2m\omega_0}}(\hat{a}^\dagger + \hat{a}) \tag{C.5}$$

$$\hat{p} = i\sqrt{\frac{\hbar m\omega_0}{2}}(\hat{a}^\dagger - \hat{a}) \tag{C.6}$$

165

At first order, the perturbed eigenstates are given by:

$$\tilde{\epsilon}_n = \epsilon_n + \mathcal{O}\left(\lambda^2\right) \tag{C.7}$$

$$|\tilde{n}\rangle = |n\rangle + \frac{\lambda}{3}\sum_{k\neq n}\frac{\langle k|\hat{q}^3|n\rangle}{\hbar\omega_0(n-k)}|k\rangle + \mathcal{O}\left(\lambda^2\right) \tag{C.8}$$

Using equation (2.22), we can write the real part of the standard momentum-momentum TCF for the perturbed system as:

$$\bar{c}_{pp}(t) = \frac{1}{\mathcal{Z}}\sum_l\sum_{n<l}\left(e^{-\beta\tilde{\epsilon}_n} + e^{-\beta\tilde{\epsilon}_l}\right)\left|\left\langle\tilde{n}\middle|\hat{p}\middle|\tilde{l}\right\rangle\right|^2\cos\left(\frac{\tilde{\epsilon}_l - \tilde{\epsilon}_n}{\hbar}t\right) \tag{C.9}$$

where $\mathcal{Z} = \sum_n e^{-\beta\tilde{\epsilon}_n}$ is the partition function of the system. We now consider only the contributions of frequencies close to $2\omega_0$ which are given by the pair of states such that $l = n+2$. For these states, we have at first order in λ:

$$\langle\tilde{n}|\hat{p}|\tilde{n}+2\rangle = \frac{\lambda}{3}\left[\sum_{k\neq n}\langle k|\hat{p}|n+2\rangle\frac{\langle n|\hat{q}^3|k\rangle}{\hbar\omega_0(n-k)} + \sum_{k\neq n+2}\langle n|\hat{p}|k\rangle\frac{\langle k|\hat{q}^3|n+2\rangle}{\hbar\omega_0(n+2-k)}\right] + \mathcal{O}\left(\lambda^2\right) \tag{C.10}$$

Using relations (C.4),(C.3),(C.6) and (C.5), one can easily show that:

$$\langle\tilde{n}|\hat{p}|\tilde{n}+2\rangle = i\frac{\lambda\hbar}{3m\omega_0^2}\sqrt{(n+1)(n+2)} + \mathcal{O}\left(\lambda^2\right) \tag{C.11}$$

Thus, at second order in λ, the only contribution of frequency close to $2\omega_0$ is given by:

$$\bar{c}_{pp}^{(2\omega_0)}(t) = A(\omega_0,\beta)\cos(2\omega_0 t) \tag{C.12}$$

with:

$$A(\omega_0,\beta) = \frac{\lambda^2\hbar^2}{9m^2\omega_0^4}\left(1+e^{-4\beta\epsilon_0}\right)\sum_n(n+1)(n+2)\rho_n \tag{C.13}$$

$$= \frac{\lambda^2\hbar^2}{9m^2\omega_0^4}\left(1+e^{-4\beta\epsilon_0}\right)\left[\frac{3}{4} + \frac{1}{4}\sum_n(2n+1)^2\rho_n + \sum_n(2n+1)\rho_n\right] \tag{C.14}$$

where we have denoted ρ_n the population of the n^{th} harmonic level:

$$\rho_n = \frac{e^{-\beta\epsilon_0(2n+1)}}{\sum_k e^{-\beta\epsilon_0(2k+1)}} \tag{C.15}$$

For the harmonic potential, the average total energy is given by:

$$\mathrm{Tr}\left[\hat{\rho}\hat{H}\right] = \frac{\hbar\omega_0/2}{\tanh(\beta\hbar\omega_0/2)} \equiv \Theta(\omega_0,\beta) \tag{C.16}$$

with the canonical density operator $\hat{\rho} = \sum_n \rho_n |n\rangle \langle n|$. This yields the following relation:

$$\epsilon_0 \sum_n (2n+1)\rho_n = \Theta(\omega_0, \beta) = \epsilon_0 \coth(\beta\epsilon_0) \tag{C.17}$$

The average energy fluctuations are obtained by differentiating with respect to β, giving:

$$\epsilon_0^2(\coth^2(\beta\epsilon_0) - \sum_n (2n+1)^2\rho_n) = \frac{\partial\Theta}{\partial\beta} = \epsilon_0^2(1 - \coth^2(\beta\epsilon_0)) \tag{C.18}$$

Thus

$$\sum_n (2n+1)^2\rho_n = 2\coth^2(\beta\epsilon_0) - 1 \tag{C.19}$$

Using relations (C.17),(C.19) and properties of hyperbolic functions, one can show that:

$$A(\omega_0, \beta) = \frac{4\lambda^2}{9m^2\omega_0^6}\Theta(\omega_0, \beta)\Theta(2\omega_0, \beta) \tag{C.20}$$

We use relation (2.38) to recover the Kubo-transform momentum autocorrelation spectrum from $\bar{c}_{pp}(\omega)$. The contribution of the overtone to the kinetic energy is then given, at second order in λ, by:

$$E_k(2\omega_0; \beta) = \frac{2\lambda^2}{9m^3\omega_0^6\beta}\Theta(\omega_0, \beta) \tag{C.21}$$

which yields η_Q as given by equation (5.25).

We now give the key elements to compute the resonance intensities for the bidimensional model of section 5.2. We start by splitting the Hamiltonian into:

$$\hat{H} = \hat{H}_{1,0} + \hat{H}_{2,0} + \lambda\hat{q}_1\hat{q}_2^2 \tag{C.22}$$

where $\hat{H}_{1,0}$ and $\hat{H}_{2,0}$ are the harmonic Hamiltonians of the unperturbed degrees of freedom. At first order in λ, the perturbed eigenstates are:

$$\tilde{\epsilon}_{n_1n_2} = \frac{\hbar\omega_1}{2}(2n_1+1) + \frac{\hbar\omega_2}{2}(2n_2+1) + \mathcal{O}\left(\lambda^2\right) \tag{C.23}$$

$$|\tilde{n}_1\tilde{n}_2\rangle = |n_1n_2\rangle + \frac{\lambda}{\hbar}\sum_{(k_1,k_2)\neq(n_1,n_2)} \frac{\langle k_1k_2|\hat{q}_1\hat{q}_2^2|n_1n_2\rangle}{\omega_1(n_1-k_1) + \omega_2(n_2-k_2)}|k_1k_2\rangle + \mathcal{O}\left(\lambda^2\right) \tag{C.24}$$

Using equations (C.5) and (C.6) for each degree of freedom, one can compute $\bar{c}_{p_1p_1}(t)$ and $\bar{c}_{p_2p_2}(t)$ in perturbation at second order in λ using the same method as for the previous model.

C.2 First order expansion of the Wigner distribution and of the EW0-QCF

In this section, we derive a perturbative expression of the Wigner density and of the quantum correction factor of the Edgeworth conditional momentum distribution for the potential (5.1) with the perturbation parameter λ. Both the thermal Wigner density and the EW0-QCF depend on the off-diagonal elements of the density matrix which we express in path integral form (in the continuous limit) by following reference [60] (section 12.4). In this section, we will use the shorthand notation $w(q,\Delta;\beta) \equiv \left\langle q-\frac{\Delta}{2}\middle|e^{-\beta\hat{H}}\middle|q-\frac{\Delta}{2}\right\rangle$. We then expand the path around the classical harmonic path and decompose the fluctuation path in Fourier components in order to obtain an analytical expressions of $w(q,\Delta;\beta)$ at first order in λ. Finally, we use this expression to obtain the Wigner density and the EW0-QCF at first order in λ.

For the potential (5.1), the continous path integral form of the off-diagonal density matrix elements are given by the following functional integral:

$$w(q,\Delta;\beta) = \int_{x(0)=q-\Delta/2}^{x(\beta\hbar)=q+\Delta/2} \mathcal{D}x(\tau) \exp\left\{-\frac{1}{\hbar}\int_0^{\beta\hbar} \mathrm{d}\tau \; \frac{m\dot{x}^2(\tau)}{2} + \frac{m\omega_0^2 x^2(\tau)}{2} + \frac{\lambda}{3}x^3(\tau)\right\} \tag{C.25}$$

which can be expanded at first order in λ as:

$$w(q,\Delta;\beta) = \int_{x(0)=q-\Delta/2}^{x(\beta\hbar)=q+\Delta/2} \mathcal{D}x(\tau) e^{-\frac{S_0[x]}{\hbar}}\left(1-\frac{\lambda}{3\hbar}\int_0^{\beta\hbar}\mathrm{d}\tau\; x^3(\tau) + \mathcal{O}\left(\lambda^2\right)\right) \tag{C.26}$$

with $S_0[x] = \int_0^{\beta\hbar}\mathrm{d}\tau\; \frac{m\dot{x}^2(\tau)}{2} + \frac{m\omega_0^2x^2(\tau)}{2}$ the harmonic imaginary-time action. The expansion in λ switched the problem from finding anharmonic paths to averaging a quantity on harmonic paths which is much simpler. As in ref. [60], we expand the path $x(\tau)$ about the classical harmonic path:

$$x(\tau) = x_0(\tau) + y(\tau) \tag{C.27}$$

where $x_0(\tau)$ is the classical harmonic path defined by the differential equation $m\ddot{x}_0 = m\omega_0^2 x_0$ with boundary conditions $x_0(0) = q - \Delta/2$ and $x_0(\beta\hbar) = q + \Delta/2$ which can be solved exactly as:

$$x_0(\tau) = \frac{(q-\frac{\Delta}{2})(e^{-\omega_0(\tau-\beta\hbar)} - e^{\omega_0(\tau-\beta\hbar)}) + (q+\frac{\Delta}{2})(e^{\omega_0\tau} - e^{-\omega_0\tau})}{e^{\beta\hbar\omega_0} - e^{-\beta\hbar\omega_0}} \tag{C.28}$$

and $y(\tau)$ is the fluctuation path (defined by the difference between the full path and the classical harmonic path) which has the property $y(0) = y(\beta\hbar) = 0$. One can

show (see ref. [60]) that the harmonic action is separable between the classical and fluctuation paths *i.e.* $e^{-\frac{S_0[x]}{\hbar}} = e^{-\frac{S_0[x_0]}{\hbar}} e^{-\frac{S_0[y]}{\hbar}}$. We thus obtain:

$$w(q,\Delta;\beta) = e^{-\frac{S_0[x_0]}{\hbar}} \oint \mathcal{D}y(\tau) e^{-\frac{S_0[y]}{\hbar}} \left(1 - \frac{\lambda}{3\hbar}\int_0^{\beta\hbar} \mathrm{d}\tau\ (x_0(\tau)+y(\tau))^3 + \mathcal{O}\left(\lambda^2\right)\right) \tag{C.29}$$

where the closed integral indicates a path starting and ending at 0. Due to the symmetries of the fluctuation paths the terms containing odd powers of $y(\tau)$ cancel when integrated over all paths and we obtain:

$$w(q,\Delta;\beta) = e^{-\frac{S_0[x_0]}{\hbar}} \oint \mathcal{D}y(\tau) e^{-\frac{S_0[y]}{\hbar}} \left(1 - \frac{\lambda}{3\hbar}\int_0^{\beta\hbar} \mathrm{d}\tau\ (x_0^3(\tau)+3x_0(\tau)y^2(\tau)) + \mathcal{O}\left(\lambda^2\right)\right) \tag{C.30}$$

One can show (by explicitly writing the functional integral in terms of a sum of Fourier coefficient as in ref. [60]) that the term proportional to $x_0(\tau)$ does not depend on Δ so that we can write:

$$w(q,\Delta;\beta) = w_0(q,\Delta;\beta)\left(1 - \frac{\lambda}{3\hbar}[a(q,\Delta)+b(q)] + \mathcal{O}\left(\lambda^2\right)\right) \tag{C.31}$$

with $w_0(q,\Delta;\beta)$ the harmonic off-diagonal element given by equation (4.39) and the functions a and b defined as:

$$a(q,\Delta) = \int_0^{\beta\hbar} \mathrm{d}\tau x_0^3(\tau) \tag{C.32}$$

$$b(q) = \frac{1}{I_0}\oint \mathcal{D}y(\tau) e^{-\frac{S_0[y]}{\hbar}} \int_0^{\beta\hbar} \mathrm{d}\tau\ 3x_0(\tau)y^2(\tau) \tag{C.33}$$

with the constant $I_0 = \oint \mathcal{D}y(\tau) e^{-\frac{S_0[y]}{\hbar}}$. Analytical expressions of the functions $a(q,\Delta)$ and $b(q)$ can be obtained using the Fourier decomposition of the fluctuation path. We used the symbolic computation software SageMath to obtain these analytical expressions:

$$a(q,\Delta) = \frac{q\hbar}{2\Theta(\omega_0,\beta)}\left(\frac{\Delta^2}{2} + \frac{4}{3}q^2\left(\frac{5}{2} - \frac{\Theta(2\omega_0,\beta)}{\Theta(\omega_0,\beta)}\right)\right) \tag{C.34}$$

$$b(q) = \frac{2q\hbar}{m\omega_0^2}\left(\frac{\Theta(2\omega_0,\beta)}{\Theta(\omega_0,\beta)} - 1\right) \tag{C.35}$$

with $\Theta(\omega_0,\beta) = \frac{\hbar\omega_0/2}{\tanh(\beta\hbar\omega_0/2)}$. Using the parity of $w_0(q,0;\beta)$, we obtain that the perturbed partition function $\mathcal{Z} = \int \mathrm{d}q\ w(q,0;\beta)$ is equal to the harmonic partition function $\mathcal{Z}_0$. Finally, we compute explicitly the Fourier transform of $w(q,\Delta;\beta)$ with

respect to Δ to obtain the perturbative expression of the Wigner density of equation 5.27:

$$\rho_{\text{w}}(q,p) = \rho_{\text{w},0}(q,p)\Bigg[1 - \frac{\lambda q}{m\omega_0^2}\left(\frac{\Theta(2\omega_0,\beta)}{\Theta(\omega_0,\beta)} - 1\right) - \frac{2\lambda q^3}{9\Theta(\omega_0,\beta)}\left(\frac{5}{2} - \frac{\Theta(2\omega_0,\beta)}{\Theta(\omega_0,\beta)}\right) + \frac{\lambda q p^2}{3m^2\omega_0^2\Theta(\omega_0,\beta)}\left(\frac{\Theta(2\omega_0,\beta)}{\Theta(\omega_0,\beta)} - 1\right)\Bigg] + \mathcal{O}\left(\lambda^2\right) \quad \text{(C.36)}$$

with the harmonic Wigner distribution

$$\rho_{\text{w},0}(q,p) = \frac{e^{-\frac{1}{\Theta(\omega_0,\beta)}\left(\frac{p^2}{2m} + \frac{1}{2}m\omega_0^2 q^2\right)}}{\int \mathrm{d}q\mathrm{d}p e^{-\frac{1}{\Theta(\omega_0,\beta)}\left(\frac{p^2}{2m} + \frac{1}{2}m\omega_0^2 q^2\right)}} \quad \text{(C.37)}$$

To obtain the EW0-QCF, we compute the conditional distribution of Δ of equation (4.4):

$$\rho_c(\Delta|q) = \rho_{c,0}(\Delta|q)\left[1 - \frac{\lambda}{3\hbar}\left(a(q,\Delta) - \langle a(q,\Delta)\rangle_{\rho_{c,0}|q}\right)\right] + \mathcal{O}\left(\lambda^2\right) \quad \text{(C.38)}$$

with the harmonic distribution $\rho_{c,0}(\Delta|q) = w_0(q,\Delta;\beta)/\int \mathrm{d}\Delta w_0(q,\Delta;\beta)$. Using equation (4.5) we then obtain:

$$\begin{aligned}\kappa_2(q) &= \kappa_{2,0}\left[1 - \frac{\lambda}{3\hbar}\left(\frac{\langle\Delta^2 a(q,\Delta)\rangle_{\rho_{c,0}|q}}{\langle\Delta^2\rangle_{\rho_{c,0}|q}} - \langle a(q,\Delta)\rangle_{\rho_{c,0}|q}\right)\right] + \mathcal{O}\left(\lambda^2\right) \\ &= \kappa_{2,0}\left[1 - \frac{2\lambda q}{3m\omega_0^2}\left(\frac{\Theta(2\omega_0,\beta)}{\Theta(\omega_0,\beta)} - 1\right)\right] + \mathcal{O}\left(\lambda^2\right) \end{aligned} \quad \text{(C.39)}$$

with $\kappa_{2,0}$ by equation (4.40). Using equations (4.50), we obtain the EW0-QCF of equation (5.34).

We can also show that the EW0 distribution that the WiLD samples is exact at first order in λ. The EW0 distribution is given by:

$$\rho_{\text{EW0}}(q,p) = \frac{e^{-\beta U(q) - \kappa_2(q)p^2/2\hbar^2}}{\int \mathrm{d}q\mathrm{d}p\, e^{-\beta U(q) - \kappa_2(q)p^2/2\hbar^2}} \quad \text{(C.40)}$$

with $\kappa_2(q)$ given at first order by eq. C.39 and

$$e^{-\beta U(q)} = \int \mathrm{d}\Delta \; w(q,\Delta;\beta) \tag{C.41}$$

$$= \frac{e^{-\frac{m\omega_0^2 q^2}{2\Theta(\omega_0,\beta)}}}{\sqrt{m\Theta(\omega_0,\beta)/2\pi\hbar^2}} \left[[1 - \frac{\lambda q}{m\omega_0^2}\left(\frac{\Theta(2\omega_0,\beta)}{\Theta(\omega_0,\beta)} - 1\right) \right. \tag{C.42}$$

$$\left. - \frac{2\lambda q^3}{9\Theta(\omega_0,\beta)}\left(\frac{5}{2} - \frac{\Theta(2\omega_0,\beta)}{\Theta(\omega_0,\beta)}\right)\right] + \mathcal{O}\left(\lambda^2\right) \tag{C.43}$$

We can then show that $\rho_{\text{EW0}}(q,p) = \rho_{\text{w}}(q,p) + \mathcal{O}(\lambda^2)$ and thus the WiLD samples the exact Wigner distribution at first order in λ.

Finally, we compute the successive cumulants of ρ_c to show that the Edgeworth correction does not modify the ECMA distribution at first order. The fourth order moment of ρ_c is

$$\begin{aligned}\left\langle \Delta^4 \right\rangle_{\rho_c|q} &= \left\langle \Delta^4 \right\rangle_{\rho_{c,0}|q} \left[1 - \frac{\lambda}{3\hbar}\left(\frac{\left\langle \Delta^4 a(q,\Delta)\right\rangle_{\rho_{c,0}|q}}{\left\langle \Delta^4\right\rangle_{\rho_{c,0}|q}} - \left\langle a(q,\Delta)\right\rangle_{\rho_{c,0}|q}\right)\right] + \mathcal{O}\left(\lambda^2\right) \\ &= 3\kappa_{2,0}^2\left[1 - \frac{4\lambda q}{3m\omega_0^2}\left(\frac{\Theta(2\omega_0,\beta)}{\Theta(\omega_0,\beta)} - 1\right)\right] + \mathcal{O}\left(\lambda^2\right)\end{aligned} \tag{C.44}$$

so that we obtain for the fourth order cumulant $\kappa_4(q) = \left\langle \Delta^4 \right\rangle_{\rho_c|q} - 3\kappa_2^2(q) = \mathcal{O}(\lambda^2)$. If we now suppose that, for any even integer m, all of the cumulants from κ_j for j between 4 and $m-2$ (included) are null at first order in λ, we can use the recursion formula for the cumulants:

$$\begin{aligned}\kappa_m(q) &= \left\langle \Delta^m \right\rangle_{\rho_c|q} - \sum_{j=2,\text{ even}}^{m-2} \binom{m-1}{j-1} \kappa_j(q) \left\langle \Delta^{m-j} \right\rangle_{\rho_c|q} \\ &= \left\langle \Delta^m \right\rangle_{\rho_c|q} - (m-1)\kappa_2(q) \left\langle \Delta^{m-2} \right\rangle_{\rho_c|q}\end{aligned} \tag{C.45}$$

For this expression, using similar reasoning as above for κ_4, one can show that $\kappa_m(q) = \mathcal{O}(\lambda^2)$. Therefore, by the recursion principle, all of the cumulants of ρ_c of order higher than two are null at first order in λ and thus the Edgeworth correction does not contribute to the first order expansion of the ECMA and WiLD distributions.

C.3 Full expressions of the combination bands intensities in LHA

The contributions of the combination bands to the LSC-LHA vibrational density of states are:

$$\eta_{\mathrm{LHA}}(\beta;\omega_1+\omega_2) = \eta_{\mathrm{Q}}(\beta;\omega_1+\omega_2)\ \gamma^{\mathrm{LHA}}_{\omega_1+\omega_2}$$
$$\eta_{\mathrm{LHA}}(\beta;\omega_1-\omega_2) = \eta_{\mathrm{Q}}(\beta;\omega_1-\omega_2)\ \gamma^{\mathrm{LHA}}_{\omega_1-\omega_2}$$
$$\eta_{\mathrm{LHA}}(\beta;2\omega_2) = \eta_{\mathrm{Q}}(\beta;2\omega_2)\ \gamma^{\mathrm{LHA}}_{2\omega_2}$$

with (the last step of the perturbative calculation is performed on a formal computing software, more compact expressions might potentially be found):

$$\begin{aligned}\gamma^{\mathrm{LHA}}_{\omega_1+\omega_2} =& \Big[\hbar^2\beta\Theta(\omega_1,\beta)(\omega_1^4\omega_2^2+2\omega_1^3-\omega_1^2\omega_2^4-2\omega_1\omega_2^5)-\Theta^2(\omega_2,\beta)(16\omega_1^2\omega_2^2+8\omega_1\omega_2^3)\\ &+\beta\Theta(\omega_1,\beta)\Theta^2(\omega_2,\beta)(-4\omega_1^4-8\omega_1^3\omega_2+4\omega_1^2\omega_2^2+8\omega_1\omega_2^3)\\ &+\Theta(\omega_1,\beta)\Theta(\omega_2,\beta)(4\omega_1^4+16\omega_1^3\omega_2+20\omega_1^2\omega_2^2-8\omega_1\omega_2^3-8\omega_2^4)\Big]\\ &/\Big[8\omega_2(\omega_1\Theta(\omega_2,\beta)+\omega_2\Theta(\omega_1,\beta))(\omega_1^2-\omega_2^2)\Theta(\omega_1+\omega_2)\Big]\end{aligned}$$

$$\begin{aligned}\gamma^{\mathrm{LHA}}_{\omega_1-\omega_2} =& \Big[\hbar^2\beta\Theta(\omega_1,\beta)(\omega_1^4\omega_2^2-2\omega_1^3-\omega_1^2\omega_2^4+2\omega_1\omega_2^5)-\Theta^2(\omega_2,\beta)(16\omega_1^2\omega_2^2-8\omega_1\omega_2^3)\\ &+\beta\Theta(\omega_1,\beta)\Theta^2(\omega_2,\beta)(-4\omega_1^4+8\omega_1^3\omega_2+4\omega_1^2\omega_2^2-8\omega_1\omega_2^3)\\ &+\Theta(\omega_1,\beta)\Theta(\omega_2,\beta)(4\omega_1^4-16\omega_1^3\omega_2+20\omega_1^2\omega_2^2+8\omega_1\omega_2^3-8\omega_2^4)\Big]\\ &/\Big[8\omega_2(\omega_1\Theta(\omega_2,\beta)-\omega_2\Theta(\omega_1,\beta))(\omega_1^2-\omega_2^2)\Theta(\omega_1-\omega_2)\Big]\end{aligned}$$

$$\gamma^{\mathrm{LHA}}_{2\omega_2} = \frac{\Theta(\omega_2,\beta)(\omega_1^2-4\omega_2^2)+3\omega_2^2\Theta(\omega_1,\beta)}{\Theta(\omega_2,\beta)(\omega_1^2-\omega_2^2)}$$